

**USE OF METHODS TO INVESTIGATE TRANSPORT  
PHENOMENA OF MULTIPHASE TURBULENT FLOW**

by

**ANDREW ROBINSON**

A thesis submitted to  
The University of Birmingham  
For the degree of  
**DOCTOR OF PHILOSOPHY**

School of Chemical Engineering

University of Birmingham

December 2014

UNIVERSITY OF  
BIRMINGHAM

**University of Birmingham Research Archive**

**e-theses repository**

This unpublished thesis/dissertation is copyright of the author and/or third parties. The intellectual property rights of the author or third parties in respect of this work are as defined by The Copyright Designs and Patents Act 1988 or as modified by any successor legislation.

Any use made of information contained in this thesis/dissertation must be in accordance with that legislation and must be properly acknowledged. Further distribution or reproduction in any format is prohibited without the permission of the copyright holder.

## ABSTRACT

The mixing of multiphase turbulent flow within a column is investigated using Positron-Emission Particle-Tracking (PEPT) to understand the controlling phenomena of convection of heat towards the inside surface of its wall in the measurement of the inside-wall heat transfer coefficient by inverse analysis. This is part of a design options study initiated by Rolls-Royce for a key process in the reclamation of uranium from uranium bearing materials.

The column contains water and electrolyte and loose metallic swarf. Compressed air is distributed into the column from a perforated plate and hence the multiphase flow is gravity driven. A dynamic assessment of mixing is provided through the framework of the Reynolds-Averaged Navier-Stokes (RANS) equation in the evaluation of stresses within the multiphase flow. Inverse analysis of heat conduction across the wall of the column provides measurement of the inside-wall heat transfer coefficient.

The mixing of swarf coincides with the convergence of the stationary dynamics of the multiphase turbulent flow measured using PEPT. Tikhonov regularisation affords the resolution of the inside-wall heat transfer coefficient of the inverse analysis. A common global gas hold-up between different flows segregates the controlling phenomena of momentum transfer and convection of heat towards the inside surface of the column wall.

## ACKNOWLEDGEMENTS

For guidance and presentation of the work contained within this thesis I would like to thank Professor Peter Fryer (University of Birmingham), Professor Mark Simmons (University of Birmingham), Dr Philip Robbins (University of Birmingham) and Steve Curr (Rolls-Royce Submarines, Chief Technologist - Core).

For the preparation of particle tracers and provision of the TRACK algorithm used in the PEPT investigation I would like to thank Professor David Parker (University of Birmingham), Dr Thomas Leadbeater (University of Birmingham) and Dr Joseph Garagiuli (University of Birmingham).

For the additional funding to complete the write-up of this work I would like to thank Rolls-Royce.

# TABLE OF CONTENTS

<b>Chapter 1: INTRODUCTION</b>	1
1.1 Process design and engineering	1
1.2 Chemical processing and risk	3
1.2.1 The swarf dissolver process	3
1.2.2 Modification of swarf dissolver geometry	4
1.3 Operation of cylinder concept for the dissolution of swarf	6
1.4 Aims and structure of thesis	7
<b>Chapter 2: THERMOCHEMISTRY OF SWARF DISSOLUTION AND THERMAL OPERATING ENVELOPE OF CYLINDER CONCEPT</b>	9
2.1 Introduction	9
2.2 Enthalpy of dissolution	10
2.3 Thermal operating envelope	16
2.3.1 Parameterisation	16
2.3.2 Linear programming and model equations	
<b>Chapter 3: LITERATURE SURVEY</b>	23
3.1 Introduction	23
3.2 Chemical processing and measurement of transport phenomena	24
3.3 Positron-Emission Particle-Tracking (PEPT)	26
3.4 Advancements in the PEPT technique	26
3.4.1 The RAL camera and track algorithm	27
3.4.2 The ADAC forte camera	29
3.4.3 PEPT Particle tracers	30
3.5 Applications of the PEPT technique	31
<i>Parker et al. (1993) Positron emission particle tracking – a technique for studying flow within engineering equipment</i>	32
<i>Parker et al. (1997b) Positron emission particle tracking studies on spherical particle motion in rotating drums</i>	33
<i>Stewart et al. (2001) Granular flow over a flat bladed stirrer</i>	36
<i>Bakalis &amp; Fryer (2004) Measuring velocity distributions of viscous fluids using positron emission particle tracking (PEPT)</i>	38
<i>Guida et al. (2010) PEPT measurements of solid-liquid flow field and spatial phase distribution in concentrated monodisperse stirred suspensions</i>	40
3.6 Summary of the PEPT technique	42
3.7 Boundary inverse methods for heat conduction	43
3.8 Application and development of the IHCP	45
<i>Stolz (1960) Numerical solutions to an inverse problem of heat conduction for simple shapes</i>	45
<i>Beck (1967) Surface heat flux determination using an integral method</i>	46
<i>Imber &amp; Khan (1972) Prediction of transient temperature distributions with</i>	47

<i>embedded thermocouples</i>	
<i>Beck (1977) Criteria for comparison of methods of solution of the inverse heat conduction problem</i>	47
<i>Weber (1981) Analysis and solution of the ill-posed inverse heat conduction problem</i>	48
<i>Scott &amp; Beck (1985) Analysis of order of sequential regularisation solution of inverse heat conduction problem</i>	49
<i>Alifanov (1994) Inverse heat transfer problems</i>	50
3.9 Summary of boundary inverse methods	51
<b>Chapter 4: MIXING OF SWARF AND VISCOUS FLUID WITHIN CYLINDER CONCEPT</b>	<b>53</b>
4.1 Introduction	53
4.2 The distribution of gas within a column of viscous fluid	54
4.2.1 The perforated plate and column used to investigate mixing within the cylinder concept	56
4.3 Dissipative phenomena and continuity	57
4.4 Flow description of a viscous fluid	60
4.5 Mixing of swarf within a turbulent flow of a viscous fluid	65
4.6 The PEPT technique	68
4.7 Flow visualisation	71
4.8 Computational Fluid Dynamics of the free surface of the air-water interface	73
4.8.1 Phase field method	74
4.8.2 Simulation of a void rising through water	77
4.8.3 Results of simulation	80
4.9 PEPT experiments	82
4.10 Eulerian-Lagrangian analysis of PEPT data	84
4.11 Results of Eulerian-Lagrangian analysis of PEPT experiments	88
4.11.1 Lagrangian trajectories of the PEPT particle tracer	88
4.11.2 Instantaneous velocity, vorticity and Reynolds stress spectra	89
4.11.3 Ensemble averaging and convergence of mean tensor components	91
4.11.4 Volume force and swarf occupancy belonging to the stationary dynamics of mixing of swarf	93
4.12 Conclusion	95
<b>Chapter 5: HEAT TRANSFER WITHIN CYLINER CONCEPT</b>	<b>157</b>
5.1 Introduction	157
5.2 Green's function and inverse analysis	157
5.2.1 Inverse analysis	160
5.3 Analysis by regularised boundary inverse method	162
5.3.1 Least-squares and Tikhonov regularisation	162
5.3.2 Duhamel's theorem and auxiliary problems	164
5.4 Sensitivity and simulation of regularisation	168
5.4.1 Transient model	169
5.4.2 Regularisation	173
5.5 Temperature measurement and inconel wall	176

5.6 Inverse experiments	178
5.7 Results of inverse experiments	180
5.7.1 Inside-wall heat transfer coefficient of air-water-swarf flow	181
5.7.2 Flow perturbations and local heat convection	183
5.8 Conclusion	185
<b>Chapter 6: CONCLUSION</b>	<b>223</b>
6.1 Transfer of momentum within the air-water-swarf column	224
6.2 Transfer of heat within the air-water-swarf column	225
6.3 Contributions and further work	226
6.3.1 Further work	228
APPENDIX 1 TAYLORS THEOREM AROUND INCIDENCE $i$	230
APPENDIX 2 ERROR PROPAGATION IN CALCULATED VELOCITY AND REYNOLDS TENSOR COMPONENTS	232
APPENDIX 3 MATLAB <sup>®</sup> m-files	236
APPENDIX 4	257
REFERENCES	262

## LIST OF FIGURES

### CHAPTER 1

**Figure 1.1** The operation of the batch process of swarf dissolution within the cylinder concept. 8

### CHAPTER 2

**Figure 2.1** Arbitrary thermal operating envelope for the cylinder concept. The drawn lines coincide with equations (2.56), (2.57) and (2.58) of Subheading 2.3.2. The bound shaded region indicates the envelope. 22

### CHAPTER 4

**Figure 4.1** A drawing showing the arrangement of the Perspex column and polypropylene assembly (Rolls-Royce drawings). 117

**Figure 4.2** A drawing of the inconel perforated plate showing the number of holes and array pattern (Rolls-Royce drawings). 118

**Figure 4.3** Image of heterogeneous flow of air-water column for flow visualisation experiment 1; superficial gas velocity 6.1 cm/s. Internal column diameter of 144 mm. TIFF image belongs to file flow\_vis\_ext\_1.avi. 119

**Figure 4.4** Image of heterogeneous flow of air-water column for flow visualisation experiment 2; superficial gas velocity 6.1 cm/s, 1 kg of dissolved sodium chloride. Internal column diameter of 144 mm. TIFF image belongs to file flow\_vis\_ext\_2.avi. 120

**Figure 4.5** Image of heterogeneous flow of air-water-swarf column for flow visualisation experiment 3; superficial gas velocity 6.1 cm/s, 1 kg of dissolved sodium chloride, 500 g of loose swarf. Internal column diameter of 144 mm. TIFF image belongs to file flow\_vis\_ext\_3.avi. 121

**Figure 4.6** Image of heterogeneous flow of air-water-swarf column for flow visualisation experiment 4; superficial gas velocity 6.1 cm/s, 500 g of loose swarf. Internal column diameter of 144 mm. TIFF image belongs to file flow\_vis\_ext\_4.avi. 122

**Figure 4.7** The individual domains and boundary conditions (bc) of the simulation of a void rising through a column of water. The simulation is for 2-dimensional axisymmetric flow. Domain **A** represents the initial spherical void of diameter 20 mm. Both domains **B** and **C** represent the column of water initially at rest. The column diameter is 144 mm. 123

**Figure 4.8** Free triangular mesh used in the simulation of a void rising through a column of water. In the region of the phase field interface the maximum element size is 0.5 mm and corresponds to the denser mesh region to the left of the domain. Some non-uniformity of the mesh occurs because of the curvature of the interface in this region. Total number of mesh elements equals 41530. 124

**Figure 4.9** Mass conservation of the air void throughout the duration of the simulation. The maximum change in mass of the air void during the simulation is ~0.7%. 125

**Figure 4.10** The simulation of the generation and shedding of instantaneous vorticity from the free-surface of the interface as the air void rises through a column of water initially at rest. The initial shape of the air void is spherical and of diameter 20 mm. 126

**Figure 4.10** Continued. 127

**Figure 4.11** The simulation of axial velocity of the air void and within the surrounding water as the void rises through a column of water initially at rest. The 128



initial shape of the air void is spherical and of diameter 20 mm.	
<b>Figure 4.11</b> Continued.	129
<b>Figure 4.12</b> The simulation of radial velocity of the void and within the surrounding water as the air void rises through a column of water initially at rest. The initial shape of the air void is spherical and of diameter 20 mm.	130
<b>Figure 4.12</b> Continued.	131
<b>Figure 4.13</b> The simulation of dynamic pressure within the air void and surrounding water as the void rises through a column of water initially at rest. The initial shape of the air void is spherical and of diameter 20 mm.	132
<b>Figure 4.13</b> Continued.	133
<b>Figure 4.14</b> A photograph of heterogeneous flow within the air-water-swarf column prior to PEPT experiments.	134
<b>Figure 4.15</b> A photograph of the static swarf bed within the air-water-swarf column prior to PEPT experiments.	135
<b>Figure 4.16</b> A photograph of the air-water-swarf column positioned between the PEPT camera heads. The perforated plate protrudes 50 mm into the field of view and the flow is monitored over a height of 400 mm.	136
<b>Figure 4.17</b> Instantaneous axial velocity spectra for PEPT experiment 3 in grid segment 2,5 ( $r = 2.16$ cm, $z = 11$ cm); superficial air velocity 7.2 cm/s. Axial velocity calculated using equation (4.49) from the trajectory of a 500 micron particle tracer sampled at ~50 Hz over a duration of 120 minutes.	137
<b>Figure 4.18</b> Instantaneous Reynolds shear stress spectra for PEPT experiment 3 in grid segment 2,5 ( $r = 2.16$ cm, $z = 11$ cm); superficial air velocity 7.2 cm/s. Instantaneous velocities calculated using equation (4.49) from the trajectory of a 500 micron particle tracer sampled at ~50 Hz over a duration of 120 minutes.	138
<b>Figure 4.19</b> Instantaneous axial velocity spectra for PEPT experiment 4 in grid segment 3,7 ( $r = 3.6$ cm, $z = 15$ cm); superficial air velocity 7.2 cm/s, 500 g of loose swarf. Axial velocity calculated using equation (4.49) from the trajectory of a 500 micron particle tracer sampled at ~50 Hz over a duration of 120 minutes.	139
<b>Figure 4.20</b> Instantaneous Reynolds shear stress spectra for PEPT experiment 4 in grid segment 3,7 ( $r = 3.6$ cm, $z = 15$ cm); superficial air velocity 7.2 cm/s, 500 g of loose swarf. Instantaneous velocities calculated using equation (4.49) from the trajectory of a 500 micron particle tracer sampled at ~50 Hz over a duration of 120 minutes.	140
<b>Figure 4.21</b> Instantaneous angular velocity (axial) spectra for PEPT experiment 4 in grid segment 3,7 ( $r = 3.6$ cm, $z = 15$ cm); superficial air velocity 7.2 cm/s, 500 g of loose swarf. Angular velocity calculated using equation (4.49) from the trajectory of a 500 micron particle tracer sampled at ~50 Hz over a duration of 120 minutes.	141
<b>Figure 4.22</b> Global instantaneous axial velocity for PEPT experiment 1; superficial air velocity 4.1 cm/s. Axial velocity calculated using equation (4.49) from the trajectory of a 500 micron particle tracer sampled at ~50 Hz over a duration of 120 minutes.	142
<b>Figure 4.23</b> Global instantaneous radial velocity for PEPT experiment 1; superficial air velocity 4.1 cm/s. Radial velocity calculated using equation (4.49) from the trajectory of a 500 micron particle tracer sampled at ~50 Hz over a duration of 120 minutes.	143
<b>Figure 4.24</b> Global instantaneous axial velocity for PEPT experiment 2; superficial air velocity 4.1 cm/s, 1 kg of dissolved sodium chloride. Axial velocity calculated	144

using equation (4.49) from the trajectory of a 500 micron particle tracer sampled at ~50 Hz over a duration of 120 minutes.

**Figure 4.25** Global instantaneous radial velocity for PEPT experiment 2; superficial air velocity 4.1 cm/s, 1 kg of dissolved sodium chloride. Radial velocity calculated using equation (4.49) from the trajectory of a 500 micron particle tracer sampled at ~50 Hz over a duration of 120 minutes. 145

**Figure 4.26** Global instantaneous azimuthal vorticity spectra for PEPT experiment 1; superficial air velocity 4.1 cm/s. Azimuthal vorticity calculated using derivatives of asymmetric differencing as shown in equation (4.51) from the trajectory of a 500 micron particle tracer sampled at ~50 Hz over a duration of 120 minutes. 146

**Figure 4.27** Global instantaneous azimuthal vorticity spectra for PEPT experiment 2; superficial air velocity 4.1 cm/s, 1 kg of dissolved sodium chloride. Azimuthal vorticity calculated using derivatives of asymmetric differencing as shown in equation (4.51) from the trajectory of a 500 micron particle tracer sampled at ~50 Hz over a duration of 120 minutes. 147

**Figure 4.28** Global instantaneous azimuthal vorticity spectra for experiment 3; superficial air velocity 7.2 cm/s. Azimuthal vorticity calculated using derivatives of asymmetric differencing as shown in equation (4.51) from the trajectory of a 500 micron particle tracer sampled at ~50 Hz over a duration of 120 minutes. 148

**Figure 4.29** Global instantaneous azimuthal vorticity spectra for experiment 4; superficial air velocity 7.2 cm/s, 500 g of loose swarf. Azimuthal vorticity calculated using derivatives of asymmetric differencing as shown in equation (4.51) from the trajectory of a 500 micron particle tracer sampled at ~50 Hz over a duration of 120 minutes. 149

**Figure 4.30** Global instantaneous azimuthal vorticity spectra for experiment 6; superficial air velocity 4.1 cm/s, 1 kg of dissolved sodium chloride, 500 g of loose swarf. Azimuthal vorticity calculated using derivatives of asymmetric differencing as shown in equation (4.51) from the trajectory of a 500 micron particle tracer sampled at ~50 Hz over a duration of 200 minutes. 150

**Figure 4.31** Convergence of Reynolds shear stress and axial velocity towards their mean values for PEPT experiment 4 in grid segment 3,7 ( $r = 3.6$  cm,  $z = 15$  cm). 151

**Figure 4.32** Convergence of azimuthal tensor component for PEPT experiment 6 in grid segment 4,16 ( $r = 5.04$  cm,  $z = 33.0$  cm); superficial air velocity 4.1 cm/s, 1 kg of dissolved sodium chloride, 500 g of loose swarf. Instantaneous velocities calculated using equation (4.49) from the trajectory of a 500 micron particle tracer sampled at ~50 Hz over a duration of 200 minutes. 152

**Figure 4.33** Reynolds shear stress at different superficial air velocities: ■ = *Menzel et al.* 7.2 cm/s, ● = PEPT experiment 3 (7.2 cm/s), ■ = *Menzel et al.* 4.8 cm/s, ● = PEPT experiment 1 (4.1 cm/s). 152

**Figure 4.34** Occupancy of swarf for PEPT experiment 7; superficial air velocity 4.1 cm/s, 1 kg of dissolved sodium chloride, 500 g of loose swarf. Indices obtained from the trajectory of a directly activated piece of swarf sampled at ~20 Hz over a duration of 60 minutes. 153

**Figure 4.35** Occupancy of swarf for PEPT experiment 5; superficial air velocity 7.2 cm/s, 500 g of loose swarf. Incidences obtained from the trajectory of a directly activated piece of swarf sampled at ~20 Hz over a duration of 60 minutes. 154

**Figure 4.36** Volume force ( $\text{mN/cm}^3$ ) resolved from the tensor components of the LHS of equation (4.31) for PEPT experiment 6; superficial air velocity 4.1 cm/s, 1 kg 155

of dissolved sodium chloride, 500 g of loose swarf. Instantaneous velocities calculated using equation (4.49) from the trajectory of a 500 micron particle tracer sampled at ~50 Hz over a duration of 200 minutes. Ensemble averaging of the instantaneous velocities is achieved using equation (4.24) for the calculation of the mean field terms.

**Figure 4.37** Volume force ( $\text{mN/cm}^3$ ) resolved from the tensor components of the LHS of equation (4.31) for PEPT experiment 4; superficial air velocity 7.2 cm/s, 500 g of loose swarf. Instantaneous velocities calculated using equation (4.49) from the trajectory of a 500 micron particle tracer sampled at ~50 Hz over a duration of 120 minutes. Ensemble averaging of the instantaneous velocities is achieved using equation (4.24) for the calculation of the mean field terms. 156

## CHAPTER 5

**Figure 5.1** Temperature transient of fluid calculated using equation (5.46). Temperature transients of the inside surface of the wall at  $r = a = 72$  mm calculated using equation (5.47) for different wall thickness ( $b - a$ ). Transient temperature differences between the fluid and inside surface of the wall at  $r = a = 72$  mm calculated using equation (5.46) and (5.47). In all calculations  $h = 1000 \text{ W/m}^2 \text{ }^\circ\text{C}$ . 189

**Figure 5.2** Temperature transient of fluid calculated using equation (5.46). Temperature transients of the inside surface of the wall at  $r = a = 72$  mm calculated using equation (5.47) for different wall thickness ( $b - a$ ). Transient temperature differences between the fluid and inside surface of the wall at  $r = a = 72$  mm calculated using equation (5.46) and (5.47). In all calculations  $h = 2000 \text{ W/m}^2 \text{ }^\circ\text{C}$ . 190

**Figure 5.3** Temperature transient of fluid calculated using equation (5.46). Temperature transients of the inside surface of the wall at  $r = a = 72$  mm calculated using equation (5.47) for different wall thickness ( $b - a$ ). Transient temperature differences between the fluid and inside surface of the wall at  $r = a = 72$  mm calculated using equation (5.46) and (5.47). In all calculations  $h = 3000 \text{ W/m}^2 \text{ }^\circ\text{C}$ . 191

**Figure 5.4** Sensitivity elements for a Dirichlet boundary condition at  $r = a = 72$  mm calculated using equation (5.28) for different wall thickness ( $b - a$ ) and sampling rate. 192

**Figure 5.5** Sensitivity elements for a Neumann boundary condition at  $r = a = 72$  mm calculated using equation (5.37) for different wall thickness ( $b - a$ ) and sampling rate. 193

**Figure 5.6** Simulation of inverse solution of normal heat flux at  $r = a = 72$  mm calculated using equation (5.15) and the simulated temperature history of equation (5.47) and (5.51) at  $r = b = 76.25$  mm. Value of regularisation coefficient is  $10^{-7}$ . Sensitivity elements of sensitivity matrix of equation (5.15) calculated using equation (5.37). 194

**Figure 5.7** Simulation of inverse solution of temperature of inside surface of wall at  $r = a = 72$  mm calculated using equation (5.15) and the simulated temperature history of equation (5.47) and (5.51) at  $r = b = 76.25$  mm. Value of regularisation coefficient is 10. Sensitivity elements of sensitivity matrix of equation (5.15) calculated using equation (5.28). 195

**Figure 5.8** Simulation of inverse solution of inside-wall heat transfer coefficient belonging to the inside surface of the wall at  $r = a = 72$  mm. Calculation of inside-wall heat transfer coefficient is achieved by dividing the calculated inverse heat flux of the inside surface of the wall at  $r = a = 72$  mm by the difference of the fluid 196

temperature (equation (5.46)) and the calculated inverse temperature of the inside surface of the wall at  $r = a = 72$  mm.

**Figure 5.9** A drawing of the inconel wall of the inconel cylinder used in the inverse analysis of the inside-wall heat transfer coefficient for air-water-swarf flow. Inconel bosses along the height of the column house mineral insulated thermocouples using PTFE compression fittings (Rolls-Royce drawings). 197

**Figure 5.10** A photograph of a PTFE compression fitting used to house mineral insulated thermocouples in inconel bosses. 198

**Figure 5.11** A photograph of mineral insulated thermocouples inside inconel cylinder. 199

**Figure 5.12** A photograph of the location of polyimide thin film thermocouples on the outside surface of the inconel cylinder. Polyimide thermocouples are orthogonal to mineral insulated thermocouples. 200

**Figure 5.13** A photograph of the insulated outside surface of the inconel cylinder. 201

**Figure 5.14** Transient profile of temperature of fluid and insulated outside surface of the wall for inverse experiment 1 achieved by the addition of boiling water at the top of the inconel column. Temperature is measured at heights 100 mm and 350 mm. 202

**Figure 5.15** Inverse solution of normal heat flux of inside surface of the wall at  $r = a = 72$  mm for experiment 1 at height 350 mm calculated using equation (5.15). The sensitivity matrix of equation (5.15) is constructed of sensitivity elements obtained from equation (5.37) for wall thickness  $(b - a) = 4.25$  mm. Superficial air velocity of 4.1 cm/s, 1 kg of dissolved sodium chloride, 500 g of loose swarf. 203

**Figure 5.16** Inverse solution of temperature of inside surface of the wall at  $r = a = 72$  mm for experiment 1 at height 350 mm calculated using equation (5.15). The sensitivity matrix of equation (5.15) is constructed of sensitivity elements obtained from equation (5.28) for wall thickness  $(b - a) = 4.25$  mm. Measured fluid temperature taken from mineral insulated thermocouples at height 350 mm. Superficial air velocity of 4.1 cm/s, 1 kg of dissolved sodium chloride, 500 g of loose swarf. 204

**Figure 5.17** Inverse solution of heat transfer coefficient belonging to inside surface of the wall at  $r = a = 72$  mm for experiment 1 at height 350 mm. The inverse normal heat flux is divided by the difference between the inverse temperature of the inside surface of the wall at  $r = a = 72$  mm and the measured fluid temperature at height 350 mm. The centre of the circle indicates where Tikhonov regularisation is localised and where the inside-wall heat transfer coefficient is resolved. Superficial air velocity 4.1 cm/s, 1 kg of dissolved sodium chloride, 500 g of loose swarf. 205

**Figure 5.18** Inverse solution of heat transfer coefficient belonging to inside surface of the wall at  $r = a = 72$  mm for experiment 1 at height 350 mm. The inverse normal heat flux is divided by the difference between the inverse solution of temperature of the inside surface of the wall at  $r = a = 72$  mm and the measured fluid temperature at height 350 mm. Superficial air velocity 4.1 cm/s, 1 kg of dissolved sodium chloride, 500 g of loose swarf. 206

**Figure 5.19** Inverse solution of normal heat flux of inside surface of the wall at  $r = a = 72$  mm for experiment 1 at height 100 mm calculated using equation (5.15). The sensitivity matrix of equation (5.15) is constructed of sensitivity elements obtained from equation (5.37) for wall thickness  $(b - a) = 4.25$  mm. Superficial air velocity of 4.1 cm/s, 1 kg of dissolved sodium chloride, 500 g of loose swarf. 207

**Figure 5.20** Inverse solution of temperature of inside surface of the wall at  $r = a = 72$  mm for experiment 1 at height 100 mm calculated using equation (5.15). The sensitivity matrix of equation (5.15) is constructed of sensitivity elements obtained from equation (5.37) for wall thickness  $(b - a) = 4.25$  mm. Superficial air velocity of 4.1 cm/s, 1 kg of dissolved sodium chloride, 500 g of loose swarf. 208

mm for experiment 1 at height 100 mm calculated using equation (5.15). The sensitivity matrix of equation (5.15) is constructed of sensitivity elements obtained from equation (5.28) for wall thickness  $(b - a) = 4.25$  mm. Measured fluid temperature taken from mineral insulated thermocouple at height 100 mm. Superficial air velocity of 4.1 cm/s, 1 kg of dissolved sodium chloride, 500 g of loose swarf.

**Figure 5.21** Inverse solution of heat transfer coefficient belonging to inside surface of the wall at  $r = a = 72$  mm for experiment 1 at height 100 mm. The inverse normal heat flux is divided by the difference between the inverse temperature of the inside surface of the wall at  $r = a = 72$  mm and the measured fluid temperature at height 100 mm. The centre of the circle indicates where Tikhonov regularisation is localised and where the inside-wall heat transfer coefficient is resolved. Superficial air velocity 4.1 cm/s, 1 kg of dissolved sodium chloride, 500 g of loose swarf. 209

**Figure 5.22** Inverse solution of normal heat flux of inside surface of the wall at  $r = a = 72$  mm for experiment 2 at height 350 mm calculated using equation (5.15). The sensitivity matrix of equation (5.15) is constructed of sensitivity elements obtained from equation (5.37) for wall thickness  $(b - a) = 4.25$  mm. Superficial air velocity of 7.2 cm/s, 500 g of loose swarf. 210

**Figure 5.23** Inverse solution of temperature of inside surface of the wall at  $r = a = 72$  mm for experiment 1 at height 350 mm calculated using equation (5.15). The sensitivity matrix of equation (5.15) is constructed of sensitivity elements obtained from equation (5.28) for wall thickness  $(b - a) = 4.25$  mm. Measured fluid temperature taken from mineral insulated thermocouples at height 350 mm. Superficial air velocity of 7.2 cm/s, 500 g of loose swarf. 211

**Figure 5.24** Inverse solution of heat transfer coefficient belonging to inside surface of the wall at  $r = a = 72$  mm for experiment 2 at height 350 mm. The inverse normal heat flux is divided by the difference between the inverse temperature of the inside surface of the wall at  $r = a = 72$  mm and the measured fluid temperature at height 350 mm. The centre of the circle indicates where Tikhonov regularisation is localised and where the inside-wall heat transfer coefficient is resolved. Superficial air velocity 7.2 cm/s, 500 g of loose swarf. 212

**Figure 5.25** Inverse solution of normal heat flux of inside surface of the wall at  $r = a = 72$  mm for experiment 2 at height 100 mm calculated using equation (5.15). The sensitivity matrix of equation (5.15) is constructed of sensitivity elements obtained from equation (5.37) for wall thickness  $(b - a) = 4.25$  mm. Superficial air velocity of 7.2 cm/s, 500 g of loose swarf. 213

**Figure 5.26** Inverse solution of temperature of inside surface of the wall at  $r = a = 72$  mm for experiment 2 at height 100 mm calculated using equation (5.15). The sensitivity matrix of equation (5.15) is constructed of sensitivity elements obtained from equation (5.28) for wall thickness  $(b - a) = 4.25$  mm. Measured fluid temperature taken from mineral insulated thermocouple at height 100 mm. Superficial air velocity of 7.2 cm/s, 500 g of loose swarf. 214

**Figure 5.27** Inverse solution of heat transfer coefficient belonging to inside surface of the wall at  $r = a = 72$  mm for experiment 2 at height 100 mm. The inverse normal heat flux is divided by the difference between the inverse temperature of the inside surface of the wall at  $r = a = 72$  mm and the measured fluid temperature at height 100 mm. The centre of the circle indicates where Tikhonov regularisation is localised and where the inside-wall heat transfer coefficient is resolved. Superficial air velocity 7.2 215

cm/s, 500 g of loose swarf.

**Figure 5.28** Inverse solution of normal heat flux of inside surface of the wall at  $r = a = 72$  mm for experiment 3 at height 350 mm calculated using equation (5.15). The sensitivity matrix of equation (5.15) is constructed of sensitivity elements obtained from equation (5.37) for wall thickness  $(b - a) = 4.25$  mm. Superficial air velocity of 4.1 cm/s, 1 kg of dissolved sodium chloride, 500 g of loose swarf. 216

**Figure 5.29** Inverse solution of temperature of inside surface of the wall at  $r = a = 72$  mm for experiment 3 at height 350 mm calculated using equation (5.15). The sensitivity matrix of equation (5.15) is constructed of sensitivity elements obtained from equation (5.28) for wall thickness  $(b - a) = 4.25$  mm. Measured fluid temperature taken from mineral insulated thermocouple at height 350 mm. Superficial air velocity of 4.1 cm/s, 1 kg of dissolved sodium chloride, 500 g of loose swarf. 217

**Figure 5.30** Inverse solution of heat transfer coefficient belonging to inside surface of the wall at  $r = a = 72$  mm for experiment 3 at height 350 mm. The inverse normal heat flux is divided by the difference between the inverse temperature of the inside surface of the wall at  $r = a = 72$  mm and the measured fluid temperature at height 350 mm. The centre of the circle indicates where Tikhonov regularisation is localised and where the inside-wall heat transfer coefficient is resolved. Superficial air velocity 4.1 cm/s, 1 kg of dissolved sodium chloride, 500 g of loose swarf. 218

**Figure 5.31** Inverse solution of normal heat flux of inside surface of the wall at  $r = a = 72$  mm for experiment 3 at height 100 mm calculated using equation (5.15). The sensitivity matrix of equation (5.15) is constructed of sensitivity elements obtained from equation (5.37) for wall thickness  $(b - a) = 4.25$  mm. Superficial air velocity of 4.1 cm/s, 1 kg of dissolved sodium chloride, 500 g of loose swarf. 219

**Figure 5.32.** Inverse solution of temperature of inside surface of the wall at  $r = a = 72$  mm for experiment 3 at height 100 mm calculated using equation (5.15). The sensitivity matrix of equation (5.15) is constructed of sensitivity elements obtained from equation (5.28) for wall thickness  $(b - a) = 4.25$  mm. Measured fluid temperature taken from mineral insulated thermocouples at height 100 mm. Superficial air velocity of 4.1 cm/s, 1 kg of dissolved sodium chloride, 500 g of loose swarf. 220

**Figure 5.33** Inverse solution of heat transfer coefficient belonging to inside surface of the wall at  $r = a = 72$  mm for experiment 3 at height 100 mm. The inverse normal heat flux is divided by the difference between the inverse temperature of the inside surface of the wall at  $r = a = 72$  mm and the measured fluid temperature at height 100 mm. The circle indicates where Tikhonov regularisation is localised and where the inside wall heat-transfer coefficient is resolved. Superficial air velocity 4.1 cm/s, 1 kg of dissolved sodium chloride, 500 g of loose swarf. 221

**Figure 5.34** Axial velocities of water close to the inside surface of the wall for flow investigated by inverse analysis. Axial velocity values are taken from tables 3.5, 3.6, 3.7 and 3.8 of reported PEPT experiments of corresponding flow. PEPT experiment 6: superficial air velocity 4.1 cm/s, 1 kg of dissolved sodium chloride, 500 g of loose swarf. PEPT experiment 2: superficial air velocity 4.1 cm/s, 1 kg of dissolved sodium chloride. PEPT experiment 4: superficial air velocity 7.2 cm/s, 500 g of loose swarf. PEPT experiment 3: superficial air velocity 7.2 cm/s. Values for height 90 mm taken from grid segments (5,4). Values for height 110 mm taken from grid segments (5,5). Values for height 350 mm taken from grid segments (5,17). 222

## LIST OF TABLES

### CHAPTER 4

<b>Table 4.1</b> Flow visualisation experiments and corresponding AVI files.	72
<b>Table 4.2</b> Transport properties of fluids used in the simulation ( <i>Gebhart et al., 1988; Rogers &amp; Mayhew, 1980; Bureau International des Poids et Mesures, 2006</i> ).	80
<b>Table 4.3</b> Summary of PEPT experiments.	83
<b>Table 4.4</b> Measured quantities for PEPT experiment 1.	97
<b>Table 4.5</b> Measured quantities for PEPT experiment 2.	101
<b>Table 4.6</b> Measured quantities for PEPT experiment 3.	105
<b>Table 4.7</b> Measured quantities for PEPT experiment 4.	109
<b>Table 4.8</b> Measured quantities for PEPT experiment 6.	113

### CHAPTER 5

<b>Table 5.1</b> Thermal parameters of inconel wall ( <i>www.specialmetals.com</i> ).	169
<b>Table 5.2</b> Summary of inverse experiments.	179

## NOMENCLATURE

### Abbreviations

ALARP	As Low as Reasonably Practicable
ASCII	American Standard Code for Information Interchange
ASTM	American Society for Testing and Materials
AVI	Audio Video Interleave
BDF	Backward Differentiation Formula
CFD	Computational Fluid Dynamics
CMC	Critical Micelle Concentration
DOS	Design Option Study
GUI	Graphical User Interface
HFA	Hot Film Anemometry
IAEA	International Atomic Energy Agency
IHCP	Inverse Heat Conduction Problem
ISD	Inherently Safe Design
PEPT	Positron-Emission Particle-Tracking
PET	Positron Emission Tomography
PIC	Positron Imaging Centre
PTFE	Polytetrafluoroethylene
RAL	Rutherford Appleton Laboratory
RANS	Reynolds Averaged Navier-Stokes
TIFF	Tagged Image File Format
UNS	Unified Numbering System

### CHAPTER 2

#### Parameters

$c_p$	heat capacity of coolant	$\text{J kg}^{-1} \text{ } ^\circ\text{C}^{-1}$
$D_o$	outer diameter of the cylinder wall	m
$d_e$	hydraulic diameter	m
$H$	enthalpy	J
$\Delta H^\circ$	standard enthalpy change	$\text{J mol}^{-1}$ or $\text{J kg}^{-1}$
$\Delta H_f^\circ$	standard enthalpy change of formation	$\text{J mol}^{-1}$ or $\text{J kg}^{-1}$
$\Delta H_{\text{swarf}}^\circ$	standard enthalpy change of dissolution of swarf	$\text{J mol}^{-1}$ or $\text{J kg}^{-1}$
$h$	overall heat transfer coefficient	$\text{W m}^{-2} \text{ } ^\circ\text{C}^{-1}$
$h_i$	heat transfer coefficient of the inside surface of the cylinder wall	$\text{W m}^{-2} \text{ } ^\circ\text{C}^{-1}$
$h_o$	heat transfer coefficient of the outside surface of the cylinder wall	$\text{W m}^{-2} \text{ } ^\circ\text{C}^{-1}$
$k$	thermal conductivity	$\text{W m}^{-1} \text{ } ^\circ\text{C}^{-1}$
$k_w$	thermal conductivity of water	$\text{W m}^{-1} \text{ } ^\circ\text{C}^{-1}$
$l$	length of water jacket	m
$m_c$	mass flow rate of coolant	$\text{kg s}^{-1}$
$m'_c$	mass flow rate of coolant per unit area	$\text{kg m}^{-2} \text{ s}^{-1}$



$P$	pressure	Pa
$Q$	rate of cooling	W
$\mathbb{R}$	real set	
$q$	heat transferred	J
$q_p$	heat transferred at constant pressure	J
$\mathfrak{R}$	rate of heating	W
$S_{surr}$	entropy of surroundings	$\text{J kg}^{-1} \text{ } ^\circ\text{C}^{-1}$
$S$	entropy	$\text{J kg}^{-1} \text{ } ^\circ\text{C}^{-1}$
$\Delta S$	entropy change	$\text{J kg}^{-1} \text{ } ^\circ\text{C}^{-1}$
$s$	wall thickness	m
$T$	temperature	$^\circ\text{C}$
$T_{c0}$	initial temperature of coolant	$^\circ\text{C}$
$T_c$	temperature of coolant	$^\circ\text{C}$
$U$	internal energy	J
$V$	volume	$\text{m}^3$
$w$	work	J
$z$	axial coordinate	m
$z_0$	initial fill level within cylinder	m

### Greek symbols

$\mu$	dynamic viscosity	Pa s
$\mu_s$	dynamic viscosity at wall	Pa s
$\nu$	rate of dissolution of swarf	$\text{kg s}^{-1}$

### CHAPTER 3

#### Parameters

$f_{opt}$	fraction of coincidences discarded	
$N$	size of set of coincidences	
$f$	probability density	
$r$	radial coordinate	m
$R$	radius	m

### CHAPTER 4

#### Parameters

$a$	major axis of ellipse	m
$\mathbf{A}, \mathbf{B}, \mathbf{C}$	arbitrary vectors	
$b$	minor axis of ellipse	m
$\mathbf{e}_1, \mathbf{e}_2, \mathbf{e}_3$	arbitrary unit vectors	
$\mathbf{e}_r, \mathbf{e}_\theta, \mathbf{e}_z$	cylindrical unit vectors	
$d_e$	diameter of sphere of equivalent volume to bubble	m
$f_{mix}$	mixing energy	$\text{J m}^{-3}$
$f$	arbitrary function	

<b>F</b>	volume force	$\text{N m}^{-3}$
<b>F</b> <sub>buoyancy</sub>	buoyancy term of volume force	$\text{Nm}^{-3}$
<b>F</b> <sub>mixing</sub>	volume force due to mixing	$\text{Nm}^{-3}$
<b>F</b> <sub>gravity</sub>	volume force due to gravity	$\text{Nm}^{-3}$
<b>g</b> <sub>z</sub>	gravity vector	$\text{m s}^{-2}$
<b>G</b>	chemical potential	$\text{N m}^{-2}$
<b>I</b>	unitary matrix	
<b>L</b> <sub>B</sub>	operating height of column	m
<b>L</b> <sub>R</sub>	column height at rest	m
<b>n</b>	number of observed quantities	
<b>n</b>	vector normal of surface or interface	
<b>P</b>	pressure	Pa
<b>r, θ, z</b>	cylindrical coordinates	m, rad
<b>Re</b> <sub>e</sub>	Bubble Reynolds (equivalent bubble diameter)	
<b>s</b>	displacement	m
<b>s</b>	displacement vector	m
<b>S</b>	surface	$\text{m}^2$
<b>t</b>	time	s
<b>t'</b>	time domain of convergence	s
<b>t</b> <sub>0</sub>	time of convergence	s
<b>Δt</b>	time step	s
<b>T</b>	general stress tensor	$\text{Nm}^{-2}$
<b>u</b>	instantaneous velocity	$\text{m s}^{-1}$
<b>u'</b>	fluctuating velocity	$\text{m s}^{-1}$
<b>ū</b>	mean velocity	$\text{m s}^{-1}$
<b>u</b> <sup>*</sup>	lagrangian velocity	$\text{m s}^{-1}$
<b>u</b> <sub>r</sub>	radial component of instantaneous velocity	$\text{m s}^{-1}$
<b>u'</b> <sub>r</sub>	radial component of fluctuating velocity	$\text{m s}^{-1}$
<b>ū</b> <sub>r</sub>	mean radial velocity	$\text{m s}^{-1}$
<b>u</b> <sub>z</sub>	axial component of instantaneous velocity	$\text{m s}^{-1}$
<b>u'</b> <sub>z</sub>	axial component of fluctuating velocity	$\text{m s}^{-1}$
<b>ū</b> <sub>z</sub>	mean axial velocity	$\text{m s}^{-1}$
<b>ū</b> <sub>θ</sub>	mean azimuthal velocity	$\text{m s}^{-1}$
<b>U</b> <sub>b</sub>	bubble terminal velocity	$\text{m s}^{-1}$
<b>V</b>	volume	$\text{m}^3$
<b>x, y, z</b>	Cartesian coordinates	m
<b>Δz</b>	axial step	m
<b>z'</b>	final axial coordinate of particle tracer	m

### Greek symbols

<b>α</b> <sub>g</sub>	volume fraction of air
-----------------------	------------------------

$\alpha_w$	volume fraction of water	
$\alpha_s$	volume fraction of swarf	
$\gamma$	mobility	$\text{m}^3 \text{s kg}^{-1}$
$\varepsilon$	interface thickness	$\text{m}$
$\boldsymbol{\varepsilon}$	rate of strain tensor	$\text{s}^{-1}$
$\varepsilon_g$	local gas hold-up	
$\varepsilon_G$	global gas hold-up	
$\varepsilon_t$	ratio of time steps	
$\varepsilon_z$	ratio of axial steps	
$\kappa$	curvature	$\text{m}^{-1}$
$\lambda$	mixing energy density	$\text{N}$
$\mu$	dynamic viscosity	$\text{Pa s}$
$\nu$	kinematic viscosity	$\text{m}^2 \text{s}^{-1}$
$\rho$	density	$\text{kg m}^{-3}$
$\rho_g$	density of air	$\text{kg m}^{-3}$
$\rho_w$	density of water	$\text{kg m}^{-3}$
$\bar{\rho}_w$	volume averaged density of water	$\text{kg m}^{-3}$
$\sigma$	surface tension coefficient	$\text{N m}^{-1}$
$\sigma_{x,y,z}$	standard deviation on reported location of particle tracer	
$\boldsymbol{\sigma}$	stress normal to interface	$\text{N m}^{-2}$
$\phi$	phase field function	
$\chi$	mobility tuning parameter	$\text{m s kg}^{-1}$
$\omega'_\theta$	angular component of fluctuating velocity	$\text{m s}^{-1}$
$\Omega_\theta$	azimuthal vorticity	$\text{s}^{-1}$
$\Omega_r$	radial vorticity	$\text{s}^{-1}$
$\Omega$	vorticity	$\text{s}^{-1}$

## CHAPTER 5

### Parameters

$[\mathbf{A}]$	model system	
$[\mathbf{A}]^{-1}$	inverse model system	
$C_m$	constant of eigenvalue	
$f_i$	expression for boundary condition at $r = i$	
$\Delta^n f_j$	finite differencing for $n^{\text{th}}$ order derivative of boundary condition vector	
$\{\hat{\mathbf{f}}\}$	sought boundary condition vector	$^\circ\text{C}$ or $\text{W m}^{-2}$
$\{\hat{\mathbf{f}}_{\text{abs}}\}$	absolute boundary condition vector	$^\circ\text{C}$ or $\text{W m}^{-2}$

$\{\hat{\mathbf{f}}_0\}$	initial boundary condition vector	$^{\circ}\text{C}$ or $\text{W m}^{-2}$
$G$	1-dimensional Green's function	
$\frac{\partial G}{\partial n}$	normal derivative of greens function	
$h_i$	inside-wall heat transfer coefficient	$\text{W m}^{-2} \text{ } ^{\circ}\text{C}^{-1}$
$[\mathbf{H}]$	regularisation matrix	
$[\mathbf{H}]'$	transpose of regulariation matrix	
$J_0, Y_0, J_1, Y_1$	bessel functions	
$k$	thermal conductivity	$\text{W m}^{-1} \text{ } ^{\circ}\text{C}^{-1}$
$N_m$	normalisation coefficient	
$r$	radial coordinate	$\text{m}$
$r'$	radial coordinate of Green's function	$\text{m}$
$S$	least-squares sum	
$t$	time	$\text{s}$
$\{\mathbf{t}\}$	time vector	$\text{s}$
$T$	temperature	$^{\circ}\text{C}$
$\{\mathbf{T}\}$	analytical temperature vector	$^{\circ}\text{C}$
$\hat{T}_j$	estimated temperature component	$^{\circ}\text{C}$
$T'_0$	initial temperature	$^{\circ}\text{C}$
$T_f$	fluid temperature	$^{\circ}\text{C}$
$\frac{\partial T}{\partial n}$	normal derivative of temperature	$^{\circ}\text{C m}^{-1}$
$\{\mathbf{x}\}$	cause	
$[\mathbf{X}]$	sensitivity matrix	$1$ or $^{\circ}\text{C W}^{-1}\text{m}^2$
$[\mathbf{X}]'$	transpose of sensitivity matrix	
$\{\mathbf{y}\}$	effect	
$Y_j$	measured temperature component	$^{\circ}\text{C}$
$\{\mathbf{Y}\}$	measured temperature vector	$^{\circ}\text{C}$
$\{\mathbf{Y}_0\}$	initial measured temperature vector	$^{\circ}\text{C}$
$\{\mathbf{Y}\}_{\text{sim}}$	simulated temperature vector	$^{\circ}\text{C}$
$Z$	variable of normal distribution	
$\{\mathbf{Z}\}$	vector of variable of normal distribution	$^{\circ}\text{C}$
<b>Greek symbols</b>		
$\alpha$	Thermal diffusivity	$\text{m}^2\text{s}^{-1}$
$\beta_m$	eigenvalue	
$\varepsilon$	error	$^{\circ}\text{C}$

$\gamma$	Tikhonov regularisation coefficient	
$\mu$	mean of error	$^{\circ}\text{C}$
$\phi$	solution to auxiliary problem	$^{\circ}\text{C}$
$\phi_n$	time vectorised solution of the auxiliary problem	$^{\circ}\text{C}$
$\{\Phi\}$	vector of solution to auxiliary problem	$^{\circ}\text{C}$
$\psi_m$	eigenfunction	
$\sigma$	standard deviation of noise	
$\tau$	time domain of Green's function	s

# CHAPTER 1

## INTRODUCTION

Rolls-Royce has initiated development of processes belonging to present reclamation of uranium from waste residues of manufacturing operations. Key to reclamation is a swarf dissolution process whereby chemical action of acids the swarf and its uranium content is dissolved into an aqueous liquor. The introduction starts with a generic outline of methodology used for development of a process. The immediate stakeholder and business requirements of Rolls-Royce are then discussed in relation to present process development methodology so that the development of the swarf dissolution process meets said requirements and is capable to its inputs, outputs and environment. The main analysis herein is for a thermal operating envelope of a design concept of the swarf dissolution process. A thermal operating envelope is necessary to provide assurance in the operation of the swarf dissolution process because the chemical dissolution of swarf is highly exothermic.

### 1.1 Process design and engineering

Rolls-Royce is a manufacturer and in this context its strategy and business objectives necessitate process engineering. Opportunity for improvement of processes is driven by both cost and returns or gain through reducing/eliminating foreseeable process risk. Cost incentives are associated with the efficiency of processes and recycle or reclamation of valuable commodities. Under a negative perspective of process risk a positive gain is achieved through change or modification of a process that prevents or mitigates process risk; succinctly this is also directly proportional to the efficiency of processes. Risk is now looked on as integral to

the decisions made in process engineering (*Haimes, 2009; Hazelrigg, 1996*). It is part of a design activity that is logical, scientific and iterative. The traditional design activity is summarised by *White (2009)* and contains generic stages:

1. **Problem definition** Business objective and functional requirements of a process.
2. **Design option studies (DOSs)** Preliminary design concepts of a process are drawn.
3. **Parameterisation** Evaluation and optimisation of design concepts using parameters.
4. **Analysis** Parameter measurements and attainable magnitudes.
5. **Operational specification** Display of parameters indicating correct operation of a process.
6. **Prototype and testing** Business objective and functional requirements are reaffirmed and met.
7. **Final design** Installation of business objective.

Modified from *White (2009)*.

The problem definition is the basis and begins the design activity of a process. A dialogue of statements is built around the business strategy and objectives. Relationships and communication are established providing assurance throughout the design activity (*Hazelrigg, 1996*). The design activity is hierarchical and relationships of a process focus on functional requirements to give optimality through a reductionistic or disciplinary approach to design. Convergence of the design activity towards installation of a process is dependent upon information because it is a decisional exercise. The availability of information is iterative; analysis of a process improves information and follows DOSs and parameterisation.

DOSs is methodology of assignment of priorities or probabilities in the development of preliminary design concepts of a process and is partly uncertain. Parameterisation of the

design concepts is the application of science to process design and initiates process engineering. Mathematical constraints can now act on the empirical determinacy of analysis and they are translated from the functional requirements of the problem definition. Analysis provides attainable magnitudes of parameters that describe the dynamics of a process. The operational specification of a process is the solution to the constraints and, graphically this is the operating envelope of a process. Disparity exists in the uncertainty of DOSs with the determinacy of parameterisation and analysis; innovation to reflection and commitment (*Schön, 1983*).

An axiomatic approach to the design activity of a process which is based upon fundamental principles is logical in process engineering. Processes are highly functional and call for efficiency. *Yasuhara & Suh, (1980)* and *Stoll, (1990)* have looked at precedents for the effectiveness of design activities and design solutions. They found that convergence is from dominant design criteria. Firstly, there should be independent functional requirements. However, this is not always possible within process engineering because the complexity of the process dynamics may require assumptions in its description. When it is possible to factorise a process, symmetry is an invaluable tool. The independence of the functional requirements ensures that the design is not under or over constrained. Secondly, the functional requirements should be satisfied by a single physicality within the design. This simplification will avoid a superfluous design solution forcing the functional requirements to be met more efficiently in operability and therefore reduced process risk.

## 1.2 Chemical processing and risk

### 1.2.1 The swarf dissolver process

For Rolls-Royce uranium is a high value commodity and there is a strong driver to reclaim and reuse it. The processing of uranium bearing materials by Rolls-Royce gives rise to



residues, including uranium bearing swarf. The major constituent of the swarf is zirconium and the density of swarf is  $\sim 6.52 \text{ g/cm}^3$ . The swarf has varied morphology and its length and thickness are of magnitude  $10^0$ - $10^1$  cm and  $10^{-3}$ - $10^{-1}$  cm respectively. The uranium within the swarf is reclaimed by Rolls-Royce using aqueous chemical processing. The swarf dissolver enables the dissolution of swarf by chemical action of aqueous acids. Both nitric and hydrofluoric acids are required for total dissolution of swarf. The dissolution of swarf progresses by chemical redox; nitric acid is the oxidant and hydrofluoric acid the complexant. The chemical dissolution of swarf by both acids is highly exothermic. The mechanisms and heat of chemical dissolution of swarf are worked through in Chapter 2 Section 2.2.

The loose swarf is loaded into an open bath containing a prefill of water. The dissolution of swarf starts with the addition of hydrofluoric and nitric acids from a submerged feed. The rate of dissolution of swarf is controlled by the rate of addition of acids. Distribution of argon within the bath and gaseous products of the chemical dissolution of swarf (Chapter 2 Section 2.2) provide mixing of swarf and acids, and an internal water coil provides forced cooling. The process gases are extracted by a ducted fume hood.

### 1.2.2 Modification of swarf dissolver geometry

The cost incentive of reclamation of uranium by Rolls-Royce is further complemented by risk management, which can derive value for the business. Management of risk is achieved by defining hazard as source of harm, and risk as the likelihood of a harmful outcome (*Hood & Jones, 1996*). The requirement of risk management is imposed by stakeholders of the business including regulatory authorities that enforce operational standards. Risk management has multiple components to which risk assessment is a key factor. Risk assessment is both objective and subjective. Objective assessment of risk looks at what has gone wrong. Subjective assessment of risk looks at what could go wrong; it is perceived risk (*Haimes,*

2009). Objectively, harmful outcomes are recognised from the history of processing present in industry specific incident reports and databases. Subjectively, harmful outcomes are imagined from logical evaluation of scenarios and trials that can have a true/false outcome i.e. harm or no harm. Both types of risk assessment constitute risk communication, intelligence, monitoring and acceptance.

The International Atomic Energy Agency (IAEA) is an important stakeholder of uranium processing. Alongside countries and territories it has established a community of risk communication and risk intelligence. Parallel with the findings of the criticality incident at Tokaimura in 1999, Rolls-Royce has reviewed the risks associated with its processing of uranium in order to ensure that they are as low as reasonably practicable (ALARP) and consistent with modern best practice. This is the problem definition for the modification of the swarf dissolution process (Section 1.1 and Subheading 1.2.1).

Risk treatment includes both prevention and mitigation of risk. Mitigation generally involves indirect treatment of risk through control procedures and technologies that are additional to a process. However, prevention of risk is naturally implicit to a process when implemented through design. Inherently Safe Design (ISD) is central to the DOSs completed by Rolls-Royce and is risk prevention. ISD is the avoidance and minimisation of harmful outcomes through controlled design and fits with the traditional steps of working with risk; to identify, prevent and control hazards (*Kletz, 1998*). The modification from the DOSs is to change the geometry of the swarf dissolution process to a cylinder that has a fixed internal diameter of 144 mm. The modification and operation of the swarf dissolution process is displayed in figure 1.1 and is discussed in Section 1.3. The fixed internal diameter is the controlled design and radiological constraint of criticality assessment for a geometrically favourable cylinder. Because the modification of process geometry is innovative chemical analysis of swarf

dissolution and analysis of process dynamics is required to avoid overheating and to verify installation of the cylinder concept. Both analyses will provide assurance in maximising process efficiency, maintaining process control and process strategy. The rate of heating from the chemical dissolution of swarf within the cylinder concept is the chemical constraint, and is controlled by the rate of addition of acids (Figure 1.1).

ISD is an axiomatic approach to a design activity and additional to risk presents opportunities of cost incentives because it is effectively an efficiency exercise. As discussed in Section 1.1 an axiomatic approach to a design activity avoids a superfluous design solution reducing risk in process operability. Process operability conforms to acceptable conditions, amenable to parameterisation and therefore optimisation. An optimisation using both the radiological and chemical constraints of the cylinder concept will provide a thermal operating envelope and will consider the inputs, outputs and environment of the swarf dissolution process (Section 1.1). The construction of a thermal operating envelope is discussed in Chapter 2 Section 2.3.

### 1.3 Operation of cylinder concept for the dissolution of swarf

The operation of the cylinder concept for the dissolution of swarf by both hydrofluoric and nitric acids is shown in figure 1.1. The cylinder concept is operated as a batch process. The loose swarf is loaded from the top of the column into a prefill of water. The mass of loose swarf within the cylinder concept is 500 g. The addition of the prefill is from the base of the column and prevents a swarf fire from the chemical reaction of swarf with acids. The dissolution of swarf starts with the addition of acids from the base of the column alongside distribution of argon. The dissolution of swarf is controlled by the rate of addition of acids. The total volume of prefill and acids within the cylinder concept is 11.25 litres. The distribution of argon provides mixing within the cylinder concept throughout the duration of the dissolution of swarf, and aids forced cooling of the swarf dissolution process by an

external water jacket. Both argon and the gaseous products of dissolution of swarf leave the process from the top of the column.

#### 1.4 Aims and structure of thesis

The aims of the thesis build from a thermal operating envelope for the cylinder concept of the DOSs presented by Rolls-Royce for the modification of the swarf dissolution process (Sections 1.1, 1.2 and 1.3). The main aim is a sufficient magnitude of the heat transfer coefficient of the inside surface of the cylinder wall and its measurement. The magnitude of this parameter will depend upon the employed turbulence of the multiphase flow within the cylinder concept. Therefore, the turbulent flow must be investigated to inform design and assess effectiveness of convection of heat towards the inside surface of the wall.

The use of gravity-driven turbulent flow by distribution of gas from the base of the cylinder concept is investigated, and will require measurement techniques to assess and understand:

1. The stresses within the flow and the resultant occupancy of swarf within the cylinder concept.
2. The convection of the multiphase flow and, therefore, the transfer of heat to the inside surface of the cylinder wall.

Chapters 2-6 of this thesis contain respectively the thermochemistry of swarf dissolution and thermal operating envelope of the cylinder concept, a literature survey of measurement techniques and methods, analysis and measurement of turbulent multiphase flow, analysis and measurement of the heat transfer coefficient of the inside surface of the cylinder wall, and the conclusion.

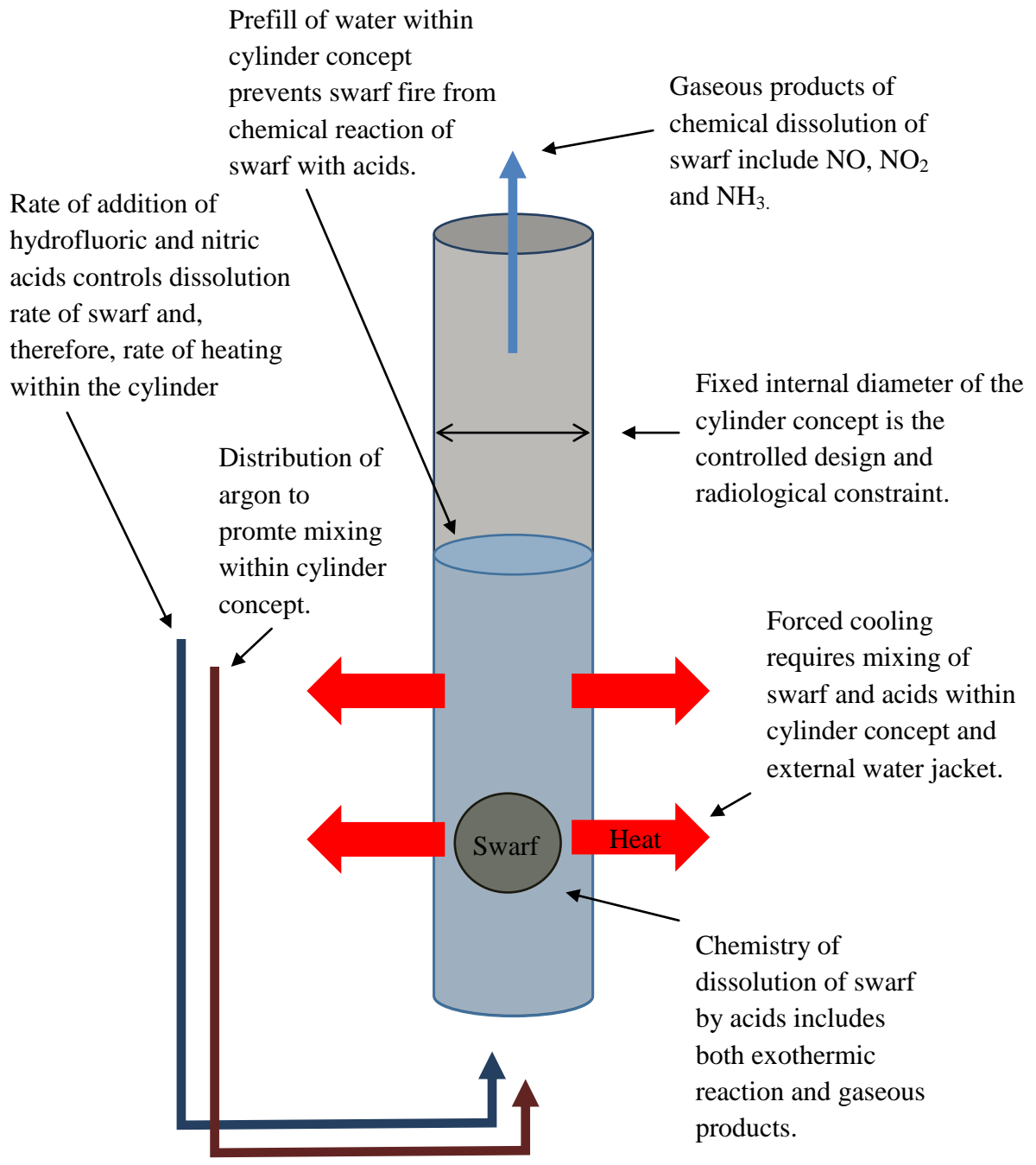


**Figure 1.1** The operation of the batch process of swarf dissolution within the cylinder concept.

## CHAPTER 2

# THERMOCHEMISTRY OF SWARF DISSOLUTION AND THERMAL OPERATING ENVELOPE OF CYLINDER CONCEPT

### 2.1 Introduction

A thermal operating envelope is drawn for the cylinder concept indicating acceptable regions of process operation based upon design parameters such as internal diameter and cylinder length (Chapter 1 Sections 1.1 and 1.2) (Section 2.3). The rate of heating within the cylinder concept from the chemical dissolution of swarf is the parameter that defines process operation, and is the chemical constraint as discussed in Chapter 1 Section 1.2. The rate of addition of hydrofluoric and nitric acids controls the rate of dissolution of swarf and therefore the rate of heating (Chapter 1 Section 1.3). The enthalpy of chemical dissolution of swarf by both hydrofluoric and nitric acids is evaluated using Hess cycles (Section 2.2).

Dominant non-linear effects of heat transfer belonging to the cylinder concept are modeled (Section 2.3). This is the axial variation in temperature of the coolant flowing through the external water jacket for which a differential heat balance can be written. The internal convection of heat within the cylinder concept, conduction through its wall and external convection of the water jacket is modeled in series using an overall heat transfer coefficient. The entropy change of the coolant is used to construct an efficiency constraint that is used to select the design of the external water jacket with consideration of rates of cooling.

## 2.2 Enthalpy of dissolution

The enthalpy differential of a system at constant pressure is defined as (*McQuarrie & Simon, 1997, p. 780-783*):

$$dq_p = (dU - \delta w) = dH, \quad \delta w = -PdV \quad (2.1)$$

The enthalpy accounts for the heat transferred to a system when it undergoes expansive work (gaseous) at constant pressure i.e. (*McQuarrie & Simon, 1997, p. 780-783*):

$$dU < dq, \quad dq = dq_p \quad (2.2)$$

The enthalpy differential is exact and the enthalpy of a system is only dependent upon its state:

$$\Delta H = \oint dH = 0 \quad (2.3)$$

Enthalpy is a state function. Because the enthalpy differential is exact, enthalpies are combinatory and additive (*McQuarrie & Simon, 1997, p. 787-797*). This is summarised by Hess's law (*McQuarrie & Simon, 1997, p. 787-797*). For chemical reactions this is useful when calculating standard enthalpy changes. The standard enthalpy change of a chemical substance is defined for its state at a specified temperature referenced at 1 bar pressure. Standard enthalpies of formation refer to the enthalpy change of forming a chemical substance from its constituent chemical elements under those conditions. Standard enthalpies of formation are combined to form a Hess cycle; the resultant is the enthalpy change for the chemical reaction of interest (*McQuarrie & Simon, 1997, p. 787-797*). Standard enthalpies can be used to assess the heat of dissolution because the swarf dissolver will operate under

atmospheric pressure with no phase change of chemical substances with temperature. The temperature dependency of the enthalpies will be weak.

Zirconium is the major constituent of swarf. Therefore, the thermochemistry between the swarf and acids is constructed around this substance. Zirconium dissolves in a mixture of hydrofluoric and nitric acids. Observations made by *Klein et al. (1994)* include:

1. Dissolution is progressively hindered by an increase in nitric acid concentration.
2. As the nitric acid concentration increases the enthalpy of dissolution increases to a maximum and the hydrogen evolution decreases.

The observations support a transient reaction to dissolution. It is likely that the mechanism of dissolution proceeds via a zirconium oxide surface because of the oxidising nature of nitric acid and the passivity of zirconium. Considering the different reduction products of nitric acid several Hess cycles can be formulated using standard enthalpies of formation. The standard enthalpies required are (*Atkins, 1998*):

$$\Delta H_f^\circ (\text{HNO}_{3(\text{aq})}) = -207.36 \text{ kJ mol}^{-1} \quad (2.4)$$

$$\Delta H_f^\circ (\text{H}_2\text{O}_{(\text{l})}) = -285.83 \text{ kJ mol}^{-1} \quad (2.5)$$

$$\Delta H_f^\circ (\text{NO}_{(\text{g})}) = 90.25 \text{ kJ mol}^{-1} \quad (2.6)$$

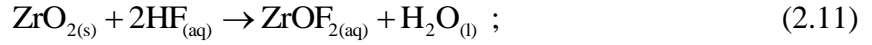
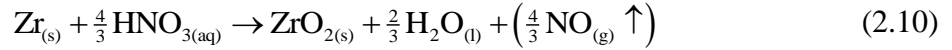
$$\Delta H_f^\circ (\text{NO}_{2(\text{g})}) = 33.18 \text{ kJ mol}^{-1} \quad (2.7)$$

$$\Delta H_f^\circ (\text{NH}_{4(\text{aq})}^+) = -132.51 \text{ kJ mol}^{-1} \quad (2.8)$$

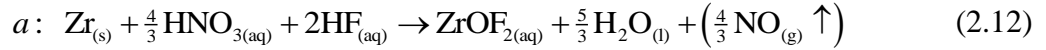
$$\Delta H_f^\circ (\text{NO}_{3(\text{aq})}^-) = -205.00 \text{ kJ mol}^{-1} \quad (2.9)$$



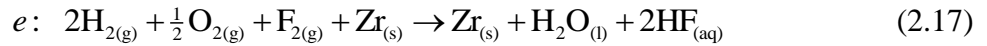
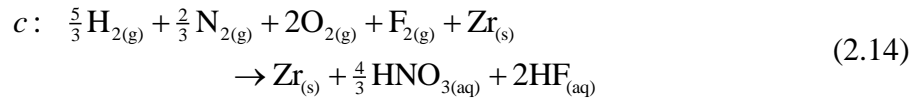
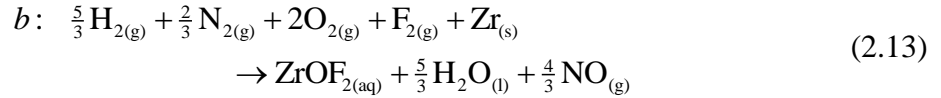
## Reduction to nitric oxide



the overall dissolution reaction:



The Hess cycle:



$$\Delta H^\circ (a) = \Delta H^\circ (b) - \Delta H^\circ (c) \quad (2.18)$$

$$\Delta H^\circ (c) = \frac{4}{3} (-207.36 \text{ kJ mol}^{-1}) + 2\Delta H_f^\circ (\text{HF}_{(aq)}) \quad (2.19)$$

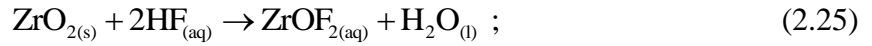
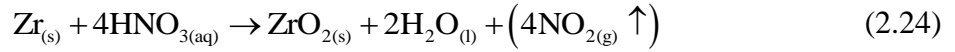
$$\Delta H^\circ (d) = -651.53 \pm 0.98 \text{ kJ mol}^{-1} (\text{Cordfunke et al., 1987}) \quad (2.20)$$

$$\Delta H^\circ (b) = \Delta H_f^\circ (\text{ZrOF}_{2(aq)}) + \frac{5}{3} (-285.83 \text{ kJ mol}^{-1}) + \frac{4}{3} (90.25 \text{ kJ mol}^{-1}) \quad (2.21)$$

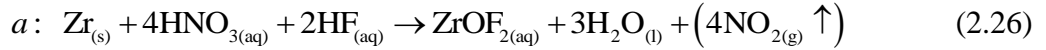
$$\begin{aligned}\Delta H_f^\circ(\text{ZrOF}_{2(\text{aq})}) &= \Delta H^\circ(d) + \Delta H^\circ(e) \\ &= (651.53 \pm 0.98 \text{ kJ mol}^{-1}) + (-285.83 \text{ kJ mol}^{-1}) + \dots \\ &\quad 2\Delta H_f^\circ(\text{HF}_{(\text{aq})})\end{aligned}\quad (2.22)$$

$$\begin{aligned}\therefore \Delta H^\circ(a) &= (-651.53 \pm 0.98 \text{ kJ mol}^{-1}) + \frac{8}{3}(-285.83 \text{ kJ mol}^{-1}) + \dots \\ &\quad \frac{4}{3}(90.25 \text{ kJ mol}^{-1}) - \frac{4}{3}(-207.36 \text{ kJ mol}^{-1}) \\ &= -1016.93 \pm 0.98 \text{ kJ mol}^{-1} \quad (-11147.61 \pm 10.74 \text{ kJ kg}^{-1})\end{aligned}\quad (2.23)$$

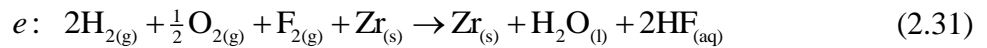
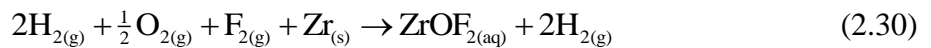
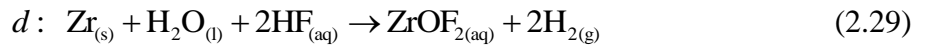
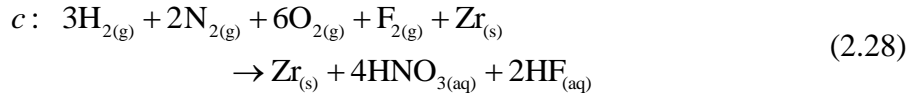
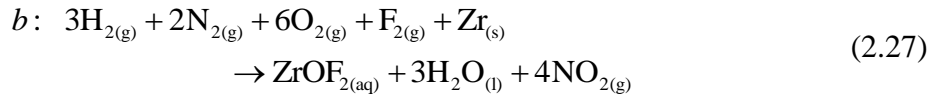
### Reduction to nitrogen dioxide



the overall dissolution reaction:



The Hess cycle:



$$\Delta H^\circ (a) = \Delta H^\circ (b) - \Delta H^\circ (c) \quad (2.32)$$

$$\Delta H^\circ (c) = 4(-207.36 \text{ kJ mol}^{-1}) + 2\Delta H_f^\circ (\text{HF}_{(\text{aq})}) \quad (2.33)$$

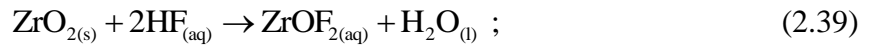
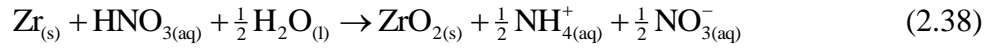
$$\Delta H^\circ (d) = -651.53 \pm 0.98 \text{ kJ mol}^{-1} \text{ (Cordfunke et al., 1987)} \quad (2.34)$$

$$\Delta H^\circ (b) = \Delta H_f^\circ (\text{ZrOF}_{2(\text{aq})}) + 3(-285.83 \text{ kJ mol}^{-1}) + 4(33.18 \text{ kJ mol}^{-1}) \quad (2.35)$$

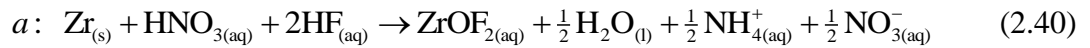
$$\begin{aligned} \Delta H_f^\circ (\text{ZrOF}_{2(\text{aq})}) &= \Delta H^\circ (d) + \Delta H^\circ (e) \\ &= (651.53 \pm 0.98 \text{ kJ mol}^{-1}) + (-285.83 \text{ kJ mol}^{-1}) + \dots \\ &\quad 2\Delta H_f^\circ (\text{HF}_{(\text{aq})}) \end{aligned} \quad (2.36)$$

$$\begin{aligned} \therefore \Delta H^\circ (a) &= (-651.53 \pm 0.98 \text{ kJ mol}^{-1}) + 4(-285.83 \text{ kJ mol}^{-1}) + \dots \\ &\quad 4(33.18 \text{ kJ mol}^{-1}) - 4(-207.36 \text{ kJ mol}^{-1}) \\ &= -832.69 \pm 0.98 \text{ kJ mol}^{-1} \text{ } (-9127.97 \pm 10.74 \text{ kJ kg}^{-1}) \end{aligned} \quad (2.37)$$

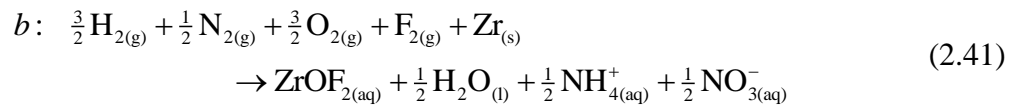
### Reduction to the ammonium ion

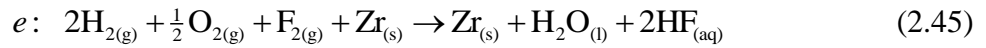
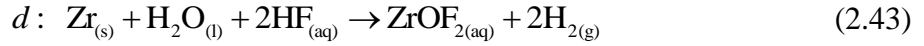
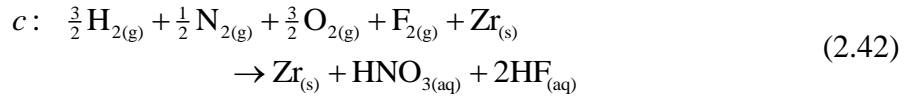


the overall dissolution reaction:



The Hess cycle:





$$\Delta H^\circ (a) = \Delta H^\circ (b) - \Delta H^\circ (c) \quad (2.46)$$

$$\Delta H^\circ (c) = (-207.36 \text{ kJ mol}^{-1}) + 2\Delta H_f^\circ (\text{HF}_{(\text{aq})}) \quad (2.47)$$

$$\Delta H^\circ (d) = -651.53 \pm 0.98 \text{ kJ mol}^{-1} \text{ (Cordfunke et al., 1987)} \quad (2.48)$$

$$\begin{aligned} \Delta H^\circ (b) &= \Delta H_f^\circ (\text{ZrOF}_{2(\text{aq})}) + \frac{1}{2} (-285.83 \text{ kJ mol}^{-1}) + \dots \\ &\quad \frac{1}{2} (-132.51 \text{ kJ mol}^{-1}) + \frac{1}{2} (-205.00 \text{ kJ mol}^{-1}) \end{aligned} \quad (2.49)$$

$$\begin{aligned} \Delta H_f^\circ (\text{ZrOF}_{2(\text{aq})}) &= \Delta H^\circ (d) + \Delta H^\circ (e) \\ &= (651.53 \pm 0.98 \text{ kJ mol}^{-1}) + (-285.83 \text{ kJ mol}^{-1}) + \dots \\ &\quad 2\Delta H_f^\circ (\text{HF}_{(\text{aq})}) \end{aligned} \quad (2.50)$$

$$\begin{aligned} \therefore \Delta H^\circ (a) &= (-651.53 \pm 0.98 \text{ kJ mol}^{-1}) + \frac{3}{2} (-285.83 \text{ kJ mol}^{-1}) + \dots \\ &\quad \frac{1}{2} (-132.51 \text{ kJ mol}^{-1}) + \frac{1}{2} (-205.00 \text{ kJ mol}^{-1}) - (-207.36 \text{ kJ mol}^{-1}) \\ &= -1041.67 \pm 0.98 \text{ kJ mol}^{-1} \quad (-11418.82 \pm 10.74 \text{ kJ kg}^{-1}) \end{aligned} \quad (2.51)$$

The calorimeter value for the enthalpy of dissolution of zirconium in nitric and hydrofluoric acid is  $\Delta H^\circ = -1041.8 \pm 6.9 \text{ kJ mol}^{-1}$  (Klein et al., 1994). This value is for a closed experiment. The swarf dissolver (Chapter 1 Sections 1.2 and 1.3) is not a closed process and

observation of nitric oxide during dissolution of swarf in the present process vessel indicates that the enthalpy of dissolution will be a weighted value of different reduction products. However, the closeness of the enthalpy value for the reduction to ammonium ions in equation (2.51) with the calorimeter value obtained by *Klein et al. (1994)*, indicates the validity of the mechanism of dissolution and cycles proposed. The enthalpy calculations give a benchmark for thermal performance and are now used in the construction of a thermal operating envelope for the cylinder concept.

## 2.3 Thermal operating envelope

### 2.3.1 Parameterisation

The cylinder concept of the DOSs has undergone primary parameterisation and analysis by criticality assessment at Rolls-Royce (Chapter 1 Section 1.2). For this study the fixed diameter of the geometrically favourable cylinder begins the secondary parameterisation and analysis. This is the thermal operating envelope. The fixed internal diameter of the cylinder concept is the common parameter within the iteration of the design activity and is principal to the chemical constraint of the rate of heating (Chapter 1 Sections 1.1 and 1.2).

### 2.3.2 Linear programming and model equations

Using an optimisation method the process constraints give the permissible values of the process variables (*Hazelrigg, 1996*) (Chapter 1 Sections 1.1 and 1.2). Linear programming is a simple and effective optimisation method when few variables are constrained and can be handled analytically. Factorisation and logarithm transform non-linear model equations, which describe the dynamics of a process, into linear relationships that can be drawn as lines. The process constraints are expressed by conditional and unconditional inequalities. Conditional inequalities are discrete while unconditional inequalities are relaxed and belong to a continuum. Graphically these inequalities are the curves that bound process operability.

They map the domain of the operating envelope for a process (Chapter 1 Section 1.1). The gradient and intercept of the lines are then used to optimise the process variables according to the domain.

From the parameterisation of a process the model equations of the process dynamics are derived in accordance with the physical laws of the transport phenomena (e.g. Fourier's law and Newton's law of cooling). The model equations are parametric. Process engineering employs science in a predictive manner. Calculus links the process dynamics to the design activity and its operators are the differential and integral. The differential allows examination of a process and the integral reconstruction of a process.

The thermal operating envelope for the jacketed cylinder concept is now constructed (Chapter 1 Section 1.3). The differential heat balance across the wall of the cylinder is:

$$c_p m_c (dT_c/dz) = \pi D_o h (T - T_c), \quad z = 0, \quad T_c = T_{c0} \quad (2.52)$$

The heat balance is for a constant and uniform temperature within the cylinder and constant heat capacity of the coolant within the external water jacket. The change in coolant temperature along the axis of the cylinder is modeled as a stationary system. Its solution and components of the overall heat transfer coefficient across the cylinder wall are:

$$T_c(z) = T + (T_{c0} - T) e^{-\pi D_o h z / c_p m_c} \quad (2.53)$$

where:

$$1/h = 1/h_1 + k/s + 1/h_o \quad (2.54)$$

The expression for the overall heat transfer coefficient has been taken from *Coulson & Richardson (2003, p. 383)*. The rate of cooling in the annulus of the water jacket and rate of heating within the cylinder is:

$$Q = c_p m_c (T_c(z) - T_{c0}), \quad \mathfrak{R} = \nu \Delta H_{\text{swarf}}^{\circ} \quad (2.55)$$

The rate of heating is specified by the rate of dissolution of swarf and the enthalpy of chemical dissolution of swarf as discussed in Section 2.2. In the extreme scenario the rate of dissolution of swarf is equal to the stoichiometric rate of addition of acids; the stoichiometry of chemical dissolution is given in the Hess cycles of Section 2.2. From the rate of heating the thermal operating envelope is drawn by substitution of equation (2.53) into equation (2.55) for the rate of cooling:

$$Q \geq \mathfrak{R}, \quad z \geq z_0 \quad (2.56)$$

$$\ln \left[ \frac{Q}{c_p m_c (T_{c0} - T)} + 1 \right] = \ln[\dots] = -\pi D_o h z / c_p m_c \quad (2.57)$$

$$\text{Substitute } \mathfrak{R} \text{ for } Q \quad |\ln[\dots]| \geq |f(\mathfrak{R})| \quad \text{i.e. } Q \geq \mathfrak{R} \quad (2.58)$$

In equation (2.56) the rate of cooling must be greater or equal to the rate of heating, and the height of the prefill of the cylinder concept gives an additional constraint. In figure 2.1 an arbitrary thermal envelope is displayed for a selection of rates of cooling. This couples the enthalpy of dissolution to the thermal performance of the swarf dissolver. The intersection of the curves gives the minimum magnitude of the heat transfer coefficient required for the constant operating temperature. This magnitude is related to the gradients of the drawn lines

through equation (2.57). The direction of the inequalities in equation (2.56) gives the operating envelope and is the shaded region in figure 2.1.

The flow in series required for heat transfer and summarised by equation (2.54) is given by the length scales of the process. Thermodynamics is used to inform their design. The entropy change of the coolant irrespective of mass flow rate is:

$$\Delta S = \Delta S_{surr} = c_p \ln(T_c/T_{c0}) \quad (2.59)$$

$$T_c > T_{c0} \Rightarrow \ln(T_c/T_{c0}) > 0 \Rightarrow \Delta S > 0; \text{ irreversible path} \quad (2.60)$$

The efficiency of heat transfer to the coolant is paralleled by the required rate of cooling (mass flow rate of coolant) and will drop at its expense. The positive entropy change or irreversibility indicates that the cooling by the external water jacket is spontaneous under the thermal conditions specified. This irreversibility with substitution of the heat balance solution and entropy of coolant develops the efficiency constraint:

$$h/m_c = \frac{c_p}{\pi D_o z} \ln \left[ \frac{T_{c0} - T}{T_{c0} e^{\Delta S/c_p} - T} \right] \quad (2.61)$$

$$T_{c0} < T, \quad h/m_c \in \mathbb{R} \Rightarrow T_{c0} e^{\Delta S/c_p} - T < 0 \quad (2.62)$$

$$0 < \Delta S < c_p \ln(T/T_{c0}) \quad (2.63)$$

The efficiency constraint of equation (2.63) determines the limiting form of the  $h/m_c$  ratio of equation (2.61) for the thermal conditions specified i.e.  $\Delta S$  is a measure of heat transfer efficiency.



As previously expressed the resistance to heat transfer is in series. The components of the overall heat transfer coefficient have their respective geometries, length scales and flows. Turbulence is employed within the diameter of the cylinder to promote mixing and heat transfer to the wall. However, within the annulus of the water jacket either laminar or turbulent flow could suffice. Here the difference in length scales of the heat transfer in series is a couple of magnitudes. The inside wall heat transfer coefficient and wall conductivity are the controlling resistances. The outside-wall heat transfer coefficient can be tailored to complement those resistances. For the design activity this coupling conservatively aids in the selection of either flow regime within the annulus of the water jacket.

If efficiency of the coolant is desired over short processing time of the swarf dissolution process, the domain of operability is constructed from the efficiency constraint of equation (2.63). The operating temperature of the cylinder concept is chosen and initial temperatures of coolant are specified. The efficiency constraint of equation (2.63) is then used to find the limit of the  $h/m_c$  ratio for maximum coolant efficiency. The design of the external water jacket will dictate the magnitude of the  $h/m_c$  ratio because the heat transfer coefficient of the outside surface of the cylinder wall and, therefore, the overall heat transfer coefficient, will be a function of mass flow rate of coolant. The lines of equation (2.57) are then drawn for the magnitude of the overall heat transfer coefficient, initial coolant temperatures, operating temperature and mass flow rate of coolant. Along with the prefill constraint of equation (2.56) and the lines of equation (2.57) the intersection of the permissible rate of heating or chemical constraint is found by the intercepts on the logarithm of dimensionless rate. The constraints, lines, intersection and intercept are shown in figure 2.1. If the rate of cooling is not sufficient the efficiency of the coolant is dropped at its expense. The mass flow rate of coolant is

increased allowing for a greater rate of heating and therefore a shorter allocated processing time of the swarf dissolution process.

## CHAPTER 2 FIGURES

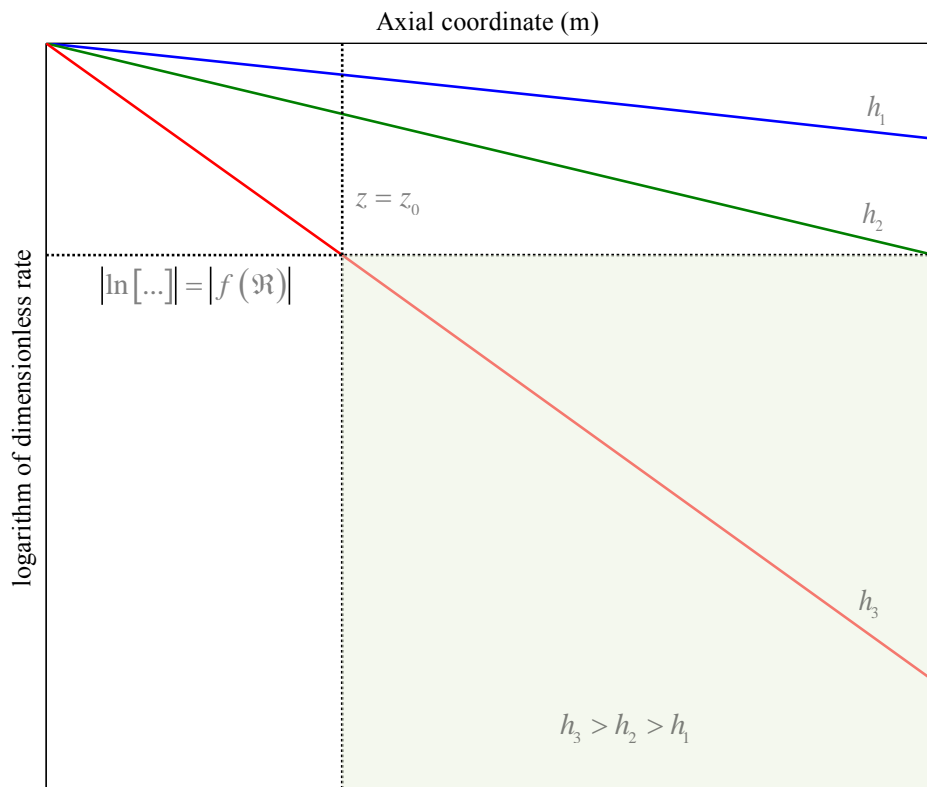


**Figure 2.1** An arbitrary thermal operating envelope for the cylinder concept. The drawn lines coincide with equations (2.56), (2.57) and (2.58) of Subheading 2.3.2. The bound shaded region indicates the envelope.

## CHAPTER 3

### LITERATURE SURVEY

#### 3.1 Introduction

To provide mixing within the cylinder concept distribution of gas from the base of the column is employed and will complement mixing provided by the gaseous products of chemical dissolution of swarf (Chapter 1 Section 1.3). The operation of the cylinder concept has similarity to bubble columns and slurry bubble columns (*Kantarci, 2004*). Bubble columns have wide application in chemical, petrochemical, biochemical and metallurgical operations because of advantages in both design and operation. Excellent heat transfer is observed for bubble columns and their simplicity through lack of moving parts provides low maintenance and operating costs. Typical magnitudes of heat transfer coefficients within bubble columns and slurry bubble columns range from 1000-10000 W/ m<sup>2</sup> °C (*Prakash, 1999; Praksh et al. 2001; Li & Prakash, 2002; Kumar et al., 1992; Kim et al. 1986*). The magnitude of the heat transfer coefficient increases with superficial gas velocity in the range 5-30 cm/s (*Prakash, 1999; Praksh et al. 2001; Li & Prakash, 2002; Kumar et al., 1992; Kim et al. 1986*). The superficial gas velocity is based upon the column cross-sectional area and air flow rate through the gas distributor at its base (*Prakash, 1999; Praksh et al. 2001; Li & Prakash, 2002; Kumar et al., 1992; Kim et al. 1986*).

Because of the disparity in size, shape and density of swarf belonging to the swarf dissolution process compared with literature of slurry bubble columns, emphasis is placed upon measurement techniques and methods that can be used to investigate transport phenomena of

a working model of the cylinder concept. The literature survey that follows concentrates on the attributes of measurement techniques and methods that are useful and necessary for the characterisation of transport phenomena within a working model. The characterisation of multiphase flow dependent upon distribution of gas is discussed further in Chapter 4 alongside the requirements of the design, operation and analysis of the cylinder concept.

### 3.2 Chemical processing and measurement of transport phenomena

Chemical processing has an extensive history and spans many industries. Central to this sector is thermodynamics and the controlled transfer of heat and momentum. Heat and momentum are transport phenomena and path specific. They are dissipative in nature and can be described by differential analysis. Many techniques are available for the measurement of transport phenomena within different process vessels. This has created a wealth of understanding, mainly in the boundary conditions that define the path of heat and momentum transfer and characterise a process.

For a batch process containing material phases a source term is dominant in the transport of momentum. The divergence theorem then presides and accounts for the transfer (flux or stress) within the system alongside accumulation. As a flow measurement technique Positron-Emission Particle-Tracking (PEPT) has all the attributes to allow the resolution of large-scale multiphase turbulence (*Parker et al. 1993; Parker et al. 2002*) (Sections 3.4, 3.5 and 3.6) (Chapter 4 Sections 4.4, 4.5, 4.6, 4.9, 4.10 and 4.11). From observation the form of turbulence explicitly conforms to the property of a tensor given by the vectorised Reynolds Averaged Navier-Stokes (RANS) equation (*Hinze, 1975; Bradshaw, 1978; McComb, 1990*) (Chapter 4 Section 4.4 and 4.5). The novelty in this study is the development in the confidence that PEPT can be used in the measurement of the individual tensor components of the RANS equation, particularly the Reynolds stress tensor. For the gravity-driven turbulent multiphase flow

within the cylinder concept the actual stress operating between the disparate phases can then be seen (Chapter 4 Section 4.11). Alongside turbulence measurements PEPT can also image mixing of a discrete phase or granular flow such as swarf (*Parker et al., 1997b; Guida et al., 2010*) (Sections 3.5 and 3.6) (Chapter 4 Section 4.11). Therefore, the implementation of turbulence to promote mixing and heat transfer within the cylinder concept can be assessed.

The measurement of heat transfer across a wall of a process vessel is a true boundary condition problem. The process must be considered to choose the best measurement technique. Analysis of heat transfer across the wall of the cylinder concept using transient decay of temperature does not require a fixed constant heat source, and during measurement the transport phenomena are more representative of the process compared with forced or stationary analysis. Therefore, transient decay is more applicable to a batch process such as the swarf dissolution process. The boundary condition of interest is sought via inverse analysis which operates upon a temperature transient through its history at a given location (*Beck et al., 1985; Alifanov, 1994*) (Chapter 5 Sections 5.2, 5.3 and 5.4). The heat transfer coefficient of the inside surface of the cylindrical wall can then be inferred from the measurement of temperature at the outside surface of the cylindrical wall using transient decay (Chapter 5 Sections 5.6 and 5.7). The use of inverse analysis for the measurement of heat transfer across the wall of the cylinder concept is also more accurate compared with conventional heat transfer probe techniques that can only approach the wall (*Prakash, 1999; Praksh et al., 2001; Li & Prakash, 2002; Kumar et al., 1992; Kim et al., 1986*).

The literature covering the individual measurement techniques is now discussed and summarised to highlight key attributes that are useful and pertinent to the measurement of properties of transport phenomena for the cylinder concept of the swarf dissolution process.

### 3.3 Positron-Emission Particle-Tracking (PEPT)

PEPT locates the position of a radioactive particle tracer with time between aligned adjacent camera heads (*Parker et al., 1993*); the trajectory of the particle tracer is therefore acquired within this domain (*Parker et al., 1993; Parker et al., 1997b; Stewart et al., 2001; Bakalis & Fryer, 2004; Guida et al., 2010*). The radioactivity is positron emission producing pairs of back-to-back gamma-ray photons. The common radionuclide employed is  $^{18}\text{F}$  (*Leadbeater et al., 2012*). Detection of the back-to-back gamma-ray photon pairs by the camera heads is termed a coincidence. For triangulation of the particle tracer two coincidences are required and the angle between the coincidence lines (photon emissions) gives redundancy.

### 3.4 Advancements in the PEPT technique

PEPT is a measurement technique that can be used to investigate momentum transfer and its effects. The PEPT technique originated from the closely related imaging technique Positron Emission Tomography (PET) (*Hawkesworth et al., 1986 & Parker et al., 1997b*). The PEPT technique has been developed and is currently used at the Positron Imaging Centre (PIC), University of Birmingham, UK. Advances in the PEPT technique over the last few decades are partitioned principally by the installation and use of two cameras of different electronic architectures (*Parker et al., 1993; Parker et al., 1997a; Parker et al., 2002*).

The PEPT technique was developed after recognising the potential of applying PET to engineering systems. The first camera was constructed at the Rutherford Appleton laboratory UK in 1984 and is referred to in literature as the RAL camera. In 1985 the RAL camera was installed at the PIC and its first application provided tomographic reconstruction of lubricant distribution in an operating aero-engine and gearbox (*Stewart et al., 1988*). Since this first application of the RAL camera a wide range of applications of positron measurements to engineering systems have been made (*Parker et al., 1993; Parker et al., 1997b; Stewart et al.,*

2001; Bakalis & Fryer, 2004; Guida et al., 2010). This breadth naturally followed the capabilities of the RAL camera up to its succession in 2002 by the ADAC forte camera (Parker et al., 2002). The development of the PEPT technique with camera specification is now discussed.

#### 3.4.1 The RAL camera and track algorithm

The RAL camera has a sensitive detector area of  $600 \times 300 \text{ mm}^2$  when operated in coincidence mode for the detection of back-to-back gamma-ray photon pairs (Parker et al., 1997a). Its inherent spatial resolution or interrogation width is  $\sim 8 \text{ mm}$  and the efficiency of detecting incident gamma-rays from this region is  $\sim 7\%$  (Parker et al., 1993; Parker et al., 1997a). The intrinsic sampling frequency of the RAL camera for the coincidence mode is  $\sim 3000 \text{ Hz}$  (Parker et al., 1993; Parker et al., 1997a). Because of the low camera efficiency, at high particle tracer activity, a high rate of random and scattered coincidences outnumbers genuine coincidences. This keeps the useful sampling frequency of the RAL camera lower than the intrinsic sampling frequency ( $\sim 2000\text{-}3000 \text{ Hz}$ ) (Parker et al., 1993; Parker et al., 1997a). For PET imaging normally 1 hour is required to obtain a sufficient number of coincidences from a fluid tracer (Parker et al., 1997a). Therefore, imaging can only be performed on engineering systems that reside in a stationary state. The majority of investigations by the RAL camera rely on the PEPT technique (Parker et al., 1997a), which uses an algorithm called TRACK to locate a particle tracer with time (Parker et al., 1993) (Section 3.3). The confidence in this development follows the ability of the algorithm to optimise the minimisation of location uncertainty of the particle tracer by:

1. Ascertaining the number or set size of coincidences required for triangulation within the flow.
2. Filtering corrupt events caused by scattering of gamma-ray photons.



The algorithm is parametric and allows for optimisation of many possible experimental conditions (*Parker et al., 1993*). A selective iteration across many coincidences is used to minimise the variance of the triangulated location of the particle tracer (*Parker et al., 1993*). The two main parameters are the size of the set of coincidences  $N$  and the fraction of coincidences within this size that are discarded  $f_{opt}$  (*Parker et al., 1993*). The freedom of these two parameters enables good measurement statistics and both upper and lower limits exist for confidence in computing triangulation of the particle tracer. As the set size of coincidences is increased the movement of the particle tracer becomes noticeable to the finite size of the set of coincidences i.e. the set size of coincidences used to triangulate the location of the particle tracer contain movement of the particle tracer above its own finite dimensions and therefore location. The events at the beginning and end of the set of coincidences then appear random in the triangulated location of the particle tracer. Alternatively, for a constant size of the set of coincidences the faster the particle tracer moves the greater the uncertainty in its triangulated location (*Parker et al., 1993*). Reducing the size of the set of coincidences can improve this uncertainty but only to a lower limit past which further reduction gives poor statistics (*Parker et al., 1993*). Scattering of the coincidences also results in a greater uncertainty in the triangulated location of the particle tracer and is dependent upon geometry and material (*Parker et al., 1993*). The fraction of coincidences discarded by the TRACK algorithm compensates for the scattering effect and has an optimum value dependent upon particle tracer activity and location (*Parker et al., 1993*).

For the RAL camera ultimate precision depends on the separation coordinate (z-coordinate). Polar intensity (or loss) of coincidences is a function of the separation of camera heads because the sensitive detector area of the camera heads is finite. Ideally, the redundancy of triangulation is met by two pairs of coincidences and the angle that separates them. The useful

sampling frequency of the RAL camera (~2000-3000 Hz) coincides with a separation of 300 mm for a particle tracer of activity 4 MBq (*Parker et al., 1993*). Any particle tracer activity above this value is superfluous unless the separation of the camera heads is extended (*Parker et al., 1993*). Typical uncertainties of particle tracer location associated with its velocity and measured using the RAL camera are: 5 mm for 1 m/s located at 250 Hz and, 2 mm for 0.1 m/s located at 25 Hz (*Parker et al., 1997a*).

### 3.4.2 The ADAC forte camera

In 1999 a fully digital ADAC forte camera was installed at the PIC offering enormous improvements in sampling frequency and efficiency compared with the RAL camera (*Parker et al., 2002*). This step was supported by numerous previous applications of the PEPT technique to engineering systems where it had proved powerful (*Parker et al., 1997b; Stewart et al., 2001*). The ADAC forte camera was constructed at ADAC laboratories US and has a fully digital architecture enhancing camera speed and quality. The performance of the ADAC forte camera is discussed by *Parker et al. (2002)*. The ADAC forte camera has a sensitive detector area of  $510 \times 380 \text{ mm}^2$  when operated in coincidence mode for the detection of gamma-ray photons (*Parker et al., 2002*) (Section 3.3). Its inherent spatial resolution or interrogation width is ~6 mm and the efficiency of detecting incident gamma-rays from this region is ~23% (*Parker et al., 2002*). The intrinsic sampling frequency of the ADAC forte camera for the coincidence mode is ~100 kHz (*Parker et al., 2002*). Adjusting for camera efficiency the useful sampling frequency is at least 50 kHz (*Parker et al., 2002*). As for the RAL camera, ultimate precision of the ADAC forte camera depends on the separation coordinate of the camera heads. However, because of the better specification of the ADAC forte camera it can operate with lower particle tracer activities further enhancing the application of the PEPT technique. This was summarised by *Parker et al. (2002)*, stating:

“...a factor of 10 improvement in the precision of location at optimum rates, enabling more microscopic studies of particle/surface interactions to be performed, or the tracking of faster particles (well over 10 m/s). As accurate tracking can be achieved using less activity, there is scope for developing a wider range of tracer particles, including smaller particles.”

Therefore, over the last decade the application of PEPT to the investigation of process dynamics has markedly improved. The higher sampling rate of the ADAC Forte camera reduces the location drift of the particle tracer for a given size of set of coincidences  $N$  and, also increases the measurement population size improving the statistics (Subheading 3.4.1). Typically, a particle tracer travelling at 1 m/s has its location resolved within 0.5 mm at 250 Hz (*Parker et al., 2002*).

### 3.4.3 PEPT particle tracers

Particle tracer properties are of equal importance to the functioning and development of the PEPT technique. The particle tracers must have the same properties as the material phases being studied. A representative description of the dynamics of an engineered system is then obtained. With a high sampling rate, optimal triangulation of an erratic fast moving particle tracer is achieved if it has high activity; the high activity compensates for the loss and scattering of the back-to-back gamma-ray photon coincidences (Subheading 3.4.1).

Two principal labelling techniques are used to produce radioactive particle tracers. Direct activation enables particle tracers of diameter 1 mm and above to be labelled (*Parker et al., 1993*). A  $^3\text{He}$  beam generated by the University of Birmingham MC40 cyclotron is used to bombard glass beads converting some of their oxygen atoms to the  $^{18}\text{F}$  positron emitter (*Parker et al., 1993; Parker et al., 1997b*). The  $^{18}\text{F}$  positron emitter provides a clean source of

back-to-back gamma-rays and has a half-life sufficient to provide necessary activity throughout typical experiments (*Parker et al., 1993*). The range of activities of the  $^{18}\text{F}$  particle tracer required by most investigations is 4 MBq (*Parker et al., 1993*). Indirect activation is used to produce particle tracers of diameter less than 1 mm (*Leadbeater et al., 2012*). A  $^3\text{He}$  beam is used to activate purified water producing  $^{18}\text{F}$  ions (*Leadbeater et al., 2012*). Adsorption of these ions onto ion-exchange beads completes labelling (*Leadbeater et al., 2012*). Strong base anion exchange resins are preferred. Quaternary ammonium derivatives are converted to the fluoride form and then  $^{19}\text{F}$  counter-ions are exchanged with  $^{18}\text{F}$  ions producing activities greater than 11 MBq (*Fan et al., 2006*). A layer of epoxy resin is then applied to the surface of the labelled ion-exchange bead (*Leadbeater et al., 2012*). This hardens and seals the ion-exchange bead preventing leaching of activity into liquid phases (*Leadbeater et al., 2012*).

### 3.5 Applications of the PEPT technique

PEPT has been used to investigate many types of processes (*Parker et al., 1993; Parker et al., 1997b; Stewart et al., 2001; Bakalis & Fryer, 2004; Guida et al., 2010*). These investigations are useful in highlighting the attributes of PEPT that are generic and applicable to mixing processes. The processes investigated include granular flow, single and multiphase flow and rotational flow that is mechanically or gravity driven (*Parker et al., 1993; Parker et al., 1997b; Stewart et al., 2001; Bakalis & Fryer, 2004; Guida et al., 2010*). In all of these investigations PEPT is primarily used to study the momentum transfer and occupancy of material phases within the process. The reputation that has been built at the PIC improves the appreciation of the PEPT technique and the considerable scope for using positron-emitting tracers to study momentum transfer and its effects. The potential of PEPT is still being

realised with its application. Individual PEPT investigations of different processes and flow are now discussed:

*Parker et al. (1993) Positron emission particle tracking – a technique for studying flow within engineering equipment*

The recirculation mechanism of a horizontal rotating drum containing glass beads features in both the development and practical utilisation of PEPT (*Parker et al., 1993*). This closed system neatly displays the types of information that can be extracted from the trajectory data of a PEPT particle tracer (*Parker et al., 1993*). Spatially, PEPT cannot image instantaneous quantities. *Parker et al. (1993)* describe the infancy of the PEPT technique as an integrable picture of quantities contained within the trajectory of the particle tracer. This is ergodicity or the reconstruction of quantities with time, and grounding for studying the dynamics of processes using the PEPT technique. Quantities that have a unique solution and that fill space can be imaged (*Parker et al., 1993*). These quantities are called macroscopic quantities. An integrated picture of occupancy and mean velocity field is given by *Parker et al. (1993)*.

A grid is superimposed upon the geometry of the horizontal drum and a directly activated glass bead is used as a particle tracer (*Parker et al., 1993*) (Subheading 3.4.3). The occupancy is a display of weighted incidences of the particle tracer within each grid segment and the mean velocity field is obtained by averaging of successive trajectories of the particle tracer within each grid segment (*Parker et al., 1993*). The size of the grid is chosen to give the desirable spatial resolution of the macroscopic quantity. With the display of macroscopic quantities the convolution of particle tracer trajectories within the grid segments gives inherent statistics that are useful for quantifying mixing within processes (*Parker et al., 1993*). The spread of velocity distributions within each grid segment complements position vs. time plots of the particle tracer (*Parker et al., 1993*). However, the position vs. time plots

are only useful if a mean location of the particle tracer occurs. The variance from the mean location is an indication of mixing (*Parker et al., 1993*). This combination of measurement of macroscopic quantities and their statistics gave early anticipation in proving the full potential of the PEPT technique. The summary given by *Parker et al., (1993)* recognised this potential, stating:

“It is clear that several other macroscopic quantities could be extracted to describe the motion, depending on the topic under study, leading to a much deeper insight into the phenomena involved than could be obtained using any previous experimental technique.”

*Parker et al. (1997b) Positron emission particle tracking studies on spherical particle motion in rotating drums*

*Parker et al. (1997b)* used PEPT to investigate granular motion in a partially filled horizontal rotating drum. The industrial applications of such a device include mixing, drying, coating, granulation, milling and chemical reaction in rotary kilns (*Parker et al., 1997b*). The investigation furthered the understanding of mixing within a granular rotating drum assisting in the prediction of heat transfer through its bed. This is important for the design and engineering of rotary kilns (*Parker et al., 1997b*). The mechanism of circulation within granular rotating drums is known (*Henein et al., 1983*). This provides a good test for the value of information obtained from the PEPT measurements and the further potential of the PEPT technique (*Parker et al., 1997b*).

The granular flow within a horizontal rotating drum is characterised by six modes of motion (*Henein et al., 1983*). *Slipping* of the granular material occurs at low speeds and the majority of the material remains at rest. This is followed by *slumping* where the material is now periodically lifted up the wall and slides down again. As the rotation is increased *rolling* of a

sliding surface layer occurs. The material at the bottom of the granular bed rotates with the drum feeding into the sliding surface. The granular bed is in stationary motion. At elevated speeds the sliding surface becomes curved or free and material is lifted higher before entering the sliding surface. The granular bed is now *cascading*. Approaching *centrifuging*, *ataracting* occurs where material is projected into the open space above the granular bed. Industrial rotary kilns operate within the *rolling* mode of motion and for this reason all experiments performed by *Parker et al. (1997b)* were at the limits of this mode.

The trajectories of 1.5 mm and 3 mm glass beads within drums of internal diameters of 100 mm, 136 mm and 144 mm were measured (*Parker et al., 1997b*). A single directly activated glass bead was used as a particle tracer in individual experiments (Subheading 3.4.3). All experiments had similar fill levels of ~30% by volume. Integration of occupancy and mean velocity is over spatial grids of  $2.5 \times 2.5 \text{ mm}^2$  and  $5 \times 5 \text{ mm}^2$  respectively (*Parker et al., 1997b*). The grids are in the  $r\theta$  plane in polar coordinates and the velocity vector is displayed central to a grid segment. The calculated occupancy displayed the position of the free surface and the transition from rolling to cascading mode by its curvature (*Parker et al., 1997b*). The mean velocity field clearly showed the division of the active (sliding) and bed layers (*Parker et al., 1997b*). For all experiments it is seen from the spatial resolution of the mean velocity field that within the  $r\theta$  plane the active layer occupies the same region.

Radial profiles of tangential velocity over a central 20 mm strip  $30^\circ$  from vertical shows the boundary between the active and bed layers i.e. at the boundary the tangential velocity is zero (*Parker et al., 1997b*). The intersection of this boundary layer with radius is found to be independent of drum speed for all experiments and all profiles have a constant ratio of layer thickness (radial); the bed layer is 1.5 times thicker than the active layer. Angular velocity distributions within the 20 mm strip indicate levels of granular bed motion and conditions of

slip for all experiments between the limits of the *rolling* mode (*Parker et al., 1997b*). The strip is divided into two regions, 6 mm from the wall and 6-12 mm from the wall. At higher drum speeds the angular velocity distributions become broader for all experiments and, for the 3 mm glass beads multiple distributions in the 6 mm region are observed with centroids at higher values (*Parker et al., 1997b*). Hence, the observed slip is greater for the 3 mm glass beads and the outermost layers closest to the wall appear to roll over one another. This action fits with the observation of multiple distributions of angular velocity (*Parker et al., 1997b*). The angular velocity distributions at low drum speeds show that the granular bed is not at rest contrary to the description given by *Henein et al. (1983)* of the *slipping* mode (*Parker et al., 1997b*). The width of the angular velocity distributions in the 6-12 mm region gives an indication of the extent of motion within the granular bed. *Parker et al. (1997b)* suggested that this phenomenon is related to the size and spherical shape of the glass beads.

A Lagrangian analysis of the glass bead tracers further provides detailed information on the mixing within the granular bed of the horizontal rotating drum (*Parker et al., 1997b*). Plots of radial and axial position vs. time display the circulation time of the tracers within the granular bed (*Parker et al., 1997b*). Averaging the circulation time over radial slices shows that the bed circulates uniformly irrespective of radial location. Radial mixing contributes to the variance of circulation time and is seen in the correlation of position vs. time plots (*Parker et al., 1997b*). The change in spatial dispersion or location distributions of the glass bead tracers with time indicate the time intervals required to achieve levels of homogeneity of occupancy across regions within the horizontal drum. For strong mixing the location distributions become flatter and broader with time (*Parker et al., 1997b*). Strong axial dispersion is found within the granular bed a consequence of axial transport within the active layer (*Parker et al.,*



1997b). The effectiveness and efficiency of the PEPT technique is summarised by *Parker et al. (1997b)* stating:

“Some of these results could have been obtained individually by other techniques. An important attribute of the PEPT technique is that from the history of the single tracer particle most desired information on bulk properties can be extracted, so that the mechanisms linking different phenomena can be elucidated.”

*Stewart et al. (2001) Granular flow over a flat-bladed stirrer*

*Stewart et al. (2001)* have investigated granular flow over a flat-bladed stirrer. The flow within the stirrer was comprised of 2 to 2.4 mm glass beads (*Stewart et al., 2001*). One of the beads was irradiated with a  $^3\text{He}$  beam and served as the particle tracer (*Stewart et al., 2001*). *Stewart et al. (2001)* found that PEPT could follow a directly activated glass bead up to a velocity of 2 m/s, and a directly activated glass bead moving at 1 m/s could be located within 5 mm at 20 Hz. From the trajectory data of the glass bead tracer mean velocity fields, residence times across the blade, occupancy data and velocity distributions within cells were calculated (*Stewart et al., 2001*). Detailed analysis for 2.8 kg of glass beads and 20 rpm shaft speed is provided (*Stewart et al., 2001*). The effects of blade speed and fill level were also investigated (*Stewart et al., 2001*).

The occupancy data in front and behind the blade captured the bed surface shape well (*Stewart et al., 2001*). The axial, radial and tangential velocities of the glass bead tracer were resolved very well across the geometry (*Stewart et al., 2001*). The mean velocity field captured and elucidated the recirculation mechanism of the glass beads around the flat bladed stirrer (*Stewart et al., 2001*). The mechanism was seen by resolving all velocity components in the axial (vertical) and polar (horizontal) planes. A grid of  $\Delta\theta = 10^\circ$ ,  $\Delta z = 10$  mm, and

$\Delta r = 20$  mm was used to construct the mean velocity field (*Stewart et al., 2001*). In comparison with previous investigations it was found that the PEPT results corroborated with established behaviour but also provided further insight into the granular flat-bladed stirrer. For example PEPT could test the existence of a stagnant zone outside the influence of the blade (*Stewart et al., 2001*). Stagnant glass beads would have a negative angular velocity when transformed relative to the angular velocity of the shaft (*Stewart et al., 2001*). This is visible by the skewed angular velocity distribution of the glass bead tracer across the geometry of the flat-bladed stirrer, and indicates that the inherent PEPT statistics can test for segregation of momentum transfer and momentum zones (*Stewart et al., 2001*). This is an important and powerful result.

The effectiveness of the design of the flat-bladed stirrer for mixing of granular materials is assessed by the calculated residence time between blades (*Stewart et al., 2001*). A residence time links the spatial and temporal scales of the driver (flat-bladed stirrer) to the scales within the flow and measures efficiency of mixing. The crossing of the glass bead tracer between blades was expressed by the number of required blade passes (*Stewart et al., 2001*). This informative investigation has shown attributes of PEPT that are generic and applicable to the investigation of mixing processes. Momentum transfer has been related to process parameters. The concluding remarks by *Stewart et al. (2001)* indicate the significance of PEPT towards process design and engineering, stating:

“The work provides a thorough account of the flow structure that arises in one particular class of device for the stirring of powders and granules. This is the most complete account that has been offered to date for this class of equipment, a proper understanding of which is essential for the proper design of equipment and the proper control of product properties. The flow structure has been illustrated by calculation

of some parameters which are needed by the chemical engineer in achieving these objectives. The data files obtained from PEPT can be used to assist any process operation by appropriate coupling of the information on local particle density and particle velocity with process kinetics, be it heat transfer, mass transfer or chemical reaction or for the assistance in modelling operations such as breakage and agglomeration.”

*Bakalis & Fryer (2004) Measuring velocity distributions of viscous fluids using positron emission particle tracking (PEPT)*

*Bakalis & Fryer (2004)* have used PEPT to investigate isothermal and non-isothermal laminar pipe flow for viscous fluids. Industrial chemical processes mainly involve the manipulation of heat and momentum transfer in opaque fluids with complex rheological behaviour that are often time-dependent (*Bakalis & Fryer, 2004*). Because of the penetrating behaviour of the back-to-back gamma-ray coincidences PEPT is an ideal technique for studying such flows (*Bakalis & Fryer, 2004*) (Section 3.3). PEPT can measure the dynamics of a process but cannot image the time-dependency of the instantaneous velocity field of a viscous fluid. Instantaneous resolution is only provided by the trajectory of a particle tracer; a localised kinematic description. PEPT images the mean velocity field through convolution algorithms of trajectories of the particle tracer. Thus although tracer kinematics are resolved instantaneously, PEPT can only be used to investigate the dynamics (force, mass) of processes that converge and reside in a stationary state. Through the convolution of trajectories it is therefore important that the particle tracer(s) occupy all parts of the process geometry. Because the tracer is exposed to both determinant and random flow behaviour within an experiment its location is not dispersion free. The particle tracer will have a spatial probability density proportional to the geometry or spatial grid (*Bakalis & Fryer, 2004*). For

axial motion within the  $rz$  plane of a cylinder the normalised probability density irrespective of determinant flow is:

$$df(r) = 2rdr/R^2 \quad (3.1)$$

Thus the occupancy of the tracer will be skewed towards larger radii (*Bakalis & Fryer, 2004*).

*Bakalis & Fryer (2004)* measured the flow of three fluids each having different constitutive shear stress: a Newtonian fluid (37% sucrose solution), a shear-thinning fluid (1% CMC solution), and a Herschel-Bulkley fluid (35% sucrose solution, 1% CMC solution). The flow was contained within an aluminium pipe of diameter 19 mm fitted with an external shell heat exchanger (*Bakalis & Fryer, 2004*). For non-isothermal flow the coolant temperature was held at 5°C and the internal fluid at 70°C (*Bakalis & Fryer, 2004*). Indirectly activated ion-exchange beads were used as particle tracers (*Bakalis & Fryer, 2004*) (Subheading 3.4.3). Two sizes of beads (240 and 600 microns) gave an occupancy that conformed to the normalised probability density of equation (3.1) (*Bakalis & Fryer, 2004*). This gives confidence in the use of a convolution algorithm and indicates that the statistics belonging to the kinematics of the particle tracer are representative of the process geometry. The axis of the pipe was calibrated using 10-12 stationary particle tracers around the surface of the pipe at two axial positions (*Bakalis & Fryer, 2004*). The equation of a circle was fitted to these two sets and a rotation matrix was then used to rotate and realign data (*Bakalis & Fryer, 2004*). Regression of the trajectory of the particle tracer was used to calculate its velocity by fitting a line to 15 consecutive locations (*Bakalis & Fryer, 2004*). If the standard deviation of the radial location was greater than 0.5 mm the axial velocity values were discarded (*Bakalis & Fryer, 2004*). Scattering of the gamma-ray photon coincidences appeared as jumps in the

PEPT trajectory data (*Bakalis & Fryer, 2004*) (Subheading 3.4.1). These points were removed prior to regression (*Bakalis & Fryer, 2004*).

Both tracer sizes (240 and 600 microns) gave the total resolution of the radial profile of the mean axial velocity for the three different viscous fluids (*Bakalis & Fryer, 2004*). The isothermal profile was compared with the analytical solution for pipe flow and the non-isothermal profile with a CFD simulation (*Bakalis & Fryer, 2004*). The experimental profiles of the mean axial velocity agreed very well with the calculated profiles (*Bakalis & Fryer, 2004*). As particle tracers have finite size, occupancy close to the wall was low (*Bakalis & Fryer, 2004*). To improve occupancy tracers should be as small as possible (*Bakalis & Fryer, 2004*). However, this presents limitations because tracer activity and therefore measurement uncertainty is poorer the smaller the particle tracer becomes (*Bakalis & Fryer, 2004*).

*Guida et al. (2010) PEPT measurements of solid-liquid flow field and spatial phase distribution in concentrated monodisperse stirred suspensions*

*Guida et al. (2010)* applied PEPT to the study of turbulent solid-liquid suspensions in a stirred vessel. In their investigation the use of PEPT is to generalise turbulent mixing within stirred vessels (*Guida et al., 2010*). *Guida et al. (2010)* discuss the literature belonging to the design of mechanical agitation for solids suspension in viscous fluids, and recognise the potential of the PEPT technique at further aiding this activity. Qualitative descriptions of flow fields are correlated with occupancy, dimensional analysis and a variance model of dispersion (*Guida et al., 2010*). The investigation builds on a full understanding of the usefulness of the Lagrangian nature of the PEPT technique. The resolution of occupancy is developed by using a uniform spatial grid (*Guida et al., 2010*). Specific to mixing processes turbulence is purposefully implemented so that the location of discrete entities is not dispersion free. Dispersive processes are characterised by at least one spatial and temporal correlation that is

second-order or higher (e.g. position vs. time). The occupancy is now a result of determinant motion. The observed level of non-homogeneity in the occupancy across the geometry depends upon the prevalence of mean flow (recirculation) to dispersive forces.

The stirrer geometry comprises a flat-base cylindrical vessel of diameter 288 mm fitted with four baffles of width 28.8 mm (*Guida et al., 2010*). Agitation is by a 6 bladed 45° pitched-turbine of diameter 144 mm and height 28.8 mm (*Guida et al., 2010*). The turbine has either an up (PBTU) or down (PBSD) configuration and its clearance from the base of the cylindrical vessel is 72 mm (*Guida et al., 2010*). The solids phase consisted of glass beads ~3 mm in diameter and density 2485 kg/m<sup>3</sup> and the liquid phase is a salt solution (*Guida et al., 2010*). All experiments were performed at the minimum rotational speed for solids suspension (*Guida et al., 2010*). Solids fraction of the glass beads varied from 0-40 wt% (*Guida et al., 2010*). For the solids phase the particle tracer is a directly activated glass bead and for the liquid phase the particle tracer is an indirectly activated 600 micron ion-exchange bead (*Guida et al., 2010*) (Subheading 3.4.3). The density of the ion-exchange bead tracer is identical to the density of the salt solution (*Guida et al., 2010*). Both the glass bead and ion-exchange bead tracers undergo positron emission via the <sup>18</sup>F isotope (*Guida et al., 2010*) (Subheading 3.4.3). A least-squares method is used to calculate particle tracer velocity (*Guida et al., 2010*). The mean flow fields obtained by *Guida et al. (2010)* resolved the important changes in the momentum of the suspensions. A significant drop in momentum occurred in the impeller discharge region above 10.6% loading and repositioning of the recirculation (flow loop) was seen (*Guida et al., 2010*). Azimuthally and radially averaged solids concentration showed that PBTU configuration performed better at suspending particles (*Guida et al., 2010*). For the PBTU/PBSD configurations the radial dispersion of particles was similar (*Guida et al., 2010*).

Applying dimensional analysis a flow number is defined and assesses the affect of solids loading on mean flow (*Guida et al., 2010*). The analysis utilises the horizontal edge of the turbine (discharge region) which relates to the volumetric flow rate (*Guida et al., 2010*). As expected the observed index of flow discharge for the PBTU/PBTD configurations are practically identical. At high wt% the flow number indicates that momentum is being transferred predominantly to the solids phase; the solids flow number increases while the liquid flow number decreases (*Guida et al., 2010*). The action of gravity is seen between the difference in PBTD/PBTU flow numbers and volumetric discharge. A global continuity condition is used to check the validity of the mass balance where for a constant density the global convection should be zero i.e. the liquid and solid phases remain within the confines of the stirrer. The PEPT measurements confirmed this condition (*Guida et al., 2010*). A global uniformity index uses a variance model to assess homogeneity of solids concentration (*Guida et al., 2010*). This model confirms that the PBTD configuration performs better than the PBTU configuration for overall mixing (*Guida et al., 2010*).

### 3.6 Summary of the PEPT technique

As with all measurement techniques there are steps in the acquisition of useful results. These steps usually involve the reception of raw information or signals in relation to physical phenomena, the processing of these signals and the confidence of realising the measurement as expressed through measurement statistics or uncertainty. The expanse of application of the measurement technique can then be seen. For PEPT unique information from positron emission of a particle tracer is gained and lost in triangulation of its location (Sections 3.3, 3.4, and 3.5). This occurs at great rates and can allow the fine resolution of the trajectory of a particle tracer (Section 3.4). The signals or coincidences of back-to-back gamma-ray photons can be described as loss, scattered, genuine and random (Sections 3.3, 3.4, and 3.5). The

genuine coincidences in relation to the particle tracer activity and camera specification permit the redundancy of triangulation to be met, and a sufficient population size for a required confidence in the calculated location of the tracer (Section 3.4). This is specific to the motion investigated (Section 3.4). The novelty of PEPT and its applications, particularly towards the flow of viscous fluids is how its Lagrangian nature complements the resolution of stationary dynamics (mass, force) (Section 3.5). Ergodicity expresses convergence of macroscopic quantities over time and for example occupancy and mean velocity fields can be calculated (Section 3.5). Here, PEPT proves powerful when multiple material phases constitute flow (Section 3.5). The sizes of spatial grids give freedom in resolving important length scales and also present statistics for the converged macroscopic quantities (Section 3.5). These statistics are useful in elucidating local momentum transfer (Section 3.5).

For the calculation of the Reynolds stress tensor discussed in Section 3.2 the instantaneous velocities of the turbulent flow must be measured to high precision. The error in the instantaneous velocity is propagated through to the calculation of the Reynolds stress tensor (Chapter 4 Section 4.10). The reported accuracy of the location of particle tracers for different velocities justifies the use of PEPT for the calculation of the Reynolds stress tensor (Section 3.4). The granular flow studies using PEPT also indicate the usefulness of the PEPT technique for studying the flow of swarf (Section 3.5). PEPT should provide a complete multiphase characterisation of turbulent flow for the cylinder concept of the swarf dissolution process.

### 3.7 Boundary inverse methods for heat conduction

Using Fourier's law correlations can be built between the temperature histories at locations and the boundary condition at a surface. The boundary condition can then be calculated from the temperature history (*Beck et al., 1985; Alifanov, 1994*). This is an inverse heat conduction problem (IHCP) (*Beck et al., 1985; Alifanov, 1994*). The IHCP is primarily of use in



situations where the surface or boundary condition of interest is exposed to a harsh physical and/or chemical environment. This can be a high surface heat flux or surface temperature or where corrosive chemicals are present. In these situations it is impractical to use direct measurement at the surface. IHCP also sits naturally with extreme thermal boundary conditions because it is a transient method. The correlations or inversion processes that have been used include Duhamel's theorem, Laplace transform, hyperbolic transformation and indirect difference schemes (*Stolz, 1960; Beck, 1967; Imber & Khan, 1972; Beck, 1977; Weber, 1981; Scott & Beck, 1985; Beck et al., 1985; Alifanov, 1994*). Common to all of these methods is the approximation of a well posed solution and the instability of the inversion process to noise within the temperature history.

An additional driver for the use of IHCP is cost that further complements the practical significance of the IHCP. *Alifanov (1994)* summarises, stating: "Heat transfer experiments can be quite costly and limited to one test, especially when dealing with a full-scale test of machines and equipment." It is therefore important to apply new methodology to gain more information from investigations enabling the simplification of an experiment while maintaining accuracy. IHCP serves these purposes (*Alifanov, 1994*). Hence, there is a requirement to develop reliable methods of solving the IHCP (*Alifanov, 1994*). For a long time scepticism of inverse methods hindered the development of solution theory. Mathematically it was accepted that inverse methods were unsolvable and of no practical importance. Over the last half century the development of solution theory for inverse methods and their application has proved that this viewpoint is incorrect. This development paralleled the common place and use of the microprocessor.

### 3.8 Application and development of the IHCP

Application of the IHCP for the measurement of a boundary condition is shown by numerous investigations (*Alifanov, 1994; Beck et al., 1985*). The solution theory of the IHCP is now discussed highlighting the attributes of the methods towards the form of the inverse solution:

*Stolz (1960) Numerical solutions to an inverse problem of heat conduction for simple shapes*

*Stolz (1960)* describes IHCP as the calculation of a sought boundary condition from knowledge of interior temperature. An inherent uncertainty for the IHCP solution exists because the boundary condition is damped at interior points (*Stolz, 1960*). This will be independent of solution method (*Stolz, 1960*). Heat conduction for a silver sphere of radius 1 in. was considered by *Stolz (1960)*. An analytical solution of the temperature response for a unit heat flux is discretised using a fixed time step (*Stolz, 1960*). This discretised equation is then inverted and compared with Duhamel's theorem (*Duhamel, 1830; Carslaw & Jaeger, 1947*) (*Stolz, 1960*). Duhamel's theorem can be written as an integral equation to relate the surface heat flux to a temperature history at a given location (*Carslaw & Jaeger, 1947*). The inverted equation provides the heat flux vector with time for a given temperature response (*Stolz, 1960*). A heat balance is used to smooth the discrete heat flux by reporting its value at the midpoint of the time steps (*Stolz, 1960*). An optimum time step exists for the construction of the heat flux. If the time step is too small the solution oscillates (*Stolz, 1960*). The silver sphere was subject to a severe heat flux of triangular profile with time, and using the analytical temperature response the optimum time step for the inversion was found to be 0.025 s (*Stolz, 1960*). To overcome the inherent uncertainty in the IHCP the temperature response should be as close as possible to the surface of the sought boundary condition (*Stolz, 1960*).

*Beck (1967) Surface heat flux determination using an integral method*

*Beck (1967)* considers the stability of an inverse solution on decreasing the magnitude of the time step and notes for previous methods the solution can oscillate (*Stolz, 1960*). The geometry considered was a semi-infinite body heated with a constant heat flux (*Beck, 1967*). Three points on the geometry are considered. These are the surface and two interior points equally separated from the surface (*Beck, 1967*). The heat flux at the first interior point is calculated from the temperature history at the second interior point (*Beck, 1967*). A comparison of the exact solution with this inverse solution tests the precision and therefore validity of the inversion process (*Beck, 1967*).

Both the partial differential heat conduction equation and integral methods can be used to construct the inverse solution (*Beck, 1967*). An integral method is chosen because of its greater simplicity but at a cost that only linear heat conduction can be described (*Beck, 1967*). Duhamel's theorem provides an integral equation (*Stolz, 1960*). The integral equation is a Volterra equation and is integrated numerically using the trapezoidal rule (*Beck, 1967*). A recurrence relation is obtained for the heat flux from the temperature history (*Beck, 1967*). To improve the inverse solution least-squares is employed to further increase the number of terms of the temperature history in a modified recurrence relation (*Beck, 1967*). This is consistent with causality; a greater number of future temperature (effect) measurements are used to calculate a past heat flux (cause). It was shown that this improved inversion process allowed smaller time steps to be used without oscillation in the inverse solution (*Beck, 1967*). The dimensionless time-step was reduced by a factor of four (*Beck, 1967*).

*Imber & Khan (1972) Prediction of transient temperature distributions with embedded thermocouples*

*Imber & Khan (1972)* present an IHCP that utilises a series solution obtained through the Laplace transform of the parabolic heat conduction equation. The geometry was a finite slab backed with a semi-infinite dimension formed as a composite of two regions of different thermal parameters (*Imber & Khan, 1972*). The thickness of the slab is 0.5 ft. (*Imber & Khan, 1972*). The Laplace transform provides a spatial temperature distribution with time (*Imber & Khan, 1972*). Direct analytical solution of the parabolic heat conduction equation provides temperature traces at two interior positions for a given surface condition (*Imber & Khan, 1972*). The time vector of the discrete analytical solution is fitted to a polynomial which in turn with least-squares optimisation is used to find the coefficients of the series solution at the interior positions (*Imber & Khan, 1972*). The general temperature distribution can then be written in terms of the coefficients (*Imber & Khan, 1972*). For an initial condition of zero and unit surface temperature rise the extrapolation from the interior positions of the general temperature distribution gives very accurate surface temperature (*Imber & Khan, 1972*). Interior positions of 0.30 ft. and 0.66 ft. were used (*Imber & Khan, 1972*). The strength of this method is that it allows transients of long duration to be investigated, and can be applied to geometries that have no thermal symmetry (*Imber & Khan, 1972*). However, the boundary condition needs to be known a priori to calculate the coefficients of the series belonging to the Laplace transform.

*Beck (1977) Criteria for comparison of methods of solution of the inverse heat conduction problem*

For the integral methods that use Duhamel's theorem no treatment of noise within the temperature history had previously been considered (*Stoltz, 1960; Beck, 1967*) (*Beck, 1977*). The noise also causes solution instability that is seen in oscillations similar to those of the

solution with an ill chosen time-step (*Stoltz, 1960; Beck, 1967*) (*Beck, 1977*). The least-squares approach is replaced by the principle of maximum likelihood if the errors within the temperature history are correlated (*Beck, 1977*). It was found that the measurement errors are correlated if the time steps are small and the measurements are from the same thermocouple (*Beck, 1977*). The principle of maximum likelihood reduces to least-squares if the measurement error is random (*Beck, 1977*). Using the previous inverse method of *Beck (1967)* it was found that the instability caused by noise in the temperature history can be alleviated by using larger time-steps (*Beck, 1977*). For noise that has a standard deviation of 0.001 of the rise of the temperature history, the minimum dimensionless time step that can be used without significant loss of accuracy is found to be 0.05 (*Beck, 1977*). To combat this restriction a method by *Tikhonov (1963, 1967)* was discussed. Here, a regularisation parameter is used to introduce bias so that the measured temperature history approaches the exact temperature history (*Beck, 1977*). The bias is zeroth-order and is applied to the magnitude of the surface heat flux (*Beck, 1977*). The exact temperature history is obtained from the direct problem of the partial differential heat conduction equation. It is noted that the Tikhonov method has no inherent statistical basis and that because the method employs Duhamel's theorem it can only provide inverse solutions for linear problems (*Beck, 1977*).

#### *Weber (1981) Analysis and solution of the ill-posed inverse heat conduction problem*

*Weber (1981)* recasts the IHCP from the parabolic to a hyperbolic partial differential equation describing heat conduction. This automatically gives a well-posed solution and overcomes oscillatory behaviour caused by noise in the temperature history (*Beck, 1967; Beck, 1977*) (*Weber, 1981*). However, the hyperbolic equation must be satisfied by certain combinations of boundary conditions otherwise the equation is underdetermined (*Morse & Feshbach, 1953, p.706*). Therefore, the hyperbolic equation as a description of heat conduction is not generic.

Unlike integral methods the hyperbolic equation can describe non-linear heat conduction *Weber (1981)*. Therefore, the hyperbolic equation could be of significant benefit for the investigation of transients of long duration and extreme boundary conditions. The hyperbolic equation would also resolve any fine structure because no explicit smoothing is applied *Weber (1981)*. For the simple geometries investigated a noise of 1% within the temperature history gave a noise of 2-3% in the sought boundary condition *Weber (1981)*.

*Scott & Beck (1985) Analysis of order of sequential regularisation solution of inverse heat conduction problem*

*Scott & Beck (1985)* investigates the affect of regularisation order of the Tikhonov method on resolution. The geometry is a 1-dimensional planar slab with a prescribed heat flux at one of its surfaces and temperature measurement at the other insulated surface (*Scott & Beck, 1985*). The problem is solved analytically and provides a comparison with the inverse solution by simulation using randomly generated noise (*Scott & Beck, 1985*). A pulse, square and triangular heat flux are used as test scenarios (*Scott & Beck, 1985*). The regularisation order can take any value, however, the order is useful in terms of solution magnitude, gradient and curvature. These properties of the inverse solution curve relax the applied bias allowing for example points of maxima/minima and inflections. For regularisation of second-order the curvature is optimised over the sought boundary condition vector. Therefore, points of inflection are allowed. This prevents distortion of the inverse solution if the sought boundary condition has high curvature and therefore gives greater resolution. Likewise if the regularisation is of first-order points of maxima/minima are allowed. A combination of regularisation orders can be used (*Scott & Beck, 1985*). The effect of noise in the temperature history on regularisation order was also investigated (*Scott & Beck, 1985*). Regularisation of

second-order is most sensitive to noise and regularisation of first-order is least sensitive to noise (*Scott & Beck, 1985*).

*Alifanov (1994) Inverse heat transfer problems*

*Alifanov (1994)* provides a rework of the Tikhonov method. The direct problem is constructed using an integral equation from which the unknown solution of this equation must be found (*Alifanov, 1994*). The unknown solution is the inverse solution or sought boundary condition. The kernel of the integral equation is a statement of the direct problem. The integral equation sums the unknown solution over time to get the present temperature at a location. Therefore, the history of the unknown solution can be decomposed. The discretisation of the integral equation gives a matrix relation and a vectorised history of the unknown solution. Using a Lagrange multiplier a variational functional of this matrix relation can be expressed and a residual compared with a metric representing error (*Alifanov, 1994*). The residual is between the estimated and measured temperature. Minimisation of the functional by the Lagrange multiplier provides a least-squares problem for the estimation of the unknown solution for a given kernel (*Alifanov, 1994*). The kernel of the integral equation allows the IHCP to be recast as an initial value problem that is continuous. The Tikhonov regularisation parameter is found to be the reciprocal of the Lagrange multiplier (*Alifanov, 1994*). *Alifanov (1994)* then employs Green's function for the kernel and finds a general form of a regularisation operator and therefore regularised least-squares problem.

Another approach discussed by *Alifanov (1994)* for the solution of the IHCP is the gradient method. An automatic criterion of optimisation is based upon the surface of a residual of the estimated and measured temperature. The directional gradient of the surface provides an iterative method for convergence onto the optimum value of the sought boundary condition (*Alifanov, 1994*). Unlike Tikhonov regularisation the gradient method has no inherent control

of measurement error. The residual due to error is segregated from the solution residual and a stopping criterion is used instead of simulation (*Alifanov, 1994*). This gives similar correction to Tikhonov regularisation; the solution can appear over- or under-regularised. The Gradient methods presented by *Aifannov (1994)* are the favoured modern IHCP solution methods because they do not require prior information on the sought boundary condition, and allow quick application of the IHCP. The analysis and algorithms of the Gradient methods presented by *Alifanov (1994)* have not changed and similar to Tikhonov regularisation the IHCP becomes an initial value problem that is continuous (*de Faoite et al., 2014*). Both the reworked Tikhonov regularisation and gradient methods can also be applied to non-linear heat conduction (*Alifanov, 1994*).

### 3.9 Summary of boundary inverse methods

From the physical aspects of heat transfer processes the use of the IHCP is sensible in concept towards extreme surface conditions. However, with particular regard to the engineering of processes the practical significance of the IHCP has become established with the development of its own solution theory (Section 3.8). Early methods provided approximations of well posed solutions but were restricted by the magnitude of the time step dictated by the geometry and thermal parameters of the domain (Section 3.8). With no formal treatment of error within the temperature history a stringent requirement for noise free data also presented further restriction (Section 3.8). This barrier was alleviated by the Tikhonov method, which can permit any time step and reduces the effects of noise within the inverse solution through applied bias of a regularisation operator (Section 3.8).

*Alifanov (1994)* used functional analysis to provide a powerful rework of solution theory including the Tikhonov method. Here the IHCP is recast as an initial value problem that is continuous (Section 3.8). The inverse solution of the sought boundary condition is inferred



from a complete set of future temperature measurements and therefore no restriction is placed upon the time step (Section 3.8). This availability of maximum information maintains a high accuracy of the modern IHCP that provides high efficiency in the investigation of heat transfer through the simplification of experiments. All that is required is the measurement of a temperature transient at locations across a process geometry, which can be obtained within the environment of the conditions of a process under investigation. For the Tikhonov method the general form of the regularisation operator is found; operation is on the magnitude, gradient and curvature of the inverse solution of the sought boundary condition and is exclusive or combinatory (Section 3.8). Alongside Tikhonov regularisation gradient methods are also introduced by *Alifanov (1994)*. Iterations of the sought boundary condition follow the directional gradient of the surface of a functional giving local optimisation of the boundary condition and convergence of the inverse solution. Because of this directionality no simulation is required (Section 3.8).

The inverse solutions of both Tikhonov regularisation and gradient methods are similar (*Alifanov, 1994*). Both methods combat the effects of noise within the temperature history. However, for Tikhonov regularisation the correction of error is sequential, local and specific through the selection of the regularisation operator (*Scott & Beck, 1985; Alifanov, 1994*) (Section 3.8). Therefore, if the form of sought boundary condition is modeled prior to the IHCP the regularisation operator allows greater flexibility because it can be applied to features of the sought boundary condition. Because of this greater flexibility Tikhonov regularisation is chosen for the IHCP analysis of the heat transfer coefficient of the inside surface of the wall for the cylinder concept of the swarf dissolution process (Chapter 5 Section 5.3).

## CHAPTER 4

### MIXING OF SWARF AND VISCOUS FLUID WITHIN CYLINDER

#### CONCEPT

##### 4.1 Introduction

Sufficient mixing of the swarf and acids within the cylinder concept of the swarf dissolution process is important and must complement both the radiological and chemical constraints discussed in Chapter 1 Section 1.2. Specifically, the fixed diameter of the cylinder will require a sufficient overall heat transfer coefficient for cooling of the process. The implementation of turbulent stresses within the cylinder concept will promote the transfer of swarf and acids and, therefore heat, to the inside surface of its wall. An analysis of the length scales and flow within the cylinder concept required for cooling is necessary (Chapter 1 Section 1.2) (Chapter 2 Section 2.3). An understanding of this mixing will inform, assess and justify design of the cylinder concept (Chapter 1 Section 1.2) (Chapter 2 Section 2.3). The momentum source must also complement the radiological and chemical constraints (Chapter 1 Subheading 1.2.2). Gravity-driven momentum by distribution of gas from the base of the cylinder concept is compatible with the material phase of substances; an impeller would crash with the swarf. A buoyancy term of inert gas distribution and the process chemistry, which produces gaseous products, will both promote turbulent stresses (Chapter 1 Section 1.3). The gaseous products of the process chemistry are evaluated in the calculations of the enthalpy of the dissolution of swarf discussed in Chapter 2 Section 2.2.

To model the mixing in the cylinder concept an air-water-swarf column is used (Subheading 4.2.1). The volume force arising from the buoyancy term is:

$$\mathbf{F}_{\text{buoyancy}} = -(1 - \alpha_w - \alpha_s)(\rho_w - \rho_g)\mathbf{g}_z \quad (4.1)$$

The difference in densities between the water and air dominates. Therefore, there is little difference between the volume force arising from air or inert gases such as argon. The air-water-swarf column is a good indicator of mixing of swarf for a variety of process gases including the gaseous products of the chemical dissolution of swarf.

High speed imaging has given a definitive first grasp of the length scales and periodicity that characterise the mixing and provides the initial basis for a CFD algorithm and the sampling rate of the trajectory of the particle tracer for PEPT experiments (Chapter 3 Sections 3.2 and 3.6) (Section 4.7). PEPT has been used to assess the turbulent stresses within air-water-swarf flow through indirect activation of a particle tracer that provides trajectory data within the water (Sections 4.4, 4.5, 4.6, 4.9, 4.10 and 4.11). Computational Fluid Dynamics (CFD) is used to simulate the motion and flow effects of the air-water interface, and coincides with the PEPT experiments to provide flow characterisation (Sections 4.8 and 4.11). PEPT has also provided swarf occupancy data for the air-water-swarf column through direct activation of a swarf tracer and, therefore, the actual mixing of the swarf can be shown (Section 4.11).

## 4.2 The distribution of gas within a column of viscous fluid

*Deckwer (1992, p. 9-12)* gives a concise account of the devices used for distributing gas into a column of viscous fluid. Ideally, such a device must be simple to construct, maintain, is efficient and can accommodate turbulent flow. The efficiency of a device and the flow regime of the column are determined by the global and radial gas hold-up (*Deckwer, 1992*):

$$\varepsilon_G = (L_B - L_R) / L_B, \quad \varepsilon_g = f(r) \quad (4.2)$$

The global gas hold-up is the total volume fraction of gas within a column of viscous fluid (*Deckwer, 1992*). The onset of turbulent or heterogeneous flow is characterised by the transition from a uniform to non-uniform radial gas hold-up at high gas flow rates (*Deckwer, 1992*). Non-uniformity within a device can provide the impetus for this transition (*Freedman, 1968*). *Hills (1974)* describes the change in flow features that accompany the transition from a uniform to non-uniform radial gas hold-up, stating: ‘...bubbling was no longer uniform but that large eddies were forming in the liquid, and that some larger bubbles were also being formed by coalescence’. The time scales for mixing within a viscous fluid such as water can be divided into a global recirculation onto which large eddies are superimposed (*Hills, 1974*). This global recirculation is termed “gulf-streaming”.

The simplest device for distributing gas into a column of viscous fluid is a tube followed in complexity by perforated plates, sintered plates and jets (*Deckwer, 1992*). Tubes give poor gas hold-up compared with plates and jets (*Deckwer, 1992*). Sintered plates present problems in operation and tend to become encrusted and clogged up reducing their efficiency (*Deckwer, 1992*). Jets give high gas hold-up and operate with different regions within the column (*Deckwer, 1992*). Bubbles coalesce above the jet up to an equilibrium distance and gas within this region is distributed by strongly induced recirculation in the viscous fluid (*Deckwer, 1992*). Similarly, perforated plates give high global gas hold-up compared with jets, but a more uniform radial gas hold-up close to gas entry (*Deckwer, 1992*). The design parameter of a perforated plate is porosity, the percentage of total surface area of holes to cross-sectional area of the column. The size of the holes and array pattern strongly influences the performance of distributing gas at different gas flow rates. Common arrays of holes are

concentric circles or square-pitch and their patterns can have varying degrees of uniformity along different coordinates. Common porosities for perforated plates are 0.01% to 0.08% (*Hills, 1974; Degaleesan, 2001*).

The effect of the addition of swarf above the distributor device on both gas distribution and the resultant flow is uncertain. From its characteristics the perforated plate is the most sensible choice and for this investigation this device provides gas distribution within a air-water-swarf column. Perforated plates are flexible towards the degree of uniformity in their array pattern and therefore the radial gas hold-up. This allows flexibility in the design of the air-water-swarf column to achieve:

1. The greater radial uniformity of gas distribution near to a perforated plate compared with other devices should help mimic the effects of gaseous products from the chemical dissolution of swarf during the process.
2. Consistent with the observations of *Freedman (1968)* some non-uniformity of the array pattern is helpful to promote the transition from homogeneous to heterogeneous flow at lower gas flow rates. Heterogeneous flow is inertial and characterised by turbulent stresses.

#### 4.2.1 The perforated plate and column used to investigate mixing within the cylinder concept

The perforated plate and column used to investigate the mixing of swarf within the cylinder concept is detailed in figures 4.1 and 4.2. The plate is made of inconel and sits upon a Viton o-ring housed within a polypropylene assembly (Figure 4.1). Four inconel screws are used to hold the plate tight against the Viton o-ring, one screw in each corner (Figure 4.1). The assembly is affixed to a Perspex tube via a stainless steel flange and a Viton gasket is used to seal the two faces (Figure 4.1). The length of the Perspex tube is 1200 mm and its internal

diameter is 144 mm (Figure 4.1). The plate array is a central hole surrounded by 16 holes on two concentric circles of diameter 35 mm and 68 mm (Figure 4.2). The density of holes for this array is non-uniform (Figure 4.2). Each hole is tapered to a partial depth of 1 mm across an initial diameter of 1 mm and the porosity based upon cylinder cross-section is 0.08% (Figure 4.2). Tapered holes help prevent blockage by small particles. The number and diameter of holes of the perforated plate were restricted by machining operations because inconel is a hard alloy and is difficult to machine.

Machining inside of the assembly includes the air inlet and column drain (Figure 4.1). The air inlet is symmetrical about the centre of the assembly and forms an inverted cone below the plate (Figure 4.1). A  $\frac{1}{2}$  " BSP internal thread at the bottom face of the assembly matches an adaptor nipple, which is fusion welded to a polypropylene non-return valve (Figure 4.1). This allows air to flow into the inlet but does not allow water to flow out. Beneath the non-return valve a ball valve is fusion welded and serves to drain the air inlet (Figure 4.1). The column drain is off-centre and consists of four holes, each hole 6 mm in diameter (Figure 4.1). The four holes meet to a  $\frac{1}{2}$  " BSP internal thread and again the thread matches an adaptor nipple, which is fusion welded to a ball valve (Figure 4.1).

### 4.3 Dissipative phenomena and continuity

Vector analysis is central to the investigation and development in understanding of dissipative phenomena in viscous fluids. Turbulence is an example of a dissipative phenomenon. Here, the momentum of the viscous fluid cascades through interactions on different spatial and temporal scales with the evolution of heat. The vector analysis in this section is influenced by the texts of *Lu (1977)* and *Boas (1983)*. Vectors are an abstract mathematical quantity. They are free of conceptual generalisations of space and time. Simply they are collections of numbers that can relate to a coordinate system and their operations are irrespective of

coordinate transformation. These operations have profound application to the description of transport phenomena and hence the dynamics of engineered processes. The unit operations of vector analysis are the scalar product and vector product. These operations have commutative and distributive behaviour but their special properties are in the interpretation of their definition; they are applied. Both the scalar and vector product are used in the definition of a dyadic, an entity that has commutative behaviour to that observed in momentum transfer. The scalar product is expressed by:

$$\mathbf{A} \cdot \mathbf{B} = |\mathbf{A}| |\mathbf{B}| \cos \angle(A, B), \quad 0 \leq \cos \angle(A, B) \leq \pi \quad (4.3)$$

$$\mathbf{A} \cdot (\mathbf{B} + \mathbf{C}) = \mathbf{A} \cdot \mathbf{B} + \mathbf{A} \cdot \mathbf{C}, \quad \mathbf{A} \cdot \mathbf{B} = \mathbf{B} \cdot \mathbf{A} \quad (4.4)$$

The range of the subtended angle of both vectors gives three possible scenarios if the scalar product is zero. One of the vectors is zero or the vectors are orthogonal. The vector product is expressed by:

$$\mathbf{A} \times \mathbf{B} = [|\mathbf{A}| |\mathbf{B}| \sin \angle(A, B)] \mathbf{n}, \quad 0 \leq \angle(A, B) \leq \pi \quad (4.5)$$

$$\mathbf{A} \times (\mathbf{B} + \mathbf{C}) = \mathbf{A} \times \mathbf{B} + \mathbf{A} \times \mathbf{C}, \quad \mathbf{A} \times \mathbf{B} = -\mathbf{B} \times \mathbf{A} \quad (4.6)$$

The unit vector is orthonormal to the plane of both vectors. The sinusoidal phase gives a right-handed rotation to the unit vector through the subtended angle. The range of the angle gives three possible scenarios if the vector product is zero. One of the vectors is zero or the vectors are parallel. Using triplet notation a resultant vector from some origin can always be drawn. This allows a determinant form.

The dyadic and its commutative behaviour are defined by:

$$\mathbf{A} \times (\mathbf{B} \times \mathbf{C}) = \mathbf{B} \mathbf{A} \cdot \mathbf{C} - \mathbf{C} \mathbf{A} \cdot \mathbf{B} \quad (4.7)$$

The reality of the dyadic entities on the RHS of equation (4.7) is manifested through the scalar product. A vector is produced. Taking arbitrary components of the vectors for a dyadic in equation (4.7) gives components of a tensor:

$$\begin{aligned} \mathbf{CA} = & C_1 A_1 \mathbf{e}_1 \mathbf{e}_1 + C_1 A_2 \mathbf{e}_1 \mathbf{e}_2 + C_1 A_3 \mathbf{e}_1 \mathbf{e}_3 + \dots \\ & C_2 A_1 \mathbf{e}_2 \mathbf{e}_1 + C_2 A_2 \mathbf{e}_2 \mathbf{e}_2 + C_2 A_3 \mathbf{e}_2 \mathbf{e}_3 + \dots \\ & C_3 A_1 \mathbf{e}_3 \mathbf{e}_1 + C_3 A_2 \mathbf{e}_3 \mathbf{e}_2 + C_3 A_3 \mathbf{e}_3 \mathbf{e}_3 + \dots \end{aligned} \quad (4.8)$$

For the above scalar product, vector product and dyadic operations their commutative behaviour labels planes and enables the *del* operator to relate surface integrals to volume integrals with physical application. For a cylindrical coordinate system the *del* operator and displacement vector in component form are:

$$\nabla = \mathbf{e}_r \partial / \partial r + (\mathbf{e}_\theta / r) \partial / \partial \theta + \mathbf{e}_z \partial / \partial z \quad (4.9)$$

$$d\mathbf{s} = \mathbf{e}_r dr + r \mathbf{e}_\theta d\theta + \mathbf{e}_z dz \quad (4.10)$$

The *del* operator can also form a dyadic. Using equation (4.7) a vector relation can be constructed to evaluate this dyadic:

$$\nabla \times (\nabla \times \mathbf{A}) = \nabla \nabla \cdot \mathbf{A} - \nabla \cdot \nabla \mathbf{A} \quad (4.11)$$

This is the foundation of field mechanics and the relations of the *del* operator are integrable to the Eulerian description of a vector field. From the origin a vector of coordinates draws out surfaces along curves. The coordinates coincide with the basis vectors of the coordinate system. From applying the above operations transport phenomena over planes, surfaces and volumes can be studied. The integral form of the *grad* operator is:



$$\nabla P = \lim_{V \rightarrow 0} (1/V) \int_S \mathbf{n} P \, dS \quad (4.12)$$

The integral form of the *curl* operator is:

$$\nabla \times \mathbf{u} = \lim_{V \rightarrow 0} (1/V) \int_S \mathbf{n} \times \mathbf{u} \, dS \quad (4.13)$$

The integral form of the *div* operator is:

$$\nabla \cdot \mathbf{u} = \lim_{V \rightarrow 0} (1/V) \int_S \mathbf{n} \cdot \mathbf{u} \, dS \quad (4.14)$$

Multiplying the *div* operator acting on the velocity of the fluid by its density gives the total outward mass flux over a volume element. Therefore, when the divergence of the velocity field is expressed with accumulation of mass, a mass source and mass sink, continuity is developed. Continuity is applicable to all transport phenomena; mass, momentum and heat. The *div* operator gives the total outward flux for both convective (forced) and diffusive (entropic) transport. Therefore, for a convective process with no mass accumulation, source or sink the continuity condition is:

$$\nabla \cdot \mathbf{u} = 0 \quad (4.15)$$

Continuity develops all transport equations.

#### 4.4 Flow description of a viscous fluid

The flow of a viscous fluid such as water is characterised by its viscosity. This is the parameter that determines the inherent shear stress within the flow caused by molecular interaction. When the viscous fluid is contained within a geometry at low flow rates the velocity profile is continuous and steady. This is called laminar flow. The momentum transferred within the flow is purely molecular (viscous) in nature. As the flow rate is

increased fluctuations or eddies occur and these begin to transfer momentum additional and of magnitude greater than the viscous contribution. This is an inertial contribution and now the velocity and density of the viscous fluid are of greater significance in determining the shear stress within the flow. This is called turbulent flow. The transition from laminar to turbulent flow has been characterised by *Reynolds (1883)*. The magnitude of the dimensionless Reynolds number labels the transition. This number is the ratio of inertial to viscous effects and belongs to the geometry and flow scenario.

The vectorised Navier-Stokes equation is applicable to both laminar and turbulent flow (*COMSOL AB, 2013*):

$$\rho \partial \mathbf{u} / \partial t = \mu \nabla \cdot \nabla \mathbf{u} - \rho \mathbf{u} \cdot \nabla \mathbf{u} - \nabla P \quad (4.16)$$

Its limitation to direct solution is in finding a solution method that can resolve the spatial and temporal scales of turbulence in an evolutionary manner (naturally). The instabilities that start the cascade of fluctuations develop from the initial and boundary conditions. Turbulence is time-variant on its smallest temporal scale. The duality of the present understanding of turbulence is the deterministic underpinnings of the Navier-Stokes equation against the observed stochastic nature of the fluid velocity (*Hinze, 1975; Bradshaw, 1978; McComb, 1990*). The averaging of the fluid velocity is reproducible (*Hinze, 1975; Bradshaw, 1978; McComb, 1990*). Because of the limitation of direct solution of the Navier-Stokes equation and stochastic conformance, progression within the understanding of turbulence is mainly statistical (*Hinze, 1975; Bradshaw, 1978; McComb, 1990*). The universal description of turbulence is the vectorised Reynolds-Averaged Navier-Stokes (RANS) equation (*COMSOL AB, 2013*):

$$\rho \frac{\partial \bar{\mathbf{u}}}{\partial t} = \mu \nabla \cdot \nabla \bar{\mathbf{u}} - \rho \bar{\mathbf{u}} \cdot \nabla \bar{\mathbf{u}} - \nabla P - \rho \nabla \cdot \overline{(\mathbf{u} - \bar{\mathbf{u}})(\mathbf{u} - \bar{\mathbf{u}})} \quad (4.17)$$

$$\mathbf{u} = \mathbf{u}' + \bar{\mathbf{u}} \quad (4.18)$$

The instantaneous velocity field is expressed through the mean and fluctuating velocity field. Both the instantaneous and fluctuating velocity fields are considered random variables and Gaussian. The Gaussian function is compatible with the commutative and distributive behaviour of the operators described in Section 4.3.

Transfer of momentum by turbulent eddies implies that there must be strong correlations between the respective components of the fluctuating velocity field. Packets of momentum are exchanged from different coordinate directions. As flow structures, vortices dominate turbulent flow. The vorticity of the instantaneous velocity field is (*Ottino, 1990, p. 53*):

$$\boldsymbol{\Omega} = \nabla \times \mathbf{u} \quad (4.19)$$

The growth and decimation of the vortices in the instantaneous velocity field are controlling factors and give rise to the components of the fluctuating velocity field. The transport equation for vorticity is (*Ottino, 1990, p. 56*):

$$\rho \frac{\partial \boldsymbol{\Omega}}{\partial t} = \rho \boldsymbol{\Omega} \cdot \nabla \mathbf{u} - \rho \mathbf{u} \cdot \nabla \boldsymbol{\Omega} + \mu \nabla \cdot \nabla \boldsymbol{\Omega} \quad (4.20)$$

Equation (4.20) is obtained by applying the *curl* operator to the vectorised Navier-Stokes equation. Interaction of vorticity with velocity gradients alongside convection and diffusion of vorticity provide mechanisms for the growth and destruction of vortices. The interaction of vorticity with velocity gradients is purely a 3-dimensional phenomenon. For lower dimensionality (e.g. axisymmetric flow) there is no interaction of vorticity with velocity gradients through the scalar product. Under this symmetry only convection and diffusion of

vorticity operate and only the azimuth has a nonzero component of vorticity in cylindrical coordinates:

$$\rho \frac{\partial \Omega_\theta}{\partial t} = -\rho u_r \frac{\partial \Omega_\theta}{\partial r} - \rho u_z \frac{\partial \Omega_\theta}{\partial z} + \mu \left( \nabla^2 \Omega_\theta + \frac{2}{r^2} \frac{\partial \Omega_r}{\partial \theta} - \Omega_\theta / r^2 \right) \quad (4.21)$$

$$\Omega_\theta = \frac{\partial u_r}{\partial z} - \frac{\partial u_z}{\partial r} \quad (4.22)$$

The nonlinearity of the convection of vorticity propagates the cascade of fluctuations within the turbulent flow. The viscous diffusion dissipates vorticity at the smallest length scales where kinetic energy is transferred into heat. Therefore, at moderate to high Reynolds number the convection of vorticity dominates in axisymmetric non-irrotational flow (*Fan & Tsuchiya, 1990, p. 6-7*).

The motion of a viscous fluid can be described in either a Lagrangian or Eulerian analysis. Lagrangian analysis is an extension of kinematics and does not involve any mass or force in its analysis; it is calculus of only single coordinates and time. Conversely, a dynamic analysis of both mass and force, gives a Eulerian analysis and a vectorised field. From the Eulerian description the Lagrangian description is obtained by integrating the vector components, of which the magnitudes are the trajectories of the pathlines:

$$\mathbf{s}(t) = \mathbf{s}(t=0) + \int_0^t \mathbf{u}(t')^* dt', \quad \mathbf{u}(t)^* = \mathbf{u}(\mathbf{s}(t), t) \quad (4.23)$$

The vectorised Navier-Stokes equation is a Eulerian description of fluid motion. Integration of the kinematic descriptions requires known initial conditions. An iteration within the coordinate components can then mimic a sampling rate of a trajectory. However, if the precise initial conditions are not known it is more informative to use a Taylor series expansion of the coordinate in time. The diagonality of the terms is then interpreted as perturbations to the

velocity. If the flow is turbulent the velocity becomes a random variable and then multiple independent trajectories (ensemble) can be averaged to give a mean velocity. This is an essential part of ergodicity and has the mathematical context of convergence. It can be expressed through the mean of an ensemble by (*Drew & Passman, 1999, p. 105-120*):

$$\bar{\mathbf{u}} = 1/n [\mathbf{u}_1 + \mathbf{u}_2 + \mathbf{u}_3 + \dots \mathbf{u}_n] = 1/t \int_0^t \mathbf{u}(t') dt' = \text{const.}, \quad t \geq t_0 \quad (4.24)$$

Hence, the mean becomes a constant of time and the dynamics reside in a stationary state i.e. the time-dependent operators of equation (4.17) vanish:

$$\mu \nabla \cdot \nabla \bar{\mathbf{u}} - \rho \bar{\mathbf{u}} \cdot \nabla \bar{\mathbf{u}} - \nabla P - \rho \nabla \cdot \overline{(\mathbf{u} - \bar{\mathbf{u}})(\mathbf{u} - \bar{\mathbf{u}})} = 0 \quad (4.25)$$

Turbulence can therefore become stationary. It is a dissipative phenomenon, a condition for convergence of dynamics. The usefulness of ergodicity is that experimentally it allows point-wise sampling, simplifying the requirements of an investigation. It also satisfies the Eulerian construction from independent Lagrangian trajectories over time. For a discrete data set this is an explicitly mapped transformation of the trajectories to the indices of the spatial coordinates.

Both Eulerian and Lagrangian analyses of motion have their own qualities for the theoretical and experimental investigation of turbulence. The Lagrangian analysis sits naturally with the stochastic description of turbulence. Here, random trajectories are averaged to construct a field. It is useful to use both descriptions simultaneously. The convolution of the random Lagrangian trajectories presents natural integration of statistics and complements the form of the RANS equation. A Lagrangian description of deformation of a viscous fluid also leads to a relation for vorticity (*Lu, 1977, p. 335*):

$$d\mathbf{s} \cdot \nabla \mathbf{u} = d\mathbf{s} \cdot \boldsymbol{\varepsilon} + \frac{1}{2} \boldsymbol{\Omega} \times d\mathbf{s} \quad (4.26)$$

The deformation of a viscous fluid caused by interfaces can therefore be related to its local vorticity. Equation (4.26) is a relation for the relative velocity of a particle with respect to an arbitrary origin. If the vector differential is considered to be a function of time the deformation can be calculated from a particle trajectory; the deformations in time and space complement one another.

#### 4.5 Mixing of swarf within a turbulent flow of a viscous fluid

Within this study the mixing of swarf by turbulent flow of a viscous fluid is considered a direct effect of momentum transfer. Therefore, this is a dynamic (mass, force) assessment of mixing and the resolved force should coincide with the observed occupancy of swarf. The resolution of force can be obtained indirectly from the vectorised RANS equation discussed in Section 4.4. The RANS equation is a momentum balance over a volume element and addition of momentum is achieved through the volume force, which acts as a source term. For multiphase flow the RANS equation can be volume averaged (*Drew & Passman, 1999*):

$$\begin{aligned} & \overline{(1 - \alpha_g - \alpha_s)} \mu \nabla \cdot \nabla \bar{\mathbf{u}} - \overline{(1 - \alpha_g - \alpha_s)} \bar{\rho}_w \bar{\mathbf{u}} \cdot \nabla \bar{\mathbf{u}} - \overline{(1 - \alpha_g - \alpha_s)} \nabla P \\ & - \overline{(1 - \alpha_g - \alpha_s)} \bar{\rho}_w \nabla \cdot (\mathbf{u} - \bar{\mathbf{u}})(\mathbf{u} - \bar{\mathbf{u}}) + \mathbf{F} = 0 \end{aligned} \quad (4.27)$$

The addition of momentum through the volume force is of great significance because it enables the effect of discrete phases on the viscous fluid to be evaluated. For actual measurement of stress the coupling of individual source terms is implicit. This can be a result of interfaces and the combined action of gravity.

The volume averaging in equation (4.27) is consistent with the ensemble averaging and ergodicity of equation (4.24). On convergence of the stationary dynamics of equation (4.27)

the volume fractions lose their time-dependency and the occupancies of the discrete phases become functions of only space:

$$\partial/\partial t \rightarrow 0, \quad (1 - \alpha_g - \alpha_s) = f(t, s) \rightarrow \overline{(1 - \alpha_g - \alpha_s)} = f(s) \quad (4.28)$$

$$\alpha_w = (1 - \alpha_g - \alpha_s) \quad (4.29)$$

For the Eulerian description of equation (4.27) the density of the viscous fluid is replaced by the volume averaged density of the viscous fluid i.e. the volume element has the possibility of occupancy of the viscous fluid and discrete phases:

$$\rho_w \rightarrow \bar{\rho}_w \quad (4.30)$$

For a Lagrangian description the trajectories can follow the flow of the viscous fluid in the presence of the occupancies of the discrete phases consistent with equation (4.28). In this instance and by ergodicity the reconstruction of the Eulerian description of equation (4.27) is for the density of the viscous fluid, not the volume averaged density of the viscous fluid.

The volume averaging in equation (4.27) is also consistent with the volume averaging of momentum balance equations given by *Drew & Passman (1999, p. 126)*.

For the turbulent nature of heterogeneous air-water-swarf flow, the stress modeling within the water is provided by the vectorised RANS equation. With convergence to a steady-state and by the divergence theorem the force at the interface, or combined interfaces, is balanced with the net outflow of momentum described by the dissipative stresses. This allows the force to be resolved from the mean and fluctuating velocity components of the water. Thus, by virtue of weight the swarf-water interface is a momentum source alongside the air-water interface via buoyancy. However, because heterogeneous air-water-swarf flow is dominated by eddy

transport the contribution to momentum transfer by the viscous stresses in equation (4.27) are far less. The volume force and pressure term is taken over to the RHS of equation (4.27). The form of the dynamic pressure is absorbed into the volume force and the hydrostatic pressure of the weight of the water can be written explicitly. Now the volume force is the resultant responsible for motion. Therefore, the components of the viscous stress, convective acceleration and the Reynolds stress tensor for the water are evaluated:

$$\begin{aligned}
& -\overline{(1-\alpha_g-\alpha_s)\mu\nabla\cdot\nabla\bar{\mathbf{u}}} + \overline{(1-\alpha_g-\alpha_s)\bar{\rho}_w\bar{\mathbf{u}}\cdot\nabla\bar{\mathbf{u}}} \\
& + \overline{(1-\alpha_g-\alpha_s)\bar{\rho}_w\nabla\cdot(\mathbf{u}-\bar{\mathbf{u}})(\mathbf{u}-\bar{\mathbf{u}})} = \left(\mathbf{F} - \overline{(1-\alpha_g-\alpha_s)\bar{\rho}_w\mathbf{g}_z}\right)_{\text{inertial}}
\end{aligned} \tag{4.31}$$

The explicit form of the buoyancy term of the volume force for gravity-driven flow is given by equation (4.1).

As discussed in section 4.3 expanding the dyadic gives the components of the Reynolds stress tensor:

$$\begin{aligned}
\bar{\rho}_w\overline{(\mathbf{u}-\bar{\mathbf{u}})(\mathbf{u}-\bar{\mathbf{u}})} &= \mathbf{e}_r\mathbf{e}_r\bar{\rho}_w\overline{u'_ru'_r} + \mathbf{e}_r\mathbf{e}_\theta r\bar{\rho}_w\overline{u'_r\omega'_\theta} + \mathbf{e}_r\mathbf{e}_z\bar{\rho}_w\overline{u'_ru'_z} + \\
& \mathbf{e}_\theta\mathbf{e}_r r\bar{\rho}_w\overline{\omega'_\theta u'_r} + \mathbf{e}_\theta\mathbf{e}_\theta r^2\bar{\rho}_w\overline{\omega'_\theta\omega'_\theta} + \mathbf{e}_\theta\mathbf{e}_z r\bar{\rho}_w\overline{\omega'_\theta u'_z} + \\
& \mathbf{e}_z\mathbf{e}_r\bar{\rho}_w\overline{u'_zu'_r} + \mathbf{e}_z\mathbf{e}_\theta r\bar{\rho}_w\overline{u'_z\omega'_\theta} + \mathbf{e}_z\mathbf{e}_z\bar{\rho}_w\overline{u'_zu'_z}
\end{aligned} \tag{4.32}$$

The divergence of the tensor is:

$$\begin{aligned}
\nabla\cdot\bar{\rho}_w\overline{(\mathbf{u}-\bar{\mathbf{u}})(\mathbf{u}-\bar{\mathbf{u}})} &= \mathbf{e}_r\bar{\rho}_w\frac{1}{r}\frac{\partial}{\partial r}\left(\overline{ru'_ru'_r}\right) + \mathbf{e}_\theta\bar{\rho}_w\frac{\partial}{\partial r}\left(\overline{ru'_r\omega'_\theta}\right) + \mathbf{e}_z\bar{\rho}_w\frac{1}{r}\frac{\partial}{\partial r}\left(\overline{ru'_ru'_z}\right) + \\
& \mathbf{e}_r\bar{\rho}_w\frac{\partial}{\partial\theta}\left(\overline{\omega'_\theta u'_r}\right) + \mathbf{e}_\theta\bar{\rho}_w r\frac{\partial}{\partial\theta}\left(\overline{\omega'_\theta\omega'_\theta}\right) + \mathbf{e}_z\bar{\rho}_w\frac{\partial}{\partial\theta}\left(\overline{\omega'_\theta u'_z}\right) + \\
& \mathbf{e}_r\bar{\rho}_w\frac{\partial}{\partial z}\left(\overline{u'_zu'_r}\right) + \mathbf{e}_\theta\bar{\rho}_w r\frac{\partial}{\partial z}\left(\overline{u'_z\omega'_\theta}\right) + \mathbf{e}_z\bar{\rho}_w\frac{\partial}{\partial z}\left(\overline{u'_zu'_z}\right)
\end{aligned} \tag{4.33}$$

To evaluate the viscous stress components the relation in equation (4.11) is used:



Correction to figure 4.34 on p.68

$$\mu \nabla \cdot \nabla \bar{\mathbf{u}} = \mu \nabla \nabla \cdot \bar{\mathbf{u}} - \mu \nabla \times (\nabla \times \bar{\mathbf{u}}) = \mathbf{e}_r \mu \left( \nabla^2 \bar{u}_r - \frac{\bar{u}_r}{r^2} - \frac{2}{r^2} \frac{\partial \bar{u}_\theta}{\partial \theta} \right) + \mathbf{e}_\theta \mu \left( \nabla^2 \bar{u}_\theta + \frac{2}{r^2} \frac{\partial \bar{u}_r}{\partial \theta} - \frac{\bar{u}_\theta}{r^2} \right) + \mathbf{e}_z \mu \nabla^2 \bar{u}_z$$

$$\begin{aligned} \mu \nabla \cdot \nabla \bar{\mathbf{u}} &= \mu \nabla \nabla \cdot \bar{\mathbf{u}} - \mu \nabla \times (\nabla \times \bar{\mathbf{u}}) = \mathbf{e}_z \mu \nabla^2 \bar{u}_z + \mathbf{e}_\theta \left( \mu \nabla^2 \bar{u}_\theta + \frac{2}{r^2} \frac{\partial \bar{u}_r}{\partial \theta} - \frac{\bar{u}_\theta}{r^2} \right) + \\ &\mathbf{e}_z \left( \nabla^2 \bar{u}_r - \frac{\bar{u}_r}{r^2} - \frac{2}{r^2} \frac{\partial \bar{u}_\theta}{\partial \theta} \right) \end{aligned} \quad (4.34)$$

To evaluate the convective acceleration components its dyadic is expanded and the scalar product with velocity is taken:

$$\begin{aligned} \bar{\rho}_w \bar{\mathbf{u}} \cdot \nabla \bar{\mathbf{u}} &= \mathbf{e}_r \bar{\rho}_w \left( \bar{u}_r \frac{\partial \bar{u}_r}{\partial r} + \frac{\bar{u}_\theta}{r} \frac{\partial \bar{u}_r}{\partial \theta} + \bar{u}_z \frac{\partial \bar{u}_r}{\partial z} \right) + \mathbf{e}_\theta \bar{\rho}_w \left( \bar{u}_r \frac{\partial \bar{u}_\theta}{\partial r} + \frac{\bar{u}_\theta}{r} \frac{\partial \bar{u}_\theta}{\partial \theta} + \bar{u}_z \frac{\partial \bar{u}_\theta}{\partial z} \right) + \\ &\mathbf{e}_z \bar{\rho}_w \left( \bar{u}_r \frac{\partial \bar{u}_z}{\partial r} + \frac{\bar{u}_\theta}{r} \frac{\partial \bar{u}_z}{\partial \theta} + \bar{u}_z \frac{\partial \bar{u}_z}{\partial z} \right) \end{aligned} \quad (4.35)$$

Therefore, by evaluating the components on the LHS of equation (4.31) enables the actual stresses operating between the different material phases of air-water-swarf flow to be resolved and gives a true dynamic assessment of mixing of swarf (Subheadings 4.11.3 and 4.11.4). The volume force of the stationary dynamics of the turbulent multiphase flow can be calculated and compared with measured occupancies of swarf (Subheading 4.11.4).

#### 4.6 The PEPT technique

From the vector analysis in Section 4.4 and 4.5 the characterisation and measurement of multiphase turbulence and its stress requires the resolution of fluid velocity in 3-dimensional space and time. This allows the terms of the RANS equation to be evaluated and a dynamic assessment of flow. Ideally, the flow measurement technique should provide statistics of the momentum that are compatible with the stochastic form of the RANS equation. A Eulerian-Lagrangian capability of the measurement technique will ensure this requirement. Such a capability will also support the analysis of Section 4.5 where a Lagrangian analysis can evaluate the dynamic mixing of swarf within turbulent air-water-swarf flow. A sampling rate should be used to capture the periodicity of flow structures belonging to the turbulence and their dominant length scales. Sufficient data must be acquired to permit the calculation of both

instantaneous and mean components of fluid velocity. The flow measurement technique must not perturb the continuity condition of the multiphase flow and therefore non-invasive techniques are preferred, and the measurement statistics should give an uncertainty of magnitude lower than the dominant length scales.

The PEPT technique fulfils the above criteria and is discussed in Chapter 3 Sections 3.3-3.6. Trajectory data of a particle tracer is acquired over large experiment durations, and because the PEPT technique follows flow it can respond to accelerative (inertial) perturbations very well (Section 4.10). The inertia of the particle tracer is far less than the inertia of the dominant turbulent eddies responsible for mixing of swarf within air-water-swarf flow; typical diameters of particle tracers used to investigate momentum transfer within viscous fluids range from 100-600 microns with similar densities to that of the viscous fluids (*Leadbeater et al., 2012*) (Section 4.7). A spatial grid is used to discretise the geometry of the flow for the resolution of velocity components according to the ergodic theorem (Eulerian-Lagrangian capability) discussed in Sections 4.4 and 4.5 (*Parker et al., 1993; Parker et al., 1997b; Stewart et al., 2001; Bakalis & Fryer, 2004; Guida et al., 2010*) (Sections 4.10 and 4.11). Regional statistics of the velocity components can be calculated for each grid segment (*Parker et al., 1993; Parker et al., 1997b; Stewart et al., 2001; Bakalis & Fryer, 2004; Guida et al., 2010*). The PEPT technique can also be used to investigate granular motion such as the motion of swarf within turbulent air-water-swarf flow, and allows the occupancy of swarf within a air-water-swarf column to be obtained (*Parker et al., 1997; Guida et al., 2010*) (Subheading 4.11.4).

The investigations performed by *Parker et al. (1997b)* and *Guida et al. (2010)* on granular motion and motion of a viscous fluid provide good examples of the application of PEPT, and are discussed in Chapter 3 Section 3.5. *Parker et al. (1997b)* tracked a directly activated glass

bead contained within bulk motion of a granular bed inside a horizontal rotating drum. The granular flow within the horizontal rotating drum consisted of either 1.5 mm or 3 mm glass beads in separate experiments (*Parker et al., 1997b*). The activities of the glass bead tracers allowed a tracking time of 50-250 minutes and with separate spatial grids of 2.5 mm and 5 mm segments gave resolution of occupancy and mean velocity field (*Parker et al., 1997b*). The loading of the drums was ~30% by volume and the internal diameters of the drums were in the range 100-144 mm (*Parker et al., 1997b*). Regional distributions of the velocity components gave insight into the mechanism of bed recirculation and extent of mixing (*Parker et al., 1997b*).

*Guida et al. (2010)* give a full assessment of a turbulent two-phase flow (Chapter 3 Section 3.5). A granular phase of glass beads is contained within a viscous fluid of salt solution and mechanically agitated (*Guida et al., 2010*). The glass beads are 3 mm in diameter and the loading ranged from 0-40 wt% inside a cylindrical vessel of diameter 288 mm (*Guida et al., 2010*). A single glass bead was directly activated and used as the particle tracer for the granular phase (*Guida et al., 2010*). The motion of the viscous fluid was tracked using an indirectly activated particle tracer of diameter 600  $\mu\text{m}$  (*Guida et al., 2010*). For individual experiments a tracking time of 30 minutes and a non-uniform spatial grid gave the resolution of occupancy and mean velocity field for both material phases (*Guida et al., 2010*). Regional variance of occupancy was used to calculate a global index of uniformity to assess mixing of the granular phase (*Guida et al., 2010*).

*Chiti et al. (2011)* have discussed the TRACK algorithm developed by *Parker et al. (1993)* used to process raw data files. The TRACK algorithm is discussed in Chapter 3 Section 3.4. The algorithm produces an ASCII text file which gives the location of the particle tracer in Cartesian coordinates, time, and the probable error of the particle tracer location (*Chiti et al.,*

2011). Their investigation obtained PEPT data for turbulent flow of salt and sucrose solutions mechanically agitated by a Rushton turbine (*Chiti et al., 2011*). For the TRACK algorithm both the size of the set of coincidences  $N$  and the fraction of coincidences within this size that are discarded  $f_{opt}$  must be selected carefully to give good data quality (*Chiti et al., 2011*). To quantify the selection of parameters *Chiti et al. (2011)* calculated the relative standard deviation of the particle tracer location for many values of  $N$  and  $f_{opt}$  over the data sets. They found that optimum values were within the range of  $N$  from 100 to 300 and  $f_{opt}$  from 10% to 30%.

#### 4.7 Flow Visualisation

The use of high speed imaging is necessary to resolve the periodicity and length scales of turbulent flow within the air-water-swarf column prior to flow measurement using the PEPT technique (Sections 4.9, 4.10 and 4.11). This information sets the minimum sampling frequency of PEPT trajectories for the measurement of large scale turbulent eddies and provides confidence in the analysis of PEPT data (Section 4.10). The air-water-swarf column is discussed in Subheading 4.2.1. High speed imaging of the air-water-swarf column has been captured using a Photron<sup>®</sup> FASTCAM SA3 camera. At frame rates up to 2000 fps the camera has a pixel size of 17  $\mu\text{m}$  and a resolution of  $1024 \times 1024$  pixels. When the camera is fitted with a Navitar<sup>®</sup> long distance microscope lens, a 165 mm fixed working distance provides the following examples of magnification: at a magnification of 0.58 the field of view and pixel size is 30014  $\mu\text{m}$  and 29.31  $\mu\text{m}$  respectively, at a magnification of 7.0 this is reduced to 2487  $\mu\text{m}$  and 2.429  $\mu\text{m}$ . Hence, increasing the working distance between the camera and column quickly provides adequate imaging of the heterogeneous flow of the air-water-swarf column (column diameter 144 mm).

Four experiments are used to image heterogeneous flow with and without a dissolved electrolyte and/or swarf and are summarised in table 4.1. An electrolyte is used to mimic the effect of aqueous ions from the dissolution of swarf and aqueous acids on the heterogeneous flow. 1 kg of dissolved sodium chloride is used as an electrolyte (Experiments 2 and 3 of table 4.1). For each experiment in table 4.1 the volume of water is 11.25 litres and is the same as the total volume of prefill and acids within the cylinder concept (Chapter 1 Section 1.3). The superficial air velocity based upon cylinder cross-section is 6.1 cm/s. The mass of loose swarf is 500 g and the swarf has length and thickness of magnitude  $10^0$ - $10^1$  cm and  $10^{-3}$ - $10^{-1}$  cm respectively, and density  $\sim 6.52$  g/cm<sup>3</sup> (Chapter 1 Section 1.2). The mass of loose swarf is the same for the cylinder concept discussed in Chapter 1 Section 1.3. The column is backlit to provide a greater contrast for imaging of the heterogeneous flow containing dissolved sodium chloride (Experiments 2 and 3 of table 4.1).

**Table 4.1** Flow visualisation experiments and corresponding AVI files.

Experiment	Name of AVI file	Superficial air velocity (cm/s)	Addition of sodium chloride (kg)	Addition of swarf (g)
1	flow_vis_expt_1	6.1	-	-
2	flow_vis_expt_2	6.1	1	-
3	flow_vis_expt_3	6.1	1	500
4	flow_vis_expt_4	6.1	-	500

Using the Photron<sup>®</sup> FASTCAM SA3 camera an image rate of 500 fps is used to capture 5 seconds of heterogeneous flow. Each frame is saved as a Tagged Image File Format (TIFF) and then processed using MATLAB<sup>®</sup> and its built-in function *avifile*. The MATLAB<sup>®</sup> algorithm is called *movie.m* and is given in Appendix 3. The flow is played back at a reduced rate of  $\times 10$  (*avifile* processes 50 TIFF images per second of playback).

A compact disc containing the playback of the experiments of table 4.1 is provided at the back of the volume. The names of the Audio Video Interleave (AVI) files that coincide with the experiments are given in table 4.1. The experiments show that the heterogeneous flow is characterised by air voids of large spherical and elliptical cap bubbles that flatten and elongate radially as they rise through the column. On average these voids rise centrally through the column with a periodicity of  $\sim 5$  Hz. The presence of dissolved sodium chloride inhibits bubble coalescence and the voids are smaller in size. The sizes of air voids belonging to the individual experiments are displayed in figures 4.3-4.6. The inhibition of bubble coalescence caused by dissolved sodium chloride leads to a broad bubble size distribution, and the density of smaller bubbles is greater reducing the transparency of the heterogeneous flow (Figures 4.4 and 4.5 cf. Figures 4.3 and 4.6).

There is an overall reduction in air void size for the flow containing swarf (Figures 4.3 and 4.4 cf. Figures 4.5 and 4.6). The geometry of the spherical voids is described by their radius  $R$  and the geometry of the elliptical voids by their major  $a$  and minor  $b$  axes (radii). For heterogeneous flow with and without dissolved sodium chloride and/or swarf, the largest geometries of spherical and elliptical voids are  $R \sim 20$  mm,  $a \sim 20$  mm and  $b \sim 30$  mm. The internal diameter of the column provides the scale of the air voids.

#### 4.8 Computational Fluid Dynamics of the free surface of the air-water interface

The rise of air voids of similar shape dominates the flow in all of the flow visualisation experiments of Section 4.7 with or without an electrolyte and/or swarf. Therefore, the simulation of the rise of a void within water should provide a good level of flow characterisation in the evaluation of instantaneous quantities such as vorticity, velocity and pressure. COMSOL MULTIPHYSICS<sup>®</sup> ver. 4.3b employs the finite element method for the simulation of transport properties of multiphase flow. The finite element method enables the

study of complex geometries and transient behaviour. In this investigation the finite element method is used to assess the transport of momentum belonging to the rise of an individual air void through water. This provides a powerful insight into the dynamics of the interface of the rising void.

#### 4.8.1 Phase field method

To simulate multiphase flow COMSOL MULTIPHYSICS<sup>®</sup> calls the pre-built phase field method within the multiphase flow section of the fluid flow module. This is an established method for studying the motion of the interface of immiscible fluids for both phase transition and multiphase flow (*Atanovskii, 1995; Jacqmin, 1999; Yue et al., 2004; Yue et al., 2006*). The method belongs to the fixed mesh class, which employs a scalar indicator function to reconstruct the interface at each time step and supersedes interface tracking methods that call a moving mesh labelled with material points to replicate the motion of the interface (*Yue et al., 2004; Yue et al., 2006*). The development of the phase field method in literature followed the model used by *Atanovskii (1995)* to describe thermocapillary flow in a gap. In the construction of a scalar indicator function *Atanovskii (1995)* considered the excess free energy of a thin interfacial layer of mixed components with the immediate environment. The excess free energy is identified with the interfacial tension in the Gibbs theory of capillarity and the description of an interface given by *van der Waals (1893) (Atanovskii, 1995)*. The scalar indicator function is called the phase field variable. To great strength this thermodynamic formulism of an interfacial layer allows for singular events such as the coalescence and breakage of interfaces (*Jacqmin, 1999*). Interface tracking methods fail at singular events because the material points must be single valued and at high interface curvature the material points become entangled (*Jacqmin, 1999; Yue et al., 2004; Yue et al., 2006*).



For the pre-built phase field method within COMSOL MULTIPHYSICS® the coupled Navier-Stokes and Cahn-Hilliard equation convects a phase field variable that defines the interface layer and is additional to the chemical potential of mixing across this layer defined by the curvature of this variable (*Cahn & Hillard, 1958*) (*COMSOL AB, 2013*):

$$\frac{\partial \phi}{\partial t} + \mathbf{u} \cdot \nabla \phi = \nabla \cdot \gamma \nabla G \quad (4.36)$$

$$G = \lambda \left[ -\nabla^2 \phi + \frac{\phi(\phi^2 - 1)}{\varepsilon^2} \right] \quad (4.37)$$

$$\gamma = \chi \varepsilon^2 \quad (4.38)$$

A continuous monotonic phase field variable enables the physical existence and convection of the interface layer. Hence, the motion of the interface is governed by both transport equations and the state of the multiphase flow. The mixing energy takes the Cahn-Hilliard form (*Cahn & Hillard, 1958*) (*Yue et al, 2006; COMSOL AB, 2013*):

$$f_{mix}(\phi, \nabla \phi) = \frac{\lambda |\nabla \phi|^2}{2} + \frac{\lambda (\phi^2 - 1)^2}{4\varepsilon^2} \quad (4.39)$$

$$G = \frac{\partial f_{mix}}{\partial \phi} - \nabla \cdot \frac{\partial f_{mix}}{\partial \nabla \phi} \quad (4.40)$$

In reality an interface is of order Angstroms, however, within the phase field method the finite interface thickness is much larger because of attainable mesh element sizes. The interface thickness is purely a parameter of the phase field method. The tendency is for the curvature of the interface to disperse lowering the chemical potential of mixing. At high curvature, transient diffusion/solubility of the interface scales with interface thickness (*Jacqmin, 1999*).

Therefore, the interface thickness should be as small as possible (*Jacqmin, 1999*). The mobility term of equation (4.36) balances the diffusive and convective transport of the interface to maintain a constant interface thickness. The interface thickness, and therefore chemical potential, is fitted (realised) with the known surface tension to give the volume force due to mixing (*Yue et al, 2004*):

$$\mathbf{F}_{\text{mixing}} = \sigma \nabla \kappa = G \nabla \phi \quad (4.41)$$

$$\lambda = 3\sigma\varepsilon/2\sqrt{2} \quad (4.42)$$

During phase initialisation the convection terms of equation (4.36) are dropped and the phase field variable is solved for (*COMSOL AB, 2013*). The value of the phase field variable varies between  $-1$  and  $1$  for the different phases and is consistent with the volume fractions of the immiscible components belonging to the mixing energy (*COMSOL AB, 2013*). After phase initialisation the transient simulation employs the general description of the stress tensor at the interface to solve for the transport of momentum for the individual phenomena (*COMSOL AB, 2013; Drew & Passman, 1999*):

$$\mathbf{T} \cdot \mathbf{n} = \boldsymbol{\sigma} = \left[ -P\mathbf{I} + \mu \left( \nabla \mathbf{u} + (\nabla \mathbf{u})^T \right) \right] \cdot \mathbf{n} \quad (4.43)$$

The interface is convected (coupled) where the phase field variable is zero and the action of the interface is added to the Navier-Stokes equation through the volume force due to mixing and gravity (*COMSOL AB, 2013*):

$$\rho \partial \mathbf{u} / \partial t = \nabla \cdot \mathbf{T} - \rho \mathbf{u} \cdot \nabla \mathbf{u} + \mathbf{F}_{\text{mixing}} + \mathbf{F}_{\text{gravity}} = \mu \nabla \cdot \nabla \mathbf{u} - \rho \mathbf{u} \cdot \nabla \mathbf{u} - \nabla P + G \nabla \phi + \mathbf{F}_{\text{gravity}} \quad (4.44)$$

In summary the phase field method is completely Eulerian in formulation and enables the finite resolution of the interface by fitting the chemical potential to a known surface tension.

The method is therefore precise while sympathetic towards attainable mesh and finite resolution of interface. Although microscopic dynamics around the interface may not be resolved the transfer of momentum at the interface is accurate because the chemical potential is macroscopic.

#### 4.8.2 Simulation of a void rising through water

The Graphical User Interface (GUI) belonging to COMSOL MULTIPHYSICS<sup>®</sup> gives quick definition of the geometry, mesh, domains and boundaries. Symmetry is used to reduce the geometry and the simulation is for 2-dimensional axisymmetric flow. The individual domains are shown in figure 4.7. Domain B is a rectangle of width 25 mm and height 100 mm. Domain C is a rectangle of width 47 mm and height 100 mm. Both domains B and C form a rectangle of width 72 mm and height 100 mm positioned with lower left corner at the origin of the axial symmetry axis. The width of both domains B and C coincides with the internal diameter of the cylinder concept (Chapter 1 Section 1.2). The difference function of the in-built Boolean operations is used to construct the individual domains of water and air void. This function operates between the rectangle of domain B and the initial shape of the void within the rectangle given by domain A. The initial shape of the void is spherical and of diameter 20 mm. The volume of the void is within the observations of the flow visualisation experiments discussed in Section 4.7 for turbulent heterogeneous flow. Within the domains the mesh is constructed of elements of near uniform size and is displayed in figure 4.8. The free mesh parameters enable a maximum element size and growth rate of element size away from a curvature cut-off. The curvature cut-off sets the resolution around the interface of the air void between domains A and B.

For the simulation of the air void rising through water no sub-grid turbulence model is used and the flow is incompressible. The direct solution of the time-dependent Navier-Stokes

equation over small durations can resolve turbulent (inertial) behaviour of flow using a fine mesh to account for viscous dissipation (Subheadings 4.8.3 and 4.11.2). The mesh accompanying the discretisation of the transport equations is chosen to resolve the viscous dissipation in both the air void and surrounding water. However, for the air void its geometry and velocity restricts the air to laminar flow. For the water only the largest eddies are responsible for the inertial transport of momentum and the bubble Reynolds number quantifies the level of turbulence (*Fan & Tsuchiya, 1990, p. 112, p. 338*):

$$Re_e = d_e U_b / \nu \quad (4.45)$$

The magnitude of the bubble Reynolds number belonging to the air void at 80 ms into the simulation is ~9334 and indicates that the wake of the air void is turbulent (*Fan & Tsuchiya, 1990, p. 112, p. 338*); the bubble rise velocity relative to the liquid is taken to be 0.4 m/s (Figure 4.11). The discontinuity at the trailing edge of the free-surface of the air void separates the flow regimes of the void and water for a column initially at rest (*Fan & Tsuchiya, 1990, p. 6-13, p. 71-110*). The order of magnitude of eddies considered are the internal diameter of the column  $\sim 10^{-1}$  m down to  $10^{-3}$  m. Therefore, within domain C a fine mesh of maximum element size 1 mm is used. The mesh must also account for the resolution of the finite interface thickness of the phase field method. The phase field interface thickness is 0.5 mm and is also the maximum element size within both domains A and B.

The boundary conditions of the simulation are displayed in figure 4.7 and include axial symmetry (left boundary of domains B and A), continuity between domains B and C, no-slip at the wall (right boundary of domain C), and open boundaries at the top and bottom of domains B and C. The interface between the air void and water of both domains A and B is

selected with the initial interface boundary condition along with the initial condition of fluids within the separate domains.

The transient simulation has a time vector of steps 1 ms and final time 100 ms. The backward differentiation formula (BDF) solver is used throughout the simulation. The absolute tolerance of the BDF solver is set to 0.0005 m for all time steps and is the reported accuracy for all calculated variables in the SI unit system. This absolute tolerance is consistent with the maximum element size of 1 mm used in the simulation. The solver rejects a time step if the absolute tolerance is smaller than the calculated precision. The precision will be of the same order or less than the mesh element size. Anisotropic diffusion is added to the diffusion term of velocity providing numerical stabilisation in the streamline direction (*COMSOL AB, 2008; COMSOL AB, 2013*). A streamline diffusion tuning parameter of 0.17 is used throughout the simulation. This introduces artificial error that can become significant for transient simulations (*COMSOL AB, 2008*). With a small simulation time of 100 ms and a non-acute velocity over the domains the scaling of error is small. Some oscillations in velocity are observed in the simulations however these are very localised compared with the size of the domains. A mobility tuning parameter of 100 m s/kg gives a good continuous monotonic phase field function over the duration of the simulation. Mass conservation of the air void throughout the simulation is achieved and is displayed in figure 4.9. The transport properties of the fluids used in the simulation are given in table 4.2 (*Gebhart et al., 1988; Rogers & Mayhew, 1980; Bureau International des Poids et Mesures, 2006*).

**Table 4.2** Transport properties of fluids used in the simulation (*Gebhart et al., 1988; Rogers & Mayhew, 1980; Bureau International des Poids et Mesures, 2006*).

Parameter	Value	Phase	State of fluid
$\rho_1$	996.56 kg/m <sup>3</sup>	Water	1 atmosphere pressure and 26.85 °C
$\rho_2$	1.177 kg/m <sup>3</sup>	Air	1 atmosphere pressure and 26.85 °C
$\mu_1$	0.8541×10 <sup>-3</sup> Pa s	Water	1 atmosphere pressure and 26.85 °C
$\mu_2$	18.46×10 <sup>-6</sup> Pa s	Air	1 atmosphere pressure and 26.85 °C
$\sigma$	71.99×10 <sup>-3</sup> N/m	-	1 atmosphere pressure and 25°C
$g_z$	9.80665 m/s <sup>2</sup>	-	-

#### 4.8.3 Results of simulation

The simulation time is small and does not show extensive distribution of vorticity within the water. However, within this small duration the convective terms are dominant in the transport of vorticity and the generation of vorticity and subsequent shedding at the free-surface of the air-water interface is seen. The instantaneous vorticity is displayed in figure 4.10. Simultaneously, the transport of momentum associated with the vorticity is seen in the instantaneous velocity. The instantaneous axial velocity is displayed in figure 4.11 and the instantaneous radial velocity in figure 4.12.

*Fan & Tsuchiya (1990)* give an authoritative account of the wake dynamics belonging to gas voids in liquids and liquid-solid suspensions. The level of turbulence structure of the wake is dependent upon void shape and the motion of the void (*Fan & Tsuchiya, 1990*); this is both the generation and transport of vorticity. The translation of viscous fluid elements along the curved free-surface leads to rotation and is consistent with the kinematic relation of equation (4.26) given by *Lu (1977, p. 335)*. The generation of vorticity at the free-surface of the gas-liquid interface is directly proportional to its curvature (*Fan & Tsuchiya, 1990, p. 11*).

The evolution of the shape of the air void seen in the simulation agrees well with that reported by *Fan & Tsuchiya (1990, p. 21)* for a 2-dimensional void. As the void rises it develops into a kidney shape from its initial circle followed by flattening of the front free-surface with radial elongation (Figures 4.10-4.13). The dynamic pressure is displayed in figure 4.13. The change in dynamic pressure around the void as it accelerates from its initial shape parallels the change in void shape. As seen in the simulation and reported by *Fan & Tsuchiya (1990, p. 21, p. 219-264)* there is a frontal compressive force and a dilating lateral force across the void (Figure 4.13). As the void flattens and elongates there is an increase in local curvature at the trailing edge of the free-surface from which vorticity generation is at a maximum (Figure 4.10). The sharpening of the trailing edge of the free-surface as reported by *Fan & Tsuchiya (1990, p. 21-22)* is not resolved by the simulation. A finer mesh and a smaller phase field interface thickness should help.

The separation of vorticity from the free-surface of the gas-liquid interface then develops the structure of turbulence within the viscous fluid *Fan & Tsuchiya (1990)*. As discussed in Section 4.4 the non-linear terms of equation (4.20) in the transport of vorticity are responsible for the level of this structure of turbulence, and is controlled by the dimensionality or symmetry of the flow. For rectilinear motion of the gas void (or axisymmetric motion) the shedding of vorticity results from a discontinuity in the liquid velocity at the trailing edge of the gas-liquid free-surface, and is consistent with the convection of vorticity as the principal mode of transport of vorticity (*Fan & Tsuchiya, 1990, p. 111-142*). The negative dynamic pressure at the side of the gas void establishes reversed flow or recirculation behind the void, and gives the discontinuity in liquid velocity at the trailing edge of the gas-liquid free-surface (*Fan & Tsuchiya, 1990, p. 3-24 & p. 111-142*) (Figure 4.13). This is symmetric/parallel

shedding of vorticity from both trailing edges of the gas void (*Fan & Tsuchiya, 1990, p. 111-142*) and is seen in the simulation (Figure 4.10).

The shape of the gas void as it rises is the most pertinent property of the flow. The flattening and elongation of the air void as it accelerates is observed within the flow visualisation experiments, and is reproduced from the simulation which also gives the evaluation of instantaneous quantities that control the flow. Therefore, an insight into the phenomena that create multiphase turbulence can be obtained and aids flow characterisation. This is significant in flow measurement of instantaneous velocity and vorticity, and is discussed further for the PEPT technique in section 4.11. The limitations of the simulation are:

1. The axisymmetric flow of the simulation cannot account for swirl flow and asymmetric shedding of vorticity, and therefore the higher level of non-linearity (turbulence) of interaction of vorticity with velocity gradients is not seen. This is important for the rise of air voids off the symmetry axis of the column (*Fan & Tsuchiya, 1990, p. 111-142*).
2. The effects of the interaction of neighbouring air voids on the flow are not seen (Section 4.7).
3. The effects of the interaction of swarf with air voids and flow are not seen (Section 4.7).

#### 4.9 PEPT experiments

The materials and conditions of the individual PEPT experiments are summarised in table 4.3. Each experiment uses 11.25 litres of water and fills the column (Subheading 4.2.1) (Figure 4.1) to a height of ~700 mm. 1 kg of dissolved sodium chloride is used as an electrolyte. The volume of water is the same as the total volume of prefill and acids within the cylinder



concept (Chapter 1 Section 1.3). The dimensions of loose swarf are within 10-20 mm and of mass 0.01-0.05 g and density  $\sim 6.52 \text{ g/cm}^3$ . A collection of 500 g of loose swarf within the column has a static bed density of  $\sim 0.3 \text{ g/cm}^3$ . The height of the static bed is  $\sim 100 \text{ mm}$ . Photographs of the air-water-swarf column and swarf bed are displayed in figures 4.14 and 4.15.

**Table 4.3** Summary of PEPT experiments.

Experiment	Superficial air velocity	Global gas hold-up	Addition of sodium chloride and solution density	Amount of swarf	Tracer diameter	Sampling frequency	Duration
	(cm/s)	(%)	(kg)/(kg/m <sup>3</sup> )	(g)	( $\mu\text{m}$ )	(Hz)	(minutes)
1	4.1	-	-/996.56	-	$\sim 500$	>50	120
2	4.1	-	1/1085.4	-	$\sim 500$	>50	120
3	7.2	-	-/996.56	-	$\sim 500$	>50	120
4	7.2	16	-/996.56	500	$\sim 500$	>50	120
5	7.2	16	-/996.56	500	Direct activation	>20	60
6	4.1	16	1/1085.4	500	$\sim 500$	>50	200
7	4.1	16	1/1085.4	500	Direct activation	>20	60

A photograph of the arrangement of the air-water-swarf column and PEPT camera heads is shown in figure 4.16. The column is positioned centrally between the two camera heads and the separation coordinate is within 10 mm of the diameter of the base of the column. This increases the precision of triangulation for a given particle tracer activity (Chapter 3 Section 3.4). The perforated plate protrudes 50 mm into the field of view of the PEPT camera heads and the flow is monitored over a height of 400 mm. This gives measurement of bubble-swarf

phenomena close to and away from the perforated plate. Particle tracers of diameter 500 microns are used to follow the motion of the water and these employ the  $^{18}\text{F}$  radionuclide as a positron emitter (Chapter 3 Subheading 3.4.3). For the inertial flow shown in the flow visualisation experiments the inertia of the particle tracer will be far less than the inertia of the turbulent eddies (Section 4.6 and 4.7). The particle tracers are prepared from indirect activation of polymer ion-exchange beads and are finished with a thin layer of epoxy resin (Chapter 3 Subheading 3.4.3). Before coating each bead it is checked for radioactivity to ensure a tracer of sufficient lifetime for a PEPT experiment ( $^{18}\text{F}$  half-life 110 minutes). A directly activated piece of swarf (zirconium) is used as a tracer to obtain representative swarf occupancy. The occupancy is a measure of the fraction of incidences within grid segments throughout a 1 hour duration. This gives a good indication of mixing of swarf achieved by the heterogeneous air-water-swarf flow. The  $^{90}\text{Nb}$  radionuclide is produced by activating the piece of swarf with a proton beam generated by the University of Birmingham MC40 cyclotron (Chapter 3 Subheading 3.4.3). The half-life of  $^{90}\text{Nb}$  is 14.6 hours and hence is not an activity/time concern like  $^{18}\text{F}$ .

#### 4.10 Eulerian-Lagrangian analysis of PEPT data

The TRACK algorithm (*Parker et al., 1993*) is used to process the raw data files from the PEPT experiments and is discussed in Chapter 3 Section 3.4. An ASCII text file is produced which gives the location of the PEPT particle tracer in Cartesian coordinates, time, and the probable error of the particle tracer location. For the triangulation of the particle tracer a value of 250 is used for the size of set of coincidences  $N$ , and a value of 30% for the fraction of coincidences discarded  $f_{opt}$  (Chapter 3 Section 3.4). These values agree with the optimum values of the TRACK algorithm reported by *Chiti et al. (2011)* for the calculation of particle tracer trajectories belonging to turbulent flow (Section 4.6). To exploit symmetry a

transformation from Cartesian to cylindrical coordinates is made. The air-water-swarf column (Subheading 4.2.1) (Figure 4.1) has full axial symmetry and any scalar or vector field can be fully described in the  $rz$  plane:

$$\partial/\partial\theta = 0, \quad r = 0 \quad (4.46)$$

This maximises the amount of data available for analysis increasing the confidence in a calculated field. The vectors of interest become  $\mathbf{s}(r, \theta, z)$  and  $\mathbf{u}(r, \theta, z)$ . Ensemble-averaging is achieved within grid segments of  $\Delta r = 1.44 \text{ cm} \times \Delta z = 2 \text{ cm}$  and an averaged vector or scalar is displayed central for all incidences. The grid begins at a height of 20 mm above the perforated plate and ends at a height of 400 mm. The calculation of occupancy of swarf is achieved using the same grid (Section 4.9).

As discussed in Section 4.5 and 4.6 a Eulerian reconstruction from Lagrangian trajectories of turbulent stress within a viscous fluid of multiphase flow and, therefore, volume force arising from the combined action of interfaces and gravity can be calculated using equation (4.31). This is possible if the Lagrangian trajectories follow the flow of the viscous fluid because then the volume averaged density of the viscous fluid is reconstructed from the density of the viscous fluid i.e. both the stationary dynamics and volume averaging of equation (4.31) converges with time. For a PEPT particle tracer faithfully following the motion of a viscous fluid within turbulent multiphase flow the maximum resolution of length scales is then its diameter.

The radial and axial velocity is calculated along the PEPT particle tracer trajectories using an asymmetric central difference formula. The distortion is in the time step and allows for non-uniform time stepping; a condition of PEPT. From Taylor's theorem taking the different time

steps in the forward and backward schemes leads to asymmetry in the central difference around incidence  $i$  of the particle tracer trajectory:

$$d\mathbf{s} = \mathbf{e}_r dr + r\mathbf{e}_\theta d\theta + \mathbf{e}_z dz \quad (4.47)$$

$$\mathbf{s}_{i+1} - \varepsilon_i \mathbf{s}_{i-1} = (1 - \varepsilon_i) \mathbf{s}_i + 2\Delta t_2 \left. \frac{\partial \mathbf{s}}{\partial t} \right|_i + \dots \quad \varepsilon_i = \frac{\Delta t_2}{\Delta t_1} \quad (4.48)$$

$$\therefore \mathbf{u} = \left. \frac{\partial \mathbf{s}}{\partial t} \right|_i \approx \left[ \mathbf{s}_{i+1} - \varepsilon_i \mathbf{s}_{i-1} - (1 - \varepsilon_i) \mathbf{s}_i \right] / 2\Delta t_2 + O(\delta t) \quad (4.49)$$

The leading terms of the truncation associated with the asymmetric formula of equation (4.49) are:

$$\underbrace{\frac{(\Delta t_2)}{2!} \left. \frac{\partial^2 \mathbf{s}}{\partial t^2} \right|_i}_{\text{diagonal}} - \underbrace{\frac{(\Delta t_1)}{2!} \left. \frac{\partial^2 \mathbf{s}}{\partial t^2} \right|_i}_{\text{off-diagonal}} + \dots \quad (4.50)$$

One term of equation (4.50) is diagonal and the other off-diagonal and represents both the linear and rotational accelerative perturbation to the velocity; the velocity is calculated from the displacement vector which has radial, azimuthal and axial components. The Taylor series expansions are given in Appendix 1. Because of the contribution by the off-diagonal term the accelerative error is reduced. Therefore, apart from accounting for distorted time-stepping the asymmetric formula of equation (4.49) effectively accounts for the majority of acceleration either side of incidence  $i$ . Considering the inertial behaviour of heterogeneous flow this is especially advantageous (Section 4.7). The accuracy of the asymmetric formula of equation (4.49) is first-order in its time step and the truncation error is reduced through second-order effects as described by equation (4.50). The calculated instantaneous velocity (quantity) for incidence  $i$  is assigned to the grid segment to which the coordinates of incidence  $i$  fall in.

The vorticity is also calculated using an asymmetric central difference formula. The asymmetry of the trajectory provides convective acceleration along the spatial coordinates to satisfy continuity. The axial derivative is given by:

$$u_{r_{i+1}} - \varepsilon_z u_{r_{i-1}} = (1 - \varepsilon_z) u_{r_i} + 2\Delta z_2 \left. \frac{\partial u_r}{\partial z} \right|_i + \dots, \quad \varepsilon_z = \frac{\Delta z_2}{\Delta z_1} \quad (4.51)$$

This differencing is analogous to, and satisfies, the Euler relation of Lagrangian motion (*Batchelor, 1994, p.72*):

$$\Delta u_r(z, z', t) = \int_1^2 \left( \frac{\partial u_r}{\partial t} + u_z \frac{\partial u_r}{\partial z} \right) dt + O(\delta t^2) = \Delta u_r(z, t) + \Delta z \frac{\partial u_r}{\partial z} \quad (4.52)$$

The approximation of the axial derivative and therefore vorticity follows the flow because it is calculated sequentially along the trajectory of the particle tracer. Hence, the instantaneous quantities calculated through asymmetric differencing are very accurate because they account for inherent deformation of the flow over time and space and conform to the kinematic relation of equation (4.26) for the relative motion of a free-surface or interface within a viscous fluid. A sampling frequency of ~50 Hz along the trajectory of the particle tracer has been used for calculating the instantaneous and fluctuating velocities, and instantaneous vorticity. This rate is superfluous for resolving the large scale inertial structures belonging to PEPT experiments 1, 2, 3, 4 and 6 of table 4.3. The periodicity of the large voids as seen in the flow visualisation experiments for a superficial gas velocity of 6.1 cm/s are ~5 Hz (Section 4.7).

The confidence or measurement error belonging to the components of velocity and components of the Reynolds stress tensor are related to the probable error of the PEPT particle tracer location. This is the zeroth-order contribution of error in the calculation of the

components of velocity and components of the Reynolds stress tensor, and is the most significant. The error in the particle tracer location is reported by the TRACK algorithm (Sections 4.6). The chain rule can be used to evaluate the change in a tensor component as a result of a change in the instantaneous velocity components, and alongside general rules for error propagation the error in the tensor components can be evaluated. The probable error of the PEPT particle tracer location and propagation of measurement error for the instantaneous and mean components of velocity and Reynolds stress is given in Appendix 2. The measurement error is assessed continuously along the trajectory of the particle tracer and can be plotted with the incidences of turbulence spectra within individual grid segments (Subheading 4.11.2). The probable error of the PEPT particle tracer location reports a confidence of 68%. The absolute error is reported in all plots.

## 4.11 Results of Eulerian-Lagrangian analysis of PEPT experiments

### 4.11.1 Lagrangian trajectories of the PEPT particle tracer

A MATLAB<sup>®</sup> algorithm `instantaneous_velocity.m` is used to read the ASCII text file produced by the TRACK algorithm for the calculation of instantaneous velocities and associated errors. The algorithm `instantaneous_velocity.m` is given in Appendix 3. The TRACK algorithm is discussed in Chapter 3 Section 3.4 and Sections 4.6 and 4.10. The instantaneous velocities are assigned to the PEPT particle tracer trajectory with time and are calculated using equation (4.49) (Section 4.10). The vectorised *find* function within MATLAB<sup>®</sup> is used to select the sampling frequency along the PEPT particle tracer trajectory contained within the ASCII text file produced by the TRACK algorithm (Section 4.10).

The global instantaneous axial velocity of the PEPT particle tracers averages to zero over the duration of the PEPT experiments of table 4.3, and indicates that the particle tracers predominantly occupy and follow the flow of the water in the presence of occupancies of air

and swarf. This is consistent with the continuity condition of the mass of water during the duration of the PEPT experiments; the water remains within the column and therefore no resultant axial velocity of the water should be observed. Because the PEPT particle tracer faithfully follows the flow of the water the evaluation of the dynamics of a turbulent multiphase flow in Sections 4.5 and 4.10 can be applied, and avoids the requirement of explicit volume fractions (Section 4.5). This evaluation of the dynamics of a turbulent multiphase flow employs the Lagrangian-Eulerian capability of the PEPT technique (Section 4.6). Therefore, PEPT can be used to assess the stationary dynamics of mixing of swarf within multiphase turbulent air-water-swarf flow (Subheadings 4.11.3 and 4.11.4).

#### 4.11.2 Instantaneous velocity, vorticity and Reynolds stress spectra

In figures 4.17-4.21 instantaneous spectra for velocity and Reynolds shear stress are shown with their errors. The instantaneous velocities are calculated using equation (4.49) (Section 4.10). The instantaneous fluctuating velocities are calculated from the instantaneous and mean velocities using equation (4.18) (Section 4.4). The calculation of the mean velocities and mean components of the Reynolds stress tensor is discussed in Subheading 4.11.3. In figures 4.17-4.21 the magnitudes of instantaneous velocity and instantaneous Reynolds shear stress are much greater than the magnitudes of their errors, and therefore the precision and accuracy of the PEPT technique is excellent. The errors have been propagated from the probable error of the particle tracer location which reports 1 standard deviation (68% confidence) (Section 4.10). The propagation of error for the instantaneous quantities is evaluated in Appendix 2 and is calculated by the MATLAB<sup>®</sup> algorithm `instantaneous_velocity.m`.

The global instantaneous axial and radial velocities within the water for PEPT experiments 1 and 2 of table 4.3 are shown in figures 4.22-4.25. The difference in the measured magnitudes of the axial and radial velocities is similar with the difference in magnitudes given by the

CFD simulation of an air void rising through water (Figures 4.11 and 4.12) (Section 4.8). The size of the air void in the simulation is comparable in size to the air voids observed for the turbulent multiphase flow in each PEPT experiment and is discussed in Sections 4.7 and 4.8. The global instantaneous vorticity within the water for PEPT experiments 1, 2, 3, 4, and 6 of table 4.3 is shown in figures 4.26-4.30. The magnitudes of the instantaneous vorticity are consistent with the magnitudes seen in the CFD simulation (Figure 4.10) (Section 4.8). The CFD simulation provides an insight into the generation and shedding of vorticity from the free-surface of an air void and is discussed in Section 4.8. The presence of swarf is seen to reduce the global instantaneous vorticity of PEPT experiments 4 and 6 of table 4.3 compared with experiments 2 and 3 (Figure 4.27 cf. Figure 4.30; Figure 4.28 cf. Figure 4.29). Additional collisions with swarf are likely to prevent the evolution of the air void shape important in increasing local curvature of the free-surface of the void and therefore generation and magnitude of vorticity. Local curvature of the free-surface of the air void becomes more acute throughout the evolution of the void shape and is discussed in Section 4.8 along with the CFD simulation.

The similarity of the magnitudes of the instantaneous velocity and vorticity within the water between the PEPT measurements and the CFD simulation of an air void rising through water, credit that the turbulent multiphase flow of PEPT experiments 1, 2, 3, 4 and 6 of table 4.3 is characterised principally by the motion of large voids along the height of the column. Vorticity of negative sign within the water can be attributed to the rise of air voids off the symmetry axis of the column but also because the interface of a void is fluxional at coalescence and breakage as observed in the flow visualisation experiments discussed in Section 4.7. If the axial symmetry of the instantaneous flow is destroyed both positive and negative signs of vorticity are possible within the water. For coalescence and breakage of air



voids, stretching of the velocity of the water along the free-surface of the void through curvature of the interface, generates vorticity of both positive and negative sign.

#### 4.11.3 Ensemble averaging and convergence of mean tensor components

The MATLAB<sup>®</sup> algorithm `ensemble_averaging.m` calls the inbuilt vectorised *any* function to assign incidences and instantaneous velocities to grid segments. The algorithm `ensemble_averaging.m` is given in Appendix 3. The algorithm follows the trajectory of the PEPT particle tracer and eliminates any incidences outside a specific grid segment. A recurrence relation containing the MATLAB<sup>®</sup> *any* function is used to select the grid segments. The same recurrence relation is also used to average the instantaneous velocities in the calculation of mean velocities, instantaneous fluctuating velocities and mean tensor components within grid segments. Convergence of the mean velocities and mean tensor components is evaluated using an array in time containing the averaging for all grid segments. A recurrence relation evaluates the convergence of the array at given time intervals.

The ensemble averaging of the Reynolds shear stress and mean axial velocity within a grid segment is shown in figure 4.31. Equation (4.24) is used for ensemble averaging of instantaneous velocities and is consistent with equation (4.23) as the relation between Lagrangian and Eulerian descriptions of motion of a viscous fluid (Section 4.4). The dimensions of the grid used for ensemble averaging is discussed in Section 4.10. For the mean axial velocity the instantaneous axial velocities are averaged within a grid segment. For the mean Reynolds shear stress the product of the respective instantaneous fluctuating velocities within a grid segment are averaged. Magnitudes and errors for the mean axial and radial velocities, and mean axial and radial components of the Reynolds stress tensor, are given in tables 4.4-4.8 for PEPT experiments 1, 2, 3, 4 and 6 of table 4.3. The magnitudes of the errors are an order or several orders of magnitude lower than the magnitude of the mean quantities.

The errors have been propagated from the probable error of the particle tracer location which reports 1 standard deviation (68% confidence) (Section 4.10). The propagation of error for the mean quantities is evaluated in Appendix 2 and is calculated by both MATLAB<sup>®</sup> algorithms `instantaneous_velocity.m` and `ensemble_averaging.m`.

All grid segments for PEPT experiments 1, 2, 3, 4 and 6 of table 4.3 share the same behaviour as displayed in figure 4.31 for all mean radial and axial components of velocity and Reynolds stress tensor. Convergence of the mean to a limit with increasing time is seen and therefore the dynamics of the turbulent multiphase flow resides in a stationary state. Note this is the Eulerian-Lagrangian convergence time of the ensemble-averaging and is not the convergence time of the flow to a stationary state; convergence of the flow to a stationary state is of order seconds. The Eulerian-Lagrangian convergence proves that the turbulent multiphase flow resides in a stationary state because the mean quantities become a constant of time, and that the vectorised RANS equation describes the deterministic stationary dynamics. The mean shear and normal azimuthal Reynolds stress tensor components have no correlation and their convergence approaches zero. Figure 4.32 shows the convergence of an azimuthal tensor component.

The mean Reynolds shear stress of PEPT experiments 1 and 3 of table 4.3 are compared with the values measured by *Menzel et al. (1990)*. Their investigation by Hot Film Anemometry (HFA) measured stress at a height away from the effects of the air distributor. The diameter of the column used by *Menzel et al. (1990)* was 150 mm and slightly larger than the column diameter used in the present investigation. Taking the ensemble averaged values from the top of the grid gives a 1-dimensional description that can be directly compared. This comparison is shown in figure 4.33. The values of the Reynolds shear stress for the superficial air velocity 7.2 cm/s agree very well, however, the values for the superficial air velocities 4.1 and 4.8

cm/s are similar in magnitude but have different curves. A likely explanation is that the effects of the different gas distributors may be more noticeable at lower superficial gas velocities where inertial effects are less. For sub-inertial multiphase flow the effects of the air distributor will be retained along the height of the column.

#### 4.11.4 Volume force and swarf occupancy belonging to the stationary dynamics of mixing of swarf

The MATLAB<sup>®</sup> algorithm `occupancy.m` is used to calculate the swarf occupancies and reads the ASCII text file produced by the TRACK algorithm for the trajectory of a directly activated piece of swarf. Swarf occupancy belonging to the turbulent multiphase flow of PEPT experiments 5 and 7 of table 4.3 is displayed in figures 4.34 and 4.35. The occupancies display the weighted incidences of a directly activated piece of swarf within each grid segment and have been interpolated from the values central to the grid segments. This allows for a more realistic swarf distribution. The MATLAB<sup>®</sup> `interp2` function is used to perform the interpolation. The trajectory of the directly activated piece of swarf is provided by the TRACK algorithm. The grid used to construct the occupancy of swarf is discussed in Section 4.10.

The evaluation of mixing of swarf caused by turbulent stresses within the water of air-water-swarf flow is discussed in Section 4.5. From this evaluation and because the PEPT particle tracer faithfully follows the flow of the water in the presence of occupancies of air and swarf (Subheading 4.11.1), no explicit volume fractions are required for the reconstruction of the Eulerian description of dynamics from the Lagrangian trajectories of the PEPT particle tracer (Section 4.5). With the avoidance of explicit volume fractions the volume force responsible for mixing of swarf is resolved from the ensemble averaged mean field tensor components belonging to the water of air-water-swarf flow and described by equation (4.31) (Section 4.5).

The spatial derivatives of the mean tensor components of equation (4.31) belonging to the grid of the ensemble averaging are calculated using the MATLAB<sup>®</sup> *gradient* function. The ensemble averaging of the mean tensor components is discussed in Sections 4.4, 4.5 and 4.10, and the dimensions of the grid used to resolve the volume force is discussed in Section 4.10. The volume force represents the stationary dynamics of mixing within the air-water-swarf flow, and the confidence in its measurement using the PEPT technique is supported by the convergence and accuracy of the mean tensor components discussed in Subheading 4.11.3.

Figure 4.36 and 4.37 display the volume force for PEPT experiments 4 and 6 of table 4.3 alongside the corresponding swarf occupancies of PEPT experiments 5 and 7. The volume force resolved from the mean field tensor components of equation (4.31) in the  $rz$  plane is projected around the column at  $45^\circ$  intervals. This gives a greater perspective of the forces and it is easier to see how they vary within the column. The forces are displayed central within the projected grid segments and no interpolation is used in the calculation or display of the forces. In both figures 4.36 and 4.37 it is clear that the vertical dispersion of loose swarf towards the wall of the column coincides with the field of the calculated volume force. Further, the magnitude of the resolved volume force also complements the volumetric weight of the static swarf bed ( $\sim 0.3 \text{ g/cm}^3$  or  $\sim 3 \text{ mN/cm}^3$ ) (Section 4.9). For figure 4.36 the magnitude of the volume force of PEPT experiment 4 of table 4.3 is less in the region above the perforated plate compared with PEPT experiment 6. The coalescence inhibiting behaviour of dissolved sodium chloride for PEPT experiment 4 will reduce air void size and therefore buoyancy of the air-water interface (Section 4.7).

With convergence and accuracy of the mean tensor components discussed in Subheading 4.11.3, observed occupancy of swarf, and magnitude of volume forces it is clear that the stationary dynamics of mixing of swarf has been measured. This is a satisfying result and

shows that via the buoyancy term of equation (4.31) the stress at the air-water interface is dominant and controls the flow. The inertial aspects of the turbulent multiphase flow can be resolved from the flow deformation of Lagrangian trajectories measured using PEPT and described by asymmetric differencing.

#### 4.12 Conclusion

PEPT can measure and validate large scale turbulence for engineering of flow belonging to processes (Section 4.11). The technique is Lagrangian; it follows the flow and for this reason it can account for both linear and rotational deformation of flow to high accuracy (Sections 4.4, 4.10, 4.11). The high order moments of the turbulence closure are inherent within its measurements. To account for flow deformation asymmetric differencing along the trajectory of the particle tracer is used in the calculation of instantaneous velocity and vorticity (Section 4.10).

The multiphase flow of the air-water-swarf column is characterised by large air voids that rise on average along the centre of the column. The spatial and temporal scales of the air voids create non-linear generation and cascades of vorticity from the free-surface of their interface and therefore turbulent flow (Sections 4.7, 4.8 and 4.11). The dynamics of the turbulence within the water is fully described by the vectorised RANS equation (Section 4.11). Confidence in the capability of PEPT for the measurement of large scale turbulence is given in the convergence of the ensemble averaging of the stationary dynamics under the RANS framework (Subheading 4.11.3). Through flow measurement by PEPT and Eulerian-Lagrangian analysis this equation enables the resolution of the volume force acting across the air-water and swarf-water interfaces (Section 4.5) (Subheading 4.11.4). CFD corroborates with the PEPT results and reaffirms the characterisation of the multiphase flow through the evaluation of instantaneous vorticity and velocity (Section 4.8).

The measured volume force corresponds with the occupancy of swarf which indicates that the height of the column is utilised well and provides a good surface area for heat transfer (Subheading 4.11.4). To improve the occupancy of swarf, fully 3-dimensional swirl flow should be investigated. The azimuthal components of the Reynolds stress tensor would then contribute towards the resolved axial force (Section 4.5). Asymmetry in the azimuth of the perforated plate array will provide impetus for the contribution of the azimuthal tensor components:

$$\frac{\partial}{\partial \theta} \neq 0 \Rightarrow \mathbf{e}_z \rho \frac{\partial}{\partial \theta} (\overline{\omega'_\theta u'_z}) \neq 0 \text{ etc.} \quad (4.53)$$

The asymmetry required in the azimuth of the perforated plate would need to be investigated to ensure a positive axial force from the azimuthal components of the Reynolds stress tensor.

Because of the symmetry of the column and therefore flow, not all of the instantaneous quantities contribute towards the stationary dynamics of mixing of swarf (mass, force). Symmetry determines the redundancy of instantaneous measurements because of the averaging framework of the vectorised RANS equation (Subheading 4.11.3). However, the instantaneous measurements are rich in turbulence information. An instantaneous assessment of turbulence is still important because it allows the phenomena that create turbulence to be investigated. Vorticity is the most useful instantaneous quantity and can be related to the motion and evolution of the shape of the air void interface (Sections 4.8 and 4.11).

**Table 4.4** Measured quantities for PEPT experiment 1.

Grid segment	$r$	$z$	$n$	$\bar{u}_z$	$\delta\bar{u}_z$	$\bar{u}_r$	$\delta\bar{u}_r$	$\overline{u'_r u'_z}$	$\delta(\overline{u'_r u'_z})$	$\overline{u'_r u'_r}$	$\delta(\overline{u'_r u'_r})$	$\overline{u'_z u'_z}$	$\delta(\overline{u'_z u'_z})$
	(cm)	(cm)		(m/s)	( $\pm$ m/s)	(m/s)	( $\pm$ m/s)	(m <sup>2</sup> /s <sup>2</sup> )	( $\pm$ m <sup>2</sup> /s <sup>2</sup> )	(m <sup>2</sup> /s <sup>2</sup> )	( $\pm$ m <sup>2</sup> /s <sup>2</sup> )	(m <sup>2</sup> /s <sup>2</sup> )	( $\pm$ m <sup>2</sup> /s <sup>2</sup> )
				$\times 10^{-2}$	$\times 10^{-4}$	$\times 10^{-2}$	$\times 10^{-4}$	$\times 10^{-3}$	$\times 10^{-4}$	$\times 10^{-3}$	$\times 10^{-4}$	$\times 10^{-3}$	$\times 10^{-4}$
(1,1)	0.72	3.00	411	6.56	5.18	-0.91	5.18	8.54	1.64	21.9	1.08	56.4	2.89
(2,1)	2.16	3.00	1416	4.47	2.80	-1.89	2.80	14.2	0.86	23.6	0.64	55.2	1.47
(3,1)	3.60	3.00	2591	-0.83	2.09	-2.37	2.09	14.1	0.59	19.3	0.43	47.1	1.00
(4,1)	5.04	3.00	3954	-5.95	1.64	-2.23	1.64	6.40	0.38	11.1	0.26	35.3	0.66
(5,1)	6.48	3.00	2908	-5.84	1.77	-0.99	1.77	1.62	0.34	3.58	0.16	28.3	0.64
(1,2)	0.72	5.00	518	13.4	4.21	-0.60	4.21	6.14	1.48	23.7	0.93	79.5	2.65
(2,2)	2.16	5.00	1939	9.20	2.13	-0.48	2.13	16.1	0.77	30.1	0.54	80.9	1.35
(3,2)	3.60	5.00	3557	4.06	1.51	-1.06	1.51	15.5	0.51	23.0	0.34	71.9	0.90
(4,2)	5.04	5.00	5214	-4.54	1.19	-1.26	1.19	8.82	0.33	12.5	0.20	54.9	0.60
(5,2)	6.48	5.00	3923	-7.75	1.30	-0.30	1.30	2.08	0.29	3.83	0.12	40.2	0.56
(1,3)	0.72	7.00	795	16.0	3.60	-1.77	3.60	7.05	1.19	22.5	0.78	76.1	2.11
(2,3)	2.16	7.00	2217	9.81	2.15	-0.80	2.15	13.2	0.80	28.5	0.52	91.3	1.42
(3,3)	3.60	7.00	4051	5.97	1.54	-0.15	1.54	17.4	0.56	25.2	0.35	92.3	1.01
(4,3)	5.04	7.00	5991	-4.17	1.19	-1.05	1.19	10.5	0.37	15.4	0.22	71.5	0.68
(5,3)	6.48	7.00	4535	-9.35	1.27	-0.48	1.27	2.51	0.32	4.75	0.13	53.2	0.61
(1,4)	0.72	9.00	816	15.1	3.50	0.95	3.50	5.33	1.17	22.4	0.75	78.8	2.08
(2,4)	2.16	9.00	2449	10.3	2.06	-1.11	2.06	8.08	0.74	26.9	0.48	92.1	1.32
(3,4)	3.60	9.00	4368	5.38	1.54	-0.76	1.54	12.8	0.56	25.7	0.36	96.6	1.01
(4,4)	5.04	9.00	6678	-4.11	1.17	-0.87	1.17	9.08	0.37	15.6	0.21	77.1	0.68
(5,4)	6.48	9.00	5075	-11.5	1.24	-0.54	1.24	2.78	0.33	5.08	0.13	59.3	0.63
(1,5)	0.72	11.0	1020	15.5	3.03	-0.19	3.03	3.12	1.02	24.2	0.67	80.6	1.81
(2,5)	2.16	11.0	2773	11.6	1.83	-0.32	1.83	5.96	0.66	27.5	0.43	88.4	1.17
(3,5)	3.60	11.0	4510	5.35	1.44	-0.89	1.44	8.31	0.51	25.5	0.33	91.7	0.92
(4,5)	5.04	11.0	7147	-3.28	1.12	-0.27	1.12	7.55	0.36	16.8	0.21	79.8	0.67
(5,5)	6.48	11.0	5275	-12.6	1.24	-0.41	1.24	3.23	0.34	5.80	0.14	65.7	0.66

**Table 4.4** Continued.

Grid segment	$r$	$z$	$n$	$\bar{u}_z$	$\delta\bar{u}_z$	$\bar{u}_r$	$\delta\bar{u}_r$	$\overline{u'_r u'_z}$	$\delta(\overline{u'_r u'_z})$	$\overline{u'_z u'_r}$	$\delta(\overline{u'_z u'_r})$	$\overline{u'_z u'_z}$	$\delta(\overline{u'_z u'_z})$
	(cm)	(cm)		(m/s)	( $\pm$ m/s)	(m/s)	( $\pm$ m/s)	(m <sup>2</sup> /s <sup>2</sup> )	( $\pm$ m <sup>2</sup> /s <sup>2</sup> )	(m <sup>2</sup> /s <sup>2</sup> )	( $\pm$ m <sup>2</sup> /s <sup>2</sup> )	(m <sup>2</sup> /s <sup>2</sup> )	( $\pm$ m <sup>2</sup> /s <sup>2</sup> )
				$\times 10^{-2}$	$\times 10^{-4}$	$\times 10^{-2}$	$\times 10^{-4}$	$\times 10^{-3}$	$\times 10^{-4}$	$\times 10^{-3}$	$\times 10^{-4}$	$\times 10^{-3}$	$\times 10^{-4}$
(1,6)	0.72	13.0	1106	17.9	3.00	-0.41	3.00	4.21	1.00	26.6	0.69	78.1	1.76
(2,6)	2.16	13.0	3394	12.5	1.68	-0.98	1.68	4.74	0.60	30.9	0.42	86.2	1.03
(3,6)	3.60	13.0	5271	5.43	1.33	-0.81	1.33	6.01	0.46	25.6	0.30	87.5	0.82
(4,6)	5.04	13.0	7396	-3.66	1.11	-0.43	1.11	5.69	0.36	17.5	0.21	79.3	0.66
(5,6)	6.48	13.0	6000	-13.1	1.18	-0.36	1.18	2.43	0.32	5.89	0.13	61.70	0.60
(1,7)	0.72	15.0	1141	19.7	3.06	0.93	3.06	4.14	1.04	22.8	0.66	83.8	1.85
(2,7)	2.16	15.0	3552	14.8	1.71	-0.12	1.71	4.22	0.59	30.6	0.43	83.6	1.02
(3,7)	3.60	15.0	5621	5.04	1.32	-0.39	1.32	4.99	0.46	27.1	0.31	85.1	0.81
(4,7)	5.04	15.0	8079	-3.87	1.08	0.05	1.08	4.99	0.34	18.3	0.21	73.4	0.60
(5,7)	6.48	15.0	6148	-12.5	1.18	0.34	1.18	2.33	0.32	6.15	0.14	61.7	0.60
(1,8)	0.72	17.0	1154	19.9	3.03	0.97	3.03	-0.95	1.03	25.3	0.68	82.3	1.82
(2,8)	2.16	17.0	3647	16.1	1.70	-0.12	1.70	6.36	0.59	31.9	0.44	83.0	1.01
(3,8)	3.60	17.0	5938	4.61	1.31	-0.41	1.31	8.12	0.45	27.4	0.31	80.5	0.78
(4,8)	5.04	17.0	8116	-5.10	1.09	-0.09	1.09	5.26	0.33	16.7	0.20	71.8	0.60
(5,8)	6.48	17.0	5931	-12.8	1.21	-0.25	1.21	1.74	0.32	5.75	0.13	59.6	0.61
(1,9)	0.72	19.0	1086	23.4	3.08	-0.79	3.08	2.51	1.03	22.9	0.67	82.9	1.82
(2,9)	2.16	19.0	3650	16.9	1.69	0.00	1.69	4.79	0.57	31.1	0.43	76.5	0.97
(3,9)	3.60	19.0	5932	5.69	1.32	-0.55	1.32	8.80	0.44	27.5	0.31	76.1	0.76
(4,9)	5.04	19.0	8371	-4.86	1.06	-0.80	1.06	7.00	0.33	17.7	0.20	71.7	0.59
(5,9)	6.48	19.0	5550	-14.8	1.27	-0.19	1.27	2.39	0.33	6.34	0.14	57.7	0.62
(1,10)	0.72	21.0	1334	23.5	2.75	-0.18	2.75	-0.97	0.88	25.9	0.64	72.3	1.52
(2,10)	2.16	21.0	3711	16.7	1.68	-0.27	1.68	7.00	0.55	29.3	0.41	72.1	0.93
(3,10)	3.60	21.0	5894	6.64	1.32	-0.85	1.32	7.76	0.45	26.5	0.31	81.1	0.78
(4,10)	5.04	21.0	8750	-4.62	1.05	-0.53	1.05	5.50	0.31	17.8	0.20	65.2	0.55
(5,10)	6.48	21.0	6020	-14.5	1.21	-0.12	1.21	2.35	0.30	6.35	0.14	51.3	0.57



**Table 4.4** Continued.

Grid segment	$r$	$z$	$n$	$\bar{u}_z$	$\delta\bar{u}_z$	$\bar{u}_r$	$\delta\bar{u}_r$	$\overline{u'_r u'_z}$	$\delta(\overline{u'_r u'_z})$	$\overline{u'_z u'_r}$	$\delta(\overline{u'_z u'_r})$	$\overline{u'_z u'_z}$	$\delta(\overline{u'_z u'_z})$
	(cm)	(cm)		(m/s)	( $\pm$ m/s)	(m/s)	( $\pm$ m/s)	(m <sup>2</sup> /s <sup>2</sup> )	( $\pm$ m <sup>2</sup> /s <sup>2</sup> )	(m <sup>2</sup> /s <sup>2</sup> )	( $\pm$ m <sup>2</sup> /s <sup>2</sup> )	(m <sup>2</sup> /s <sup>2</sup> )	( $\pm$ m <sup>2</sup> /s <sup>2</sup> )
				$\times 10^{-2}$	$\times 10^{-4}$	$\times 10^{-2}$	$\times 10^{-4}$	$\times 10^{-3}$	$\times 10^{-4}$	$\times 10^{-3}$	$\times 10^{-4}$	$\times 10^{-3}$	$\times 10^{-4}$
(1,11)	0.72	23.0	1374	21.2	2.69	0.55	2.69	0.61	0.85	24.6	0.62	69.2	1.46
(2,11)	2.16	23.0	3905	17.1	1.63	0.95	1.63	5.70	0.53	30.4	0.42	68.6	0.88
(3,11)	3.60	23.0	5868	8.00	1.33	0.28	1.33	8.22	0.44	25.7	0.31	78.2	0.77
(4,11)	5.04	23.0	8198	-5.43	1.09	-0.40	1.09	5.47	0.32	16.2	0.20	64.2	0.56
(5,11)	6.48	23.0	5773	-15.5	1.25	-0.24	1.25	1.90	0.30	5.97	0.14	49.2	0.57
(1,12)	0.72	25.0	1163	24.0	2.92	2.40	2.92	4.50	0.97	27.4	0.70	78.4	1.66
(2,12)	2.16	25.0	3438	17.6	1.75	1.20	1.75	4.12	0.57	29.9	0.43	71.9	0.96
(3,12)	3.60	25.0	5852	9.32	1.34	1.26	1.34	8.74	0.44	25.1	0.30	79.5	0.78
(4,12)	5.04	25.0	8122	-4.74	1.09	0.60	1.09	6.80	0.32	16.4	0.20	66.8	0.58
(5,12)	6.48	25.0	5778	-15.5	1.23	-0.43	1.23	1.87	0.28	5.36	0.13	45.2	0.53
(1,13)	0.72	27.0	1202	21.2	3.00	-0.33	3.00	1.38	0.98	24.8	0.68	77.4	1.70
(2,13)	2.16	27.0	3418	17.4	1.77	0.39	1.77	7.92	0.58	30.4	0.44	70.4	0.97
(3,13)	3.60	27.0	5719	8.29	1.34	0.45	1.34	7.97	0.43	25.9	0.31	71.6	0.74
(4,13)	5.04	27.0	8385	-3.83	1.07	0.27	1.07	6.78	0.31	16.7	0.20	62.5	0.55
(5,13)	6.48	27.0	5638	-15.5	1.23	-0.09	1.23	2.82	0.29	5.80	0.14	46.8	0.54
(1,14)	0.72	29.0	1237	21.1	2.97	0.73	2.97	6.97	0.96	24.8	0.67	70.7	1.66
(2,14)	2.16	29.0	3608	16.0	1.72	-0.23	1.72	8.85	0.55	28.8	0.42	66.6	0.92
(3,14)	3.60	29.0	5326	7.87	1.39	0.06	1.39	7.58	0.45	25.3	0.32	72.4	0.77
(4,14)	5.04	29.0	7688	-4.34	1.10	0.11	1.10	6.23	0.32	16.8	0.20	61.67	0.56
(5,14)	6.48	29.0	5540	-14.2	1.25	0.52	1.25	3.45	0.30	6.32	0.14	46.8	0.56
(1,15)	0.72	31.0	1136	19.8	3.08	-0.72	3.08	5.44	0.92	23.1	0.67	62.5	1.58
(2,15)	2.16	31.0	3216	16.8	1.77	0.54	1.77	6.93	0.58	29.5	0.44	70.4	0.98
(3,15)	3.60	31.0	5308	7.55	1.35	0.27	1.35	7.03	0.43	24.9	0.31	69.8	0.74
(4,15)	5.04	31.0	7218	-4.17	1.12	0.19	1.12	5.29	0.32	15.7	0.20	58.9	0.56
(5,15)	6.48	31.0	5171	-14.7	1.28	0.18	1.28	1.70	0.29	5.88	0.14	43.7	0.54

**Table 4.4** Continued.

Grid segment	$r$	$z$	$n$	$\bar{u}_z$	$\delta\bar{u}_z$	$\bar{u}_r$	$\delta\bar{u}_r$	$\overline{u'_r u'_z}$	$\delta(\overline{u'_r u'_z})$	$\overline{u'_r u'_r}$	$\delta(\overline{u'_r u'_r})$	$\overline{u'_z u'_z}$	$\delta(\overline{u'_z u'_z})$
	(cm)	(cm)		(m/s)	( $\pm$ m/s)	(m/s)	( $\pm$ m/s)	(m <sup>2</sup> /s <sup>2</sup> )	( $\pm$ m <sup>2</sup> /s <sup>2</sup> )	(m <sup>2</sup> /s <sup>2</sup> )	( $\pm$ m <sup>2</sup> /s <sup>2</sup> )	(m <sup>2</sup> /s <sup>2</sup> )	( $\pm$ m <sup>2</sup> /s <sup>2</sup> )
				$\times 10^{-2}$	$\times 10^{-4}$	$\times 10^{-2}$	$\times 10^{-4}$	$\times 10^{-3}$	$\times 10^{-4}$	$\times 10^{-3}$	$\times 10^{-4}$	$\times 10^{-3}$	$\times 10^{-4}$
(1,16)	0.72	33.0	968	23.8	3.16	1.49	3.16	2.56	0.95	20.8	0.65	64.5	1.67
(2,16)	2.16	33.0	2978	16.6	1.78	-0.27	1.78	6.51	0.58	25.2	0.41	71.5	1.00
(3,16)	3.60	33.0	4862	7.85	1.36	-0.20	1.36	7.49	0.42	23.7	0.30	66.1	0.73
(4,16)	5.04	33.0	6795	-4.85	1.12	0.26	1.12	6.44	0.31	14.8	0.20	57.1	0.56
(5,16)	6.48	33.0	4557	-14.5	1.33	0.07	1.33	2.68	0.31	5.34	0.14	44.7	0.58
(1,17)	0.72	35.0	894	23.6	3.15	1.00	3.15	3.73	0.88	21.7	0.66	52.9	1.50
(2,17)	2.16	35.0	2670	17.1	1.86	1.55	1.86	7.85	0.60	28.8	0.45	65.6	1.01
(3,17)	3.60	35.0	4728	8.39	1.38	0.32	1.38	7.40	0.42	22.6	0.30	62.3	0.74
(4,17)	5.04	35.0	6374	-5.14	1.17	0.24	1.17	6.00	0.33	15.2	0.20	56.6	0.58
(5,17)	6.48	35.0	3925	-14.6	1.41	0.05	1.41	3.03	0.34	5.42	0.15	47.8	0.64
(1,18)	0.72	37.0	735	25.5	3.69	1.49	3.69	6.27	1.17	21.7	0.80	68.4	2.04
(2,18)	2.16	37.0	2483	17.4	2.02	0.25	2.02	5.52	0.63	24.6	0.45	64.2	1.08
(3,18)	3.60	37.0	3984	8.44	1.56	1.12	1.56	8.73	0.48	21.3	0.33	66.4	0.85
(4,18)	5.04	37.0	5585	-4.82	1.25	0.44	1.25	6.86	0.35	14.4	0.22	58.0	0.63
(5,18)	6.48	37.0	3638	-13.5	1.44	-0.04	1.44	2.58	0.35	5.88	0.16	49.5	0.66
(1,19)	0.72	39.0	636	25.9	3.87	-0.07	3.87	1.72	1.12	21.5	0.83	54.5	1.91
(2,19)	2.16	39.0	2163	17.2	2.04	-0.20	2.04	7.89	0.67	23.9	0.47	64.5	1.16
(3,19)	3.60	39.0	3326	7.08	1.62	0.28	1.62	9.98	0.50	20.7	0.34	65.2	0.88
(4,19)	5.04	39.0	4508	-4.42	1.31	0.20	1.31	8.05	0.39	14.95	0.23	63.21	0.71
(5,19)	6.48	39.0	2975	-15.1	1.52	0.20	1.52	1.80	0.37	5.70	0.16	48.3	0.70

**Table 4.5** Measured quantities for PEPT experiment 2.

Grid segment	$r$	$z$	$n$	$\bar{u}_z$	$\delta\bar{u}_z$	$\bar{u}_r$	$\delta\bar{u}_r$	$\overline{u'_r u'_z}$	$\delta(\overline{u'_r u'_z})$	$\overline{u'_r u'_r}$	$\delta(\overline{u'_r u'_r})$	$\overline{u'_z u'_z}$	$\delta(\overline{u'_z u'_z})$
	(cm)	(cm)		(m/s)	( $\pm$ m/s)	(m/s)	( $\pm$ m/s)	(m <sup>2</sup> /s <sup>2</sup> )	( $\pm$ m <sup>2</sup> /s <sup>2</sup> )	(m <sup>2</sup> /s <sup>2</sup> )	( $\pm$ m <sup>2</sup> /s <sup>2</sup> )	(m <sup>2</sup> /s <sup>2</sup> )	( $\pm$ m <sup>2</sup> /s <sup>2</sup> )
				$\times 10^{-2}$	$\times 10^{-4}$	$\times 10^{-2}$	$\times 10^{-4}$	$\times 10^{-3}$	$\times 10^{-4}$	$\times 10^{-3}$	$\times 10^{-4}$	$\times 10^{-3}$	$\times 10^{-4}$
(1,1)	0.72	3.0	169	9.17	6.53	-0.92	6.53	3.62	1.54	17.2	1.29	28.0	2.48
(2,1)	2.16	3.0	579	4.14	3.37	-2.54	3.37	8.73	0.87	21.6	0.77	31.2	1.36
(3,1)	3.60	3.0	1159	0.05	2.21	-2.52	2.21	6.55	0.49	12.69	0.39	24.30	0.81
(4,1)	5.04	3.0	1930	-2.53	1.60	-2.07	1.60	3.46	0.29	7.25	0.21	16.6	0.49
(5,1)	6.48	3.0	1393	-1.65	1.75	-0.85	1.75	0.46	0.26	2.35	0.13	14.07	0.48
(1,2)	0.72	5.0	358	12.4	5.11	-0.34	5.11	9.14	1.67	24.4	1.18	65.5	2.90
(2,2)	2.16	5.0	1270	6.99	2.62	-1.65	2.62	13.9	0.88	26.1	0.64	64.5	1.51
(3,2)	3.60	5.0	2168	0.06	1.88	-2.27	1.88	13.4	0.59	18.9	0.39	56.4	1.04
(4,2)	5.04	5.0	3432	-4.71	1.40	-1.63	1.40	6.48	0.37	10.5	0.22	42.3	0.66
(5,2)	6.48	5.0	2652	-5.57	1.43	-0.58	1.43	1.27	0.29	3.97	0.14	29.0	0.55
(1,3)	0.72	7.0	481	12.8	3.80	0.11	3.80	6.02	1.33	22.2	0.87	74.2	2.35
(2,3)	2.16	7.0	1669	7.35	2.03	-1.06	2.03	9.56	0.74	24.20	0.47	75.7	1.33
(3,3)	3.60	7.0	2667	1.46	1.56	-1.19	1.56	13.6	0.54	20.6	0.33	71.7	0.97
(4,3)	5.04	7.0	4136	-5.65	1.20	-1.12	1.20	8.28	0.36	11.6	0.19	59.3	0.66
(5,3)	6.48	7.0	3223	-7.66	1.28	-0.30	1.28	2.23	0.30	4.99	0.14	41.3	0.56
(1,4)	0.72	9.0	648	12.8	3.05	-0.31	3.05	6.95	1.08	22.7	0.68	80.5	1.92
(2,4)	2.16	9.0	1968	11.3	1.75	-0.49	1.75	12.8	0.65	24.8	0.40	86.2	1.17
(3,4)	3.60	9.0	3359	3.92	1.30	-0.90	1.30	14.9	0.48	22.1	0.29	82.3	0.86
(4,4)	5.04	9.0	5194	-4.57	1.01	-0.96	1.01	8.27	0.31	13.1	0.17	67.7	0.58
(5,4)	6.48	9.0	3659	-8.67	1.16	-0.29	1.16	2.19	0.28	5.00	0.12	48.7	0.54
(1,5)	0.72	11.0	704	17.2	3.03	0.24	3.03	4.11	1.07	21.4	0.65	83.2	1.94
(2,5)	2.16	11.0	2115	13.6	1.74	-0.25	1.74	11.2	0.67	28.1	0.43	95.4	1.19
(3,5)	3.60	11.0	3529	5.30	1.29	-0.47	1.29	13.7	0.48	23.4	0.29	88.9	0.86
(4,5)	5.04	11.0	5515	-4.41	1.00	-0.53	1.00	8.57	0.33	14.1	0.17	76.8	0.60
(5,5)	6.48	11.0	3925	-9.82	1.13	-0.22	1.13	2.88	0.30	5.68	0.12	57.6	0.58

**Table 4.5** Continued.

Grid segment	$r$	$z$	$n$	$\bar{u}_z$	$\delta\bar{u}_z$	$\bar{u}_r$	$\delta\bar{u}_r$	$\overline{u'_r u'_z}$	$\delta(\overline{u'_r u'_z})$	$\overline{u'_z u'_r}$	$\delta(\overline{u'_z u'_r})$	$\overline{u'_z u'_z}$	$\delta(\overline{u'_z u'_z})$
	(cm)	(cm)		(m/s)	( $\pm$ m/s)	(m/s)	( $\pm$ m/s)	(m <sup>2</sup> /s <sup>2</sup> )	( $\pm$ m <sup>2</sup> /s <sup>2</sup> )	(m <sup>2</sup> /s <sup>2</sup> )	( $\pm$ m <sup>2</sup> /s <sup>2</sup> )	(m <sup>2</sup> /s <sup>2</sup> )	( $\pm$ m <sup>2</sup> /s <sup>2</sup> )
				$\times 10^{-2}$	$\times 10^{-4}$	$\times 10^{-2}$	$\times 10^{-4}$	$\times 10^{-3}$	$\times 10^{-4}$	$\times 10^{-3}$	$\times 10^{-4}$	$\times 10^{-3}$	$\times 10^{-4}$
(1,6)	0.72	13.0	782	16.8	3.01	0.56	3.01	8.49	1.06	23.8	0.67	81.3	1.89
(2,6)	2.16	13.0	2321	14.3	1.72	-0.56	1.72	10.8	0.65	30.0	0.43	93.1	1.15
(3,6)	3.60	13.0	4070	5.56	1.26	-1.14	1.26	10.9	0.46	23.4	0.28	89.8	0.83
(4,6)	5.04	13.0	5573	-4.28	1.02	-0.68	1.02	8.54	0.35	15.2	0.18	82.4	0.64
(5,6)	6.48	13.0	3841	-11.5	1.15	-0.46	1.15	2.19	0.33	5.81	0.13	64.8	0.63
(1,7)	0.72	15.0	801	21.5	3.06	-0.21	3.06	0.17	1.06	24.5	0.71	75.3	1.85
(2,7)	2.16	15.0	2418	14.2	1.72	-0.75	1.72	11.5	0.65	29.6	0.43	92.6	1.14
(3,7)	3.60	15.0	3949	7.28	1.31	-0.49	1.31	10.1	0.48	26.8	0.31	89.5	0.84
(4,7)	5.04	15.0	6019	-4.92	1.00	-0.68	1.00	7.87	0.34	17.7	0.19	81.9	0.62
(5,7)	6.48	15.0	4207	-12.4	1.13	-0.21	1.13	2.96	0.31	6.24	0.13	61.1	0.59
(1,8)	0.72	17.0	809	22.7	3.04	0.31	3.04	1.81	0.98	22.8	0.66	71.4	1.71
(2,8)	2.16	17.0	2502	15.7	1.72	-0.60	1.72	8.45	0.64	31.7	0.45	89.3	1.11
(3,8)	3.60	17.0	4116	7.50	1.30	0.14	1.30	8.93	0.48	27.4	0.31	89.5	0.84
(4,8)	5.04	17.0	6364	-4.56	0.99	-0.18	0.99	6.69	0.32	17.0	0.19	77.1	0.59
(5,8)	6.48	17.0	4391	-13.1	1.12	0.03	1.12	2.51	0.31	6.06	0.13	60.3	0.58
(1,9)	0.72	19.0	755	23.2	3.15	0.41	3.15	0.27	1.07	24.8	0.71	75.2	1.89
(2,9)	2.16	19.0	2435	18.1	1.74	-0.13	1.74	2.89	0.62	30.3	0.44	83.5	1.07
(3,9)	3.60	19.0	4148	7.18	1.30	-0.43	1.30	9.11	0.47	26.0	0.31	85.3	0.82
(4,9)	5.04	19.0	6058	-4.65	1.03	-0.55	1.03	6.27	0.33	16.7	0.19	77.0	0.61
(5,9)	6.48	19.0	4338	-14.4	1.15	-0.29	1.15	2.68	0.30	5.77	0.13	58.6	0.58
(1,10)	0.72	21.0	878	22.5	2.85	1.19	2.85	1.68	0.96	24.8	0.65	76.1	1.69
(2,10)	2.16	21.0	2554	16.8	1.68	0.66	1.68	6.78	0.59	32.2	0.43	77.1	1.00
(3,10)	3.60	21.0	4118	8.43	1.31	0.44	1.31	8.91	0.45	27.6	0.31	80.2	0.79
(4,10)	5.04	21.0	5989	-4.56	1.04	0.26	1.04	7.97	0.34	18.1	0.20	74.5	0.61
(5,10)	6.48	21.0	4388	-14.9	1.16	0.05	1.16	2.71	0.30	5.97	0.13	56.0	0.57

**Table 4.5** Continued.

Grid segment	$r$	$z$	$n$	$\bar{u}_z$	$\delta\bar{u}_z$	$\bar{u}_r$	$\delta\bar{u}_r$	$\overline{u'_r u'_z}$	$\delta(\overline{u'_r u'_z})$	$\overline{u'_r u'_r}$	$\delta(\overline{u'_r u'_r})$	$\overline{u'_z u'_z}$	$\delta(\overline{u'_z u'_z})$
	(cm)	(cm)		(m/s)	( $\pm$ m/s)	(m/s)	( $\pm$ m/s)	(m <sup>2</sup> /s <sup>2</sup> )	( $\pm$ m <sup>2</sup> /s <sup>2</sup> )	(m <sup>2</sup> /s <sup>2</sup> )	( $\pm$ m <sup>2</sup> /s <sup>2</sup> )	(m <sup>2</sup> /s <sup>2</sup> )	( $\pm$ m <sup>2</sup> /s <sup>2</sup> )
				$\times 10^{-2}$	$\times 10^{-4}$	$\times 10^{-2}$	$\times 10^{-4}$	$\times 10^{-3}$	$\times 10^{-4}$	$\times 10^{-3}$	$\times 10^{-4}$	$\times 10^{-3}$	$\times 10^{-4}$
(1,11)	0.72	23.0	812	21.2	2.97	0.01	2.97	3.55	1.02	23.7	0.66	78.4	1.81
(2,11)	2.16	23.0	2455	18.3	1.72	0.76	1.72	6.63	0.59	32.8	0.45	73.9	0.99
(3,11)	3.60	23.0	4388	8.13	1.27	0.31	1.27	7.97	0.43	25.7	0.29	76.3	0.75
(4,11)	5.04	23.0	5947	-4.53	1.05	0.27	1.05	6.05	0.32	16.7	0.20	69.2	0.59
(5,11)	6.48	23.0	4305	-14.7	1.17	0.07	1.17	1.87	0.30	6.06	0.13	56.6	0.58
(1,12)	0.72	25.0	743	25.9	3.14	-0.02	3.14	0.44	1.03	26.8	0.75	68.2	1.76
(2,12)	2.16	25.0	2454	17.8	1.70	-0.18	1.70	5.54	0.57	29.2	0.42	74.7	0.98
(3,12)	3.60	25.0	4159	8.47	1.30	0.41	1.30	9.57	0.44	25.2	0.30	78.8	0.77
(4,12)	5.04	25.0	6072	-4.59	1.04	0.21	1.04	4.95	0.31	15.9	0.19	65.6	0.56
(5,12)	6.48	25.0	4068	-15.0	1.20	0.30	1.20	2.72	0.30	5.75	0.13	51.4	0.56
(1,13)	0.72	27.0	743	25.9	3.17	-0.24	3.17	-0.26	1.02	25.1	0.72	66.9	1.76
(2,13)	2.16	27.0	2297	19.3	1.78	-0.78	1.78	8.50	0.60	32.0	0.46	72.7	1.01
(3,13)	3.60	27.0	3868	8.65	1.33	-0.71	1.33	8.48	0.44	23.8	0.30	73.6	0.78
(4,13)	5.04	27.0	5955	-4.78	1.03	-0.67	1.03	7.06	0.31	16.3	0.19	63.8	0.56
(5,13)	6.48	27.0	4204	-14.4	1.16	-0.16	1.16	1.90	0.28	5.85	0.13	49.1	0.53
(1,14)	0.72	29.0	790	25.7	3.08	0.03	3.08	3.21	0.99	27.5	0.73	62.9	1.69
(2,14)	2.16	29.0	2188	19.0	1.83	0.03	1.83	7.56	0.60	31.4	0.47	64.8	0.99
(3,14)	3.60	29.0	3922	8.53	1.30	0.56	1.30	8.39	0.43	24.8	0.30	69.8	0.74
(4,14)	5.04	29.0	5688	-4.09	1.04	0.32	1.04	6.37	0.31	15.3	0.18	62.8	0.56
(5,14)	6.48	29.0	3909	-15.8	1.18	-0.36	1.18	2.53	0.28	5.54	0.13	45.9	0.52
(1,15)	0.72	31.0	780	23.0	3.04	-0.43	3.04	2.03	0.97	22.8	0.65	64.2	1.70
(2,15)	2.16	31.0	2320	18.1	1.74	0.65	1.74	7.36	0.56	27.7	0.42	63.4	0.95
(3,15)	3.60	31.0	3674	7.15	1.34	0.01	1.34	7.37	0.44	23.1	0.30	68.9	0.77
(4,15)	5.04	31.0	5060	-3.72	1.07	0.53	1.07	8.08	0.32	15.9	0.20	62.4	0.57
(5,15)	6.48	31.0	3766	-15.8	1.17	0.05	1.17	2.84	0.27	5.51	0.13	44.1	0.51

**Table 4.5** Continued.

Grid segment	$r$	$z$	$n$	$\bar{u}_z$	$\delta\bar{u}_z$	$\bar{u}_r$	$\delta\bar{u}_r$	$\overline{u'_r u'_z}$	$\delta(\overline{u'_r u'_z})$	$\overline{u'_r u'_r}$	$\delta(\overline{u'_r u'_r})$	$\overline{u'_z u'_z}$	$\delta(\overline{u'_z u'_z})$
	(cm)	(cm)		(m/s)	( $\pm$ m/s)	(m/s)	( $\pm$ m/s)	(m <sup>2</sup> /s <sup>2</sup> )	( $\pm$ m <sup>2</sup> /s <sup>2</sup> )	(m <sup>2</sup> /s <sup>2</sup> )	( $\pm$ m <sup>2</sup> /s <sup>2</sup> )	(m <sup>2</sup> /s <sup>2</sup> )	( $\pm$ m <sup>2</sup> /s <sup>2</sup> )
				$\times 10^{-2}$	$\times 10^{-4}$	$\times 10^{-2}$	$\times 10^{-4}$	$\times 10^{-3}$	$\times 10^{-4}$	$\times 10^{-3}$	$\times 10^{-4}$	$\times 10^{-3}$	$\times 10^{-4}$
(1,16)	0.72	33.0	704	23.6	3.12	0.46	3.12	-0.44	1.00	19.8	0.65	67.8	1.78
(2,16)	2.16	33.0	2049	18.7	1.81	0.70	1.81	6.36	0.56	24.9	0.41	60.8	0.96
(3,16)	3.60	33.0	3386	7.21	1.35	0.33	1.35	9.14	0.43	21.0	0.28	66.1	0.75
(4,16)	5.04	33.0	4676	-3.74	1.09	0.01	1.09	8.16	0.32	15.3	0.20	59.5	0.57
(5,16)	6.48	33.0	3590	-14.9	1.18	0.12	1.18	3.12	0.28	5.37	0.12	45.4	0.52
(1,17)	0.72	35.0	589	22.9	3.22	1.37	3.22	8.29	1.09	18.3	0.63	75.1	1.98
(2,17)	2.16	35.0	1642	20.2	1.93	0.50	1.93	6.55	0.60	23.7	0.43	60.6	1.04
(3,17)	3.60	35.0	3008	7.95	1.36	0.51	1.36	7.53	0.42	20.5	0.28	62.1	0.74
(4,17)	5.04	35.0	4168	-3.87	1.10	0.59	1.10	7.31	0.31	13.6	0.19	53.6	0.55
(5,17)	6.48	35.0	3158	-14.8	1.22	0.15	1.22	2.31	0.29	4.93	0.12	45.8	0.55
(1,18)	0.72	37.0	531	21.5	3.27	0.13	3.27	4.55	0.96	17.7	0.64	53.8	1.68
(2,18)	2.16	37.0	1672	19.7	1.87	-0.44	1.87	7.99	0.59	23.3	0.41	59.6	1.02
(3,18)	3.60	37.0	2523	7.39	1.44	0.33	1.44	8.51	0.42	20.1	0.29	55.5	0.74
(4,18)	5.04	37.0	3968	-3.12	1.11	0.31	1.11	5.57	0.30	13.3	0.19	51.3	0.55
(5,18)	6.48	37.0	2706	-13.7	1.29	0.60	1.29	2.50	0.30	4.90	0.13	42.7	0.57
(1,19)	0.72	39.0	445	24.4	3.89	-0.18	3.89	1.34	1.08	18.2	0.75	46.9	1.87
(2,19)	2.16	39.0	1387	17.9	2.15	1.57	2.15	6.35	0.66	22.8	0.48	56.4	1.14
(3,19)	3.60	39.0	2275	8.95	1.59	0.66	1.59	6.78	0.48	20.5	0.34	52.1	0.83
(4,19)	5.04	39.0	3392	-3.72	1.28	0.44	1.28	5.15	0.35	13.7	0.22	48.3	0.63
(5,19)	6.48	39.0	2193	-12.9	1.50	0.17	1.50	2.21	0.35	4.61	0.15	40.9	0.68

**Table 4.6** Measured quantities for PEPT experiment 3.

Grid segment	$r$	$z$	$n$	$\bar{u}_z$	$\delta\bar{u}_z$	$\bar{u}_r$	$\delta\bar{u}_r$	$\overline{u'_r u'_z}$	$\delta(\overline{u'_r u'_z})$	$\overline{u'_r u'_r}$	$\delta(\overline{u'_r u'_r})$	$\overline{u'_z u'_z}$	$\delta(\overline{u'_z u'_z})$
	(cm)	(cm)		(m/s)	( $\pm$ m/s)	(m/s)	( $\pm$ m/s)	(m <sup>2</sup> /s <sup>2</sup> )	( $\pm$ m <sup>2</sup> /s <sup>2</sup> )	(m <sup>2</sup> /s <sup>2</sup> )	( $\pm$ m <sup>2</sup> /s <sup>2</sup> )	(m <sup>2</sup> /s <sup>2</sup> )	( $\pm$ m <sup>2</sup> /s <sup>2</sup> )
				$\times 10^{-2}$	$\times 10^{-4}$	$\times 10^{-2}$	$\times 10^{-4}$	$\times 10^{-3}$	$\times 10^{-4}$	$\times 10^{-3}$	$\times 10^{-4}$	$\times 10^{-3}$	$\times 10^{-4}$
(1,1)	0.72	3.00	181	5.67	7.76	-1.04	7.76	7.44	2.63	30.2	1.99	58.4	4.44
(2,1)	2.16	3.00	562	3.78	4.37	-3.65	4.37	14.5	1.47	38.3	1.29	52.9	2.31
(3,1)	3.60	3.00	1154	1.24	2.90	-2.72	2.90	11.3	0.88	23.7	0.67	47.0	1.48
(4,1)	5.04	3.00	1923	-3.12	2.12	-2.32	2.12	6.85	0.56	14.6	0.39	38.6	0.97
(5,1)	6.48	3.00	1274	-6.35	2.52	-0.87	2.52	2.47	0.60	5.73	0.28	36.3	1.13
(1,2)	0.72	5.00	327	7.66	5.66	-1.49	5.66	11.0	2.00	30.4	1.45	68.2	3.43
(2,2)	2.16	5.00	949	6.52	3.37	-1.56	3.37	22.1	1.37	39.7	0.99	92.6	2.36
(3,2)	3.60	5.00	1789	1.33	2.40	-2.33	2.40	21.6	0.94	29.7	0.63	87.2	1.66
(4,2)	5.04	5.00	2739	-5.73	1.85	-2.06	1.85	14.0	0.65	17.9	0.37	76.8	1.18
(5,2)	6.48	5.00	2053	-13.0	2.03	-1.09	2.03	4.22	0.62	6.66	0.25	67.8	1.19
(1,3)	0.72	7.00	426	10.3	4.32	0.02	4.32	7.29	1.52	30.5	1.14	68.6	2.58
(2,3)	2.16	7.00	1236	7.20	2.66	-1.77	2.66	21.4	1.13	39.0	0.77	102	1.97
(3,3)	3.60	7.00	2155	3.01	1.95	-2.08	1.95	18.7	0.81	30.8	0.50	101	1.46
(4,3)	5.04	7.00	3152	-5.63	1.57	-1.50	1.57	13.7	0.59	20.5	0.33	91.0	1.08
(5,3)	6.48	7.00	2431	-14.3	1.70	-0.27	1.70	5.02	0.55	6.87	0.21	78.9	1.07
(1,4)	0.72	9.00	525	15.6	3.65	-0.52	3.65	6.35	1.28	25.1	0.83	72.7	2.28
(2,4)	2.16	9.00	1471	10.7	2.22	-1.73	2.22	14.2	0.93	36.0	0.62	103	1.63
(3,4)	3.60	9.00	2254	5.20	1.78	-2.49	1.78	18.2	0.76	31.2	0.47	116	1.37
(4,4)	5.04	9.00	3546	-5.77	1.38	-1.08	1.38	12.5	0.54	19.9	0.28	102	0.99
(5,4)	6.48	9.00	2847	-13.6	1.47	-0.09	1.47	3.37	0.50	7.82	0.19	89.6	0.97
(1,5)	0.72	11.0	582	14.7	3.50	0.15	3.50	4.66	1.26	28.0	0.84	78.1	2.21
(2,5)	2.16	11.0	1683	13.7	2.06	-0.14	2.06	9.04	0.84	38.0	0.58	101	1.46
(3,5)	3.60	11.0	2804	6.55	1.57	-0.45	1.57	12.5	0.68	33.9	0.42	114	1.22
(4,5)	5.04	11.0	4107	-4.75	1.24	-0.98	1.24	10.8	0.48	20.8	0.26	99.4	0.88
(5,5)	6.48	11.0	3021	-14.4	1.41	-0.54	1.41	3.39	0.49	7.68	0.18	93.3	0.94

**Table 4.6** Continued.

Grid segment	$r$	$z$	$n$	$\bar{u}_z$	$\delta\bar{u}_z$	$\bar{u}_r$	$\delta\bar{u}_r$	$\overline{u'_r u'_z}$	$\delta(\overline{u'_r u'_z})$	$\overline{u'_r u'_r}$	$\delta(\overline{u'_r u'_r})$	$\overline{u'_z u'_z}$	$\delta(\overline{u'_z u'_z})$
	(cm)	(cm)		(m/s)	( $\pm$ m/s)	(m/s)	( $\pm$ m/s)	(m <sup>2</sup> /s <sup>2</sup> )	( $\pm$ m <sup>2</sup> /s <sup>2</sup> )	(m <sup>2</sup> /s <sup>2</sup> )	( $\pm$ m <sup>2</sup> /s <sup>2</sup> )	(m <sup>2</sup> /s <sup>2</sup> )	( $\pm$ m <sup>2</sup> /s <sup>2</sup> )
				$\times 10^{-2}$	$\times 10^{-4}$	$\times 10^{-2}$	$\times 10^{-4}$	$\times 10^{-3}$	$\times 10^{-4}$	$\times 10^{-3}$	$\times 10^{-4}$	$\times 10^{-3}$	$\times 10^{-4}$
(1,6)	0.72	13.0	563	18.9	3.65	1.18	3.65	5.64	1.36	31.5	0.95	85.9	2.36
(2,6)	2.16	13.0	1771	17.0	2.07	-0.61	2.07	9.71	0.87	43.5	0.62	110	1.51
(3,6)	3.60	13.0	2988	7.46	1.55	-1.73	1.55	10.8	0.65	33.2	0.41	114	1.16
(4,6)	5.04	13.0	4318	-4.99	1.24	-0.77	1.24	7.37	0.47	22.3	0.27	101	0.87
(5,6)	6.48	13.0	3304	-15.15	1.37	-0.09	1.37	2.66	0.46	8.28	0.18	87.4	0.89
(1,7)	0.72	15.0	594	22.3	3.69	-0.99	3.69	2.60	1.41	31.7	0.96	99.5	2.47
(2,7)	2.16	15.0	1931	18.4	2.04	-1.03	2.04	4.54	0.83	40.7	0.60	104	1.42
(3,7)	3.60	15.0	3327	7.32	1.50	-0.90	1.50	11.1	0.60	34.5	0.40	106	1.06
(4,7)	5.04	15.0	4540	-5.69	1.24	-0.50	1.24	6.77	0.46	22.3	0.27	98.6	0.85
(5,7)	6.48	15.0	3265	-15.9	1.40	0.22	1.40	3.87	0.46	8.07	0.18	86.2	0.89
(1,8)	0.72	17.0	553	27.8	3.89	-0.36	3.89	2.08	1.54	30.5	0.98	108	2.76
(2,8)	2.16	17.0	1842	21.1	2.09	0.68	2.09	9.85	0.84	42.9	0.63	101	1.43
(3,8)	3.60	17.0	3218	8.64	1.55	0.20	1.55	10.7	0.65	35.1	0.42	113	1.15
(4,8)	5.04	17.0	4729	-5.99	1.22	-0.02	1.22	8.92	0.46	21.5	0.26	99.3	0.85
(5,8)	6.48	17.0	3606	-15.9	1.34	-0.41	1.34	3.02	0.40	6.78	0.16	74.4	0.78
(1,9)	0.72	19.0	625	26.4	3.58	0.13	3.58	5.26	1.41	28.6	0.89	106	2.52
(2,9)	2.16	19.0	1810	21.6	2.13	0.77	2.13	9.58	0.88	41.3	0.63	109	1.53
(3,9)	3.60	19.0	3105	9.12	1.59	-0.30	1.59	11.1	0.63	35.7	0.43	106	1.11
(4,9)	5.04	19.0	4676	-5.37	1.25	-0.23	1.25	10.6	0.46	22.7	0.27	96.9	0.84
(5,9)	6.48	19.0	3708	-16.1	1.32	-0.14	1.32	4.18	0.40	7.85	0.17	72.1	0.75
(1,10)	0.72	21.0	534	31.2	3.87	-0.35	3.87	3.69	1.48	28.9	0.94	104	2.65
(2,10)	2.16	21.0	1982	20.4	2.00	-0.13	2.00	10.5	0.77	42.1	0.60	90.8	1.29
(3,10)	3.60	21.0	3388	9.21	1.50	-0.10	1.50	11.3	0.58	33.1	0.39	98.1	1.03
(4,10)	5.04	21.0	4676	-5.80	1.24	-0.13	1.24	9.47	0.44	23.5	0.27	88.2	0.80
(5,10)	6.48	21.0	3747	-16.0	1.32	0.00	1.32	4.08	0.39	7.93	0.17	70.2	0.74



**Table 4.6** Continued.

Grid segment	$r$	$z$	$n$	$\bar{u}_z$	$\delta\bar{u}_z$	$\bar{u}_r$	$\delta\bar{u}_r$	$\overline{u'_r u'_z}$	$\delta(\overline{u'_r u'_z})$	$\overline{u'_r u'_r}$	$\delta(\overline{u'_r u'_r})$	$\overline{u'_z u'_z}$	$\delta(\overline{u'_z u'_z})$
	(cm)	(cm)		(m/s)	( $\pm$ m/s)	(m/s)	( $\pm$ m/s)	(m <sup>2</sup> /s <sup>2</sup> )	( $\pm$ m <sup>2</sup> /s <sup>2</sup> )	(m <sup>2</sup> /s <sup>2</sup> )	( $\pm$ m <sup>2</sup> /s <sup>2</sup> )	(m <sup>2</sup> /s <sup>2</sup> )	( $\pm$ m <sup>2</sup> /s <sup>2</sup> )
				$\times 10^{-2}$	$\times 10^{-4}$	$\times 10^{-2}$	$\times 10^{-4}$	$\times 10^{-3}$	$\times 10^{-4}$	$\times 10^{-3}$	$\times 10^{-4}$	$\times 10^{-3}$	$\times 10^{-4}$
(1,11)	0.72	23.0	629	26.5	3.53	0.24	3.53	6.13	1.27	30.1	0.89	87.1	2.20
(2,11)	2.16	23.0	1910	20.7	2.06	0.82	2.06	9.25	0.82	39.8	0.59	100	1.42
(3,11)	3.60	23.0	3264	10.0	1.53	1.19	1.53	11.7	0.60	31.9	0.40	99.9	1.05
(4,11)	5.04	23.0	4472	-5.67	1.26	0.60	1.26	11.7	0.45	22.0	0.27	89.7	0.81
(5,11)	6.48	23.0	3587	-16.4	1.35	0.07	1.35	4.83	0.40	7.51	0.17	71.1	0.77
(1,12)	0.72	25.0	671	25.4	3.43	1.12	3.43	6.29	1.29	33.4	0.92	91.5	2.24
(2,12)	2.16	25.0	1919	19.7	2.04	1.52	2.04	12.4	0.83	41.1	0.60	102	1.41
(3,12)	3.60	25.0	3106	9.24	1.59	0.42	1.59	12.04	0.65	35.85	0.44	108	1.14
(4,12)	5.04	25.0	4656	-4.60	1.24	0.16	1.24	8.21	0.43	22.6	0.27	85.7	0.78
(5,12)	6.48	25.0	3848	-15.5	1.30	0.03	1.30	3.11	0.38	7.69	0.16	69.9	0.73
(1,13)	0.72	27.0	545	26.3	3.82	-0.40	3.82	4.67	1.49	30.1	0.96	102	2.65
(2,13)	2.16	27.0	1784	20.2	2.12	0.78	2.12	11.73	0.85	40.9	0.62	103	1.45
(3,13)	3.60	27.0	2993	10.8	1.62	1.58	1.62	12.0	0.64	34.9	0.44	105	1.13
(4,13)	5.04	27.0	4606	-5.06	1.25	0.60	1.25	9.80	0.43	22.9	0.27	83.7	0.78
(5,13)	6.48	27.0	3459	-15.8	1.36	0.33	1.36	3.27	0.40	7.83	0.17	71.6	0.77
(1,14)	0.72	29.0	593	30.1	3.74	0.86	3.74	5.41	1.41	27.6	0.91	93.5	2.52
(2,14)	2.16	29.0	1657	18.3	2.19	-0.20	2.19	11.5	0.91	38.0	0.62	107	1.59
(3,14)	3.60	29.0	2890	10.1	1.64	-0.28	1.64	11.7	0.65	32.6	0.43	103	1.15
(4,14)	5.04	29.0	4196	-5.62	1.29	0.60	1.29	10.9	0.46	22.6	0.28	85.9	0.83
(5,14)	6.48	29.0	3390	-14.5	1.37	0.28	1.37	2.88	0.41	7.81	0.17	71.7	0.77
(1,15)	0.72	31.0	555	24.9	3.84	1.80	3.84	9.65	1.53	28.7	0.97	106	2.73
(2,15)	2.16	31.0	1774	18.8	2.11	0.60	2.11	7.57	0.84	36.0	0.58	100	1.47
(3,15)	3.60	31.0	2847	9.36	1.61	0.68	1.61	10.4	0.64	32.0	0.42	97.8	1.13
(4,15)	5.04	31.0	4180	-4.58	1.27	-0.30	1.27	9.91	0.44	22.4	0.28	83.4	0.80
(5,15)	6.48	31.0	3221	-14.9	1.38	-0.11	1.38	2.38	0.41	7.46	0.17	71.8	0.78

**Table 4.6** Continued.

Grid segment	$r$	$z$	$n$	$\bar{u}_z$	$\delta\bar{u}_z$	$\bar{u}_r$	$\delta\bar{u}_r$	$\overline{u'_r u'_z}$	$\delta(\overline{u'_r u'_z})$	$\overline{u'_r u'_r}$	$\delta(\overline{u'_r u'_r})$	$\overline{u'_z u'_z}$	$\delta(\overline{u'_z u'_z})$
	(cm)	(cm)		(m/s)	( $\pm$ m/s)	(m/s)	( $\pm$ m/s)	(m <sup>2</sup> /s <sup>2</sup> )	( $\pm$ m <sup>2</sup> /s <sup>2</sup> )	(m <sup>2</sup> /s <sup>2</sup> )	( $\pm$ m <sup>2</sup> /s <sup>2</sup> )	(m <sup>2</sup> /s <sup>2</sup> )	( $\pm$ m <sup>2</sup> /s <sup>2</sup> )
				$\times 10^{-2}$	$\times 10^{-4}$	$\times 10^{-2}$	$\times 10^{-4}$	$\times 10^{-3}$	$\times 10^{-4}$	$\times 10^{-3}$	$\times 10^{-4}$	$\times 10^{-3}$	$\times 10^{-4}$
(1,16)	0.72	33.0	501	25.4	3.87	-0.55	3.87	8.98	1.41	27.8	0.95	86.0	2.49
(2,16)	2.16	33.0	1747	17.0	2.07	0.58	2.07	11.8	0.82	33.3	0.55	99.3	1.45
(3,16)	3.60	33.0	2551	7.69	1.67	1.41	1.67	13.1	0.65	33.6	0.45	94.6	1.13
(4,16)	5.04	33.0	3541	-4.09	1.35	0.91	1.35	9.99	0.49	21.9	0.29	89.8	0.88
(5,16)	6.48	33.0	2863	-15.8	1.44	0.20	1.44	3.33	0.43	7.60	0.18	70.7	0.82
(1,17)	0.72	35.0	417	21.6	4.21	1.24	4.21	4.77	1.59	29.3	1.06	89.5	2.81
(2,17)	2.16	35.0	1463	17.9	2.23	1.19	2.23	10.5	0.89	36.4	0.62	98.3	1.56
(3,17)	3.60	35.0	2349	7.93	1.68	1.10	1.68	13.9	0.67	30.3	0.43	100	1.20
(4,17)	5.04	35.0	3186	-3.19	1.39	1.18	1.39	8.87	0.51	21.0	0.30	89.7	0.93
(5,17)	6.48	35.0	2422	-16.5	1.54	0.39	1.54	4.01	0.47	7.19	0.19	72.9	0.90
(1,18)	0.72	37.0	369	28.1	4.45	-0.99	4.45	5.56	1.58	27.6	1.11	75.9	2.75
(2,18)	2.16	37.0	1150	18.7	2.56	-0.53	2.56	10.4	1.01	33.9	0.70	95.0	1.76
(3,18)	3.60	37.0	2144	6.59	1.78	-0.09	1.78	12.7	0.69	30.01	0.46	89.2	1.21
(4,18)	5.04	37.0	2911	-4.08	1.49	0.84	1.49	11.4	0.54	20.9	0.31	85.0	0.98
(5,18)	6.48	37.0	2066	-14.6	1.68	0.68	1.68	4.04	0.51	6.87	0.21	70.7	0.98
(1,19)	0.72	39.0	380	21.3	4.60	1.11	4.60	2.35	1.55	21.1	1.00	72.5	2.77
(2,19)	2.16	39.0	1017	16.1	2.87	1.08	2.87	8.25	1.06	32.5	0.76	81.3	1.83
(3,19)	3.60	39.0	1706	9.35	2.20	0.69	2.20	12.5	0.86	30.6	0.57	90.2	1.52
(4,19)	5.04	39.0	2472	-4.25	1.76	0.08	1.76	10.8	0.64	20.8	0.38	83.2	1.17
(5,19)	6.48	39.0	1917	-12.0	1.91	0.19	1.91	5.24	0.64	7.88	0.25	75.9	1.22

**Table 4.7** Measured quantities for PEPT experiment 4.

Grid segment	$r$	$z$	$n$	$\bar{u}_z$	$\delta\bar{u}_z$	$\bar{u}_r$	$\delta\bar{u}_r$	$\overline{u'_r u'_z}$	$\delta(\overline{u'_r u'_z})$	$\overline{u'_r u'_r}$	$\delta(\overline{u'_r u'_r})$	$\overline{u'_z u'_z}$	$\delta(\overline{u'_z u'_z})$
	(cm)	(cm)		(m/s)	( $\pm$ m/s)	(m/s)	( $\pm$ m/s)	(m <sup>2</sup> /s <sup>2</sup> )	( $\pm$ m <sup>2</sup> /s <sup>2</sup> )	(m <sup>2</sup> /s <sup>2</sup> )	( $\pm$ m <sup>2</sup> /s <sup>2</sup> )	(m <sup>2</sup> /s <sup>2</sup> )	( $\pm$ m <sup>2</sup> /s <sup>2</sup> )
				$\times 10^{-2}$	$\times 10^{-4}$	$\times 10^{-2}$	$\times 10^{-4}$	$\times 10^{-3}$	$\times 10^{-4}$	$\times 10^{-3}$	$\times 10^{-4}$	$\times 10^{-3}$	$\times 10^{-4}$
(1,1)	0.72	3.00	72	20.0	13.72	-1.41	13.72	3.53	2.82	12.5	2.07	26.1	4.82
(2,1)	2.16	3.00	214	11.4	7.79	-3.38	7.79	8.10	1.84	14.1	1.33	33.3	3.15
(3,1)	3.60	3.00	466	-0.02	4.87	-3.65	4.87	4.95	0.88	6.92	0.61	18.6	1.53
(4,1)	5.04	3.00	955	-3.46	3.04	-2.05	3.04	1.16	0.31	3.06	0.25	5.49	0.51
(5,1)	6.48	3.00	1173	-2.21	2.29	-0.19	2.29	0.14	0.17	0.74	0.10	3.05	0.30
(1,2)	0.72	5.00	115	24.8	11.48	2.38	11.48	9.11	3.40	15.9	1.95	61.8	6.22
(2,2)	2.16	5.00	310	15.5	6.51	-1.05	6.51	13.1	2.08	21.1	1.42	53.7	3.63
(3,2)	3.60	5.00	641	1.27	4.00	-1.92	4.00	7.67	1.01	13.6	0.68	36.8	1.78
(4,2)	5.04	5.00	904	-5.39	3.08	-2.45	3.08	4.71	0.58	7.49	0.41	20.1	1.02
(5,2)	6.48	5.00	853	-6.58	2.76	-0.76	2.76	1.33	0.41	2.43	0.21	13.5	0.76
(1,3)	0.72	7.00	105	30.7	12.42	0.54	12.42	17.2	4.27	21.1	2.46	81.4	7.81
(2,3)	2.16	7.00	359	19.5	6.36	-0.72	6.36	16.2	2.37	22.8	1.41	85.7	4.30
(3,3)	3.60	7.00	735	5.02	3.76	-1.00	3.76	12.9	1.19	16.9	0.77	56.2	2.12
(4,3)	5.04	7.00	1046	-5.67	2.88	-1.58	2.88	7.96	0.73	11.0	0.46	37.3	1.31
(5,3)	6.48	7.00	998	-9.10	2.75	-0.71	2.75	0.96	0.55	3.60	0.26	26.1	1.04
(1,4)	0.72	9.00	126	26.6	11.05	1.27	11.05	4.18	4.36	20.3	2.35	86.5	8.05
(2,4)	2.16	9.00	389	20.3	6.25	0.72	6.25	13.6	2.81	24.2	1.46	113	5.22
(3,4)	3.60	9.00	728	6.22	4.09	-0.35	4.09	15.4	1.54	21.9	0.91	82.9	2.80
(4,4)	5.04	9.00	1140	-6.14	2.92	-0.71	2.92	9.78	0.89	13.6	0.52	53.8	1.62
(5,4)	6.48	9.00	1000	-11.8	2.87	0.00	2.87	2.98	0.69	4.35	0.29	38.9	1.32
(1,5)	0.72	11.0	154	20.8	9.53	0.42	9.53	0.06	3.86	21.1	2.02	104	7.18
(2,5)	2.16	11.0	434	17.8	5.73	-0.08	5.73	14.4	2.42	29.2	1.45	104	4.39
(3,5)	3.60	11.0	712	6.92	4.19	-0.26	4.19	17.5	1.71	25.4	1.01	94.7	3.10
(4,5)	5.04	11.0	1132	-5.84	3.06	-0.85	3.06	10.7	1.01	15.4	0.58	66.2	1.86
(5,5)	6.48	11.0	987	-13.9	3.11	-0.27	3.11	4.59	0.90	5.58	0.36	55.0	1.73

**Table 4.7** Continued.

Grid segment	$r$	$z$	$n$	$\bar{u}_z$	$\delta\bar{u}_z$	$\bar{u}_r$	$\delta\bar{u}_r$	$\overline{u'_r u'_z}$	$\delta(\overline{u'_r u'_z})$	$\overline{u'_r u'_r}$	$\delta(\overline{u'_r u'_r})$	$\overline{u'_z u'_z}$	$\delta(\overline{u'_z u'_z})$
	(cm)	(cm)		(m/s)	( $\pm$ m/s)	(m/s)	( $\pm$ m/s)	(m <sup>2</sup> /s <sup>2</sup> )	( $\pm$ m <sup>2</sup> /s <sup>2</sup> )	(m <sup>2</sup> /s <sup>2</sup> )	( $\pm$ m <sup>2</sup> /s <sup>2</sup> )	(m <sup>2</sup> /s <sup>2</sup> )	( $\pm$ m <sup>2</sup> /s <sup>2</sup> )
				$\times 10^{-2}$	$\times 10^{-4}$	$\times 10^{-2}$	$\times 10^{-4}$	$\times 10^{-3}$	$\times 10^{-4}$	$\times 10^{-3}$	$\times 10^{-4}$	$\times 10^{-3}$	$\times 10^{-4}$
(1,6)	0.72	13.0	195	21.07	9.08	-0.46	9.08	4.94	3.91	22.02	2.00	114.55	7.29
(2,6)	2.16	13.0	463	21.02	5.81	-0.89	5.81	18.60	2.87	30.25	1.57	131.26	5.30
(3,6)	3.60	13.0	812	7.36	4.04	-0.45	4.04	13.03	1.64	24.73	0.95	101.34	3.00
(4,6)	5.04	13.0	1270	-5.61	2.96	0.13	2.96	10.54	1.01	16.54	0.58	71.08	1.84
(5,6)	6.48	13.0	1023	-14.18	3.11	-0.06	3.11	4.71	0.96	6.70	0.38	65.89	1.84
(1,7)	0.72	15.0	172	24.16	9.39	0.98	9.39	5.62	3.87	24.99	2.09	102.44	7.15
(2,7)	2.16	15.0	589	20.06	5.12	0.07	5.12	17.62	2.23	30.01	1.27	115.95	4.08
(3,7)	3.60	15.0	832	5.25	4.11	-0.44	4.11	19.08	1.87	31.86	1.09	118.74	3.40
(4,7)	5.04	15.0	1244	-5.08	3.06	-0.14	3.06	12.39	1.10	18.96	0.63	80.11	2.02
(5,7)	6.48	15.0	1090	-15.11	3.07	-0.22	3.07	3.67	0.91	6.32	0.36	63.26	1.76
(1,8)	0.72	17.0	171	20.85	9.56	1.26	9.56	8.37	4.20	23.85	2.23	102.82	7.78
(2,8)	2.16	17.0	621	18.42	4.93	0.68	4.93	8.20	2.07	33.12	1.31	102.54	3.71
(3,8)	3.60	17.0	1011	6.24	3.72	0.27	3.72	18.76	1.66	32.19	1.02	104.65	2.99
(4,8)	5.04	17.0	1236	-5.41	3.14	-0.59	3.14	9.90	1.17	21.95	0.69	85.73	2.13
(5,8)	6.48	17.0	1198	-14.97	2.93	-0.37	2.93	2.86	0.91	6.47	0.36	69.01	1.76
(1,9)	0.72	19.0	158	28.55	9.85	0.23	9.85	1.57	4.44	23.81	2.29	116.93	8.26
(2,9)	2.16	19.0	555	18.97	5.30	0.69	5.30	13.32	2.38	32.27	1.42	119.27	4.31
(3,9)	3.60	19.0	923	9.23	3.91	0.86	3.91	14.84	1.74	31.22	1.04	113.30	3.15
(4,9)	5.04	19.0	1324	-4.18	3.05	-0.08	3.05	13.42	1.18	23.16	0.70	86.32	2.13
(5,9)	6.48	19.0	1200	-15.90	2.94	0.20	2.94	2.92	0.89	6.99	0.36	65.37	1.70
(1,10)	0.72	21.0	162	23.03	9.95	2.01	9.95	9.41	4.27	31.24	2.53	108.79	7.76
(2,10)	2.16	21.0	537	18.02	5.26	1.25	5.26	11.01	2.20	39.64	1.56	100.16	3.81
(3,10)	3.60	21.0	916	9.65	3.92	0.66	3.92	16.68	1.74	33.78	1.08	112.67	3.12
(4,10)	5.04	21.0	1341	-4.79	3.02	1.11	3.02	12.18	1.16	23.04	0.70	86.77	2.09
(5,10)	6.48	21.0	1109	-16.07	3.10	0.65	3.10	3.99	0.97	6.99	0.40	69.09	1.85

**Table 4.7** Continued.

Grid segment	$r$	$z$	$n$	$\bar{u}_z$	$\delta\bar{u}_z$	$\bar{u}_r$	$\delta\bar{u}_r$	$\overline{u'_r u'_z}$	$\delta(\overline{u'_r u'_z})$	$\overline{u'_r u'_r}$	$\delta(\overline{u'_r u'_r})$	$\overline{u'_z u'_z}$	$\delta(\overline{u'_z u'_z})$
	(cm)	(cm)		(m/s)	( $\pm$ m/s)	(m/s)	( $\pm$ m/s)	(m <sup>2</sup> /s <sup>2</sup> )	( $\pm$ m <sup>2</sup> /s <sup>2</sup> )	(m <sup>2</sup> /s <sup>2</sup> )	( $\pm$ m <sup>2</sup> /s <sup>2</sup> )	(m <sup>2</sup> /s <sup>2</sup> )	( $\pm$ m <sup>2</sup> /s <sup>2</sup> )
				$\times 10^{-2}$	$\times 10^{-4}$	$\times 10^{-2}$	$\times 10^{-4}$	$\times 10^{-3}$	$\times 10^{-4}$	$\times 10^{-3}$	$\times 10^{-4}$	$\times 10^{-3}$	$\times 10^{-4}$
(1,11)	0.72	23.0	170	23.0	9.68	2.23	9.68	9.18	4.12	32.2	2.58	113	7.39
(2,11)	2.16	23.0	589	18.6	5.03	-0.27	5.03	10.1	2.19	39.2	1.47	103	3.85
(3,11)	3.60	23.0	1009	5.55	3.61	1.72	3.61	12.3	1.46	32.4	0.97	93.4	2.57
(4,11)	5.04	23.0	1361	-4.35	2.99	1.08	2.99	11.2	1.18	22.8	0.68	89.1	2.15
(5,11)	6.48	23.0	1157	-13.4	3.05	0.17	3.05	3.52	1.00	8.49	0.43	73.4	1.92
(1,12)	0.72	25.0	189	24.0	8.98	-0.44	8.98	11.8	3.55	25.5	2.14	98.3	6.43
(2,12)	2.16	25.0	503	19.5	5.46	1.08	5.46	8.19	2.63	36.7	1.59	121	4.77
(3,12)	3.60	25.0	891	5.56	3.94	0.43	3.94	13.6	1.70	35.0	1.09	102	3.02
(4,12)	5.04	25.0	1329	-4.16	3.03	-0.04	3.03	11.0	1.16	23.4	0.70	87.3	2.10
(5,12)	6.48	25.0	1228	-11.6	2.93	-0.08	2.93	2.44	1.01	7.43	0.39	78.1	1.94
(1,13)	0.72	27.0	170	21.3	9.54	-0.05	9.54	-1.06	4.11	27.6	2.45	107	7.46
(2,13)	2.16	27.0	544	15.6	5.19	1.84	5.19	6.49	2.20	41.2	1.56	98.2	3.79
(3,13)	3.60	27.0	827	6.57	4.06	0.64	4.06	13.8	1.82	31.4	1.07	110	3.32
(4,13)	5.04	27.0	1298	-2.48	3.05	0.85	3.05	7.96	1.21	22.8	0.69	89.2	2.22
(5,13)	6.48	27.0	1144	-12.7	3.07	-0.05	3.07	3.57	1.01	8.08	0.42	72.5	1.93
(1,14)	0.72	29.0	142	19.5	10.75	0.40	10.75	5.39	4.46	26.7	2.57	106	8.15
(2,14)	2.16	29.0	480	15.0	5.64	1.53	5.64	18.3	2.64	40.1	1.70	118	4.70
(3,14)	3.60	29.0	803	7.37	4.11	1.72	4.11	13.6	1.84	37.2	1.20	105	3.27
(4,14)	5.04	29.0	1207	-3.04	3.10	0.79	3.10	10.0	1.21	21.9	0.69	87.3	2.21
(5,14)	6.48	29.0	1045	-12.7	3.19	0.39	3.19	5.15	1.15	8.53	0.45	82.5	2.21
(1,15)	0.72	31.0	116	26.5	12.08	1.09	12.08	9.59	5.66	30.1	3.16	135	10.40
(2,15)	2.16	31.0	418	15.7	5.97	-0.85	5.97	10.1	2.54	35.7	1.70	103	4.48
(3,15)	3.60	31.0	732	6.89	4.33	-1.40	4.33	14.5	2.00	33.1	1.17	113	3.64
(4,15)	5.04	31.0	1104	-1.97	3.27	-0.54	3.27	11.3	1.38	23.4	0.78	95.6	2.54
(5,15)	6.48	31.0	1057	-11.9	3.10	0.19	3.10	4.20	1.07	7.58	0.42	77.6	2.05

**Table 4.7** Continued.

Grid segment	$r$	$z$	$n$	$\bar{u}_z$	$\delta\bar{u}_z$	$\bar{u}_r$	$\delta\bar{u}_r$	$\overline{u'_r u'_z}$	$\delta(\overline{u'_r u'_z})$	$\overline{u'_r u'_r}$	$\delta(\overline{u'_r u'_r})$	$\overline{u'_z u'_z}$	$\delta(\overline{u'_z u'_z})$
	(cm)	(cm)		(m/s)	( $\pm$ m/s)	(m/s)	( $\pm$ m/s)	(m <sup>2</sup> /s <sup>2</sup> )	( $\pm$ m <sup>2</sup> /s <sup>2</sup> )	(m <sup>2</sup> /s <sup>2</sup> )	( $\pm$ m <sup>2</sup> /s <sup>2</sup> )	(m <sup>2</sup> /s <sup>2</sup> )	( $\pm$ m <sup>2</sup> /s <sup>2</sup> )
				$\times 10^{-2}$	$\times 10^{-4}$	$\times 10^{-2}$	$\times 10^{-4}$	$\times 10^{-3}$	$\times 10^{-4}$	$\times 10^{-3}$	$\times 10^{-4}$	$\times 10^{-3}$	$\times 10^{-4}$
(1,16)	0.72	33.0	124	24.0	11.34	-0.33	11.34	2.26	4.09	20.3	2.31	78.9	7.49
(2,16)	2.16	33.0	399	16.2	6.02	-0.07	6.02	10.1	2.75	36.7	1.70	110	4.95
(3,16)	3.60	33.0	731	6.56	4.18	-1.07	4.18	6.52	1.87	33.2	1.13	103	3.38
(4,16)	5.04	33.0	1023	-3.87	3.31	0.20	3.31	5.66	1.29	22.3	0.74	85.9	2.37
(5,16)	6.48	33.0	1000	-12.2	3.14	0.67	3.14	2.32	1.09	7.49	0.41	73.5	2.09
(1,17)	0.72	35.0	123	17.6	11.26	-0.02	11.26	3.40	4.29	24.1	2.63	87.0	7.74
(2,17)	2.16	35.0	414	15.7	5.90	0.58	5.90	8.62	2.51	34.4	1.63	92.6	4.45
(3,17)	3.60	35.0	653	4.40	4.44	0.91	4.44	8.07	2.01	32.8	1.19	101	3.66
(4,17)	5.04	35.0	984	-3.59	3.35	0.58	3.35	6.16	1.27	18.8	0.70	82.4	2.35
(5,17)	6.48	35.0	803	-12.9	3.53	0.21	3.53	3.60	1.24	7.08	0.45	77.6	2.39
(1,18)	0.72	37.0	107	19.3	11.86	1.19	11.86	9.69	4.65	17.3	2.28	80.3	8.73
(2,18)	2.16	37.0	351	13.3	6.63	0.13	6.63	13.2	3.18	34.1	1.88	108	5.78
(3,18)	3.60	37.0	564	6.33	4.80	1.09	4.80	12.3	2.13	29.3	1.22	105	3.89
(4,18)	5.04	37.0	825	-5.18	3.69	0.85	3.69	9.13	1.44	20.5	0.79	80.1	2.66
(5,18)	6.48	37.0	699	-12.2	3.78	0.34	3.78	5.01	1.35	6.68	0.46	78.0	2.61
(1,19)	0.72	39.0	80	15.7	14.08	0.08	14.08	8.66	4.96	19.8	2.83	74.6	9.07
(2,19)	2.16	39.0	311	10.7	6.92	-0.21	6.92	9.85	2.58	30.9	1.78	72.7	4.51
(3,19)	3.60	39.0	542	3.46	4.86	0.49	4.86	10.9	1.95	28.1	1.23	82.9	3.49
(4,19)	5.04	39.0	715	-4.71	4.03	-1.06	4.03	9.95	1.45	17.9	0.80	73.3	2.68
(5,19)	6.48	39.0	659	-10.3	3.96	0.14	3.96	4.06	1.54	7.21	0.51	82.0	2.98

**Table 4.8** Measured quantities for PEPT experiment 6.

Grid segment	$r$	$z$	$n$	$\bar{u}_z$	$\delta\bar{u}_z$	$\bar{u}_r$	$\delta\bar{u}_r$	$\overline{u'_r u'_z}$	$\delta(\overline{u'_r u'_z})$	$\overline{u'_r u'_r}$	$\delta(\overline{u'_r u'_r})$	$\overline{u'_z u'_z}$	$\delta(\overline{u'_z u'_z})$
	(cm)	(cm)		(m/s)	( $\pm$ m/s)	(m/s)	( $\pm$ m/s)	(m <sup>2</sup> /s <sup>2</sup> )	( $\pm$ m <sup>2</sup> /s <sup>2</sup> )	(m <sup>2</sup> /s <sup>2</sup> )	( $\pm$ m <sup>2</sup> /s <sup>2</sup> )	(m <sup>2</sup> /s <sup>2</sup> )	( $\pm$ m <sup>2</sup> /s <sup>2</sup> )
				$\times 10^{-2}$	$\times 10^{-4}$	$\times 10^{-2}$	$\times 10^{-4}$	$\times 10^{-3}$	$\times 10^{-4}$	$\times 10^{-3}$	$\times 10^{-4}$	$\times 10^{-3}$	$\times 10^{-4}$
(1,1)	0.72	3.00	138	8.13	8.62	-0.54	8.62	2.02	1.38	4.93	0.90	14.6	2.44
(2,1)	2.16	3.00	372	2.52	5.40	-4.00	5.40	1.72	0.67	4.85	0.55	9.86	1.09
(3,1)	3.60	3.00	1468	-1.25	2.42	-0.95	2.42	0.22	0.13	0.86	0.12	1.26	0.20
(4,1)	5.04	3.00	18472	-0.07	0.58	-0.04	0.58	-0.03	0.01	0.29	0.02	0.08	0.01
(5,1)	6.48	3.00	21944	-0.02	0.72	-0.01	0.72	-0.06	0.02	0.47	0.03	0.12	0.02
(1,2)	0.72	5.00	284	16.9	5.69	-2.24	5.69	2.70	1.47	11.3	0.88	40.8	2.67
(2,2)	2.16	5.00	709	6.50	3.49	-3.54	3.49	4.57	0.74	9.67	0.51	28.0	1.29
(3,2)	3.60	5.00	1609	-3.01	2.26	-2.57	2.26	1.99	0.25	3.82	0.21	6.84	0.40
(4,2)	5.04	5.00	5750	-0.77	1.19	-0.48	1.19	0.21	0.05	0.81	0.05	0.89	0.07
(5,2)	6.48	5.00	6518	-0.37	1.12	-0.04	1.12	-0.06	0.04	0.48	0.04	0.32	0.04
(1,3)	0.72	7.00	350	21.8	5.24	-1.27	5.24	7.41	1.42	18.1	1.03	52.0	2.45
(2,3)	2.16	7.00	1014	8.93	2.90	-1.90	2.90	10.7	0.79	17.6	0.55	45.2	1.37
(3,3)	3.60	7.00	1772	-2.11	2.02	-2.75	2.02	6.47	0.36	9.70	0.29	19.3	0.60
(4,3)	5.04	7.00	2732	-4.16	1.57	-1.82	1.57	1.88	0.18	3.82	0.14	8.36	0.29
(5,3)	6.48	7.00	2120	-2.47	1.68	-0.14	1.68	0.04	0.12	0.95	0.08	4.30	0.22
(1,4)	0.72	9.00	438	26.2	4.89	1.35	4.89	7.14	1.75	23.2	1.08	87.7	3.15
(2,4)	2.16	9.00	1129	13.0	2.98	-0.57	2.98	14.3	0.95	20.8	0.62	70.2	1.69
(3,4)	3.60	9.00	2071	0.89	2.03	-1.71	2.03	11.0	0.48	15.3	0.37	36.3	0.80
(4,4)	5.04	9.00	3145	-5.28	1.53	-1.42	1.53	3.57	0.25	6.51	0.18	19.2	0.43
(5,4)	6.48	9.00	1769	-5.75	1.88	-0.47	1.88	0.58	0.23	2.05	0.13	12.8	0.43
(1,5)	0.72	11.0	380	25.8	5.10	-0.60	5.10	13.1	2.02	23.9	1.14	117	3.71
(2,5)	2.16	11.0	1179	15.1	2.85	0.44	2.85	18.8	1.01	26.2	0.67	83.3	1.78
(3,5)	3.60	11.0	2417	2.11	1.93	-1.28	1.93	11.8	0.51	16.3	0.35	49.1	0.88
(4,5)	5.04	11.0	3378	-6.80	1.55	-1.41	1.55	5.17	0.31	8.45	0.20	30.9	0.55
(5,5)	6.48	11.0	1989	-7.46	1.91	-0.45	1.91	0.75	0.29	2.71	0.14	21.2	0.55

**Table 4.8** Continued.

Grid segment	$r$	$z$	$n$	$\bar{u}_z$	$\delta\bar{u}_z$	$\bar{u}_r$	$\delta\bar{u}_r$	$\overline{u'_r u'_z}$	$\delta(\overline{u'_r u'_z})$	$\overline{u'_r u'_r}$	$\delta(\overline{u'_r u'_r})$	$\overline{u'_z u'_z}$	$\delta(\overline{u'_z u'_z})$
	(cm)	(cm)		(m/s)	( $\pm$ m/s)	(m/s)	( $\pm$ m/s)	(m <sup>2</sup> /s <sup>2</sup> )	( $\pm$ m <sup>2</sup> /s <sup>2</sup> )	(m <sup>2</sup> /s <sup>2</sup> )	( $\pm$ m <sup>2</sup> /s <sup>2</sup> )	(m <sup>2</sup> /s <sup>2</sup> )	( $\pm$ m <sup>2</sup> /s <sup>2</sup> )
				$\times 10^{-2}$	$\times 10^{-4}$	$\times 10^{-2}$	$\times 10^{-4}$	$\times 10^{-3}$	$\times 10^{-4}$	$\times 10^{-3}$	$\times 10^{-4}$	$\times 10^{-3}$	$\times 10^{-4}$
(1,6)	0.72	13.0	468	23.7	4.56	-0.32	4.56	7.88	1.77	24.1	1.04	108	3.22
(2,6)	2.16	13.0	1352	15.5	2.62	-1.60	2.62	11.7	0.92	23.5	0.59	85.7	1.64
(3,6)	3.60	13.0	2427	2.05	1.93	-0.83	1.93	13.7	0.60	20.5	0.41	65.2	1.05
(4,6)	5.04	13.0	3751	-5.93	1.50	-0.66	1.50	7.55	0.36	11.9	0.24	42.0	0.64
(5,6)	6.48	13.0	2269	-8.86	1.80	-0.42	1.80	1.44	0.33	3.29	0.15	29.5	0.63
(1,7)	0.72	15.0	532	26.8	4.18	1.61	4.18	11.6	1.67	24.9	0.94	115	3.06
(2,7)	2.16	15.0	1601	15.3	2.39	-0.46	2.39	14.2	0.92	27.6	0.58	100	1.64
(3,7)	3.60	15.0	2438	2.83	1.89	-0.68	1.89	13.5	0.64	22.0	0.41	77.9	1.14
(4,7)	5.04	15.0	3586	-6.44	1.53	-0.91	1.53	7.53	0.42	11.1	0.24	59.7	0.78
(5,7)	6.48	15.0	2171	-10.3	1.88	-0.18	1.88	1.89	0.39	3.60	0.17	39.6	0.75
(1,8)	0.72	17.0	551	24.7	4.17	0.99	4.17	6.79	1.61	23.5	0.93	112	2.93
(2,8)	2.16	17.0	1598	16.0	2.44	1.21	2.44	19.1	1.01	31.9	0.64	114	1.79
(3,8)	3.60	17.0	2647	3.95	1.83	0.22	1.83	13.3	0.60	23.5	0.41	75.3	1.06
(4,8)	5.04	17.0	3822	-6.11	1.49	-0.09	1.49	8.75	0.45	13.5	0.25	70.5	0.83
(5,8)	6.48	17.0	2245	-11.6	1.92	-0.22	1.92	1.39	0.43	4.05	0.18	46.0	0.82
(1,9)	0.72	19.0	499	25.0	4.42	2.08	4.42	10.1	1.79	31.3	1.13	111	3.21
(2,9)	2.16	19.0	1616	18.5	2.42	1.91	2.42	17.5	1.00	32.7	0.64	120	1.79
(3,9)	3.60	19.0	2435	5.33	1.95	1.31	1.95	14.8	0.70	25.1	0.45	94.3	1.26
(4,9)	5.04	19.0	4131	-6.58	1.44	0.20	1.44	6.00	0.44	13.8	0.25	72.3	0.81
(5,9)	6.48	19.0	2256	-12.2	1.92	-0.16	1.92	2.57	0.46	4.82	0.19	50.1	0.88
(1,10)	0.72	21.0	535	21.7	4.29	0.04	4.29	2.77	1.76	29.6	1.07	114	3.17
(2,10)	2.16	21.0	1677	15.1	2.41	1.31	2.41	14.3	0.94	32.8	0.62	106	1.66
(3,10)	3.60	21.0	2978	4.98	1.79	0.94	1.79	13.7	0.66	26.5	0.41	95.9	1.18
(4,10)	5.04	21.0	4157	-5.17	1.45	0.06	1.45	7.83	0.46	16.8	0.28	74.7	0.83
(5,10)	6.48	21.0	2502	-12.1	1.77	-0.19	1.77	2.61	0.44	4.81	0.18	52.5	0.84



**Table 4.8** Continued.

Grid segment	$r$	$z$	$n$	$\bar{u}_z$	$\delta\bar{u}_z$	$\bar{u}_r$	$\delta\bar{u}_r$	$\overline{u'_r u'_z}$	$\delta(\overline{u'_r u'_z})$	$\overline{u'_r u'_r}$	$\delta(\overline{u'_r u'_r})$	$\overline{u'_z u'_z}$	$\delta(\overline{u'_z u'_z})$
	(cm)	(cm)		(m/s)	( $\pm$ m/s)	(m/s)	( $\pm$ m/s)	(m <sup>2</sup> /s <sup>2</sup> )	( $\pm$ m <sup>2</sup> /s <sup>2</sup> )	(m <sup>2</sup> /s <sup>2</sup> )	( $\pm$ m <sup>2</sup> /s <sup>2</sup> )	(m <sup>2</sup> /s <sup>2</sup> )	( $\pm$ m <sup>2</sup> /s <sup>2</sup> )
				$\times 10^{-2}$	$\times 10^{-4}$	$\times 10^{-2}$	$\times 10^{-4}$	$\times 10^{-3}$	$\times 10^{-4}$	$\times 10^{-3}$	$\times 10^{-4}$	$\times 10^{-3}$	$\times 10^{-4}$
(1,11)	0.72	23.0	515	23.3	4.32	0.40	4.32	2.15	1.85	23.0	0.97	131	3.44
(2,11)	2.16	23.0	1801	13.1	2.30	0.60	2.30	8.12	0.86	29.7	0.58	96.9	1.52
(3,11)	3.60	23.0	3047	5.77	1.76	0.27	1.76	11.4	0.62	29.4	0.43	84.4	1.07
(4,11)	5.04	23.0	4482	-5.24	1.40	0.03	1.40	6.92	0.43	16.1	0.26	70.6	0.78
(5,11)	6.48	23.0	2661	-10.6	1.75	0.07	1.75	3.11	0.45	5.20	0.18	55.2	0.85
(1,12)	0.72	25.0	593	21.6	4.13	1.30	4.13	10.2	1.55	27.6	0.99	101	2.76
(2,12)	2.16	25.0	1898	12.4	2.29	-0.33	2.29	5.04	0.84	34.9	0.61	91.4	1.44
(3,12)	3.60	25.0	3025	5.91	1.78	-0.44	1.78	7.34	0.63	27.2	0.42	89.3	1.10
(4,12)	5.04	25.0	4292	-4.49	1.44	0.06	1.44	7.16	0.45	17.5	0.27	73.3	0.81
(5,12)	6.48	25.0	2499	-11.9	1.77	-0.24	1.77	2.54	0.45	5.24	0.19	54.9	0.87
(1,13)	0.72	27.0	637	17.1	4.05	2.65	4.05	5.38	1.39	31.8	1.04	78.3	2.36
(2,13)	2.16	27.0	1806	15.6	2.40	0.43	2.40	9.24	0.89	38.3	0.68	94.4	1.51
(3,13)	3.60	27.0	2948	4.95	1.77	0.47	1.77	6.42	0.63	28.9	0.44	88.0	1.10
(4,13)	5.04	27.0	4182	-5.51	1.45	0.35	1.45	5.88	0.44	16.5	0.27	70.8	0.80
(5,13)	6.48	27.0	2550	-10.5	1.73	0.00	1.73	2.95	0.44	5.89	0.19	55.1	0.85
(1,14)	0.72	29.0	516	18.5	4.50	-1.03	4.50	1.18	1.62	30.1	1.14	88.7	2.81
(2,14)	2.16	29.0	1678	15.3	2.43	1.05	2.43	6.38	0.92	36.8	0.68	97.5	1.58
(3,14)	3.60	29.0	2852	5.28	1.77	0.20	1.77	10.8	0.63	26.5	0.42	90.3	1.12
(4,14)	5.04	29.0	3865	-4.14	1.48	0.57	1.48	5.72	0.47	16.1	0.27	72.6	0.86
(5,14)	6.48	29.0	2377	-10.9	1.78	-0.21	1.78	1.58	0.46	5.41	0.19	58.1	0.89
(1,15)	0.72	31.0	474	24.4	4.66	-0.34	4.66	0.36	1.68	29.2	1.15	85.0	2.93
(2,15)	2.16	31.0	1463	14.8	2.50	-0.55	2.50	7.97	0.94	31.2	0.64	96.4	1.65
(3,15)	3.60	31.0	2423	5.37	1.89	0.64	1.89	10.2	0.68	28.6	0.47	85.4	1.19
(4,15)	5.04	31.0	3832	-4.36	1.49	-0.38	1.49	6.13	0.47	17.1	0.28	71.2	0.84
(5,15)	6.48	31.0	2341	-10.3	1.80	0.23	1.80	1.26	0.44	5.08	0.19	52.3	0.83

**Table 4.8** Continued.

Grid segment	$r$	$z$	$n$	$\bar{u}_z$	$\delta\bar{u}_z$	$\bar{u}_r$	$\delta\bar{u}_r$	$\overline{u'_r u'_z}$	$\delta(\overline{u'_r u'_z})$	$\overline{u'_r u'_r}$	$\delta(\overline{u'_r u'_r})$	$\overline{u'_z u'_z}$	$\delta(\overline{u'_z u'_z})$
	(cm)	(cm)		(m/s)	( $\pm$ m/s)	(m/s)	( $\pm$ m/s)	(m <sup>2</sup> /s <sup>2</sup> )	( $\pm$ m <sup>2</sup> /s <sup>2</sup> )	(m <sup>2</sup> /s <sup>2</sup> )	( $\pm$ m <sup>2</sup> /s <sup>2</sup> )	(m <sup>2</sup> /s <sup>2</sup> )	( $\pm$ m <sup>2</sup> /s <sup>2</sup> )
				$\times 10^{-2}$	$\times 10^{-4}$	$\times 10^{-2}$	$\times 10^{-4}$	$\times 10^{-3}$	$\times 10^{-4}$	$\times 10^{-3}$	$\times 10^{-4}$	$\times 10^{-3}$	$\times 10^{-4}$
(1,16)	0.72	33.0	390	26.6	4.76	-0.54	4.76	0.74	1.69	26.3	1.14	81.7	2.98
(2,16)	2.16	33.0	1274	18.1	2.66	-0.33	2.66	6.24	0.99	33.8	0.71	89.1	1.71
(3,16)	3.60	33.0	2393	5.17	1.95	-0.19	1.95	6.17	0.69	25.4	0.44	89.4	1.24
(4,16)	5.04	33.0	3325	-3.69	1.59	-0.02	1.59	7.32	0.54	16.5	0.30	84.6	1.00
(5,16)	6.48	33.0	1929	-11.4	1.96	-0.48	1.96	1.39	0.50	5.59	0.22	56.2	0.95
(1,17)	0.72	35.0	334	30.1	5.42	2.94	5.42	6.40	1.99	26.5	1.30	92.9	3.53
(2,17)	2.16	35.0	1120	17.9	2.84	1.70	2.84	6.27	1.08	32.8	0.75	89.5	1.87
(3,17)	3.60	35.0	2308	4.80	1.95	0.44	1.95	7.48	0.70	25.9	0.46	88.4	1.25
(4,17)	5.04	35.0	3051	-3.81	1.63	0.28	1.63	5.64	0.51	17.2	0.31	72.9	0.93
(5,17)	6.48	35.0	1724	-11.9	2.01	0.08	2.01	1.94	0.56	5.90	0.23	61.7	1.07
(1,18)	0.72	37.0	314	22.5	5.36	3.25	5.36	-0.05	1.96	23.0	1.14	88.9	3.57
(2,18)	2.16	37.0	1127	17.3	2.88	0.72	2.88	8.03	1.11	32.4	0.77	87.6	1.93
(3,18)	3.60	37.0	1925	6.36	2.13	0.76	2.13	7.51	0.79	24.7	0.48	92.7	1.43
(4,18)	5.04	37.0	2721	-3.58	1.63	0.36	1.63	5.67	0.55	17.3	0.32	77.8	1.01
(5,18)	6.48	37.0	1459	-12.4	2.08	0.38	2.08	3.25	0.57	6.17	0.24	58.7	1.09
(1,19)	0.72	39.0	366	14.0	4.78	0.49	4.78	2.53	1.52	22.3	1.02	67.1	2.68
(2,19)	2.16	39.0	1006	15.1	2.86	1.51	2.86	7.31	1.03	30.5	0.71	75.8	1.80
(3,19)	3.60	39.0	1689	5.88	2.12	0.64	2.12	4.67	0.75	23.8	0.48	76.0	1.33
(4,19)	5.04	39.0	2205	-4.95	1.72	0.28	1.72	4.34	0.59	16.8	0.33	75.2	1.08
(5,19)	6.48	39.0	1301	-9.09	2.08	-0.03	2.08	3.59	0.63	6.42	0.25	63.7	1.22

# CHAPTER 4 FIGURES

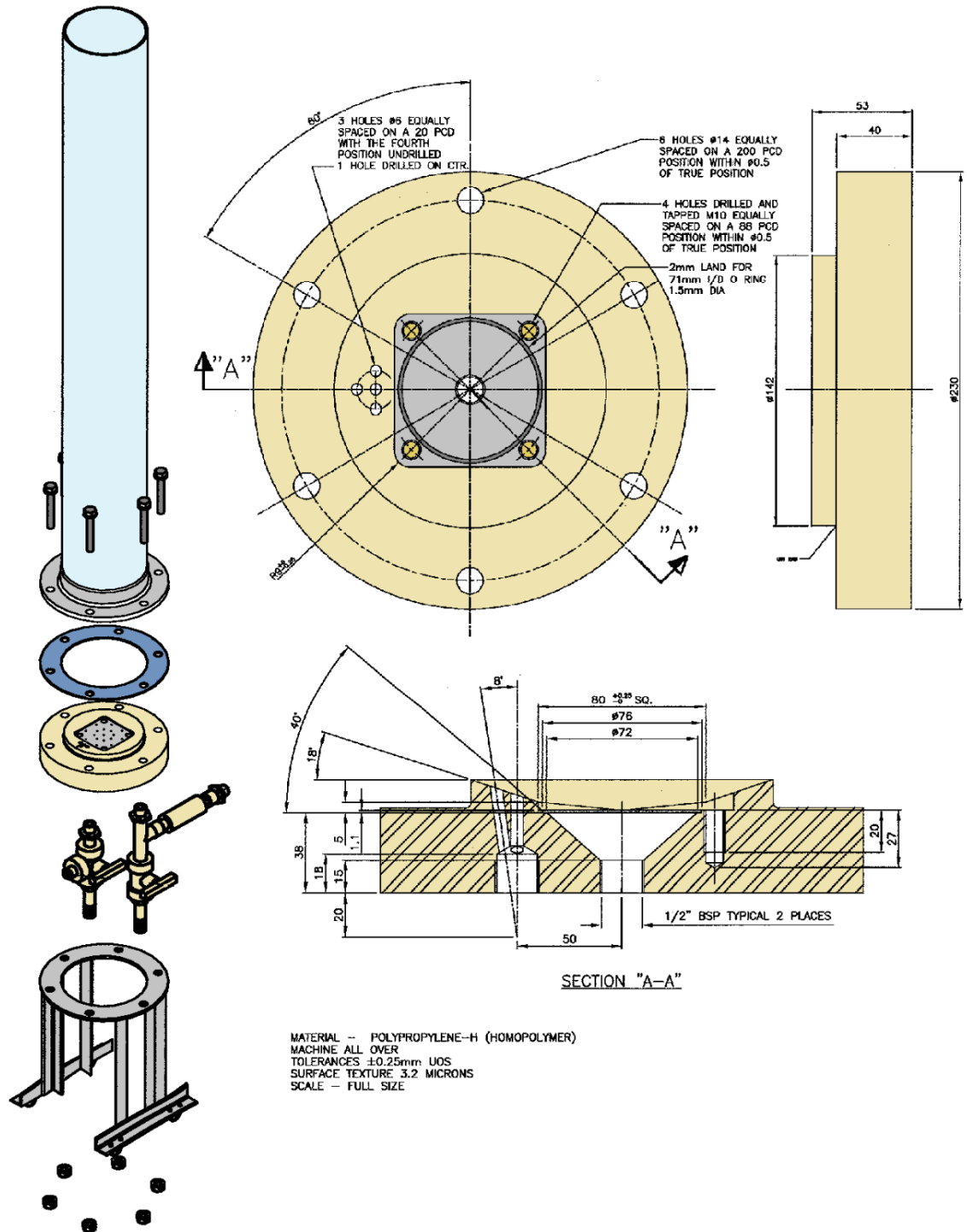
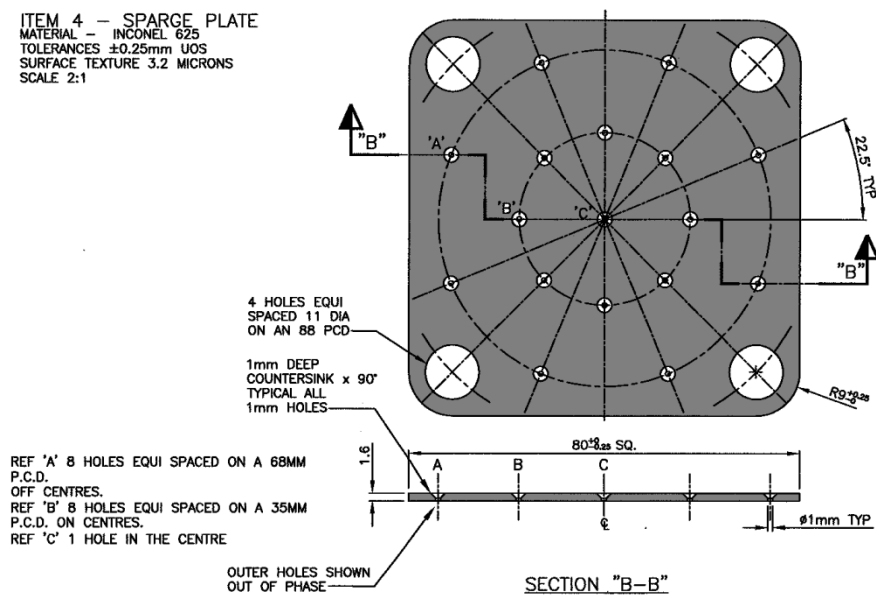
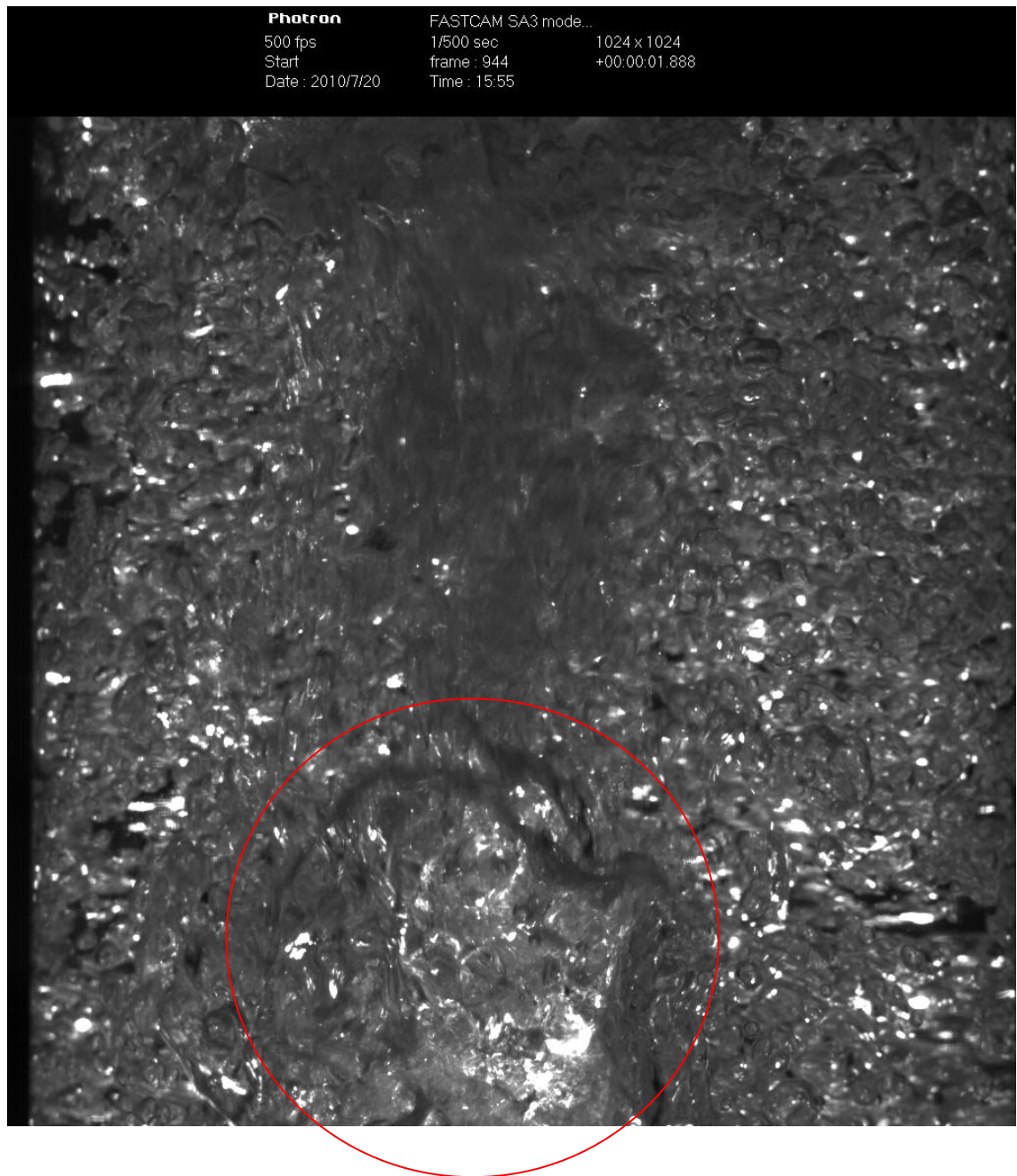


Figure 4.1 A drawing showing the arrangement of the Perspex column and polypropylene assembly (Rolls-Royce drawings).

ITEM 4 - SPARGE PLATE  
 MATERIAL - INCONEL 625  
 TOLERANCES  $\pm 0.25\text{mm}$  UOS  
 SURFACE TEXTURE 3.2 MICRONS  
 SCALE 2:1



**Figure 4.2** A drawing of the inconel perforated plate showing the number of holes and array pattern (Rolls-Royce drawings).



**Figure 4.3** Image of heterogeneous flow of air-water column for flow visualisation experiment 1; superficial gas velocity 6.1 cm/s. Internal column diameter of 144 mm. TIFF image belongs to file flow\_vis\_ext\_1.avi.



**Figure 4.4** Image of heterogeneous flow of air-water column for flow visualisation experiment 2; superficial gas velocity 6.1 cm/s, 1 kg of dissolved sodium chloride. Internal column diameter of 144 mm. TIFF image belongs to file flow\_vis\_ext\_2.avi.





**Figure 4.5** Image of heterogeneous flow of air-water-swarf column for flow visualisation experiment 3; superficial gas velocity 6.1 cm/s, 1 kg of dissolved sodium chloride, 500 g of loose swarf. Internal column diameter of 144 mm. TIFF image belongs to file flow\_vis\_ext\_3.avi.

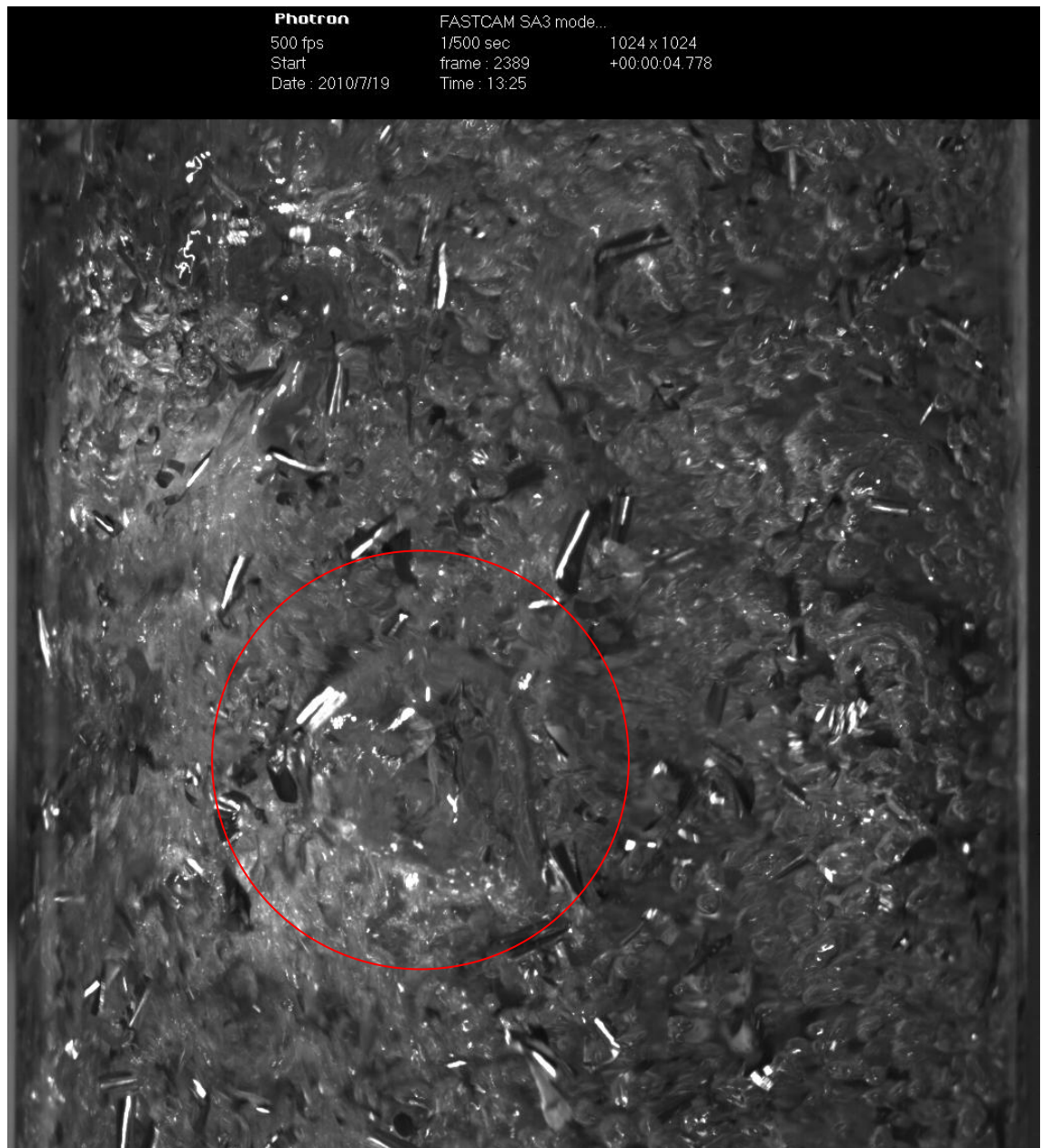


**Figure 4.6** Image of heterogeneous flow of air-water-swarf column for flow visualisation experiment 4; superficial gas velocity 6.1 cm/s, 500 g of loose swarf. Internal column diameter of 144 mm. TIFF image belongs to file flow\_vis\_ext\_4.avi.



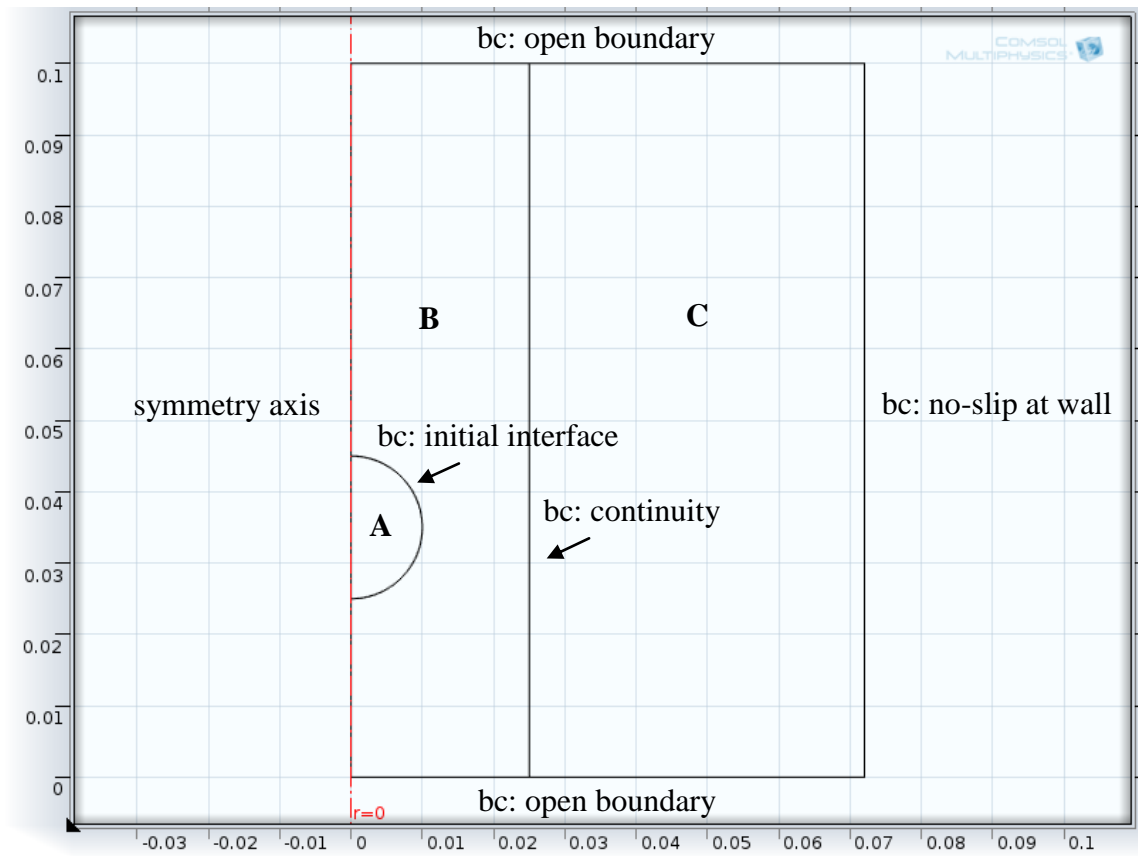


**Figure 4.7** The individual domains and boundary conditions (bc) of the simulation of a void rising through a column of water. The simulation is for 2-dimensional axisymmetric flow. Domain **A** represents the initial spherical air void of diameter 20 mm. Both domains **B** and **C** represent the column of water initially at rest. The column diameter is 144 mm.

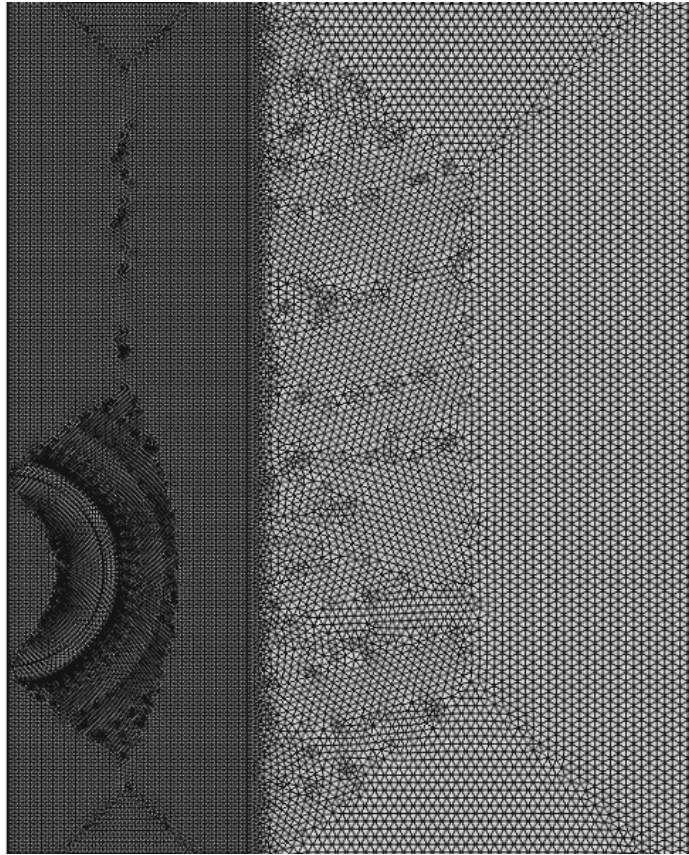


**Figure 4.8** Free triangular mesh used in the simulation of a void rising through a column of water. In the region of the phase field interface the maximum element size is 0.5 mm and corresponds to the denser mesh region to the left of the domain. Some non-uniformity of the mesh occurs because of the curvature of the interface in this region. Total number of mesh elements equals 41530.

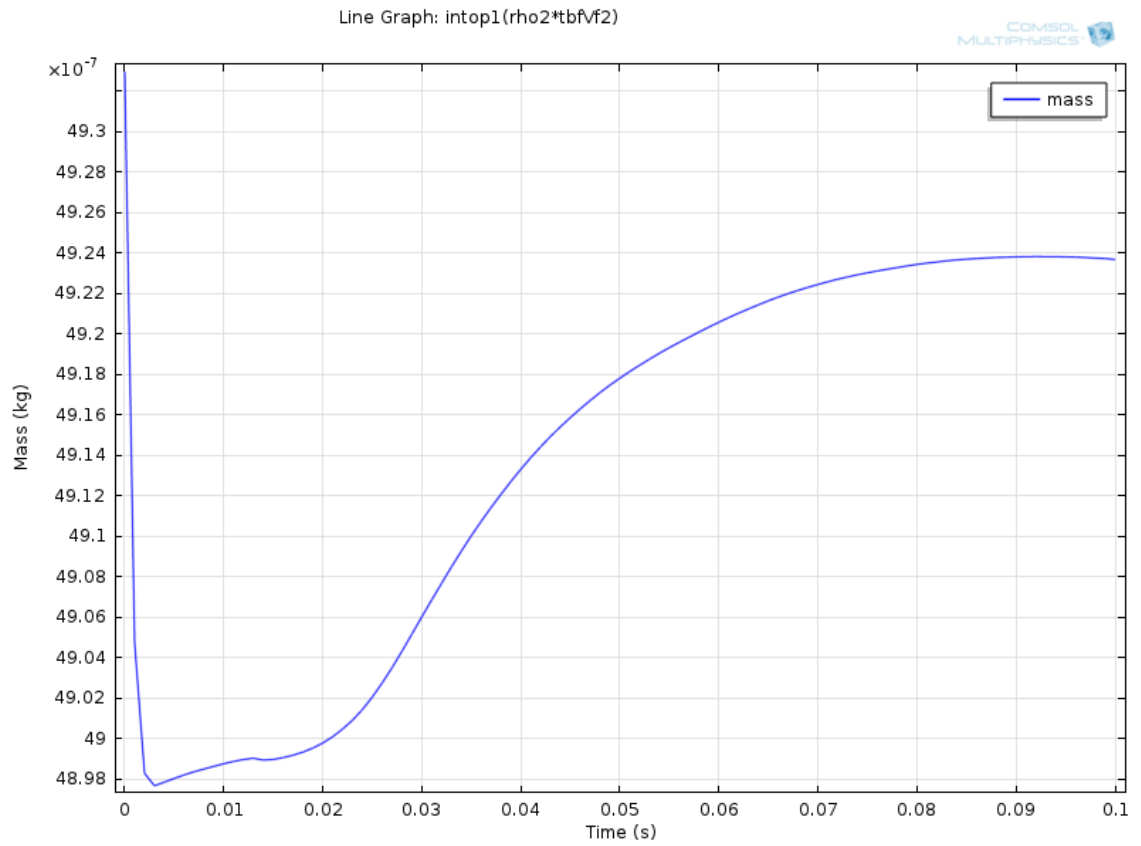


**Figure 4.9** Mass conservation of the air void throughout the duration of the simulation. The maximum change in mass of the air void during the simulation is  $\sim 0.7\%$ .

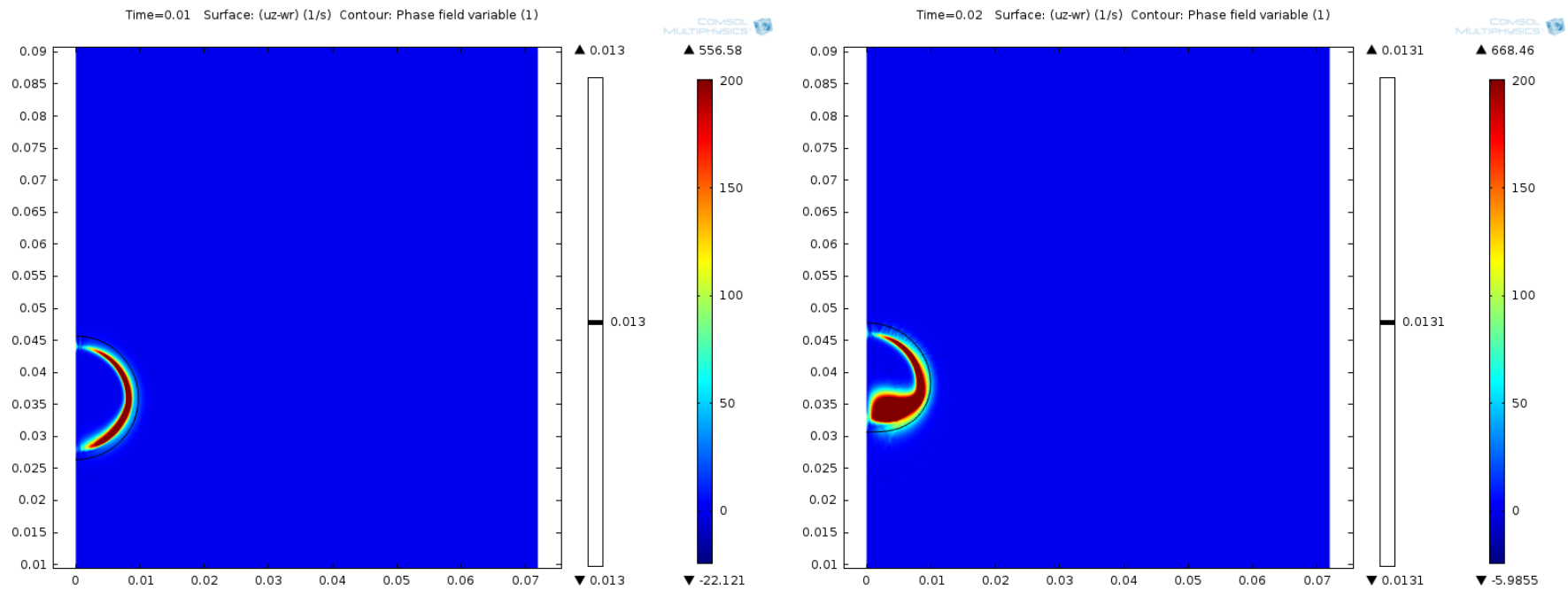


**Figure 4.10** The simulation of the generation and shedding of instantaneous vorticity from the free-surface of the interface as the air void rises through a column of water initially at rest. The initial shape of the air void is spherical and of diameter 20 mm.

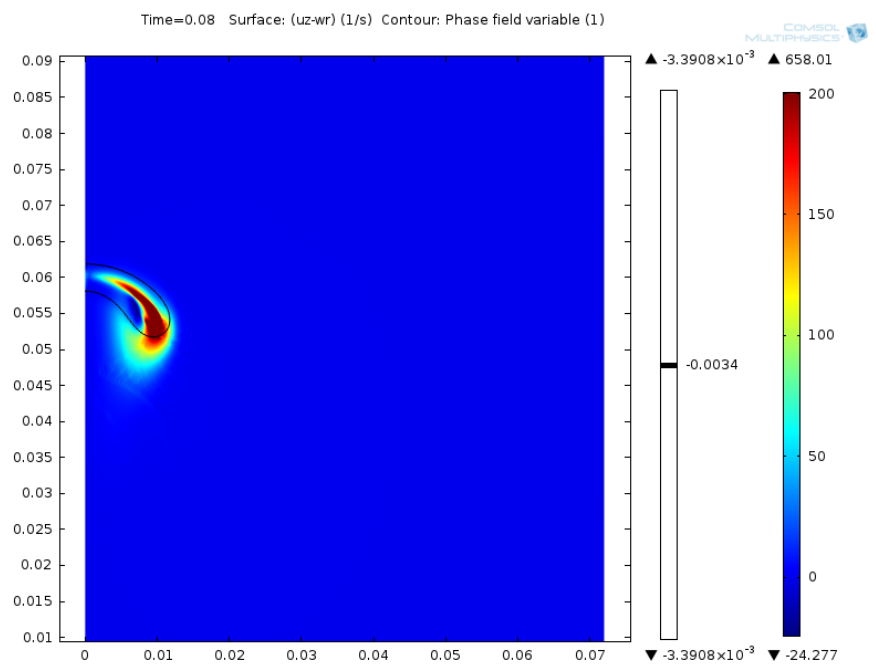
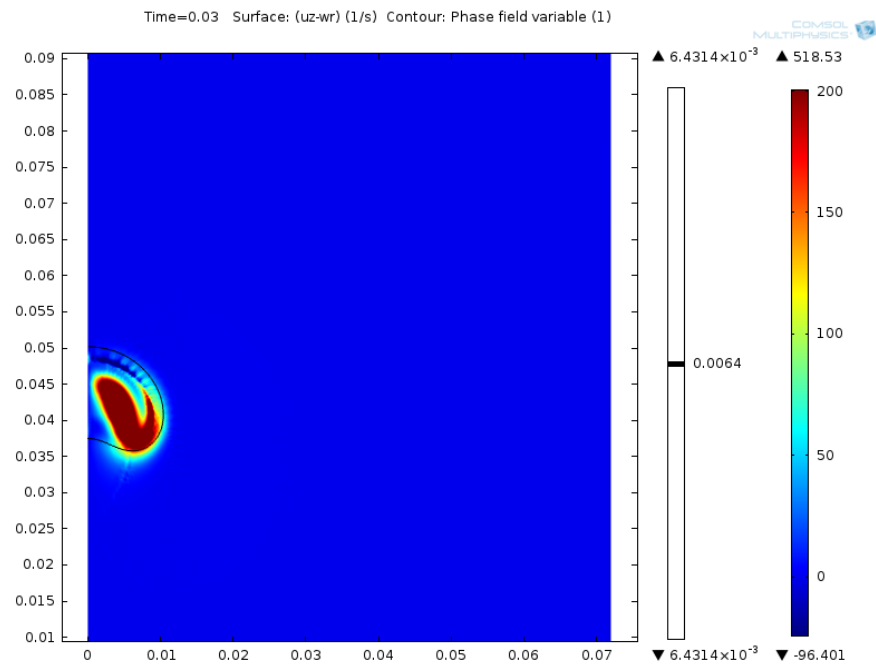


**Figure 4.10** Continued.

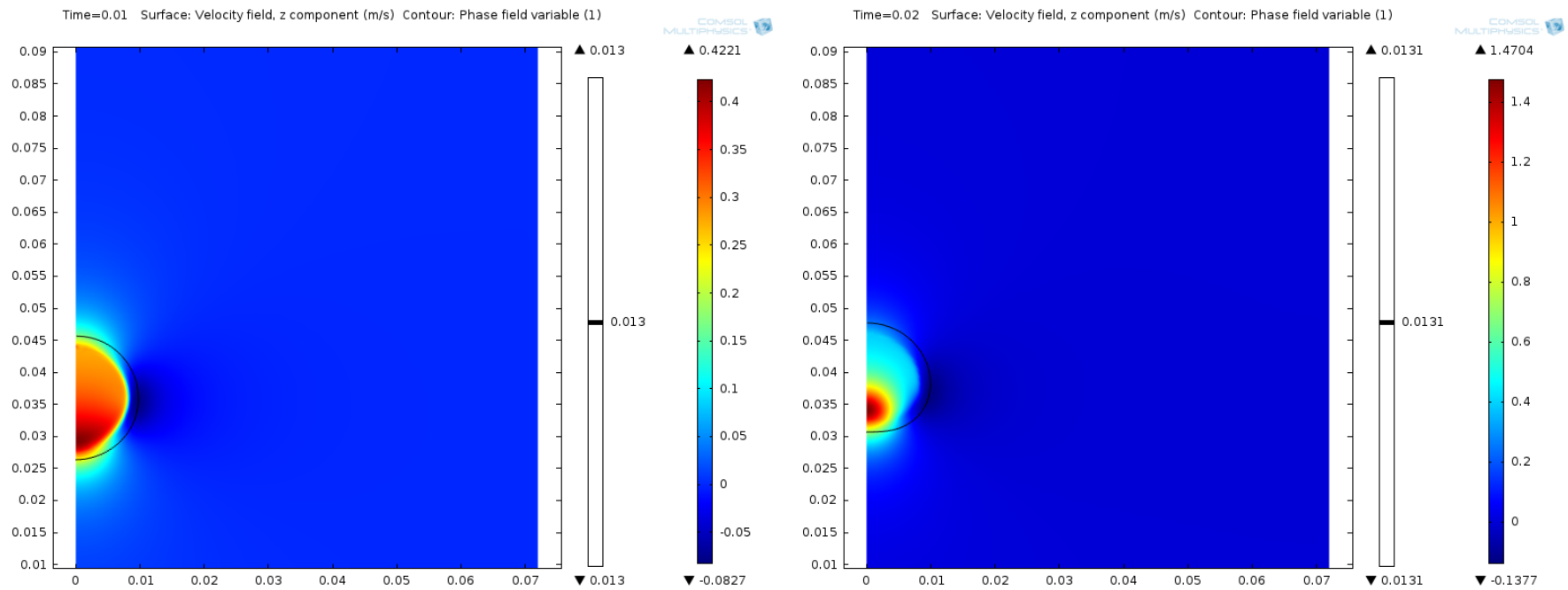


**Figure 4.11** The simulation of axial velocity of the air void and within the surrounding water as the void rises through a column of water initially at rest. The initial shape of the air void is spherical and of diameter 20 mm.

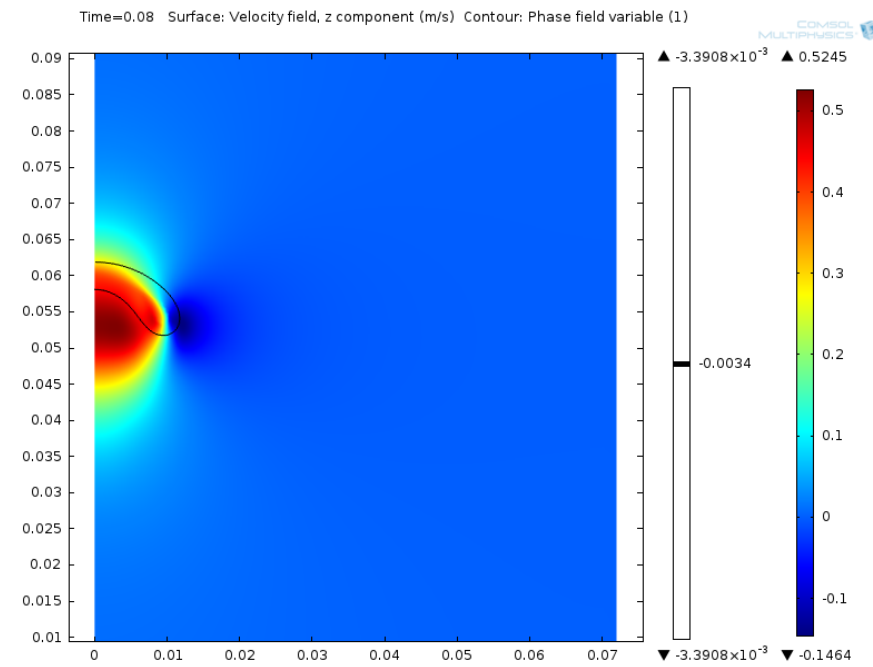
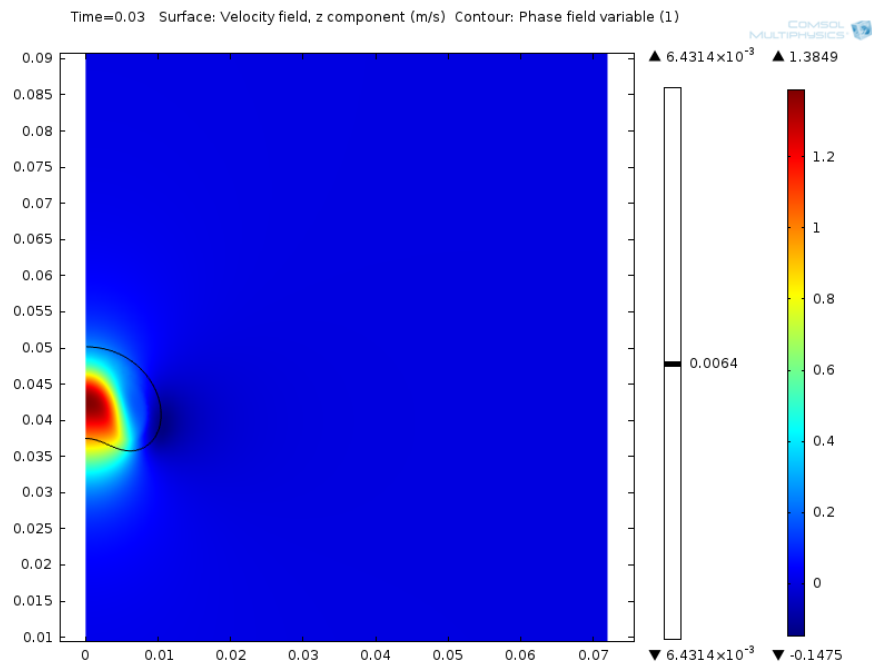
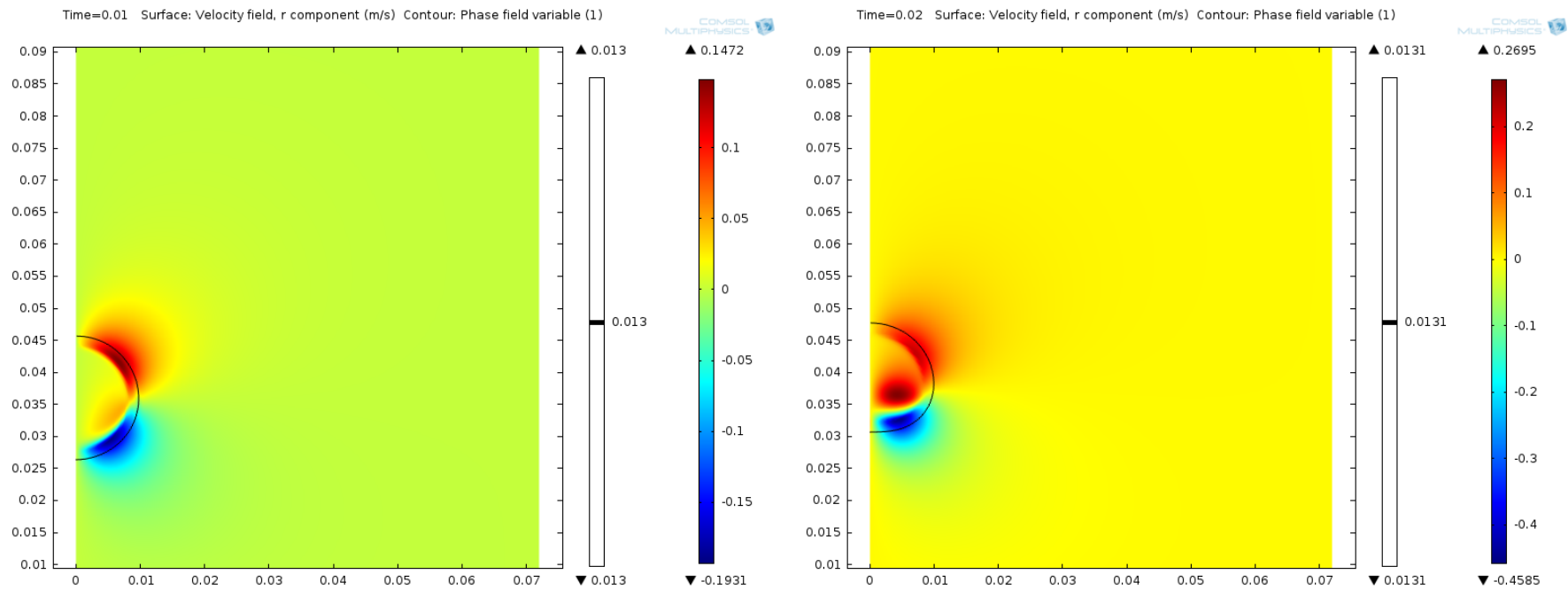
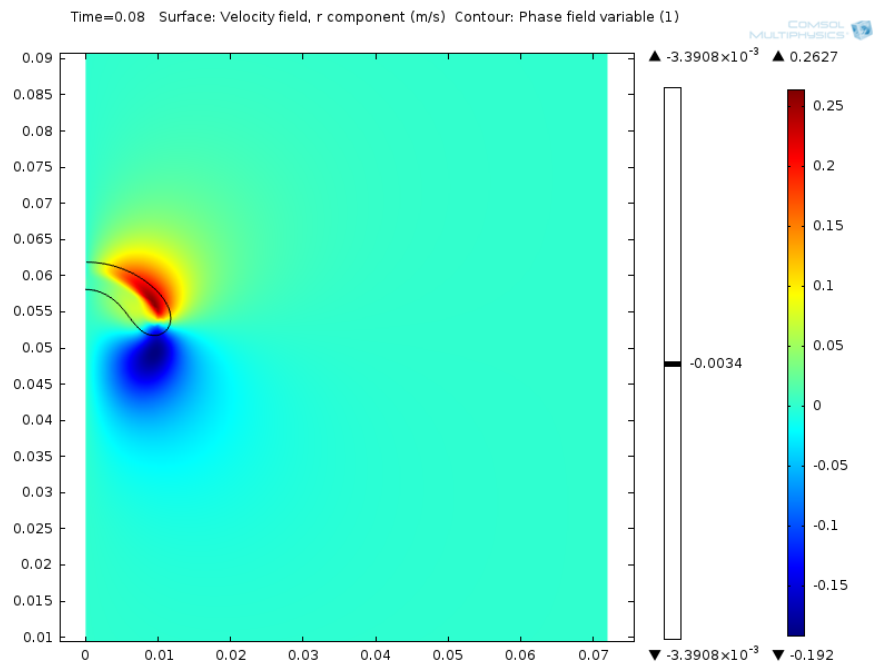
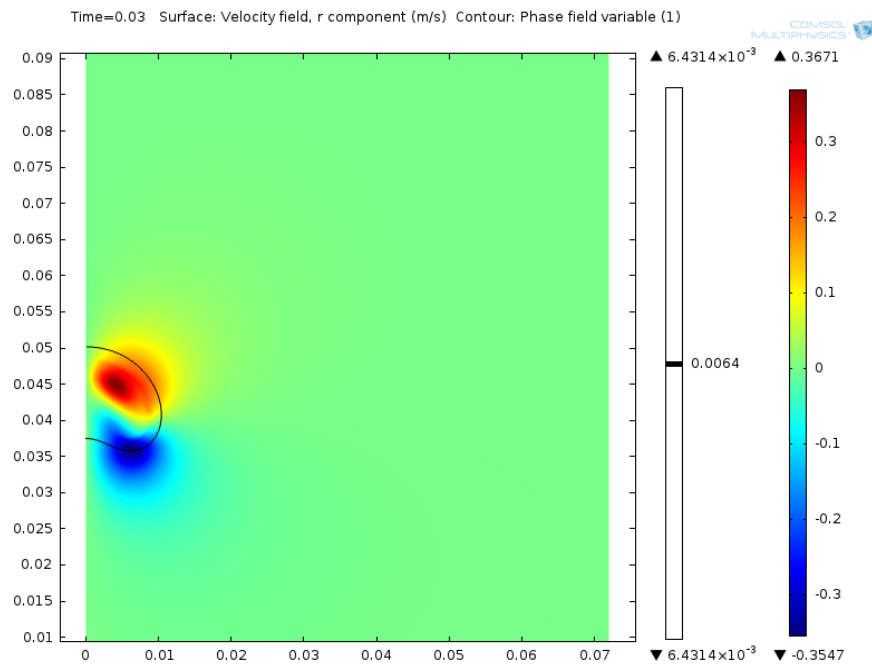


Figure 4.11 Continued.



**Figure 4.12** The simulation of radial velocity of the air void and within the surrounding water as the void rises through a column of water initially at rest. The initial shape of the air void is spherical and of diameter 20 mm.





**Figure 4.12** Continued.

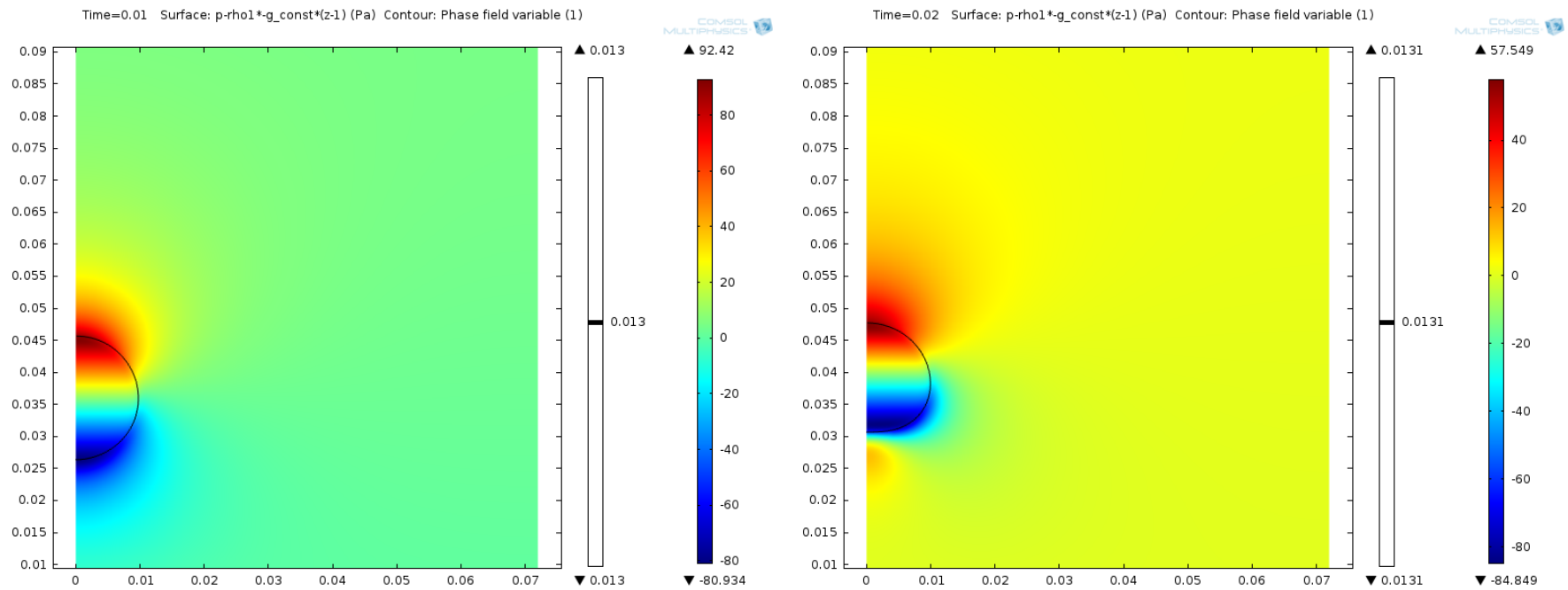


**Figure 4.13** The simulation of dynamic pressure within the air void and surrounding water as the void rises through a column of water initially at rest. The initial shape of the air void is spherical and of diameter 20 mm.

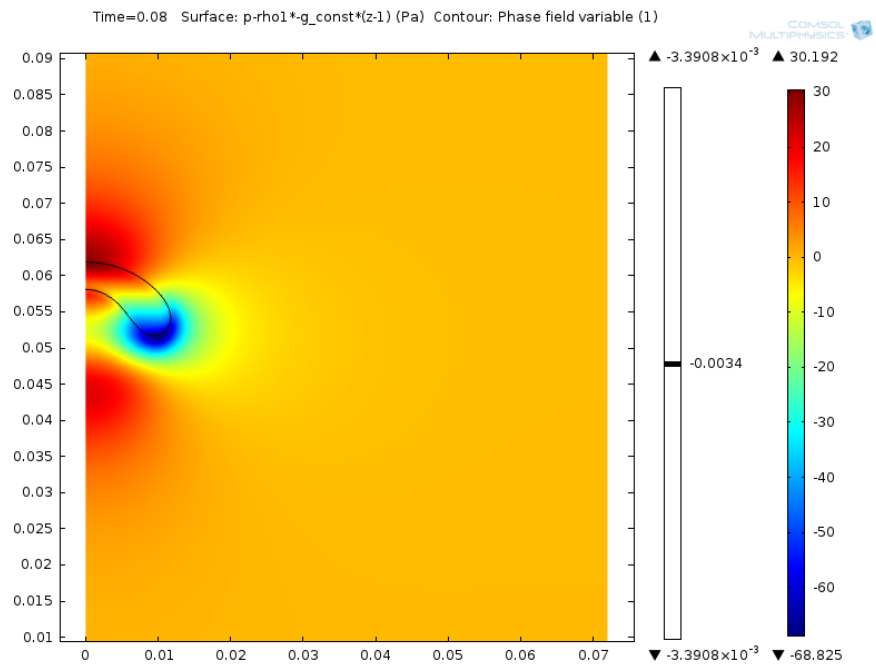
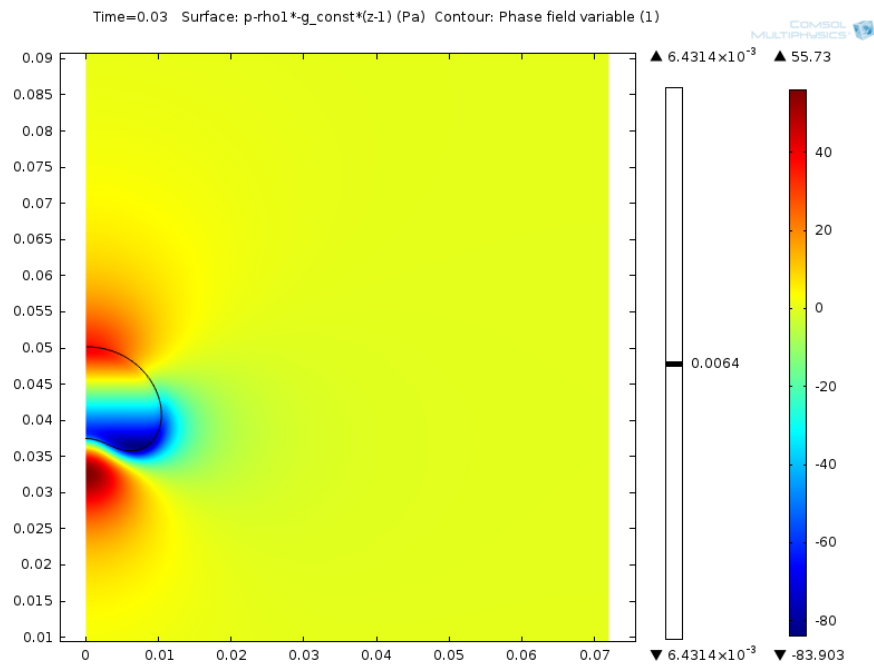


**Figure 4.13** Continued.



**Figure 4.14** A photograph of heterogeneous flow within the air-water-swarf column prior to PEPT experiments.



**Figure 4.15** A photograph of the static swarf bed within the air-water-swarf column prior to PEPT experiments.





**Figure 4.16** A photograph of the air-water-swarf column positioned between the PEPT camera heads. The perforated plate protrudes 50 mm into the field of view and the flow is monitored over a height of 400 mm.

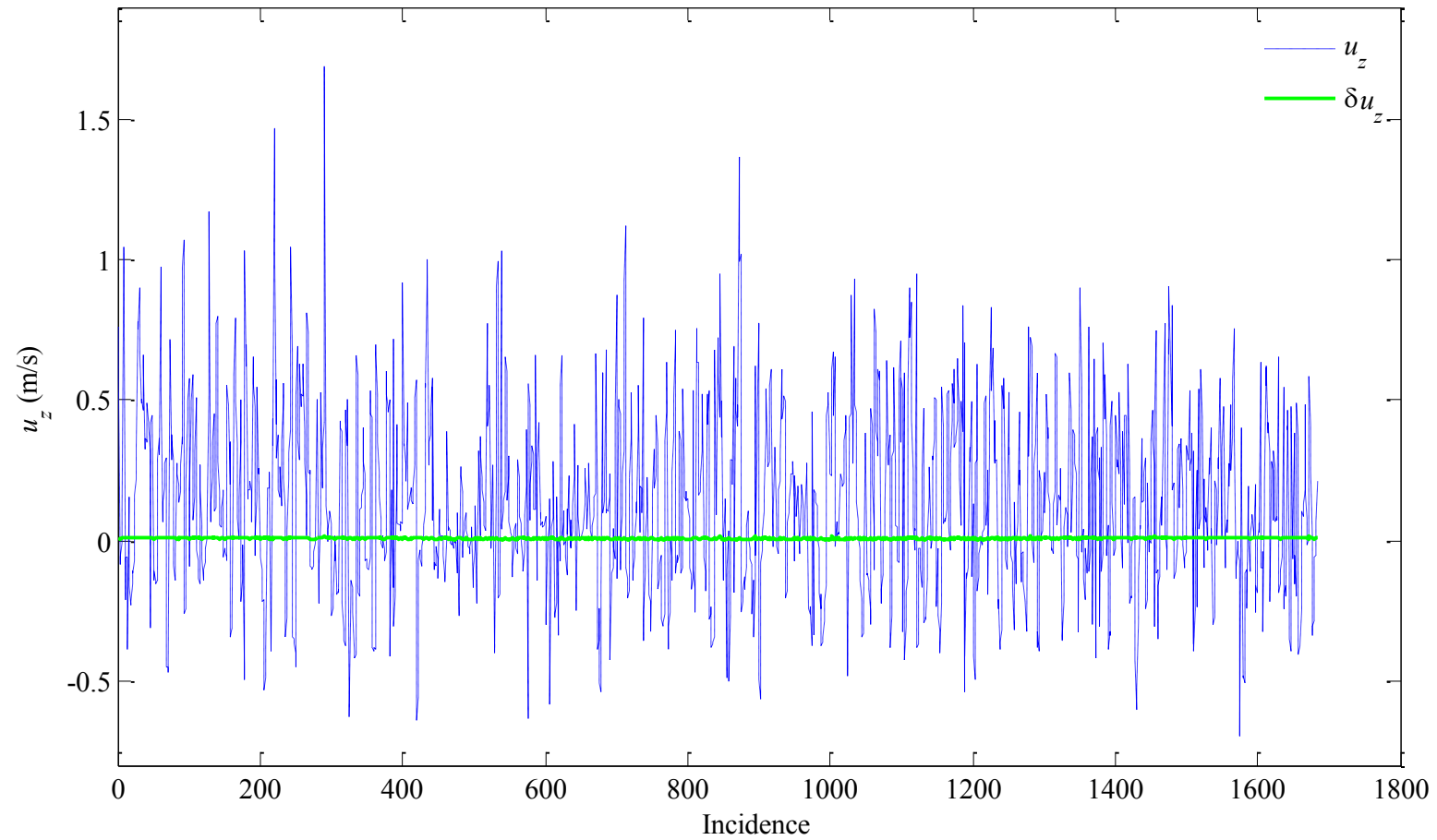


**Figure 4.17** Instantaneous axial velocity spectra for PEPT experiment 3 in grid segment 2,5 ( $r = 2.16$  cm,  $z = 11$  cm); superficial air velocity 7.2 cm/s. Axial velocity calculated using equation (4.49) from the trajectory of a 500 micron particle tracer sampled at  $\sim 50$  Hz over a duration of 120 minutes.

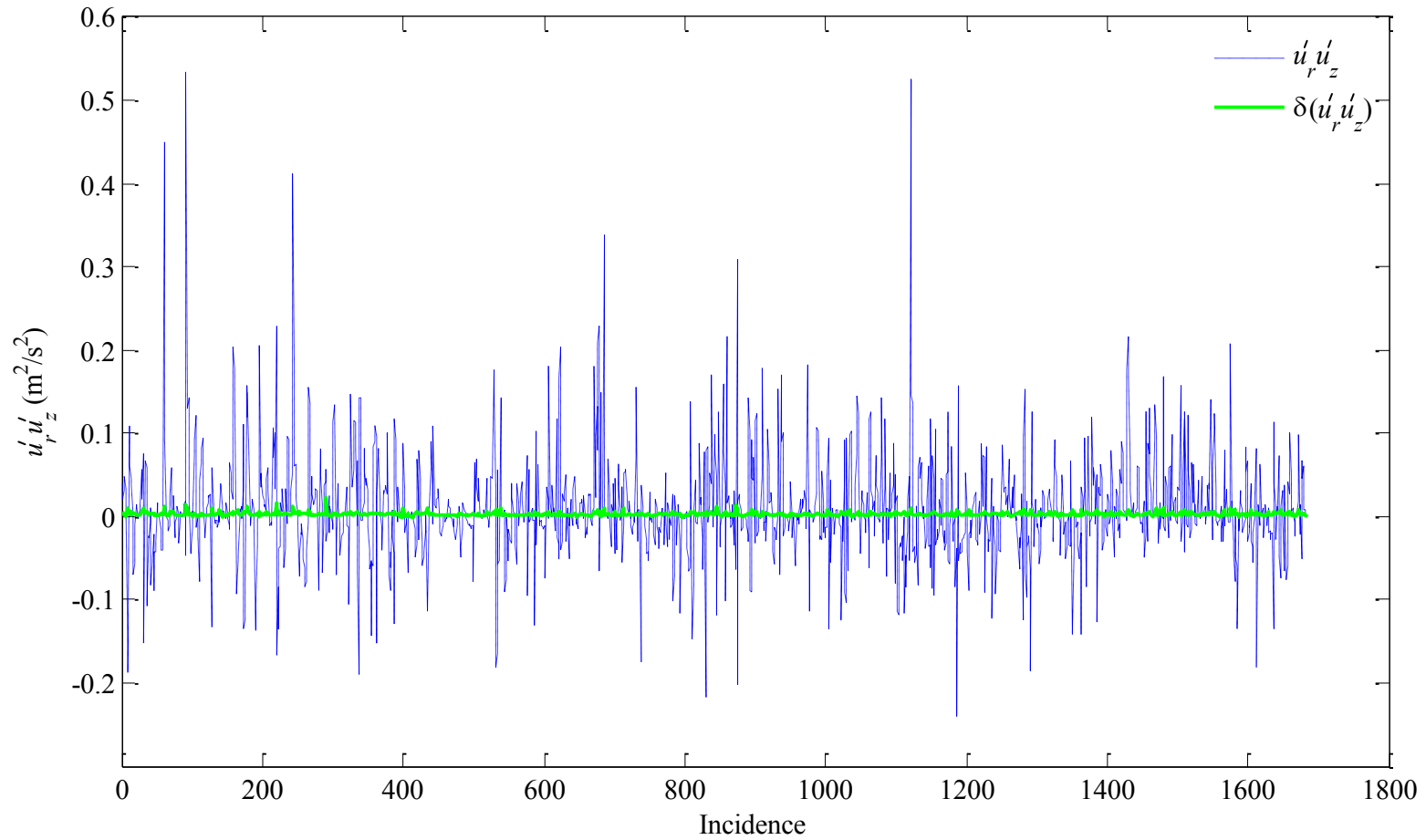


**Figure 4.18** Instantaneous Reynolds shear stress spectra for PEPT experiment 3 in grid segment 2,5 ( $r = 2.16$  cm,  $z = 11$  cm); superficial air velocity 7.2 cm/s. Instantaneous velocities calculated using equation (4.49) from the trajectory of a 500 micron particle tracer sampled at  $\sim 50$  Hz over a duration of 120 minutes.



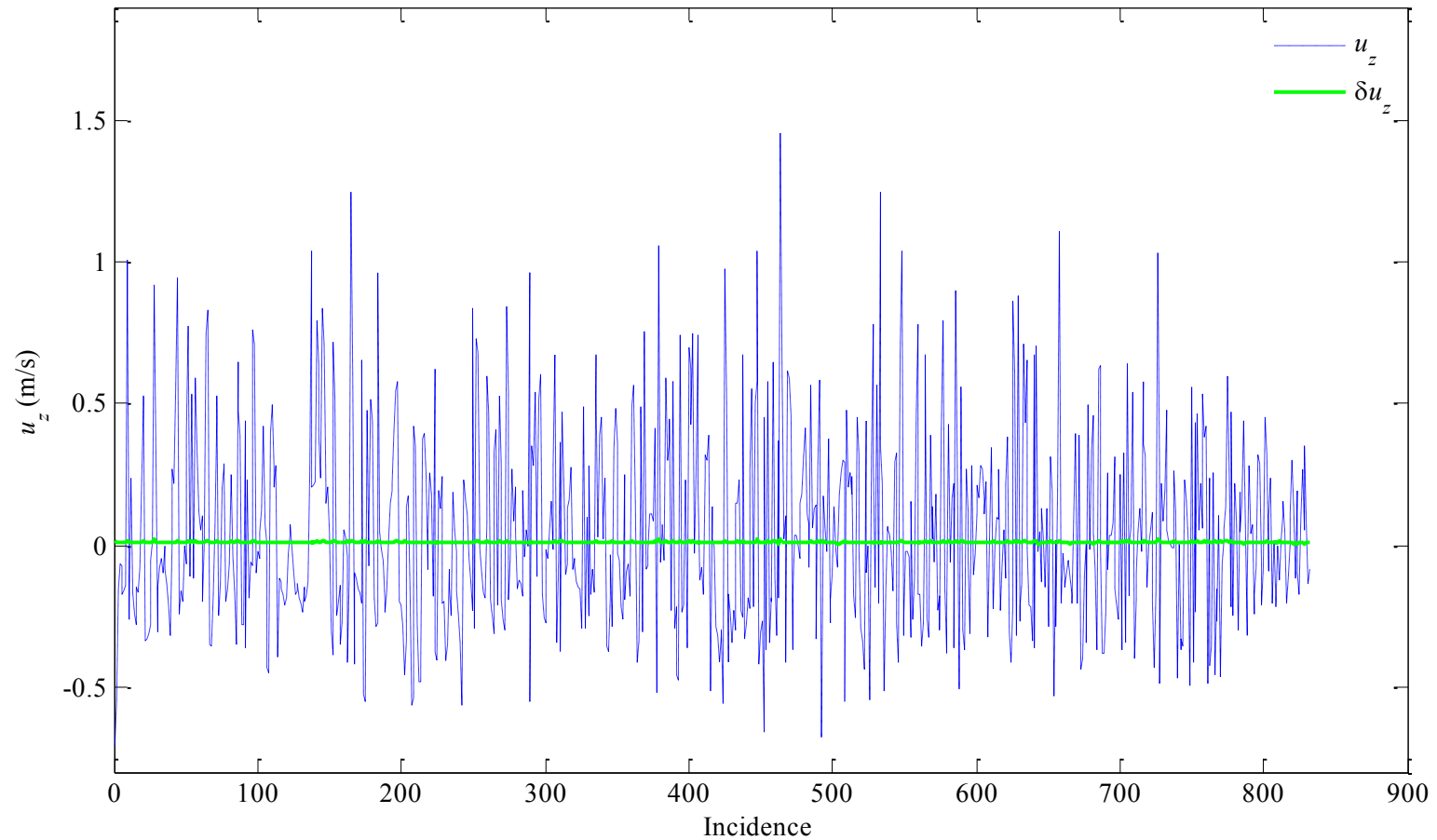


**Figure 4.19** Instantaneous axial velocity spectra for PEPT experiment 4 in grid segment 3,7 ( $r = 3.6$  cm,  $z = 15$  cm); superficial air velocity 7.2 cm/s, 500 g of loose swarf. Axial velocity calculated using equation (4.49) from the trajectory of a 500 micron particle tracer sampled at  $\sim 50$  Hz over a duration of 120 minutes.

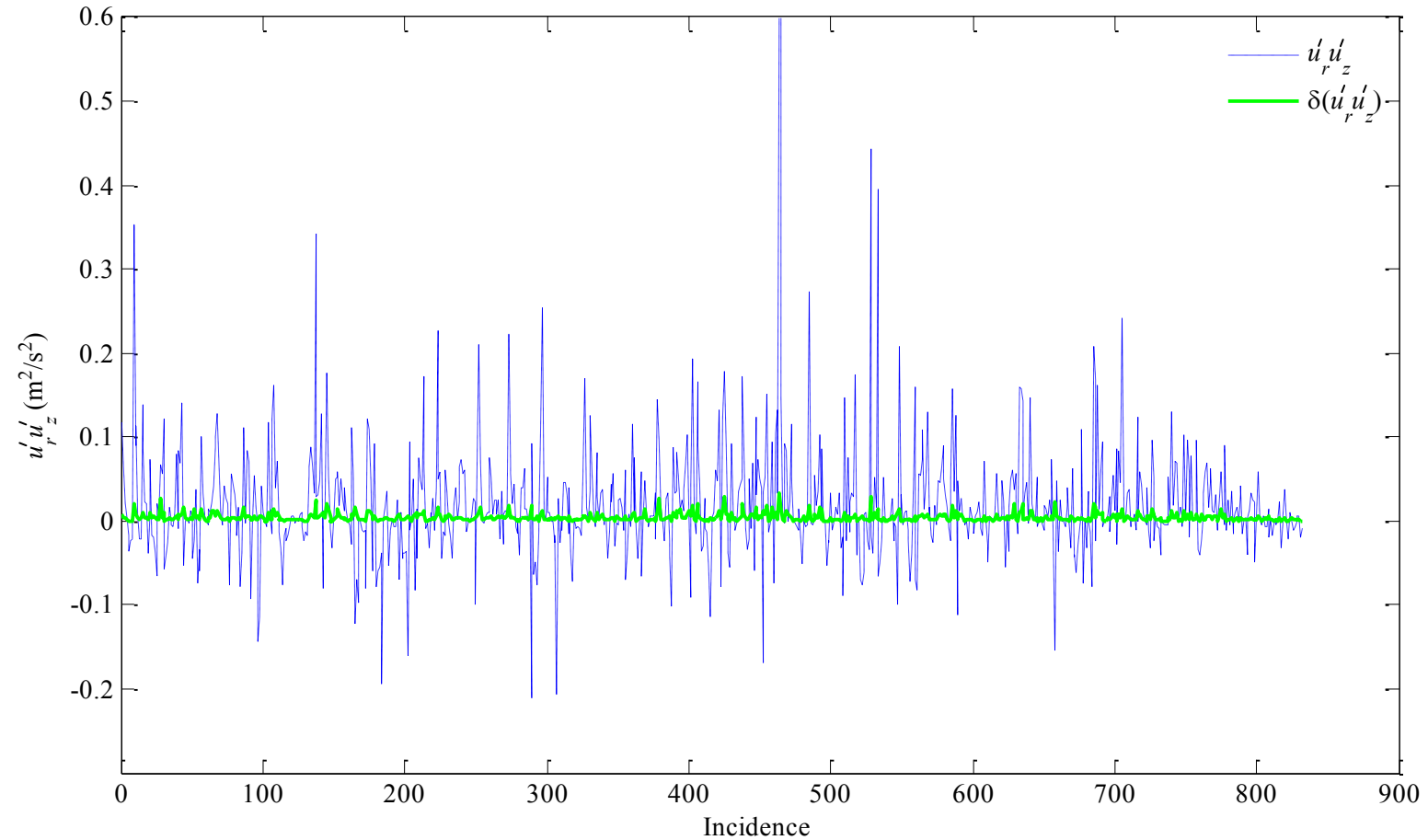


**Figure 4.20** Instantaneous Reynolds shear stress spectra for PEPT experiment 4 in grid segment 3,7 ( $r = 3.6$  cm,  $z = 15$  cm); superficial air velocity 7.2 cm/s, 500 g of loose swarf. Instantaneous velocities calculated using equation (4.49) from the trajectory of a 500 micron particle tracer sampled at  $\sim 50$  Hz over a duration of 120 minutes.

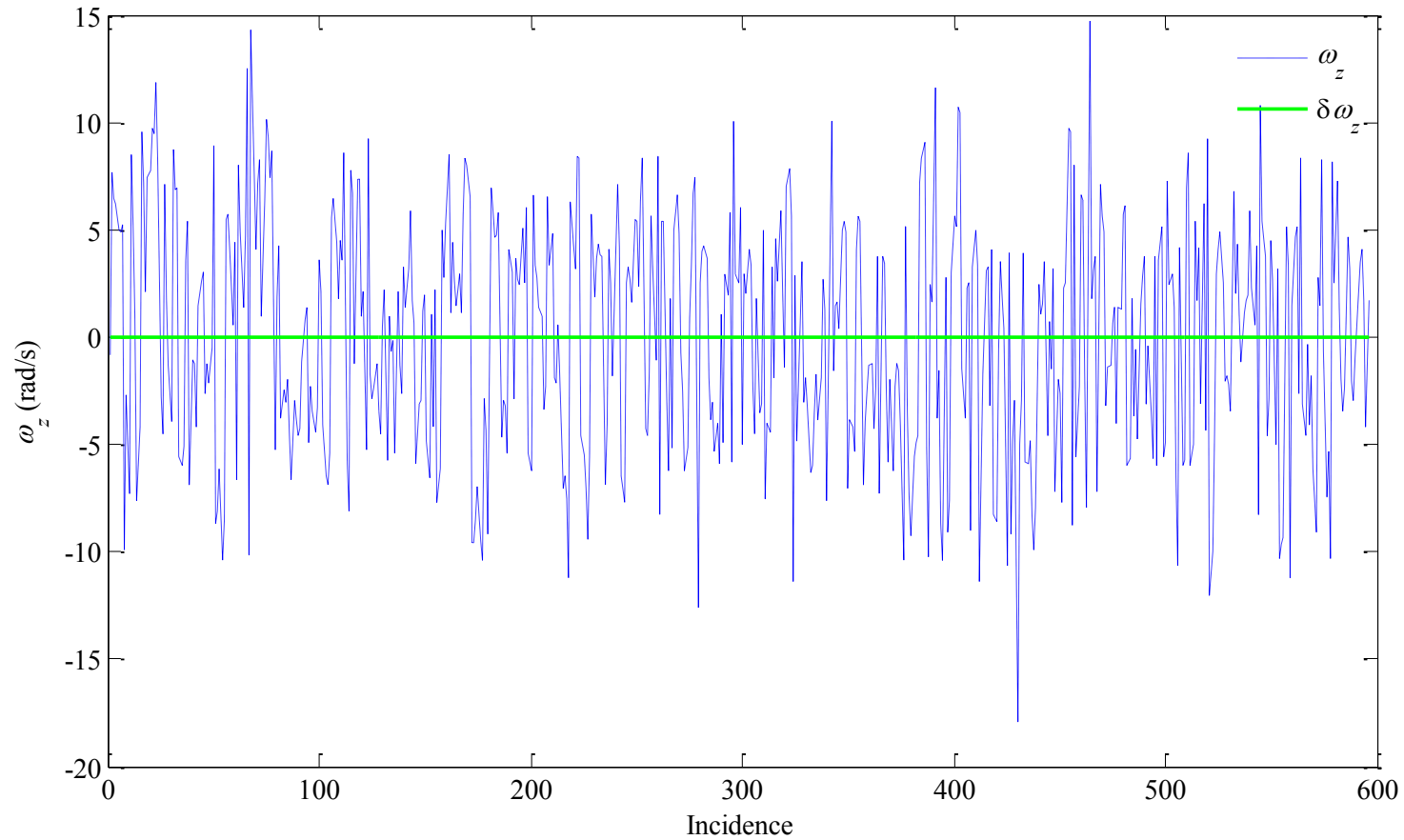


**Figure 4.21** Instantaneous angular velocity (axial) spectra for PEPT experiment 4 in grid segment 3,7 ( $r = 3.6$  cm,  $z = 15$  cm); superficial air velocity 7.2 cm/s, 500 g of loose swarf. Angular velocity calculated using equation (4.49) from the trajectory of a 500 micron particle tracer sampled at 50 Hz over a duration of 120 minutes.

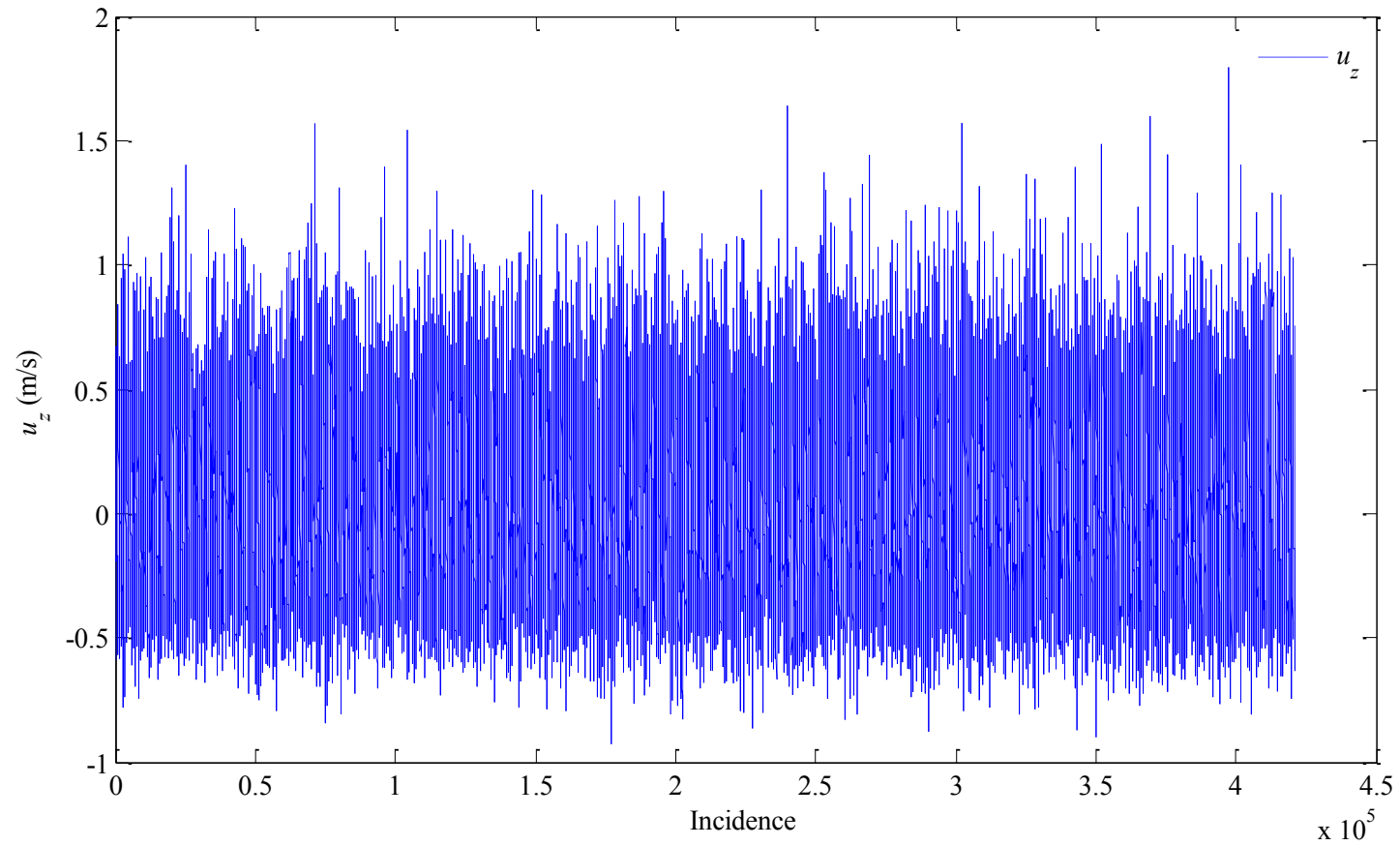


**Figure 4.22** Global instantaneous axial velocity for PEPT experiment 1; superficial air velocity 4.1 cm/s. Axial velocity calculated using equation (4.49) from the trajectory of a 500 micron particle tracer sampled at  $\sim 50$  Hz over a duration of 120 minutes.

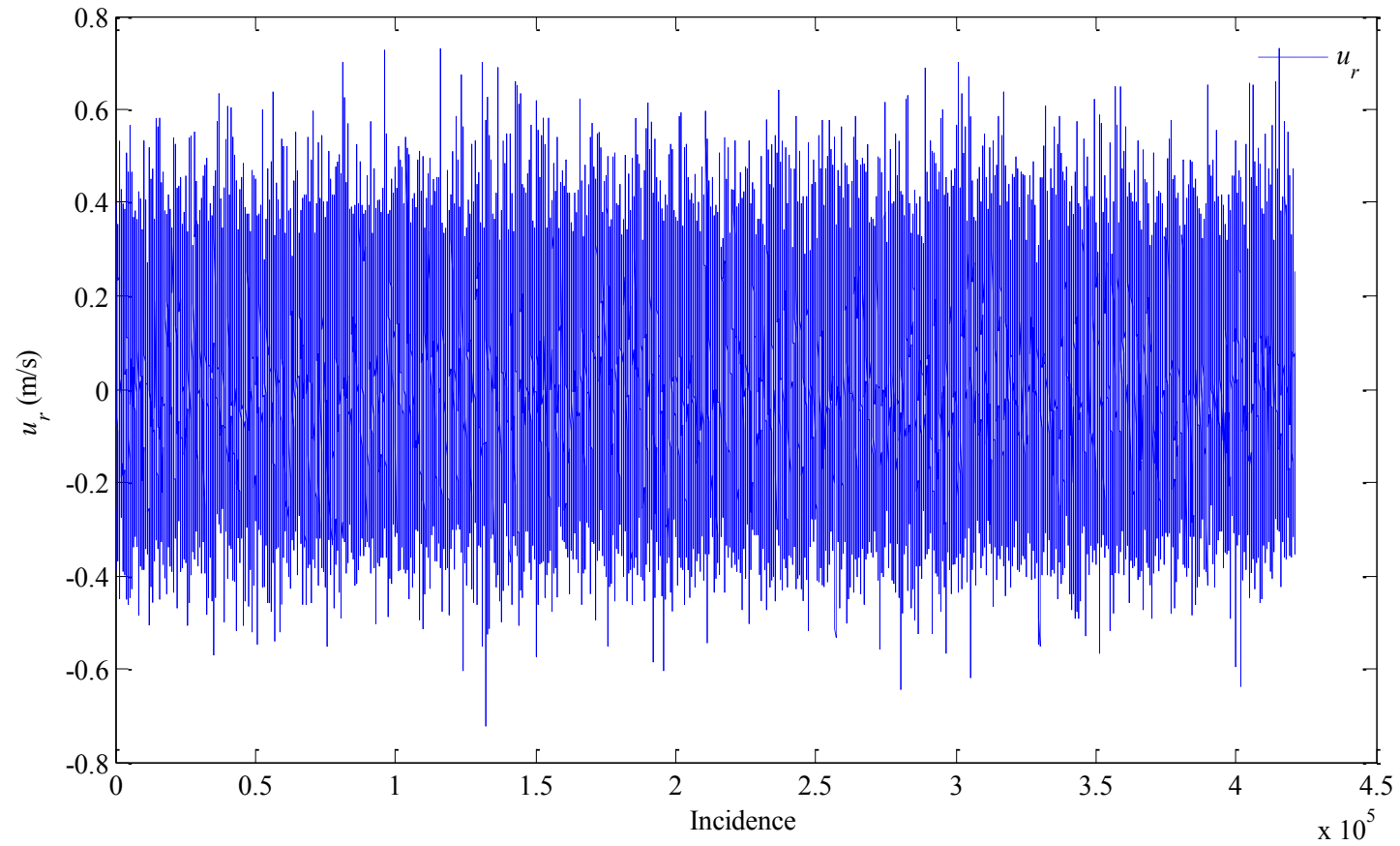


**Figure 4.23** Global instantaneous radial velocity for PEPT experiment 1; superficial air velocity 4.1 cm/s. Radial velocity calculated using equation (4.49) from the trajectory of a 500 micron particle tracer sampled at  $\sim 50$  Hz over a duration of 120 minutes.

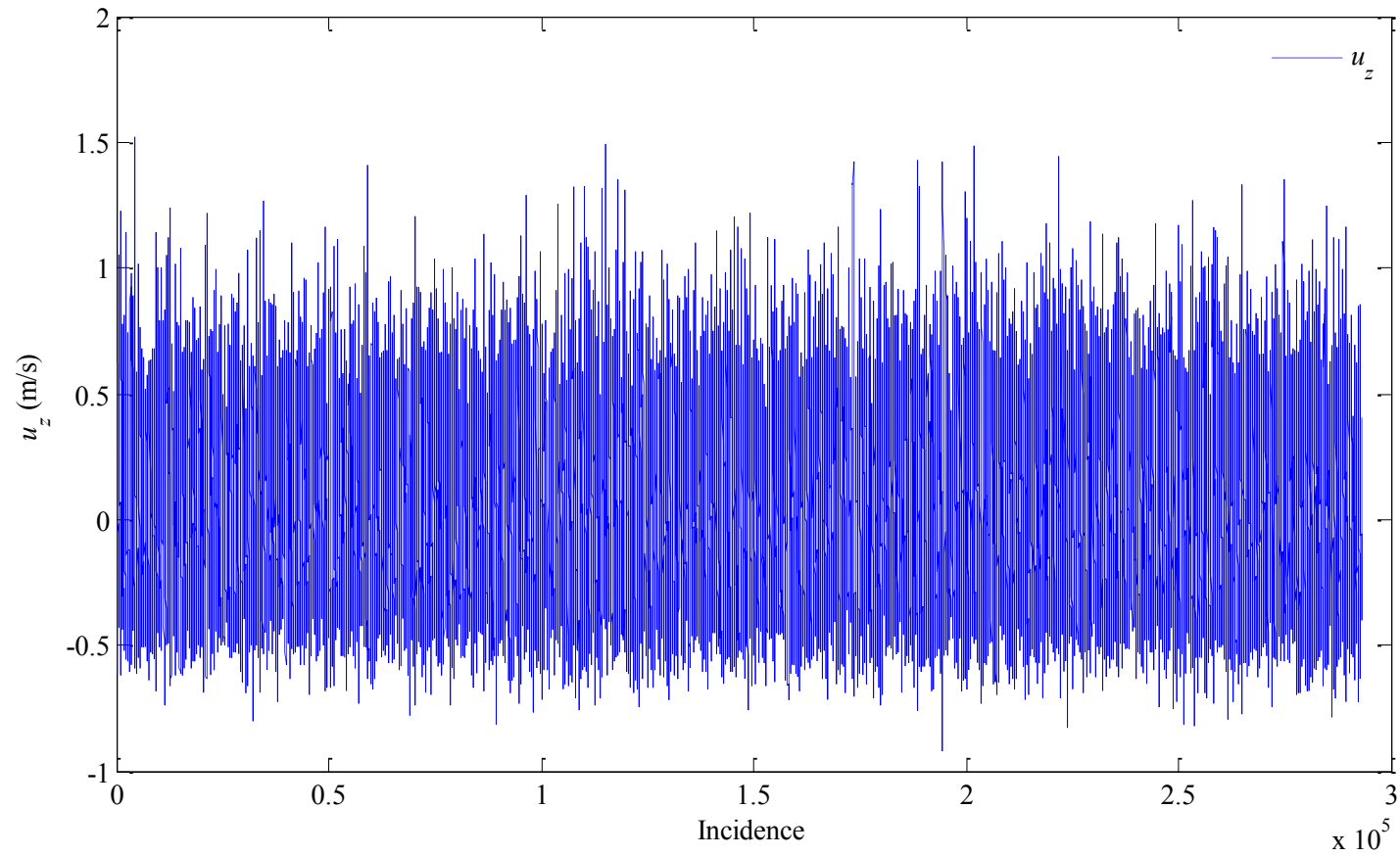


**Figure 4.24** Global instantaneous axial velocity for PEPT experiment 2; superficial air velocity 4.1 cm/s, 1 kg of dissolved sodium chloride. Axial velocity calculated using equation (4.49) from the trajectory of a 500 micron particle tracer sampled at  $\sim 50$  Hz over a duration of 120 minutes.

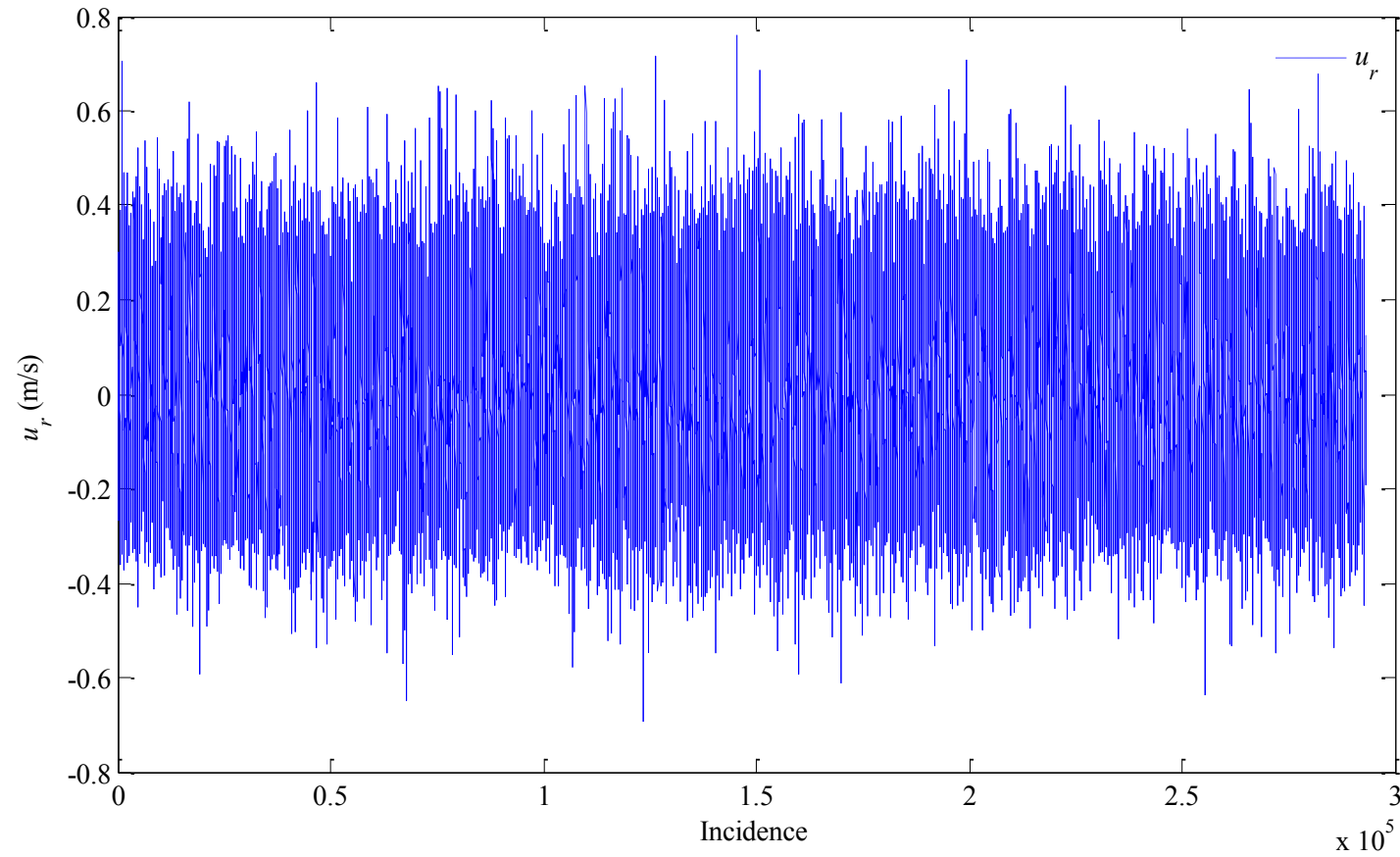


**Figure 4.25** Global instantaneous radial velocity for PEPT experiment 2; superficial air velocity 4.1 cm/s, 1 kg of dissolved sodium chloride. Radial velocity calculated using equation (4.49) from the trajectory of a 500 micron particle tracer sampled at  $\sim 50$  Hz over a duration of 120 minutes.

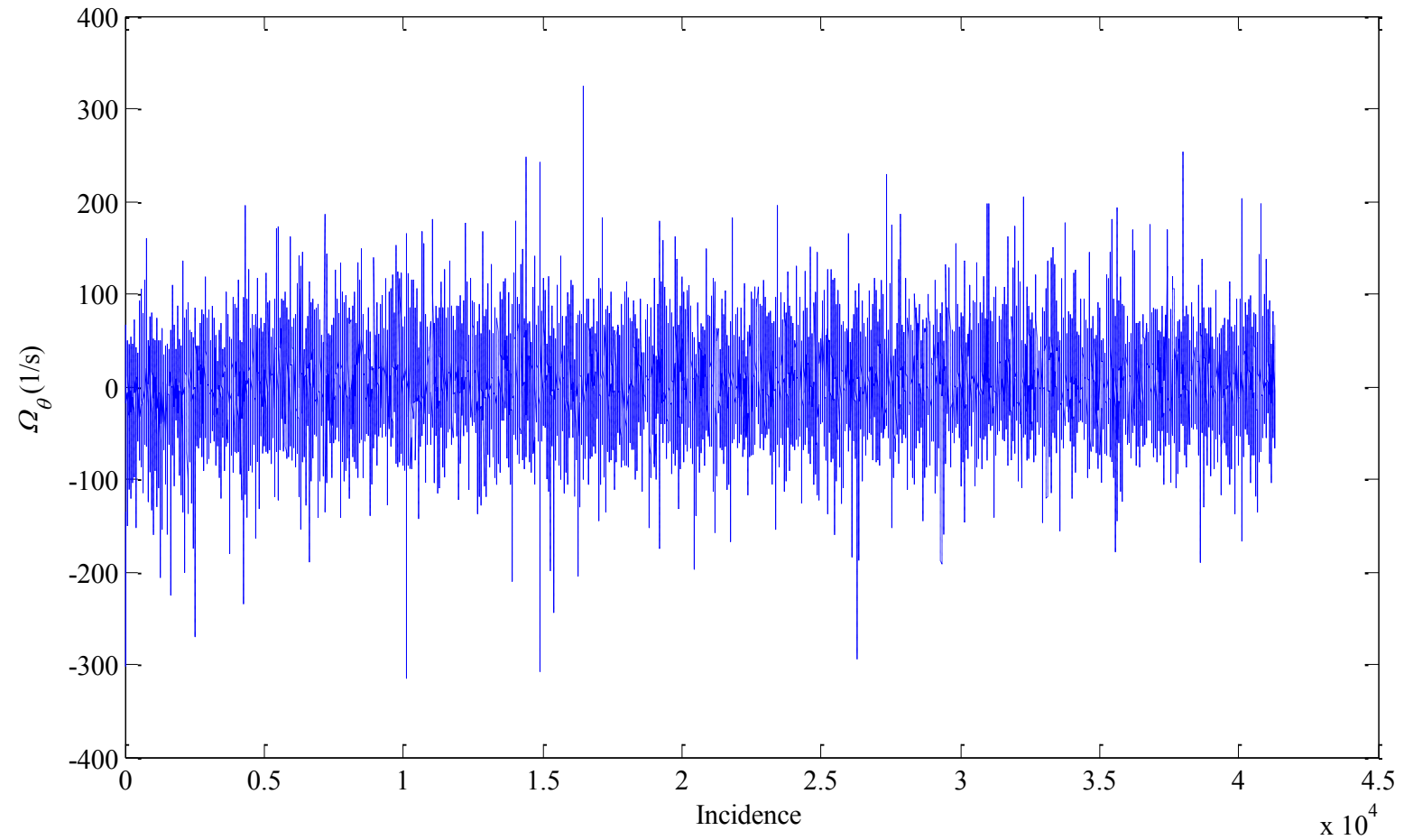


**Figure 4.26** Global instantaneous azimuthal vorticity spectra for PEPT experiment 1; superficial air velocity 4.1 cm/s. Azimuthal vorticity calculated using derivatives of asymmetric differencing as shown in equation (4.51) from the trajectory of a 500 micron particle tracer sampled at  $\sim 50$  Hz over a duration of 120 minutes.



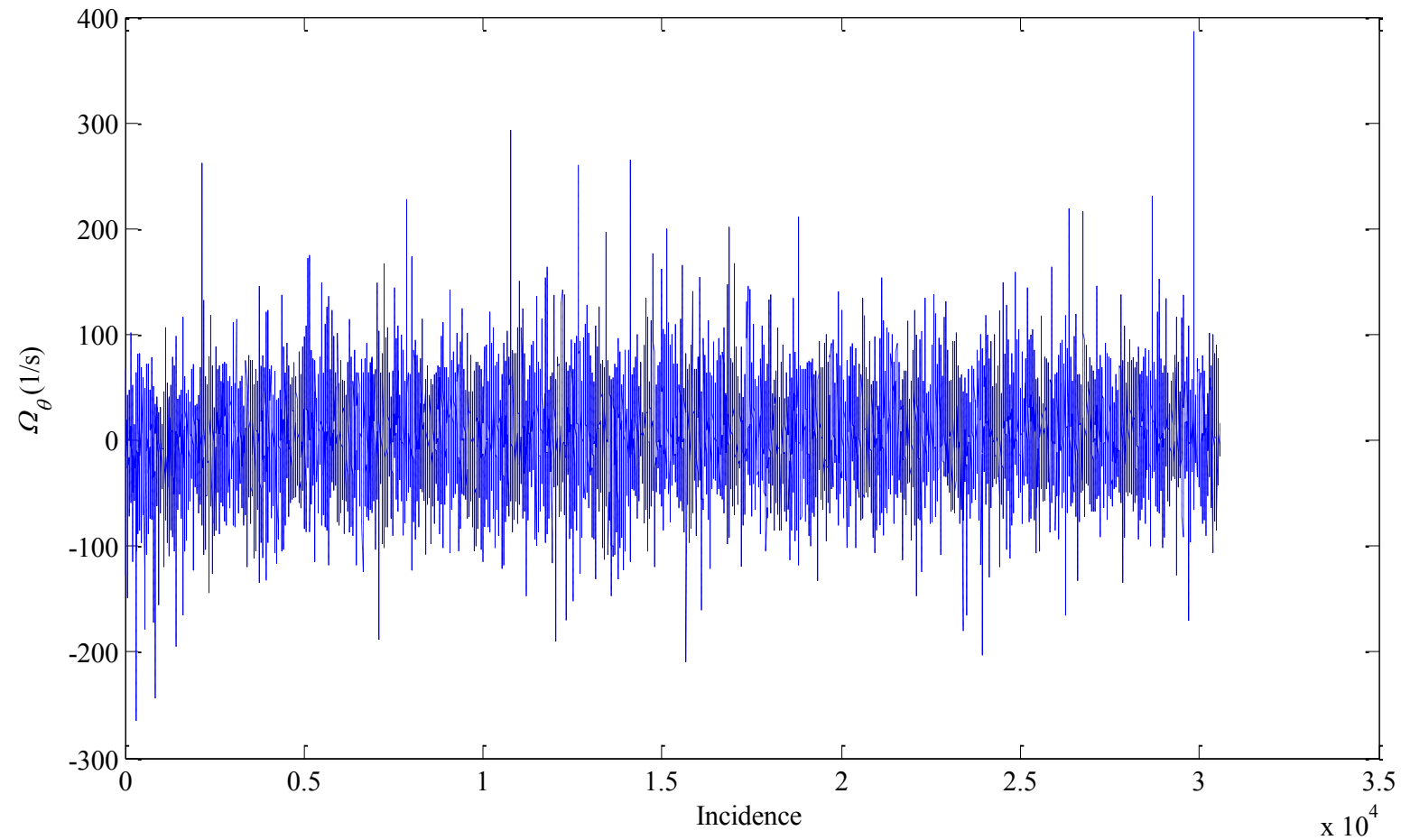


**Figure 4.27** Global instantaneous azimuthal vorticity spectra for PEPT experiment 2; superficial air velocity 4.1 cm/s, 1 kg of dissolved sodium chloride. Azimuthal vorticity calculated using derivatives of asymmetric differencing as shown in equation (4.51) from the trajectory of a 500 micron particle tracer sampled at ~50 Hz over a duration of 120 minutes.

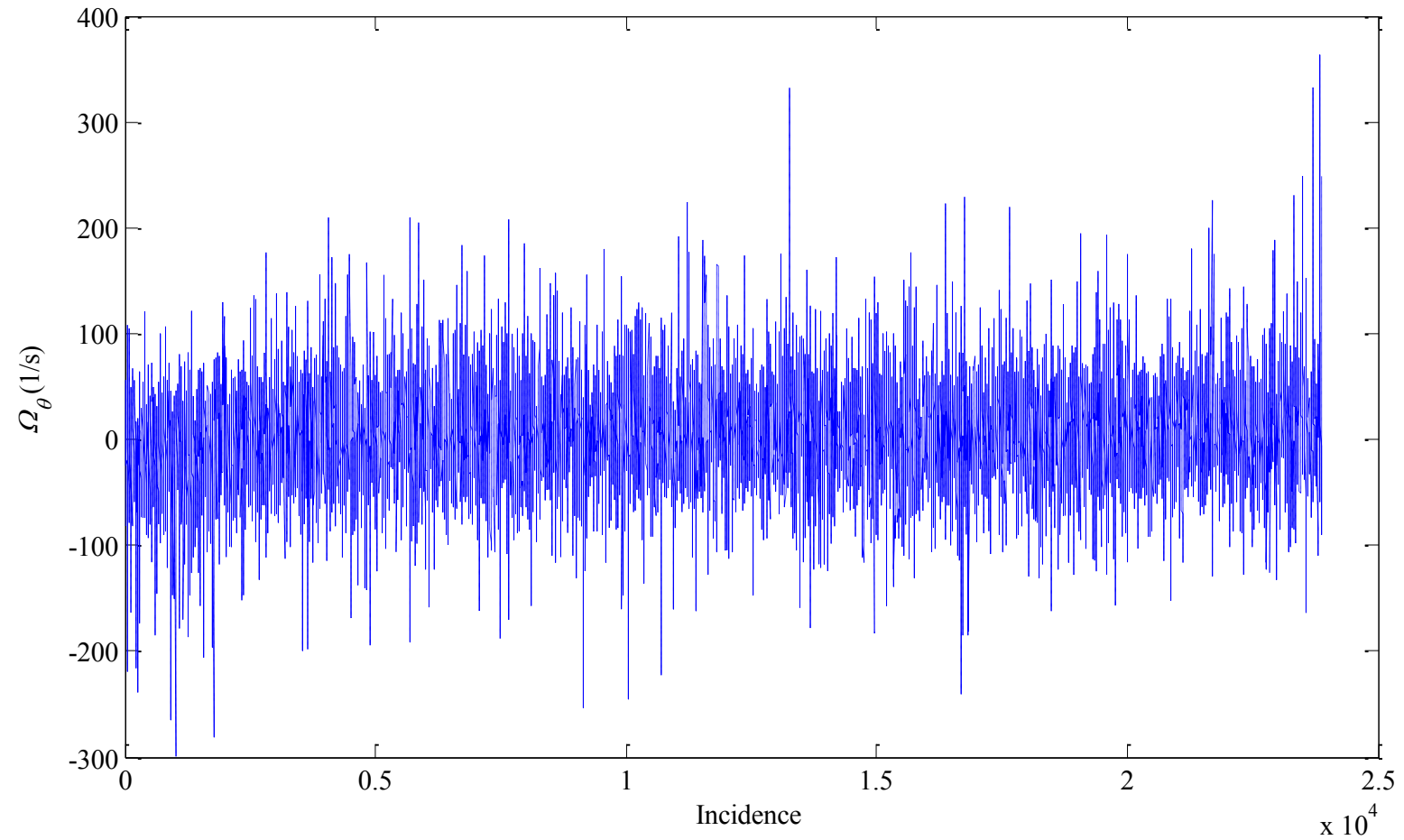


**Figure 4.28** Global instantaneous azimuthal vorticity spectra for experiment 3; superficial air velocity 7.2 cm/s. Azimuthal vorticity calculated using derivatives of asymmetric differencing as shown in equation (4.51) from the trajectory of a 500 micron particle tracer sampled at ~50 Hz over a duration of 120 minutes.

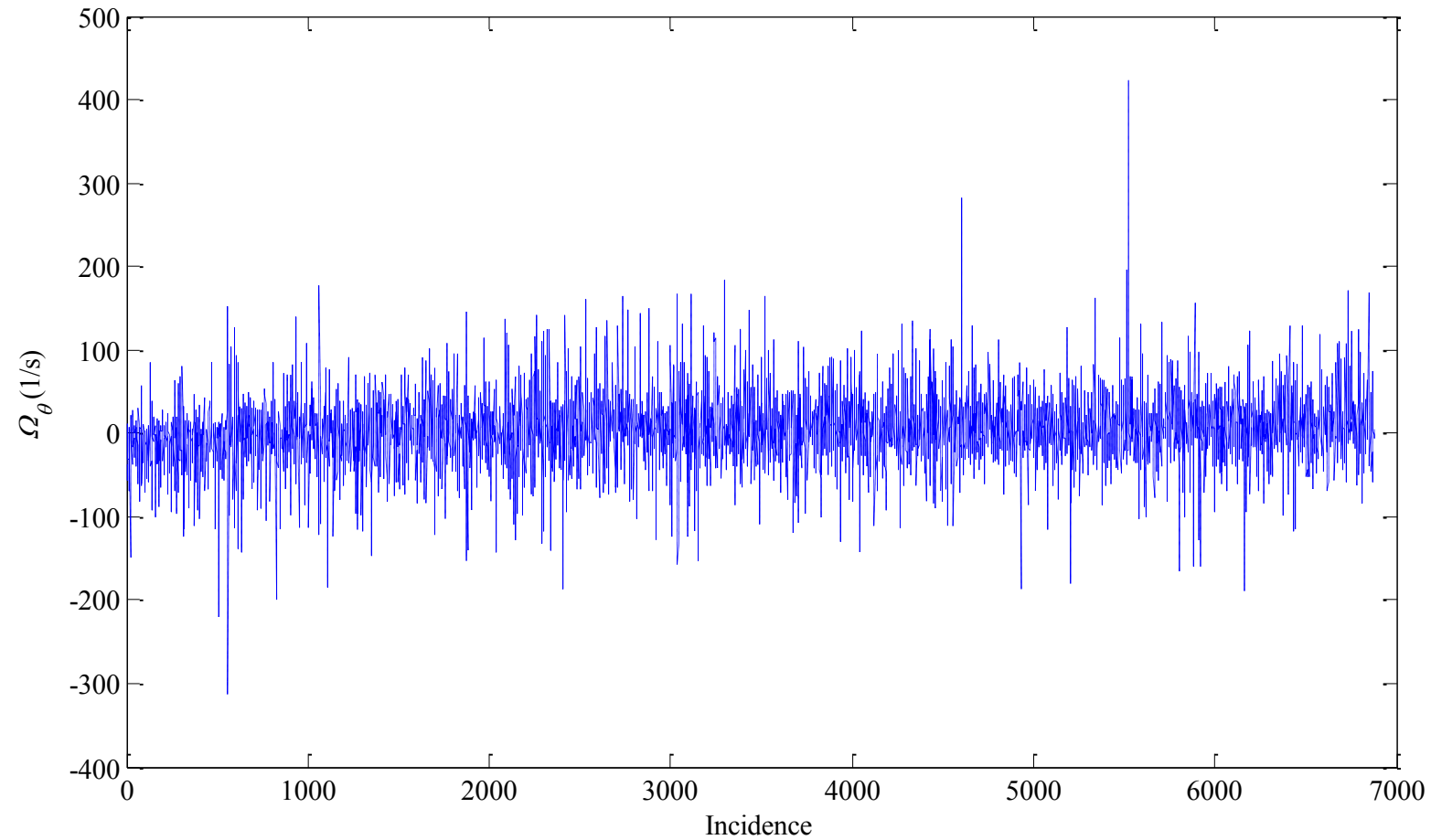


**Figure 4.29** Global instantaneous azimuthal vorticity spectra for experiment 4; superficial air velocity 7.2 cm/s, 500 g of loose swarf. Azimuthal vorticity calculated using derivatives of asymmetric differencing as shown in equation (4.51) from the trajectory of a 500 micron particle tracer sampled at ~50 Hz over a duration of 120 minutes.

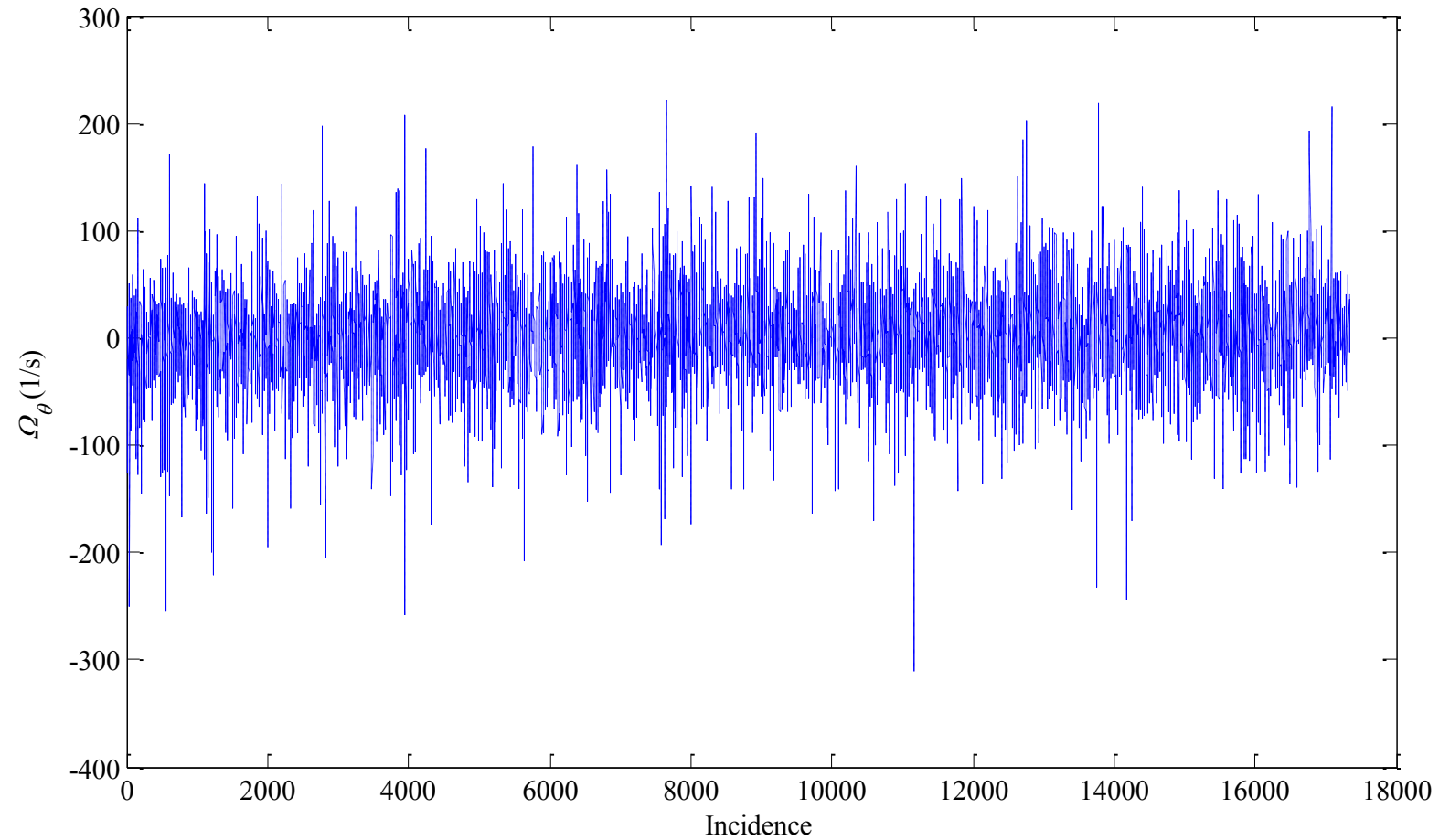


**Figure 4.30** Global instantaneous azimuthal vorticity spectra for experiment 6; superficial air velocity 4.1 cm/s, 1 kg of dissolved sodium chloride, 500 g of loose swarf. Azimuthal vorticity calculated using derivatives of asymmetric differencing as shown in equation (4.51) from the trajectory of a 500 micron particle tracer sampled at ~50 Hz over a duration of 200 minutes.

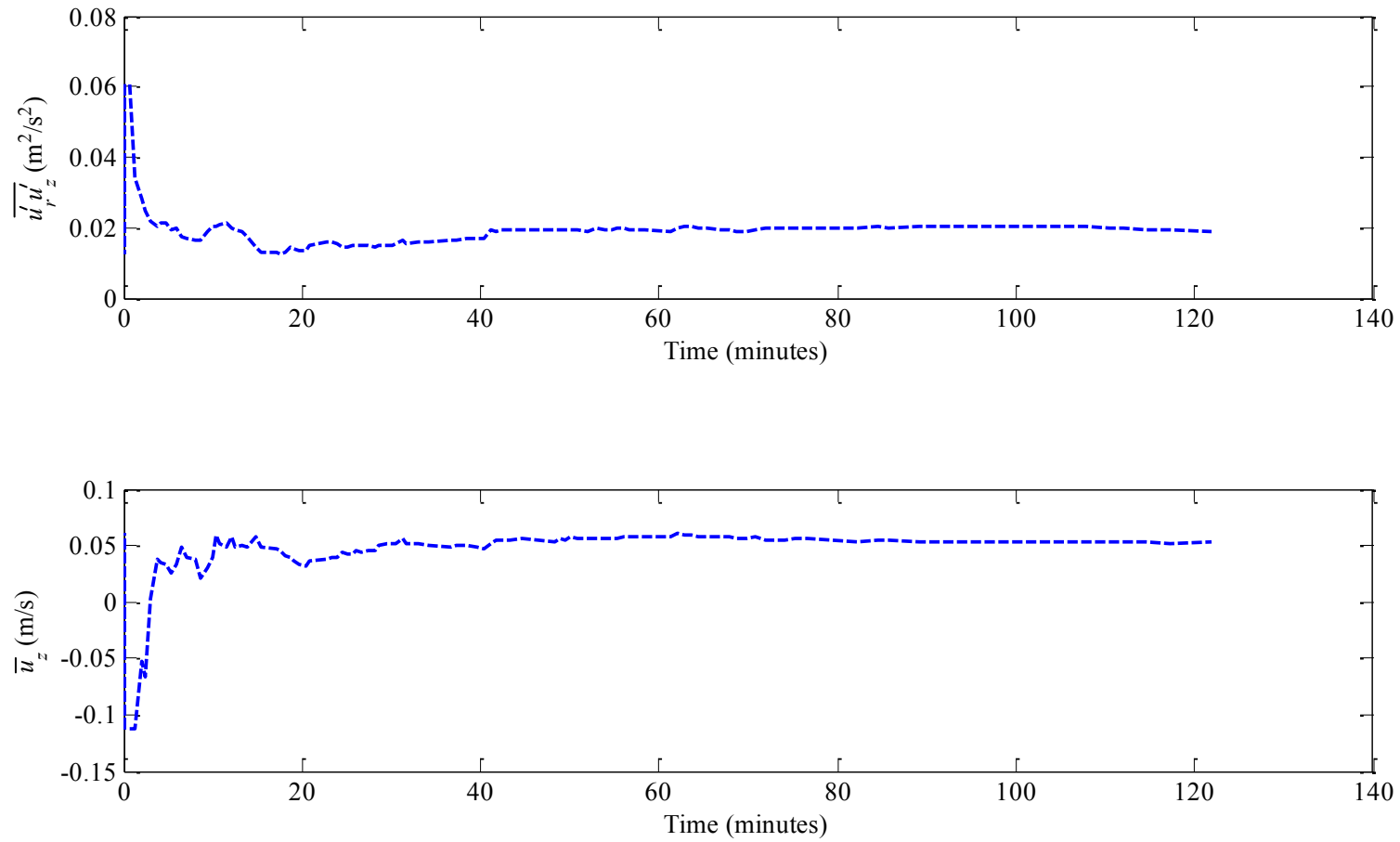


**Figure 4.31** Convergence of Reynolds shear stress and axial velocity towards their mean values for PEPT experiment 4 in grid segment 3,7 ( $r = 3.6$  cm,  $z = 15$  cm).

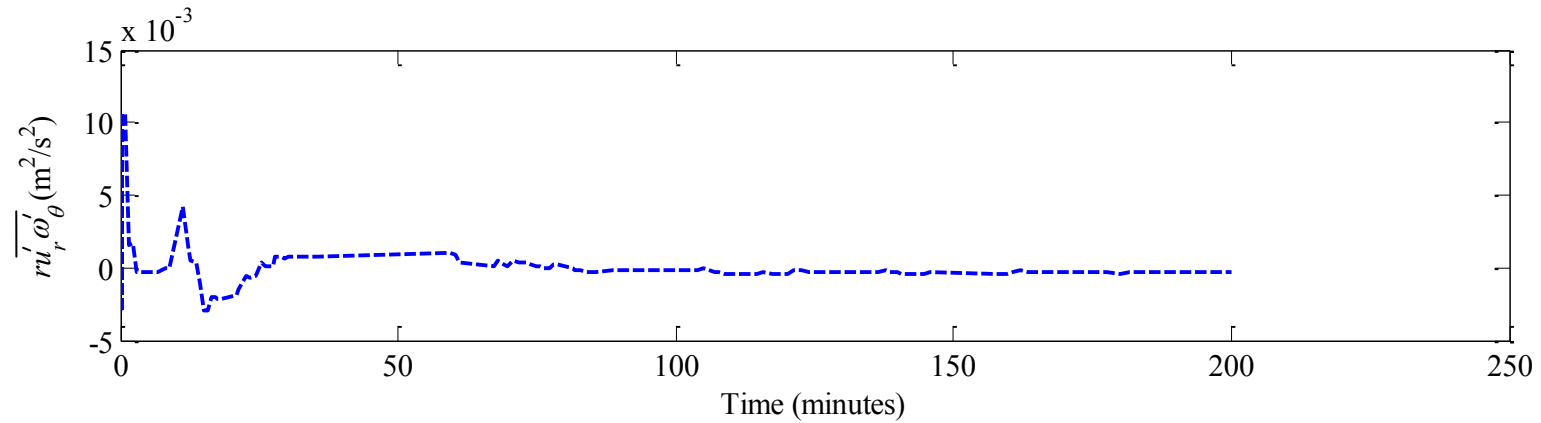


**Figure 4.32** Convergence of azimuthal tensor component for PEPT experiment 6 in grid segment 4,16 ( $r = 5.04$  cm,  $z = 33.0$  cm); superficial air velocity 4.1 cm/s, 1 kg of dissolved sodium chloride, 500 g of loose swarf. Instantaneous velocities calculated using equation (4.49) from the trajectory of a 500 micron particle tracer sampled at  $\sim 50$  Hz over a duration of 200 minutes.

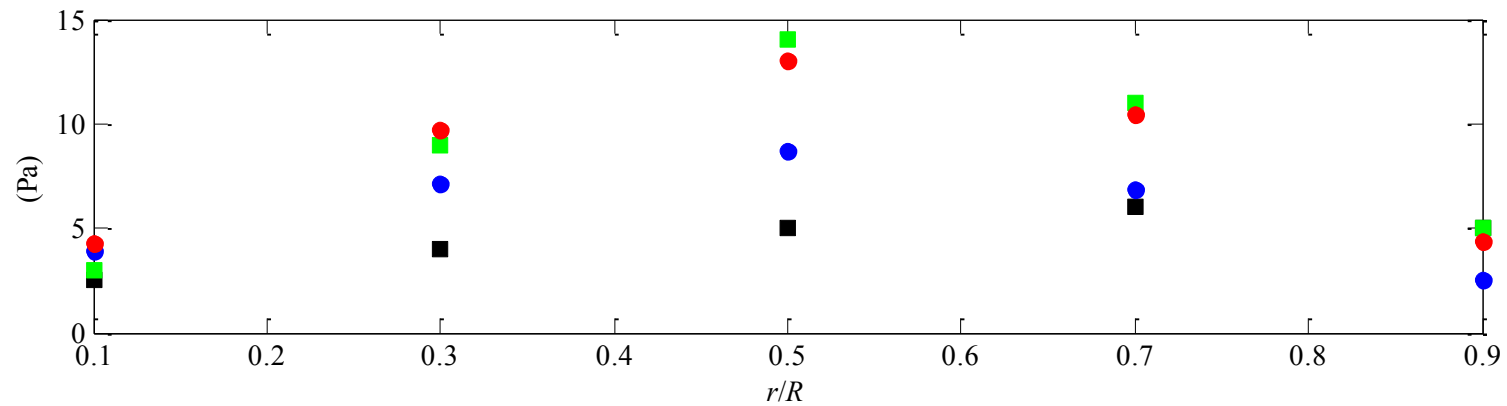


**Figure 4.33** Reynolds shear stress at different superficial air velocities: ■ = Menzel *et al.* 7.2 cm/s, ● = PEPT experiment 3 (7.2 cm/s), ■ = Menzel *et al.* 4.8 cm/s, ● = PEPT experiment 1 (4.1 cm/s).

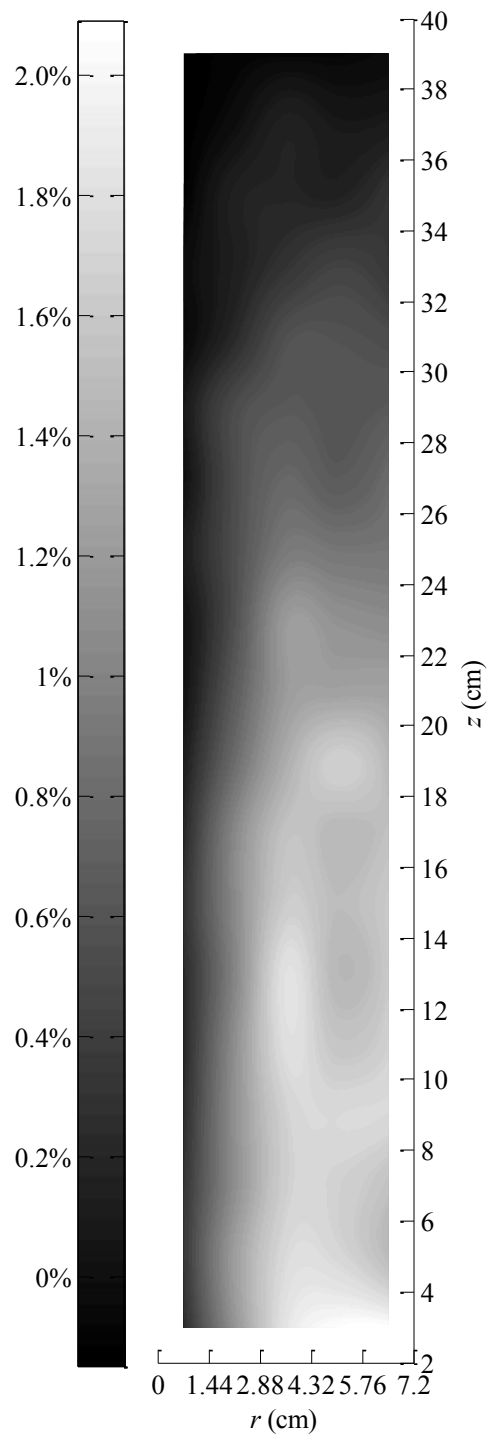


**Figure 4.34** Occupancy of swarf for PEPT experiment 7; superficial air velocity 4.1 cm/s, 1 kg of dissolved sodium chloride, 500 g of loose swarf. Incidences obtained from the trajectory of a directly activated piece of swarf sampled at ~20 Hz over a duration of 60 minutes.

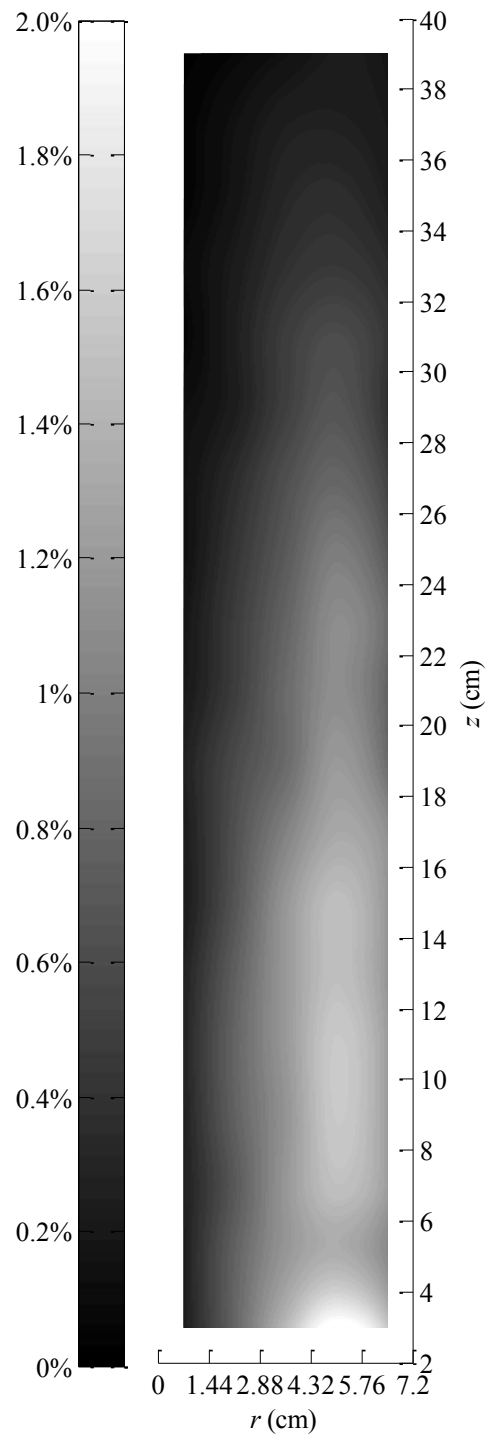


**Figure 4.35** Occupancy of swarf for PEPT experiment 5; superficial air velocity 7.2 cm/s, 500 g of loose swarf. Incidences obtained from the trajectory of a directly activated piece of swarf sampled at  $\sim 20$  Hz over a duration of 60 minutes.



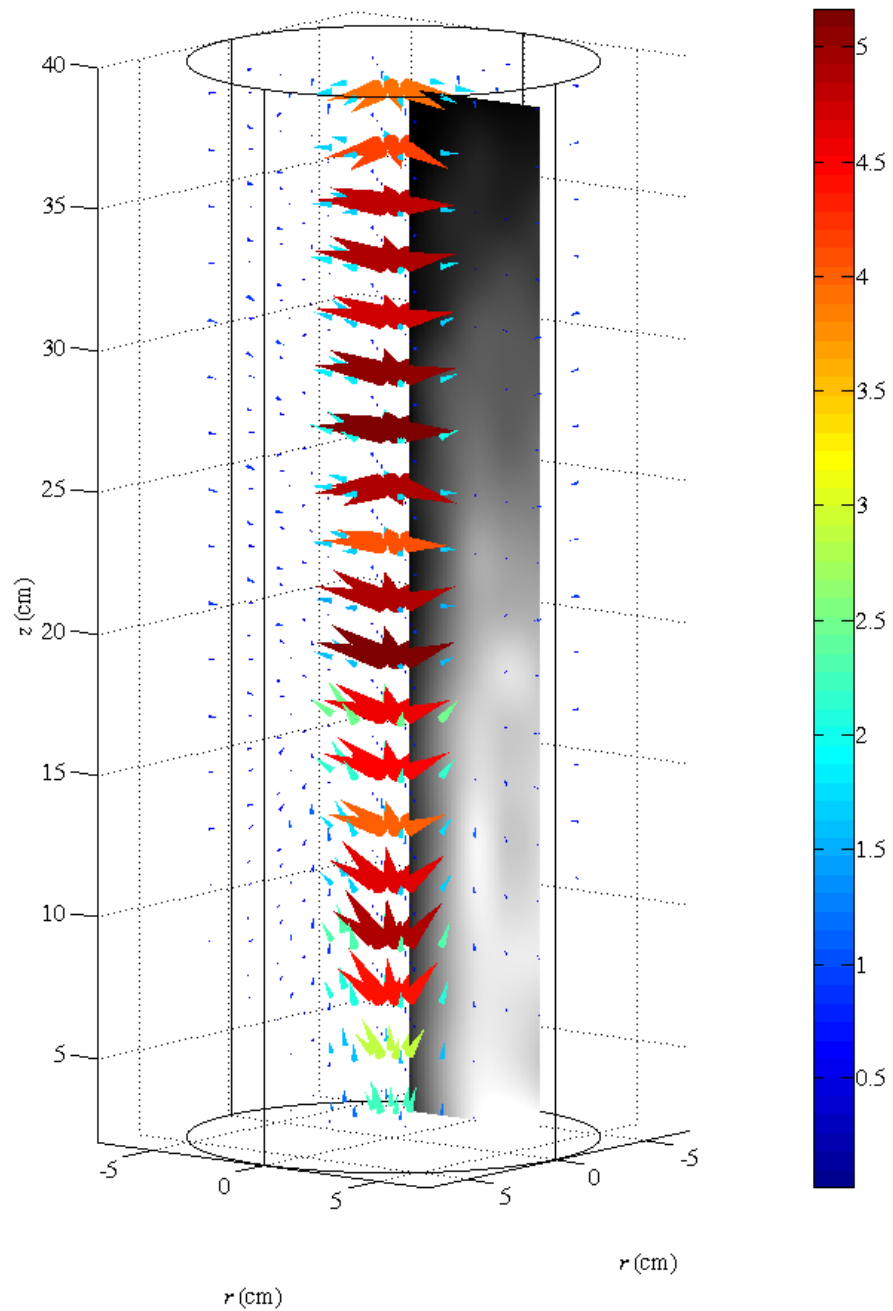


**Figure 4.36** Volume force ( $\text{mN}/\text{cm}^3$ ) resolved from the tensor components of the LHS of equation (4.31) for PEPT experiment 6; superficial air velocity 4.1 cm/s, 1 kg of dissolved sodium chloride, 500 g of loose swarf. Instantaneous velocities calculated using equation (4.49) from the trajectory of a 500 micron particle tracer sampled at  $\sim 50$  Hz over a duration of 200 minutes. Ensemble averaging of the instantaneous velocities is achieved using equation (4.24) for the calculation of the mean field terms.

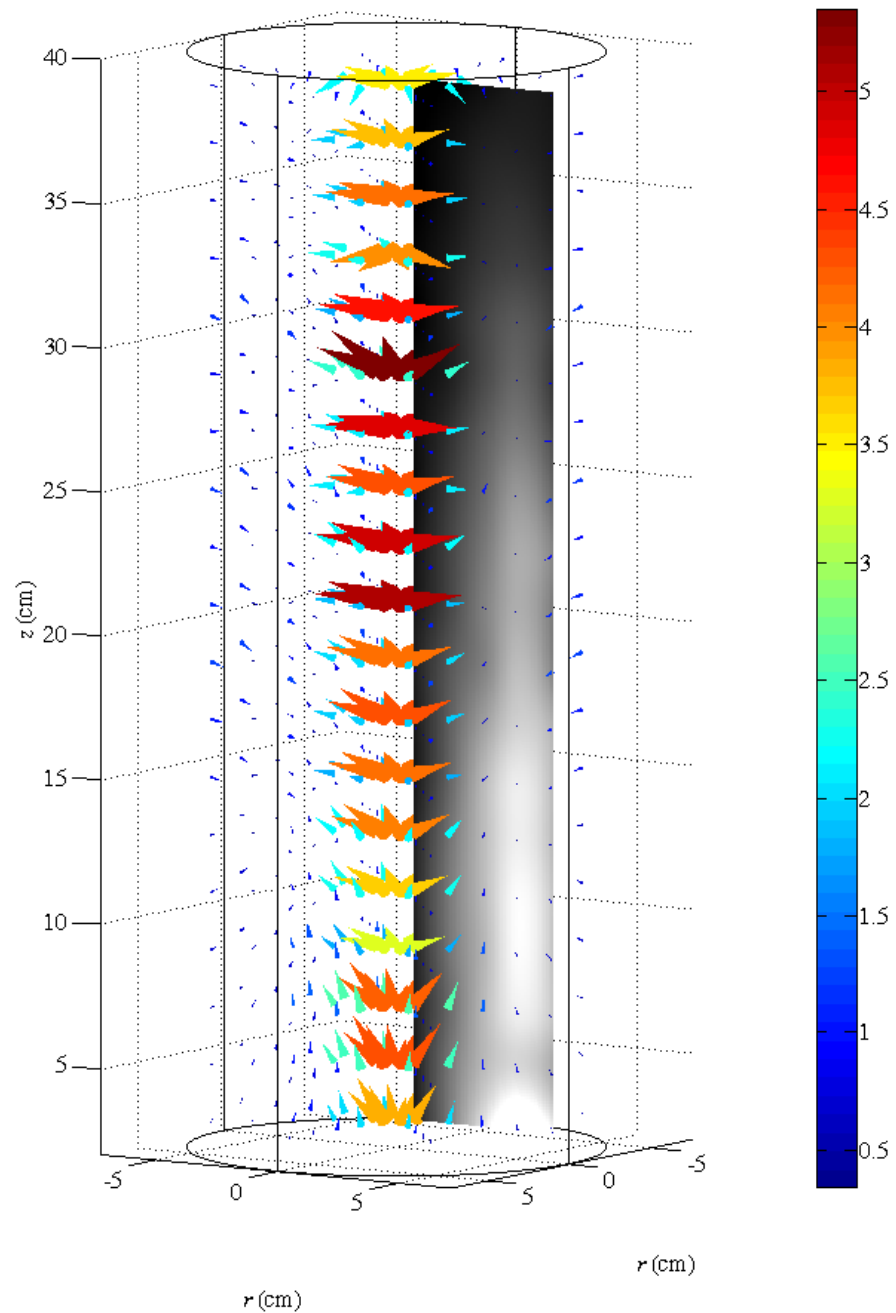


**Figure 4.37** Volume force ( $\text{mN/cm}^3$ ) resolved from the tensor components of the LHS of equation (4.31) for PEPT experiment 4; superficial air velocity  $7.2 \text{ cm/s}$ ,  $500 \text{ g}$  of loose swarf. Instantaneous velocities calculated using equation (4.49) from the trajectory of a  $500 \text{ micron}$  particle tracer sampled at  $\sim 50 \text{ Hz}$  over a duration of  $120 \text{ minutes}$ . Ensemble averaging of the instantaneous velocities is achieved using equation (4.24) for the calculation of the mean field terms.

## CHAPTER 5

### HEAT TRANSFER WITHIN CYLINDER CONCEPT

#### 5.1 Introduction

For the cylinder concept the inside-wall heat transfer coefficient contributes to the overall heat transfer coefficient and is discussed in Chapter 2 Section 2.3. The magnitude for the inside-wall heat transfer coefficient for the flow investigated in Chapter 4 is not known and must be measured. The thermal operating envelope of the cylinder concept defined in Chapter 2 Section 2.3 will require assurance that the measurement of the inside-wall heat transfer coefficient is correct and therefore of value. All significant contributions of measurement error must be known and will be both systematic and random (noise). For the analysis of the inside wall heat transfer coefficient a boundary inverse method employs an eigenvalue problem to find the magnitude of the coefficient from measurements of a temperature transient (Chapter 3 Sections 3.2, 3.7, 3.8 and 3.9). Solution of the boundary inverse method by Green's function and separation of variables gives an infinite series that has definite convergence, and is the precedence for the measurement error (Section 5.3). This is the precision to which the noise of an experiment must meet an acceptable accuracy (Section 5.4).

#### 5.2 Green's function and inverse analysis

The Green's function is indispensable when studying time-dependent boundary conditions of partial differential equations belonging to simple geometries (*Morse & Feshbach, 1953*). This is because the solutions obtained are analytical and of high precision (*Morse & Feshbach, 1953*). The solution of the partial differential heat conduction equation is cast naturally with

the method of separation of variables and therefore each solution is an infinite series (Özsisik, 1993). However, with a sufficient number of eigenvalues convergence is met and is simple to monitor to a required level of accuracy. Hence, it is easy to study acute as well as long lived temperature transients with confidence. For cylindrical coordinates the eigenfunctions are Bessel functions (Özsisik, 1993).

Green's function is used to account for non-homogeneous boundary conditions that prevent a separable form of the partial differential heat conduction equation (Morse & Feshbach, 1953; Özsisik, 1993). Such boundary conditions are time-dependent (Morse & Feshbach, 1953; Özsisik, 1993). Separation of variables provides solution to the corresponding homogeneous counterpart and is presented by Özsisik (1993, p. 99-152). Here the boundary conditions are homogeneous or separable in time. The eigenvalues and eigenfunctions of the Green's function are obtained from the homogeneous counterpart and this also constructs the initial condition of the non-homogeneity as shown for a Dirichlet boundary condition for 1-dimensional radial heat conduction (Özsisik, 1993):

$$T(r, t) = \underbrace{\int_a^b r' G\langle r, t | r', \tau \rangle \Big|_{\tau=0} T_0' dr'}_{\text{homogeneous counterpart}} - \underbrace{\alpha \int_{\tau=0}^t d\tau \sum_{i=1}^2 \left[ r' \frac{\partial G}{\partial r'} \right]_{r'=r_i}}_{\text{non-homogeneity}} f_i \quad (5.1)$$

$$G\langle r, t | r', \tau \rangle \Big|_{\tau=0} = \sum_{m=1}^{\infty} \frac{1}{N_m(\beta_m)} \psi_m(\beta_m, r) \psi(\beta_m, r') e^{-\alpha \beta_m^2 t} \quad (5.2)$$

A Dirichlet boundary condition specifies the time-dependency of temperature at a boundary and, a Neumann boundary condition the time-dependency of either heat flux or heat convection at a boundary (Özsisik, 1993, p. 214-251; Riley et al., 2001, p. 584-599).

The time-dependency of the non-homogeneity can now be found by recognising that the eigenfunctions of the Green's function of equation (5.2) form a complete set that is orthonormal. Using the definition of the Dirac delta function:

$$\sum_{m=1}^{\infty} \frac{1}{N_m(\beta_m)} \psi_m(\beta_m, r) \psi(\beta_m, r') r = \delta(r - r') \quad (5.3)$$

By causality the reciprocity relations of the Green's function gives its time-reversed equation (*Morse & Feshbach, 1953, p. 858*):

$$-\nabla^2 G - \frac{1}{\alpha} \frac{\partial G}{\partial \tau} = \frac{1}{\alpha r} \delta(r - r') \delta(t - \tau) \quad (5.4)$$

Noting that the operators that act upon the Green's function in equation (5.4) are linear the time-dependency can be expressed through a constant for each eigenvalue:

$$G\langle r, t | r', \tau \rangle = \sum_{m=1}^{\infty} \frac{1}{N_m(\beta_m)} \psi_m(\beta_m, r) \psi(\beta_m, r') C_m(t, \tau) \quad (5.5)$$

*Morse & Feshbach (1953, p. 864)* give a relation for this constant belonging to the solution of the Helmholtz equation. However, this constant can be found for the arbitrary solution by substituting this form into equation (5.4), which gives a first-order linear differential equation for the constant:

$$\nabla^2 \psi(\beta_m, r) = -\beta_m^2 \psi(\beta_m, r) \quad (5.6)$$

$$\Rightarrow \alpha \beta_m^2 C_m(t, \tau) - \frac{dC_m(t, \tau)}{d\tau} = \delta(t - \tau), \quad \tau = 0, \quad C_m(t, \tau) = e^{-\alpha \beta_m^2 t} \quad (5.7)$$

The solution to the family of curves for each eigenvalue is:

$$C_m(t, \tau) = e^{-\alpha\beta_m^2(t-\tau)} \quad (5.8)$$

The initial condition of the first-order linear differential equation is obtained from equation (5.2). The Green's function therefore evaluates the non-homogeneity as the effect of a point source which can be viewed along the  $t$  or  $\tau$  coordinate and, the time-dependency is contained within the eigenvalues of the homogeneous counterpart. Therefore, temperature transients arising from both Dirichlet and Neumann boundary conditions are fully understood (*Morse & Feshbach, 1953; Özisik, 1993*).

### 5.2.1 Inverse analysis

The fact that effect follows cause is universal and usually a linear model system is solved in an evolutionary sense (e.g. classical mechanics), that is:

$$[\mathbf{A}]\{\mathbf{x}\} = \{\mathbf{y}\} \quad (5.9)$$

But mathematically:

$$\{\mathbf{x}\} = [\mathbf{A}]^{-1} \{\mathbf{y}\} \quad (5.10)$$

and the question now is of the uniqueness of the cause obtained from the effect. If the model system of equation (5.9) is known directly (in the forward sense) then the inverse of the model system can be constructed to be continuous. Along with an initial condition, the inverse problem of equation (5.10) becomes semi well-posed with a unique solution (cause). The danger of an inverse problem is apparent when the model system is poorly or even not understood. The potential for an unlimited number of solutions then exists and the cause can only take a probabilistic form. This occurs when the model system is singular; the diagonal elements of the inverse model system become equal. The anti of an inverse problem is its

common sensitivity to measurement error. For an inverse model system its matrix is correlated and accumulative in nature, and any error in the measurable effect is amplified back to the cause. To avoid oscillatory instability regularisation is applied and corrects the effects of error observed in the cause. Regularisation is discussed in Chapter 3 Section 3.8 and 3.9. Analysis by reverse causality is conceptually strange and is disjoint to the domain of tangible engineering. However, since the usefulness of inverse methods was recognised, many examples of investigations have given evidence towards analysis of heat transfer (Chapter 3 Section 3.8). Solution theory of inverse analysis applied to heat transfer is discussed in Chapter 3 Sections 3.7, 3.8 and 3.9.

By recording the temperature history at an adjoined surface and knowing the thermal parameters of the medium, the boundary condition at the opposite surface can be analysed. This is an inverse heat conduction problem (IHCP) (Chapter 3 Sections 3.7, 3.8 and 3.9). A common solution method of the IHCP is least-squares optimisation with Tikhonov regularisation and calls heavily upon the work of Tikhonov (*Tikhonov & Arsenin, 1977*), and is discussed in Chapter 3 Sections 3.8 and 3.9. This inverse solution method has been used in many investigations and has undergone modifications to improve solution accuracy and efficiency (*Alifanov, 1994*). The construction of an inverse problem sits naturally with transient analysis. No forcing is required like as in a stationary or steady-state analysis. Hence, inverse analysis offers immense simplification of apparatus because the complexity is contained within its nature. Carefully choosing the transient lifetime affords the resolution of all flow structures responsible for the sought boundary condition (Section 5.7). For example if the boundary condition to be analysed is heat convection the periodicity of flow structures would dictate the transient lifetime for the calculation of the heat transfer coefficient (Section 5.7).

## 5.3 Analysis by regularised boundary inverse method

### 5.3.1 Least-squares and Tikhonov regularisation

The least-squares sum of the measured and functional estimated temperature vectors is used to construct an inverse model system:

$$S = \sum_j^M \left[ Y_j - \hat{T}_j(\{\hat{\mathbf{f}}\}) \right]^2 \quad (5.11)$$

The inverse model system is discussed in Subheading 5.2.1. For a cylindrical wall the measured temperature vector can give a temperature history at the outside surface. The estimated temperature vector can then relate the boundary condition at the inside surface to the measured temperature at the outside surface through the direct or forward heat conduction problem. By introducing the direct or forward heat conduction problem in the computation of the estimated temperature vector, this inverse analysis becomes semi well-posed; the direct problem can be introduced because the estimated temperature vector is expressed as a functional in the least-squares sum. Some well-posed nature of the inverse analysis is introduced because the direct heat conduction problem is continuous when starting from an initial condition that is known (*Alifanov, 1994*). Hence, the inverse solution is unique; however, solution instability can still occur by noise amplification from the random error present in the measured vector. To combat this noise a Tikhonov regularisation term is added to the least-squares sum (*Tikhonov & Arsenin, 1977*). The regularised least-squares sum is (*Scott & Beck, 1985; Alifanov, 1994*):

$$S = \sum_j^M \left[ Y_j - \hat{T}_j(\{\hat{\mathbf{f}}\}) \right]^2 + \gamma \sum_j^M (\Delta^n f_j)^2, \quad n = 0, 1, 2, \dots \quad (5.12)$$



The Tikhonov regularisation can be applied exclusively or combined through the magnitude, gradient or curvature of the sought boundary condition vector  $\{\mathbf{f}\}$ , and corresponds to  $n = 0$ , 1, or 2 respectively. The magnitude of the regularisation coefficient  $\gamma$  is best optimised by simulation, which is an important part of Tikhonov regularisation and is discussed in Section 5.4. To approach the inverse solution equation (5.12) is differentiated by the sought boundary condition vector, and the estimated vector is expressed through a Maclaurin series:

$$\hat{T}_j(\{\hat{\mathbf{f}}\}) = \hat{T}_j(\{\hat{\mathbf{f}}_0\}) + \sum_k^M \frac{\partial \hat{T}_j}{\partial \hat{f}_k} \hat{f}_k + \dots, \quad (5.13)$$

Substituting this series into the minimum of equation (5.12) gives a set of linear equations that can be expressed through the matrix equation:

$$\{\hat{\mathbf{f}}\} = \left( \gamma [\mathbf{H}]' [\mathbf{H}] + [\mathbf{X}]' [\mathbf{X}] \right)^{-1} [\mathbf{X}]' \{\mathbf{Y} - \mathbf{Y}_0\} \quad (5.14)$$

Because this relation gives the change in the boundary condition vector its absolute magnitude can be expressed:

$$\{\hat{\mathbf{f}}\} = \{\hat{\mathbf{f}}_{\text{abs}} - \hat{\mathbf{f}}_0\} \Rightarrow \{\hat{\mathbf{f}}_{\text{abs}}\} = \{\hat{\mathbf{f}}_0\} + \left( \gamma [\mathbf{H}]' [\mathbf{H}] + [\mathbf{X}]' [\mathbf{X}] \right)^{-1} [\mathbf{X}]' \{\mathbf{Y} - \mathbf{Y}_0\} \quad (5.15)$$

The sensitivity matrix is the engine of the inverse model system and is defined by:

$$[\mathbf{X}] = \begin{bmatrix} \frac{\partial \hat{T}_1}{\partial \hat{f}_1} & 0 & 0 \\ \frac{\partial \hat{T}_2}{\partial \hat{f}_1} & \frac{\partial \hat{T}_2}{\partial \hat{f}_2} & \dots & 0 \\ \vdots & & & \\ \frac{\partial \hat{T}_M}{\partial \hat{f}_1} & \frac{\partial \hat{T}_M}{\partial \hat{f}_2} & & \frac{\partial \hat{T}_M}{\partial \hat{f}_M} \end{bmatrix} \quad (5.16)$$

The sensitivity matrix is lower-triangular a result of causality rejecting the non-realism of later boundary elements affecting earlier temperature elements. The regularisation matrix is equal to the identity matrix if  $n = 0$  in equation (5.12), or a sparse diagonal matrix of finite difference coefficients if  $n = 1$  or 2. For example if the Tikhonov regularisation is applied through the curvature of the sought boundary condition, a forward 3-point differencing scheme would give (*Fornberg, 1988; Scott & Beck, 1985*):

$$[\mathbf{H}] = \begin{bmatrix} 1 & -2 & 1 & 0 & \dots & 0 \\ 0 & 1 & -2 & 1 & \dots & 0 \\ \vdots & & & & & \\ 0 & 0 & 0 & 0 & \dots & 0 \\ 0 & 0 & 0 & 0 & \dots & 0 \end{bmatrix} \quad (5.17)$$

The last two rows of the regularisation matrix are equal to zero to allow truncation. This is because of the differencing of local curvature where regularisation cannot be applied for the last two elements of the sought boundary condition.

### 5.3.2 Duhamel's theorem and auxiliary problems

The sensitivity matrix discussed in Subheading 5.3.1 is now related to the fixed internal diameter of the cylinder concept which is 144 mm (Chapter 1 Section 1.2) (Section 5.1). The domain is a cylindrical wall the outside of which is insulated and the inside surface ( $r = a = 72$  mm) is the boundary under investigation. The insulated outside surface gives redundancy and allows the inside boundary condition vector to be determined from the temperature history of the insulated outside surface ( $r = b$ ). The sensitivity matrices are then found for an arbitrary wall thickness ( $b - a$ ) using Duhamel's theorem which is presented by *Özsisik (1993, p. 590-592)*. This theorem couples the time-dependency of the boundary condition to the time-dependency of heat conduction through the wall, and employs an auxiliary problem

along with an integral equation. Using similar terminology to *Özisik*, the sensitivity matrix is evaluated by:

$$[\mathbf{X}] = \begin{bmatrix} (\phi_1 - \phi_0)_{r=b} & 0 & \dots & \dots & 0 \\ (\phi_2 - \phi_1)_{r=b} & (\phi_1 - \phi_0)_{r=b} & & & \vdots \\ \vdots & & & & \vdots \\ \vdots & & & & 0 \\ (\phi_M - \phi_{M-1})_{r=b} & \dots & \dots & (\phi_2 - \phi_1)_{r=b} & (\phi_1 - \phi_0)_{r=b} \end{bmatrix}; \quad (5.18)$$

where  $\phi_n$  is the time vectorised solution of the auxiliary problem for either a unit Dirichlet or unit Neumann boundary condition at  $r = a = 72$  mm:

$$\frac{1}{r} \frac{\partial}{\partial r} \left( r \frac{\partial \phi}{\partial r} \right) = \frac{1}{\alpha} \frac{\partial \phi}{\partial t}, \quad a < r < b \quad (5.19)$$

$$r = a, \quad k \frac{\partial \phi}{\partial r} = 1 \text{ or } \phi = 1 \quad (5.20)$$

$$r = b, \quad \frac{\partial \phi}{\partial r} = 0 \quad (5.21)$$

$$\phi = 0, \quad t = 0 \quad (5.22)$$

If the thermal parameters of the wall are independent of temperature the sensitivity matrix is not dependent on initial condition and the arbitrary direct problem and, therefore, the auxiliary problem can be formulated with initial temperature of zero. Here, the auxiliary problems have been solved by separation of variables and Green's function to account for non-homogeneity at  $r = a = 72$ mm (Section 5.2).

The Green's function for a Dirichlet boundary condition at  $r = a$  is (Özşik, 1993, p. 99-152; Morse & Feshbach, 1953, p. 791-894; Özşik, 1968, p. 243-257; Riley et al., 2001, p. 584-599):

$$G = \sum_{m=1}^{\infty} \frac{1}{N_m(\beta_m)} \psi_m(\beta_m, r) e^{-\alpha\beta_m^2(t-\tau)} \psi_m(\beta_m, r'); \quad (5.23)$$

where the eigenfunctions are:

$$\psi_m(\beta_m, r) = J_0(\beta_m r) Y_1(\beta_m b) - J_1(\beta_m b) Y_0(\beta_m r), \quad m = 1, 2, 3, \dots \quad (5.24)$$

$$N_m(\beta_m) = \int_a^b r \psi_m^2(\beta_m, r) dr \quad (5.25)$$

The eigenvalues are found from the transcendental equation:

$$J_0(\beta_m a) Y_1(\beta_m b) - J_1(\beta_m b) Y_0(\beta_m a) = 0, \quad m = 1, 2, 3, \dots \quad (5.26)$$

Then the solution by Green's function for a Dirichlet boundary condition of unit temperature rise is:

$$\phi(r, t) = -\alpha a \int_{\tau=0}^t d\tau \left( \phi_{r=a} \left( \frac{\partial G}{\partial n} \right)_{r'=a} \right) \quad (5.27)$$

Therefore the elements of the sensitivity matrix for a Dirichlet boundary condition are obtained from the elements of the vectorised form of:

$$\phi(b, t) = \alpha a \int_{\tau=0}^t d\tau \left[ \sum_{m=1}^{\infty} \frac{1}{N_m(\beta_m)} \left( \frac{\partial \psi_m(\beta_m, r)}{\partial r} \right)_{r=b} e^{-\alpha\beta_m^2(t-\tau)} \psi_m(\beta_m, a) \right]; \quad (5.28)$$

where:

$$\{\mathbf{t}\} = [0 \quad t_1 \quad \dots \quad t_M]; \quad (5.29)$$

$$\{\Phi\} = [0 \quad \phi(b, t_1) \quad \dots \quad \phi(b, t_M)] = [(\phi_0)_{r=b} \quad (\phi_1)_{r=b} \quad \dots \quad (\phi_M)_{r=b}] \quad (5.30)$$

The Green's function for a Neumann boundary condition of prescribed heat flux at  $r = a$  is (Özsisik, 1993, p. 99-152; Morse & Feshbach, 1953, p. 791-894; Özsisik, 1968, p. 243-257; Riley et al., 2001, p.584-599):

$$G = \frac{2}{b^2 - a^2} + \sum_{m=1}^{\infty} \frac{1}{N_m(\beta_m)} \psi_m(\beta_m, r) e^{-\alpha \beta_m^2 (t-\tau)} \psi_m(\beta_m, r') \quad (5.31)$$

where the eigenfunctions are:

$$\psi(\beta_m, r) = J_0(\beta_m, r), \quad \beta_m = 0 \quad (5.32)$$

$$\psi_m(\beta_m, r) = J_0(\beta_m r) Y_1(\beta_m b) - J_1(\beta_m b) Y_0(\beta_m r), \quad m = 1, 2, 3, \dots \quad (5.33)$$

$$N_m(\beta_m) = \int_a^b r \psi_m^2(\beta_m, r) dr \quad (5.34)$$

The eigenvalues are found from the transcendental equation:

$$J_1(\beta_m a) Y_1(\beta_m b) - J_1(\beta_m b) Y_1(\beta_m a) = 0, \quad m = 1, 2, 3, \dots \quad (5.35)$$

The solution by Green's function for a Neumann boundary condition of unit heat flux is:

$$\phi(r, t) = -\alpha a \int_{\tau=0}^t d\tau \left( -G_{r'=a} \left( \frac{\partial \phi}{\partial n} \right)_{r=a} \right) \quad (5.36)$$

Therefore the elements of the sensitivity matrix for a Neumann boundary condition of heat flux are obtained from the elements of the vectorised form of:

$$\phi(b,t) = \frac{\alpha a}{k} \int_{\tau=0}^t d\tau \left[ \frac{2}{b^2 - a^2} + \sum_{m=1}^{\infty} \frac{1}{N_m(\beta_m)} \psi_m(\beta_m, b) e^{-\alpha \beta_m^2 (t-\tau)} \psi_m(\beta_m, a) \right]; \quad (5.37)$$

where:

$$\{\mathbf{t}\} = [0 \quad t_1 \quad \dots \quad t_M]; \quad (5.38)$$

$$\{\Phi\} = [0 \quad \phi(b, t_1) \quad \dots \quad \phi(b, t_M)] = [(\phi_0)_{r=b} \quad (\phi_1)_{r=b} \quad \dots \quad (\phi_M)_{r=b}] \quad (5.39)$$

MATLAB<sup>®</sup> is used to compute the sensitivity matrices using the algorithms `dirichlet.m` and `neumann.m`. The algorithms are displayed in Appendix 3. The bisection method is used as a root finder for the eigenvalues on the transcendental equations, and a recurrence relation is used to construct the sensitivity matrices from the vectors  $\{\Phi\}$ .

#### 5.4 Sensitivity and simulation of regularisation

The qualitative nature of the sensitivity matrix (Section 5.3) is that it determines the best position of the thermocouple and the optimum time step for the inverse problem (Sections 5.2 and 5.3). The thermocouple position and sampling rate need to be sensitive to changes in the boundary condition to resolve the curvature of its function. Therefore, large independent sensitivity elements are desirable and the interplay of wall thickness and sampling rate need to be investigated to ensure the best resolution (Subheading 5.3.2). At the same time the inverse analysis is using a transient to measure a heat transfer coefficient (Section 5.1 and Subheading 5.4.1). Hence, the wall thickness should give an appreciable thermal mass to ensure a transient of satisfactory duration. With a longer lived transient more measurements can be taken increasing the confidence in the values reported. For this investigation an inconel wall is used and its thermal parameters are listed in table 5.1. Note the non-homogeneity of equation (5.1) is irrespective of initial condition and the sensitivity matrices can be applied to an

arbitrary Dirichlet or Neumann boundary inverse problem. An ideal transient would be a sharp increase in fluid temperature and subsequent convective heating of the wall. The analysis would then be simplified by a near constant fluid temperature and a wall surface temperature approaching this limit. Note the heat capacity of water is one order of magnitude greater than inconel.

**Table 5.1** Thermal parameters of inconel wall (*www.specialmetals.com*).

Thermal parameter	Heat capacity (J/kg °C)	Thermal conductivity (W/m °C)	Density (kg/m <sup>3</sup> )
Inconel 625 (21 °C)	410	9.8	8440

#### 5.4.1 Transient model

To develop the above arguments the transient temperature at the inside and outside surfaces of the wall is required ( $r = a = 72$  mm and  $r = b$  respectively). The transient temperature at  $r = a$  will be sought using equation (5.15) in the calculation of the wall heat transfer coefficient from the measured temperature transient of the insulated outside surface at  $r = b$ . The transient heat flux normal to the inside surface of the wall at  $r = a = 72$  mm is also of interest for said calculation, but for this development it does not need to be described explicitly and naturally becomes defined. The Green's function for a Neumann boundary condition of prescribed heat convection at  $r = a$ , and thermal insulation at  $r = b$  is (Özsisik, 1993, p. 99-152; Morse & Fesbach, 1953, p. 791-894; Özsisik, 1968, p. 243-257; Riley et al., 2001, p.584-599):

$$G = \sum_{m=1}^{\infty} \frac{1}{N_m(\beta_m)} \psi_m(\beta_m, r) e^{-\alpha\beta_m^2(t-\tau)} \psi_m(\beta_m, r') \quad (5.40)$$

where the eigenfunctions are:

$$\psi_m(\beta_m, r) = J_0(\beta_m r)Y_1(\beta_m b) - J_1(\beta_m b)Y_0(\beta_m r), \quad m = 1, 2, 3, \dots \quad (5.41)$$

$$N_m(\beta_m) = \int_a^b r \psi_m^2(\beta_m, r) dr \quad (5.42)$$

The eigenvalues are found from the transcendental equation:

$$\begin{aligned} & -\beta_m J_1(\beta_m a)Y_1(\beta_m b) + \beta_m J_1(\beta_m b)Y_1(\beta_m a) - \dots \\ & \frac{h_i}{k} \beta_m J_0(\beta_m a)Y_1(\beta_m b) + \frac{h_i}{k} \beta_m J_1(\beta_m b)Y_0(\beta_m a) = 0 \quad m = 1, 2, 3, \dots \end{aligned} \quad (5.43)$$

The transcendental equation is obtained by differentiating equation (5.41), the normal gradient of which is equal to Newton's law of cooling or heat convection at  $r = a$ . The superposition of eigenfunctions of equation (5.41) also satisfies the thermal insulation at  $r = b$ . Note heat convection is made homogeneous to allow a separable form and is discussed in Section 4.2. Then by Green's function the temperature transient across the wall is:

$$T(r, t) = -\alpha a \int_{\tau=0}^t d\tau \left[ -G_{r'=a} \left( \frac{\partial T}{\partial n} + \frac{h_i}{k} T \right)_{r=a} \right] \quad (5.44)$$

The transient fluid temperature multiplied by the ratio of the heat transfer coefficient to wall thermal conductivity completes the convective term in equation (5.44) of the inside surface of the wall at  $r = a$ :

$$\frac{\partial T}{\partial n} + \frac{h_i}{k} T = \frac{h_i}{k} T_f(\tau) \quad (5.45)$$

As a model transient the following function represents rapid heating of the fluid followed by convective heating of the wall:



$$\frac{h_f}{k} T_f(\tau) = \frac{h_f}{k} 3.675 e^1 (1 - e^{-0.5\tau}) \quad (5.46)$$

Rapid heating of the fluid occurs from the origin and the temperature transient at  $r = a$  and  $r = b$  for different wall thicknesses can be assessed:

$$T(r, t) = \frac{\alpha a h 3.675 e^1}{k} \int_{\tau=0}^t d\tau \left[ \sum_{m=1}^{\infty} \frac{1}{N_m(\beta_m)} \psi_m(\beta_m, r) e^{-\alpha \beta_m^2 (t-\tau)} \psi_m(\beta_m, a) (1 - e^{-0.5\tau}) \right] \quad (5.47)$$

MATLAB<sup>®</sup> is used to compute equation (5.47) using the algorithm `transient_model.m`. The algorithm is displayed in Appendix 3. The bisection method is used as a root finder for the eigenvalues on the transcendental equation, and a recurrence relation is used to construct the convergent series.

Figures 5.1-5.3 display the temperature transients of the inside surface of the wall at  $r = a = 72$  mm for wall thicknesses of 1, 2, 3, and 4 mm. The values of the heat transfer coefficients are 1000 W/m<sup>2</sup> °C, 2000 W/m<sup>2</sup> °C and 3000 W/m<sup>2</sup> °C for figures 5.1-5.3 respectively. The transient temperature differences between the fluid and the inside surface of the wall at  $r = a = 72$  mm are also displayed (Figures 5.1-5.3). The greatest transient lifetime and therefore the greatest number of measurements is given by the 4 mm inconel wall (Figures 5.1-5.3). This is intuitive but through this simple model the trend and form of the heat flux is evident; the heat flux is given by multiplying the transient temperature difference by the magnitude of the heat transfer coefficient (Figures 5.1-5.3). For heat transfer coefficients between 1000-3000 W/m<sup>2</sup> °C the 4 mm wall provides transient lifetimes of 30-70 s respectively (Figures 5.1-5.3). This should allow sufficient time for rapid heating of the fluid followed by inverse analysis. The transient lifetime of the temperature difference for a 4 mm wall indicates that the sampling

rate of the inverse analysis must be sub-second to second in value for resolution of the transient.

The spread of the first ten sensitivity elements of matrix (5.16) for a Dirichlet and Neumann boundary condition for a 1, 2, 3, and 4 mm inconel wall are displayed in figures 5.4 and 5.5 respectively. The sensitivity elements are obtained from the auxiliary problems in Subheading 5.3.2. Intuitively the sensitivity elements are larger the thinner the wall and therefore the greater the measurement resolution (Figures 5.4 and 5.5). However, from the above transient model a 4 mm inconel wall is necessary to give a transient of satisfactory lifetime. Along with wall thickness the sampling rate (time step) can be used to adjust the magnitude of the sensitivity elements (Subheading 5.3.2). On decreasing the sampling rate the magnitude of the sensitivity elements belonging to the 4 mm inconel wall can be increased (Figures 5.4 and 5.5). The optimum sampling frequency is therefore 1 Hz, which gives large sensitivity elements and necessary resolution of the transient for a 4 mm inconel wall.

For the measurement of the inside-wall heat transfer coefficient of the cylinder concept an optimum sampling frequency of 1 Hz is consistent with a flow periodicity of ~5 Hz observed within the flow visualisation experiments of air-water-swarf flow discussed in Chapter 4 Section 4.7; a 1 Hz sampling frequency allows the resolution of the inside-wall heat transfer coefficient for stationary flow. The flow periodicity is for a superficial air velocity of 6.1 cm/s of heterogeneous air-water-swarf flow that is characterised by large air voids that rise periodically along the height of the air-water-swarf column (Chapter 4 Section 4.7).

### 5.4.2 Regularisation

The inverse model system without Tikhonov regularisation is:

$$\left( [\mathbf{X}]' [\mathbf{X}] \right)^{-1} [\mathbf{X}] \quad (5.48)$$

Because the elements of the sensitivity matrix are correlated, matrix (5.48) becomes ill-conditioned, possessing neighbouring elements that are extremely disparate in magnitude. This makes matrix (5.48) highly sensitive to noise within the measured vector on which it operates. Hence, to condition matrix (5.48) bias is introduced reducing the disparity of neighbouring elements; this is the basis of the inverse model system with Tikhonov regularisation and is discussed in Section 5.2 and 5.3:

$$\left( \gamma [\mathbf{H}]' [\mathbf{H}] + [\mathbf{X}]' [\mathbf{X}] \right)^{-1} [\mathbf{X}]' \quad (5.49)$$

The conditioning can be applied through the magnitude, gradient or curvature of the sought boundary condition vector and is explicitly expressed by the sparse matrix  $[\mathbf{H}]$  (Section 5.3) (Chapter 3 Section 3.8). Because the ideal transient possesses high curvature an appropriate form for matrix  $[\mathbf{H}]$  is the example matrix (5.17). Tikhonov regularisation is therefore applied bias and simulation is necessary to avoid a damped boundary condition vector (*Özsisik, 1993, p. 571-610; Scott & Beck, 1985*). *Scott & Beck (1985)* compute the mean square error to select the regularisation coefficient. In the present investigation inspection of the inverse solutions obtained using equation (5.15) with the transient model is used to select the regularisation coefficients through simulation. The transient for  $h = 2000 \text{ W/m}^2 \text{ }^\circ\text{C}$  is used and the temperature vector of the insulated outside surface at  $r = b = 76.25 \text{ mm}$  obtained from equation (5.47) mimics real measurement by incorporating normally distributed noise from a

random number generator. The manufacture of the inconel wall was found to be to a thickness of 4.25 mm and is discussed in Section 5.5. The normal distribution is related to the noise distribution by:

$$Z = \frac{\varepsilon - \mu}{\sigma} \quad (5.50)$$

For a 99.9% confidence  $-3 < Z < 3$  and therefore the random number generator operates within these limits (Özsisik, 1993, p. 575-584). Because the true mean of the random error is zero, the simulated temperature vector is:

$$\{\mathbf{Y}\}_{\text{sim}} = \{\mathbf{T}\} + \sigma \{\mathbf{Z}\} \quad (5.51)$$

As usual  $\sigma$  stipulates the degree of noise associated with a measurement. Acquisition of temperature can be achieved with a total noise of  $\pm 0.1$  °C and therefore implies  $\sigma \approx 0.033$ . Procurement of a temperature measurement system is discussed in Section 5.5.

MATLAB<sup>®</sup> is used to compute equation (5.15) for the simulated temperature vector obtained from equations (5.47) and (5.51) at  $r = b = 76.25$  mm using the IBPn.m algorithm. The IBPn.m algorithm is given in Appendix 3. The inverse solution of the normal heat flux of the inside surface at  $r = a = 72$  mm is calculated from equation (5.15) containing the sensitivity matrix constructed of elements obtained from equation (5.37) for a unit prescribed heat flux at  $r = a = 72$  mm. The inverse solution of the temperature of the inside surface of the wall at  $r = a = 72$  mm is calculated from equation (5.15) containing the sensitivity matrix constructed of elements obtained from equation (5.28) for a unit temperature rise at  $r = a = 72$  mm. The explicit form of the sensitivity elements is discussed in Subheading 5.3.2. Simulations of the inverse analysis for the noise distribution are displayed in figures 5.6-5.8.

By inspection of the calculated inverse solution of heat flux normal to the inside surface of the wall at  $r = a = 72$  mm with the heat flux of the transient model (temperature difference of equations (5.47) and (5.46) multiplied by  $h = 2000 \text{ W/m}^2 \text{ }^\circ\text{C}$  at  $r = a = 72$  mm) the optimum value of the regularisation coefficient for a Neumann boundary condition of heat flux is found to be  $10^{-7}$ . Both the calculated inverse solution of heat flux and that of the transient model are displayed in figure 5.6. By inspection of the calculated inverse solution of temperature of the inside surface of the wall at  $r = a = 72$  mm with the temperature of the transient model (equation (5.47) for  $h = 2000 \text{ W/m}^2 \text{ }^\circ\text{C}$  at  $r = a = 72$  mm) the optimum value of the regularisation coefficient for a Dirichlet boundary condition of temperature is found to be 10. Both the calculated inverse solution of temperature and that of the transient model are displayed in figure 5.7. These values of the regularisation coefficients afford conditioning over the transient decay at points of sound temperature difference and representative flow, which corresponds to the midpoint of the transient decay and indicates that Tikhonov regularisation through curvature is localised. This localisation of Tikhonov regularisation results from the minimisation of curvature in equation (5.12) for both Neumann and Dirichlet boundary conditions allowing for a point of inflection in the region of the midpoint of the transient decay that prevents distortion of the inverse solutions (Chapter 3 Section 3.8). Note in figure 5.6 the inverse solution of heat flux (Neumann boundary condition) is shifted from the point of maxima of the transient model heat flux but passes very close to its point of inflection. Tikhonov regularisation is discussed further in Chapter 3 Sections 3.8 and 3.9.

Taking the difference between the fluid temperature of equation (5.46) and that of the calculated inverse solution of temperature of the inside surface of the wall at  $r = a = 72$  mm, and dividing the calculated inverse heat flux normal to the inside surface by this temperature difference gives the inverse solution for the inside-wall heat transfer coefficient. The inverse

solution of the inside-wall heat transfer coefficient belonging to the simulation is displayed in figure 5.8. The value of the inverse solution agrees well with the transient model ( $h = 2000 \text{ W/m}^2 \text{ }^\circ\text{C}$ ) in the region of the midpoint of the transient decay at 40-45 s into the simulation where the Tikhonov regularisation has been localised for the inverse analysis. Oscillations are prevalent at the start and end of the inverse analysis where the temperature history resolves only noise, and this is seen in figure 5.8 for the inverse solution of the inside-wall heat transfer coefficient.

### 5.5 Temperature measurement and inconel wall

All significant contributions of temperature measurement error must be known and will be both systematic and random (noise). Within Section 5.4 the design of experiment for the inverse analysis of the inside-wall heat transfer coefficient is outlined. The design of experiment and apparatus are the major sources of error for the inverse analysis. Within the design of experiment the precedence for the error is set and is the precision. Once the precision is set the noise of temperature measurement must meet an acceptable accuracy. The standard deviation of noise about its zero mean should at least be equal to the precision. This would be equivalent to a 68 % confidence or accuracy. From the simulations of the inverse analysis discussed in Section 5.4 a 4 mm inconel cylindrical wall of internal diameter 144 mm is required to give a transient of sufficient duration for measurement of the sought boundary condition. Convergence of the analytical solution for the sensitivity elements in Subheading 5.3.2 for this wall thickness guarantees a precision of  $0.1 \text{ }^\circ\text{C}$ ; this is met by increasing the number of eigenvalues. Therefore, minimisation of noise of temperature measurement to this precision must be met; the effect and control of this noise is assessed in the simulation of inverse analysis using Tikhonov regularisation (Subheading 5.4.2). The systematic error of

temperature measurement is offset by calibration, it is reproducible, intrinsic and characterised by its own standard deviation.

The inconel wall used in the investigation of the inside-wall heat transfer coefficient for the cylinder concept is detailed in figures 5.9 and was supplied by AALCO Ltd, Nottingham UK. The outer diameter of the inconel wall is within 152 mm  $\pm$ 1.5 mm and its thickness is within 4 mm  $\pm$ 0.25 mm. The straightness of the inconel wall is within a diameter of 6 mm central to the axis and has ovality  $\pm$ 1.5 mm over a length of 1200 mm. The inconel conforms to the material specification UNS-N 06625/ASTM B443. Fabrication of the tube was completed by MCE Engineering, Derby UK and includes fixture of inconel bosses and stainless steel flange.

Procurement of a temperature measurement system was on the basis that the supplier (TC Ltd) could achieve the required precision and accuracy, and that the calibration was externally accredited. A sub-second sampling rate was also specified. The supplier achieved the precision and a noise of accuracy  $\pm$ 0.1 °C 99.9%. The calibration was inline with the intrinsic accuracy of the type-K thermocouple ( $\pm$ 0.3 °C 95%). Calibration certificates are given in Appendix 4. Note it is of no significance that the intrinsic accuracy of the type-K thermocouple is lower than the noise because this error is reproducible and offset. The intrinsic accuracy refers to the spread of the potential systematic error for a type-K thermocouple.

A complete solution for temperature measurement and data acquisition was provided by TC Ltd, Chesterfield UK. For the measurement of fluid temperature mineral insulated inconel sheathed thermocouple assemblies are used. These thermocouple assemblies are housed within inconel bosses fixed to the inconel cylindrical wall and are held using a tapered polytetrafluoroethylene (PTFE) compression fitting. The arrangement of an inconel boss and

PTFE compression fitting is displayed in figure 5.10. The thermocouples are conductor type-K and to enhance response time the measuring junction is welded directly onto the inside of the sheath (grounded junction). Again, to further enhance response time the assemblies have swaged tips reducing the diameter of the insulator close to the measuring junction, and therefore lowering thermal mass. Sheath length is 200 mm and has diameter 4.5 mm, which is reduced to 3 mm over the 50 mm swaged tip. The arrangement of the mineral insulated thermocouples within the inconel cylinder is displayed in figure 5.11. Polyimide thin film thermocouples are used for measurement of temperature on the outside surface of the inconel wall. Like the mineral insulated assemblies the thermocouples are conductor type-K and the measuring junction is a tiny bead sandwiched within a 0.13 mm polyimide film of area 12 mm × 20 mm. The thermal mass of these thermocouples is very low and as a consequence they have millisecond response and negligible lag. Acquisition is modular and interfaced via USB to a Microsoft® Windows PC. The modules are part of the RKC SR mini system, which has a maximum sampling rate of 10 Hz and a noise distribution of ±0.1 °C. Each acquisition module is dual channel and is linked to a common communication and supply module. Proprietary software is provided by TC Ltd and is marketed as SpecView. This software is auto-configurable with the RKC SR mini system and data logging produces a .CSV file.

## 5.6 Inverse experiments

The inverse experiments for the measurement of the inside-wall heat transfer coefficient are summarised in table 5.2. The same superficial air velocities of the PEPT experiments are used and allow the heat transfer measurement of the inverse analysis to be related to the observed momentum transfer in Chapter 4. The lowest superficial air velocity of 4.1 cm/s (based upon cylinder cross-section) is for the observed onset of mixing of the swarf bed in the presence of an electrolyte (1 kg of dissolved sodium chloride). The effect of an electrolyte is investigated



because the swarf dissolution process contains an ionic solution of acids and dissolved swarf. The turbulent multiphase flow investigated in Chapter 4 is gravity-driven and to segregate important phenomena a superficial air velocity without an electrolyte for the same global gas hold-up is used (7.2 cm/s,  $\varepsilon_G = 16\%$ ).

**Table 5.2** Summary of inverse experiments.

Experiment	Superficial air velocity (cm/s)	Global gas hold-up (%)	Addition of sodium chloride (kg)	Amount of swarf (g)	Height of sensors (mm)
1	4.1	16	1	500	100, 350
2	7.2	16	-	500	100, 350
3	4.1	16	1	500	100, 350

Polyimide thermocouples are located on the outside surface of the inconel wall at the same heights as the inconel bosses that house the sheathed thermocouples. The locations of the polyimide thermocouples are displayed in figure 5.12. Heat conduction tape is used to secure the polyimide thermocouples to the outside surface of the wall. The angle between the polyimide thermocouples and inconel bosses is  $90^\circ$ . After fixture and housing of thermocouples the outside surface of the wall is insulated and is displayed in figure 5.13. For each experiment the column is prefilled with 9.55 litres of tap water and 500 g of loose swarf. The prefill and swarf is added from the top of the column. The electrolyte (1 kg of sodium chloride) is dissolved in the initial 9.55 litres of water. The air flow rate through the perforated plate is set using a rotameter and the column is sparged for five minutes. This allows the temperature of the wall and the contents of the column to steady. Temperature logging begins and is monitored in real time on a laptop display. After one minute a sharp temperature transient is achieved by adding 1.7 litres of boiling water to the centre of the

column over a duration of ~5 s. The boiling water is added from the top of the column. This addition of boiling water gives a similar transient profile to the simulation discussed in Section 5.4. A transient profile of the fluid temperature and temperature of the insulated outside surface of the wall is given in figure 5.14 for inverse experiment 1. The temperature transient across the inconel wall decays and temperature logging stops after a further minute. The rotameter is closed and the column drained. The amount of swarf and volume of water used in each experiment is the same as the amount of swarf and total volume of prefill and acids for the cylinder concept (Chapter 1 Section 1.3).

From the simulations of the inverse analysis discussed in Section 5.4 the Tikhonov regularisation is localised to the midpoint of the transient decay at the inside surface of the wall. Because of the inconel wall thickness and the addition of boiling water over a duration of ~5 s, the growth of the normal heat flux and temperature of the inside surface of the wall and then their subsequent decay to their midpoints, is separated from the end of the addition of boiling water by at least 10 s. This allows the flow inside of the inconel column to steady after the addition of boiling water so that the measurement of the inside-wall heat transfer coefficient is that of the multiphase flow. Note periodicity of large scale flow is ~5 Hz away from the perforated plate as observed for the flow visualisation experiments of heterogeneous air-water-swarf flow discussed in Chapter 4 Section 4.7.

## 5.7 Results of inverse experiments

The inverse solutions of the normal heat flux and temperature of the inside surface of the wall, measured fluid temperature, and calculated heat transfer coefficients of the inside surface of the wall are given in figures 5.15-5.33. The inverse solutions of the normal heat flux and temperature at the inside surface of the wall have been obtained from the measured temperature history at the insulated outside surface of the wall using equation (5.15) and the

MATLAB<sup>®</sup> algorithm IBPn.m (Appendix 3). The sensitivity elements of the sensitivity matrix of equation (5.15) are evaluated by equation (5.37) in the inverse analysis of the normal heat flux, and equation (5.28) in the inverse analysis of the temperature of the inside surface of the wall. The regularisation coefficients used in the inverse analysis are the same values obtained from the simulation discussed in Section 5.4. The inverse solution of the inside-wall heat transfer coefficient is calculated by dividing the normal heat flux by the difference between the measured fluid temperature and the inverse solution of the temperature of the inside surface of the wall.

The lag of the mineral insulated thermocouples is acceptable for the temperature measurements at heights 100 mm and 350 mm but could be improved to provide better resolution of the fluid temperature. The lag effects of these thermocouples are more noticeable at height 350 mm where they are closer to the addition of boiling water. Oscillations in the measured fluid temperature are seen in figures 5.16, 5.23 and 5.29 at height 350 mm. The fluid temperature is extrapolated through the mean of the measured points. At height 600 mm large oscillations in the measured fluid temperature due to the lag of the mineral insulated thermocouples prevented analysis. All of the inverse solutions (normal heat flux and temperature of inside surface of the wall) are conditioned well over the midpoint of the transient decay, and their curvature is fully resolved over sound temperature difference between the inside surface of the wall and fluid, and representative flow.

#### 5.7.1 Inside-wall heat transfer coefficients of air-water-swarf flow

For experiment 1 and 3 the computed values of the inside-wall heat transfer coefficient (Figures 5.21 and 5.33) for height 100 mm are not constant around a mean indicating that the flow is not steady over the period. A transient of longer duration is necessary to obtain the inside-wall heat transfer coefficient of stationary flow at this height using a lower sampling

frequency. All other computed values of the inside-wall heat transfer coefficient (Figures 5.17, 5.24, 5.27 and 5.30) from the inverse solutions are constant around a mean indicating that the flow is steady and representative over the midpoint of the transient decay. For these values of the inside-wall heat transfer coefficient the simulations discussed in Section 5.4 has provided the correct wall thickness and sampling rate along with Tikhonov regularisation coefficients. Oscillations are seen at the beginning and end of the transients as expected from the simulation (Figure 5.8).

The inverse solution of the heat flux and temperature of the inside surface of the wall at the midpoint of the transient decay are near identical for inverse experiments 1 and 3 at height 100 mm (Figures 5.19 and 5.20 cf. Figures 5.31 and 5.32) and similar at height 350 mm (Figures 5.15 and 5.16 cf. Figures 5.28 and 5.29). For the two experiments the measured inside-wall heat transfer coefficients at height 350 mm are within ~14 % of one another at the midpoint of the transient decay. Therefore, the measurement of the inside-wall heat transfer coefficient by a regularised boundary inverse method is reproducible. Addition of boiling water from the base of the column would improve the control of the experiment and accuracy.

Results are given for the analysis of the magnitudes of the inside-wall heat transfer coefficients belonging to the flow of PEPT experiments 4 and 6 (Chapter 4 Section 4.9). The inside-wall heat transfer coefficients belonging to the flow of PEPT experiment 4 are displayed in figure 5.27 at height 100 mm and figure 5.24 at height 350 mm. The inside-wall heat transfer coefficients belonging to the flow of PEPT experiment 6 are displayed in figures 5.21 and 5.33 at height 100 mm and figures 5.30 and 5.17 at height 350 mm. The flow of PEPT experiment 4 is of superficial air velocity 7.2 cm/s, and contains 500 g of loose swarf. The magnitudes of the inside-wall heat transfer coefficient obtained for the flow of PEPT experiment 4 are 2262 W/ m<sup>2</sup> °C at height 100 mm and 2877 W/m<sup>2</sup> °C at height 350 mm. The

flow of PEPT experiment 6 is of superficial air velocity 4.1 cm/s, and contains 1 kg of dissolved sodium chloride and 500 g of loose swarf. The magnitudes of the inside-wall heat transfer coefficient obtained for the flow of PEPT experiment 6 are 1700-1900 W/ m<sup>2</sup> °C at height 100 mm and 2319 W/ m<sup>2</sup> °C at height 350 mm for inverse experiment 1, and 2686 W/ m<sup>2</sup> °C at height 350 mm for inverse experiment 3.

### 5.7.2 Flow perturbations and local heat convection

Measurements along the height of the inconel column show how perturbations to the flow affect the magnitudes of the inside-wall heat transfer coefficients. The same global gas hold-up for both superficial air velocities enables the segregation of the perturbations; this is important because the flow is gravity driven. The perturbations are swarf occupancy and presence of an electrolyte. The local momentum transfer to the water and hence heat convection towards the inside surface of the wall is indicated by the mean axial velocities of the water. The local mean axial velocity close to the wall at heights 100 mm and 350 mm is displayed in figure 5.34 for the air-water-swarf-flow of the inverse experiments displayed in table 5.2. The axial velocity values are taken from the corresponding PEPT experiments displayed in table 4.3 of air-water-swarf flow and air-water flow of the same superficial air velocities and dissolved sodium chloride (Chapter 4 Section 4.9). The axial velocities for the different PEPT experiments are tabulated in tables 4.4-4.8. From figure 5.34 the momentum transfer observations include:

1. Overall reduction in axial velocity of the water close to the wall for air-water-swarf flow compared with air-water flow. Additional momentum transfer to swarf damps momentum transfer to water.

2. An overall reduction in axial velocity of the water close to the wall for dissolved sodium chloride for the same global gas hold-up for different superficial air velocities with and without swarf.
3. Towards the base of the column and close to the wall convective deceleration of the water leads to smaller axial velocities at height 100 mm.
4. Reduction of axial velocity of the water close to the wall for air-water-swarf flow compared with air-water flow is greater for superficial air velocity 7.2 cm/s at height 350 mm. Swarf/air void collisions are likely to reduce void size and therefore local momentum transfer. This effect would be more noticeable for superficial air velocity 7.2 cm/s because of the coalescence inhibition of dissolved sodium chloride for superficial air velocity 4.1 cm/s. As a consequence the difference in axial velocities of the water close to the wall for the air-water-swarf flow at height 350 mm is less compared with the difference at height 100 mm.

The effects of these observations of momentum transfer are seen in the magnitudes of the inside-wall heat transfer coefficients measured at different heights displayed in figures 5.17, 5.21, 5.24, 5.27, 5.30 and 5.33. The inside-wall heat transfer coefficients are smaller in magnitude at height 100 mm compared with height 350 mm and is consistent with observations 1 and 3 of the momentum transfer. Both convective deceleration and higher swarf occupancy reduce momentum transfer to the water. The swarf occupancies are displayed in figures 4.34 and 4.35. Therefore, the flow structures that contribute towards the convection of heat must have a lower frequency (periodicity) consistent with the higher inertial mass of the swarf occupancy. This agrees with the previous statement that a transient of longer duration and a lower sampling frequency is required for measuring the inside-wall heat transfer coefficient of stationary flow at height 100 mm for superficial air velocity 4.1 cm/s.

From observation 2 of the momentum transfer, the coalescence inhibition of dissolved sodium chloride for superficial air velocity 4.1 cm/s further reduces momentum transfer and gives a smaller axial velocity of water close to the wall. This in turn leads to a smaller inside-wall heat transfer coefficient for superficial air velocity 4.1 cm/s at height 100 mm.

The difference in magnitudes of the inside-wall heat transfer coefficients at height 350 mm is less between the different air-water-swarf flows. This is consistent with observation 4 of the momentum transfer. The axial velocities at height 350 mm are similar because of the combined effects of the dissolved electrolyte and swarf occupancy.

In summary the common global gas hold-up of the air-water-swarf flow segregates the controlling phenomena of the flow and therefore convection of heat towards the inside surface of the wall.

## 5.8 Conclusion

The novelty of a boundary inverse method is that it simplifies the requirements of the apparatus and experiment for the investigation of a batch process and is more representative of the transport phenomena (both heat and momentum). Traditional methods employ closed loops or internal heaters to provide heat transfer and analysis of multiphase flow within columns (*Deckwer, 1992, p. 255-277*) (Chapter 3 Section 3.2). The traditional methods perturb flow and therefore make it difficult to obtain representative measurements. In this investigation a boundary inverse method has been successful in the analysis and measurement of the inside-wall heat transfer coefficient using Tikhonov regularisation (Section 5.7).

The objective as set out at the start of this chapter was to find the magnitudes of the inside-wall heat transfer coefficient for the cylinder concept, and that the magnitudes be representative of the flow investigated in Chapter 4. Apart from considering the affects of the

method/apparatus on the flow, principally the method (analysis) should be precise and capable of resolving phenomena responsible for the convection of heat. The accuracy of the measurement of the inside-wall heat transfer coefficient must then meet the precision to an acceptable level. As described in section 5.3, the engine of the inverse analysis is its sensitivity matrix. For this investigation Green's function provides the evaluation of the sensitivity elements belonging to this matrix (Section 5.3). For precision the form of the analytical solution using Green's function is explicitly described and it is found that the sensitivity elements are convergent series (Subheading 5.3.2). The time-dependency of the Green's function is a purely eigenvalue problem contained within a separable form and superfluous eigenvalues provide truncation (Section 5.2 and Subheading 5.3.2). Therefore, the time step of the inverse analysis can be easily adjusted to the required sampling rate without loss of precision (Subheadings 5.4.1 and 5.4.2).

Simulations are used to regularise the boundary inverse method against noise in the measured vector (Subheading 5.4.2). For Tikhonov regularisation the selection of the regularisation operator allows for stationary points (e.g. points of inflection, maxima and minima) along the curve of the sought boundary condition vector (Chapter 3 Section 3.8). By careful selection of the Tikhonov regularisation parameters the Tikhonov regularisation is localised to the stationary points preventing distortion of the inverse solutions (Subheading 5.4.2). For a second-order regularisation operator regularisation acts on the curvature of the sought boundary condition allowing for points of inflection (Subheading 5.4.2).

The thermocouples and acquisition modules have an accuracy that meets the precision of the inverse analysis described in Subheading 5.4.2, and the effects of noise on the inverse solutions is combated with the simulated Tikhonov regularisation and regularisation



coefficients (Sections 5.5 and 5.7). The systematic error of the thermocouples and acquisition modules is offset by calibration that is UKAS accredited (Section 5.5).

Transport phenomena belonging to the flow within the cylinder concept has been measured and analysed (Chapter 4 Section 4.11) (Section 5.7). The magnitudes of the inside-wall heat transfer coefficients have been obtained through the inverse solution of the normal heat flux and inside-wall temperature alongside measurement of fluid temperature (Sections 5.3, 5.4, 5.5, 5.6 and 5.7). Where the inside-wall heat transfer coefficients are constant around a mean over the transient decay of the inverse solutions, the flow structures are contained, and the heat transfer coefficients are representative of stationary flow (Figures 5.17, 5.24, 5.27 and 5.30) (Subheading 5.7.1). At height 100 mm the inside-wall heat transfer coefficients are not constant around a mean over the transient decay and a transient of longer duration and a lower sampling frequency is required to obtain heat transfer coefficients representative of stationary flow (Figures 5.21 and 5.33) (Subheading 5.7.1). The higher swarf occupancy at height 100 mm damps momentum transfer decreasing the periodicity of the flow i.e. the heat convection of the flow is over resolved by the 1 Hz sampling frequency of the inverse analysis (Section 5.7). The objective in terms of measurement of the inside-wall heat transfer coefficient, confidence in this measurement and its reproducibility is met. However, further work is recommended to obtain the inside-wall heat transfer coefficient at height 100 mm for stationary flow of superficial air velocity 4.1 cm/s.

The inverse analysis has measured the attainable magnitudes of the inside-wall heat transfer coefficient for the air-water-swarf flow investigated in Chapter 4. However, superficial gas velocities are likely to be reduced within the cylinder concept because of gaseous products from chemical dissolution of the swarf (Chapter 1 Section 1.3) (Chapter 2 Section 2.2). The

gaseous products of the chemical dissolution of swarf will aid the transport phenomena of the flow.

Parallel with the potential of fully 3-dimensional swirl flow discussed in Chapter 4 Section 4.12, both axial swarf occupancy and convection could be improved within the cylinder concept. The greater dispersion of swarf would improve momentum transfer to the water in regions of high swarf occupancy, and additional to the axial and radial convection, azimuthal convection would also contribute to the convection of heat towards the inside-wall.

## CHAPTER 5 FIGURES

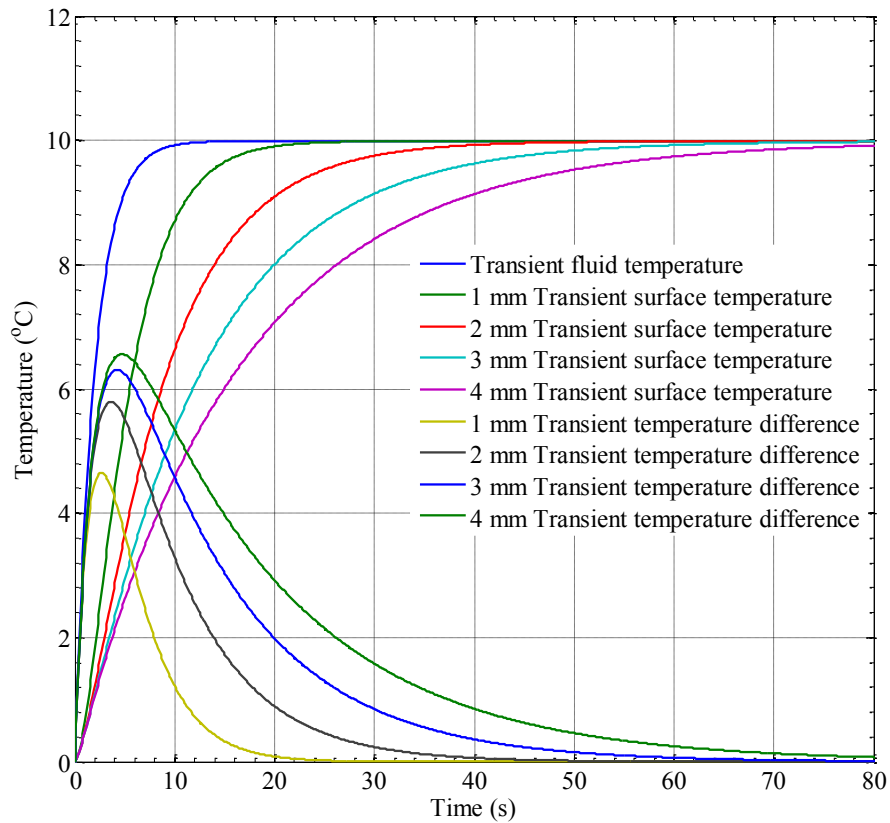


**Figure 5.1** Temperature transient of fluid calculated using equation (5.46). Temperature transients of the inside surface of the wall at  $r = a = 72$  mm calculated using equation (5.47) for different wall thickness ( $b - a$ ). Transient temperature differences between the fluid and inside surface of the wall at  $r = a = 72$  mm calculated using equation (5.46) and (5.47). In all calculations  $h = 1000 \text{ W/m}^2 \text{ }^\circ\text{C}$ .

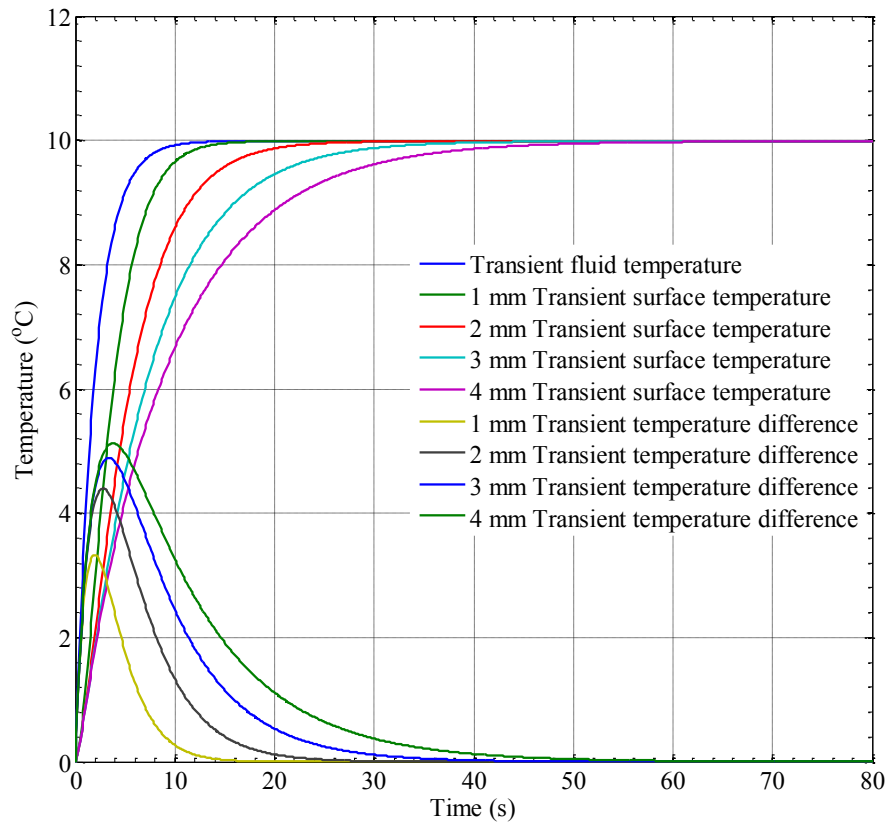


**Figure 5.2** Temperature transient of fluid calculated using equation (5.46). Temperature transients of the inside surface of the wall at  $r = a = 72$  mm calculated using equation (5.47) for different wall thickness ( $b - a$ ). Transient temperature differences between the fluid and inside surface of the wall at  $r = a = 72$  mm calculated using equation (5.46) and (5.47). In all calculations  $h = 2000 \text{ W/m}^2 \text{ }^\circ\text{C}$ .

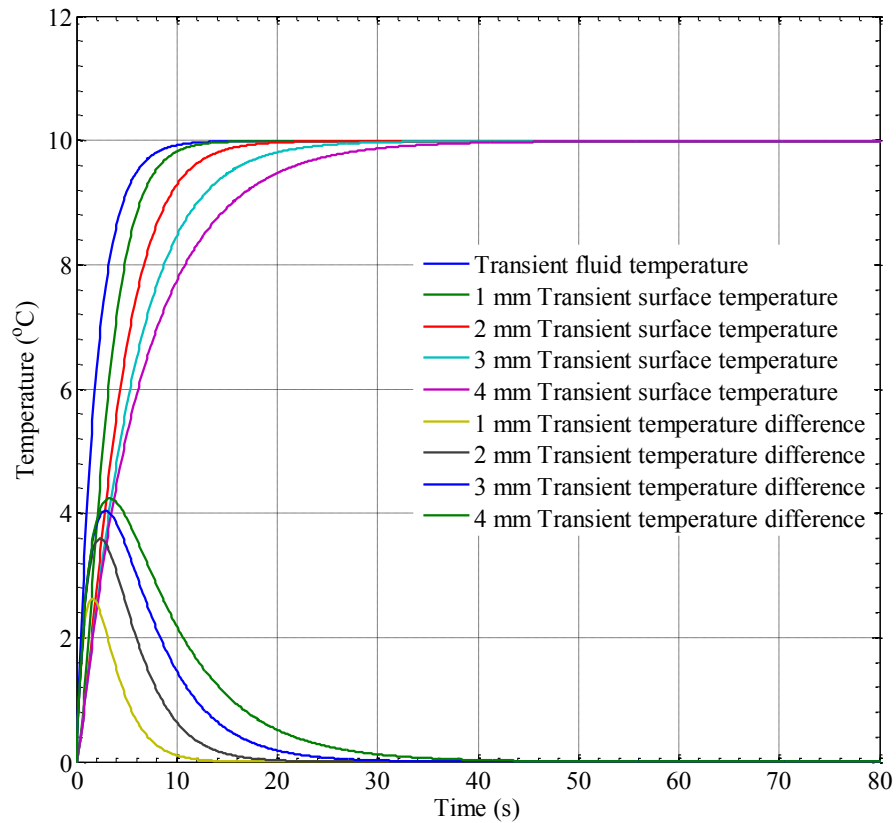


**Figure 5.3** Temperature transient of fluid calculated using equation (5.46). Temperature transients of the inside surface of the wall at  $r = a = 72$  mm calculated using equation (5.47) for different wall thickness ( $b - a$ ). Transient temperature differences between the fluid and inside surface of the wall at  $r = a = 72$  mm calculated using equation (5.46) and (5.47). In all calculations  $h = 3000 \text{ W/m}^2 \text{ }^\circ\text{C}$ .

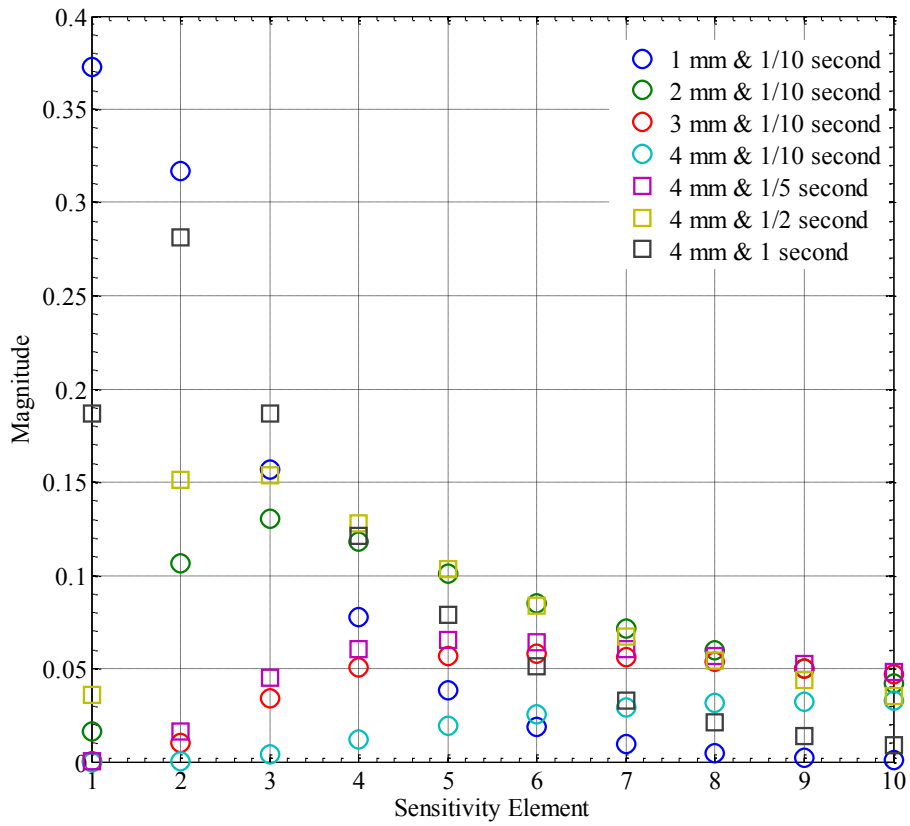


**Figure 5.4** Sensitivity elements for a Dirichlet boundary condition at  $r = a = 72$  mm calculated using equation (5.28) for different wall thickness ( $b - a$ ) and sampling rate.

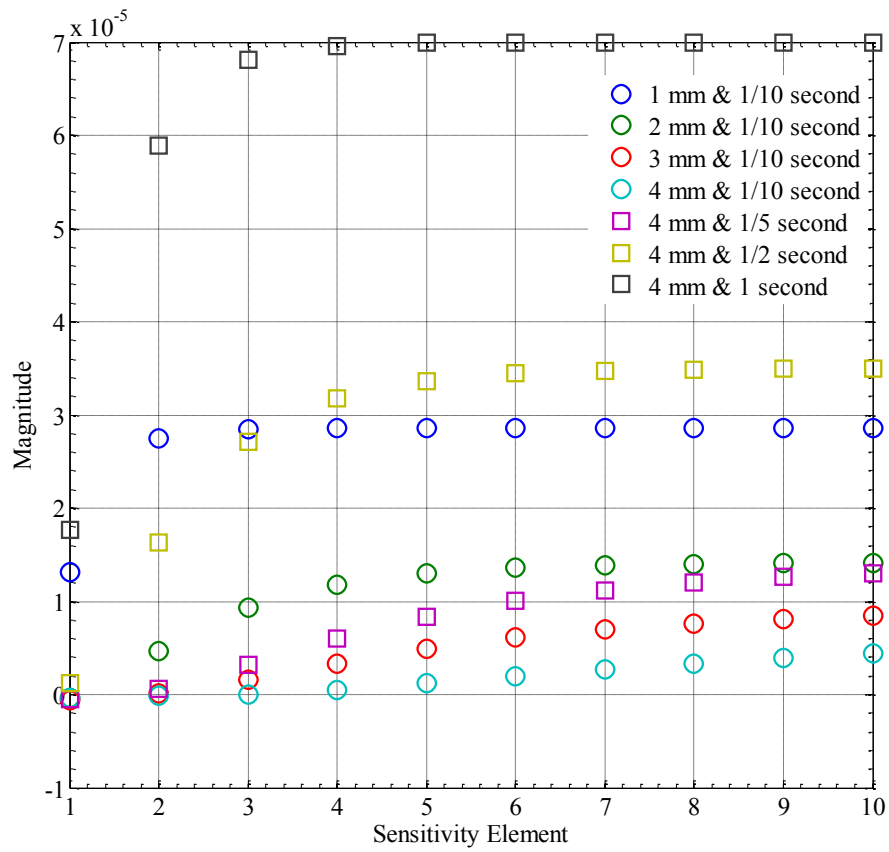


**Figure 5.5** Sensitivity elements for a Neumann boundary condition at  $r = a = 72$  mm calculated using equation (5.37) for different wall thickness ( $b - a$ ) and sampling rate.

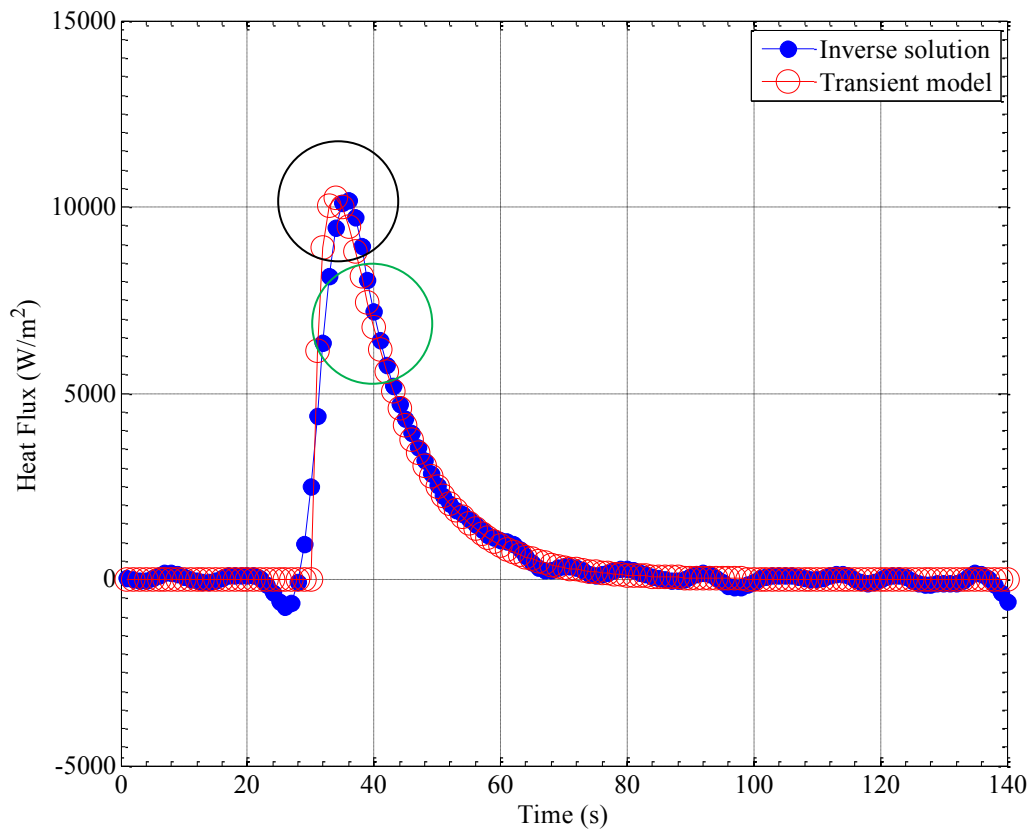


**Figure 5.6** Simulation of inverse solution of normal heat flux of inside surface of wall at  $r = a = 72$  mm calculated using equation (5.15) and the simulated temperature history of equation (5.47) and (5.51) at  $r = b = 76.25$  mm. Value of regularisation coefficient is  $10^{-7}$ . Sensitivity elements of sensitivity matrix of equation (5.15) calculated using equation (5.37). Centre of black circle gives point of maxima of transient model. Centre of green circle gives point of inflection of transient model.



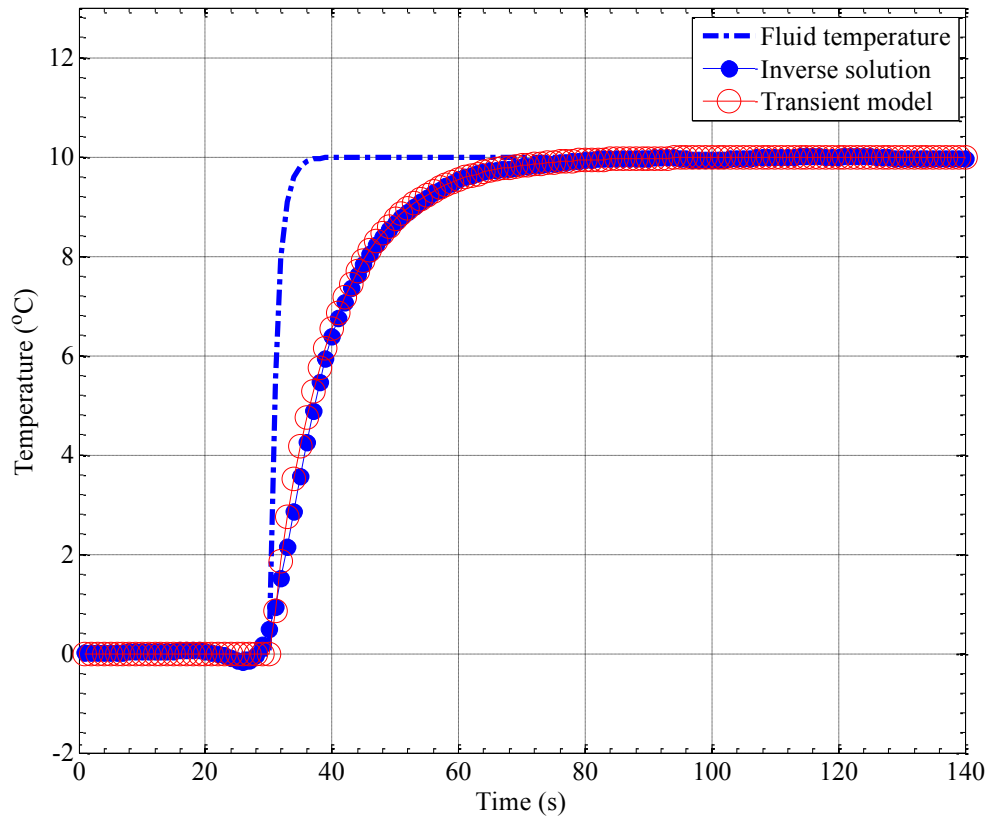


**Figure 5.7** Simulation of inverse solution of temperature of inside surface of wall at  $r = a = 72$  mm calculated using equation (5.15) and the simulated temperature history of equation (5.47) and (5.51) at  $r = b = 76.25$  mm. Value of regularisation coefficient is 10. Sensitivity elements of sensitivity matrix of equation (5.15) calculated using equation (5.28).

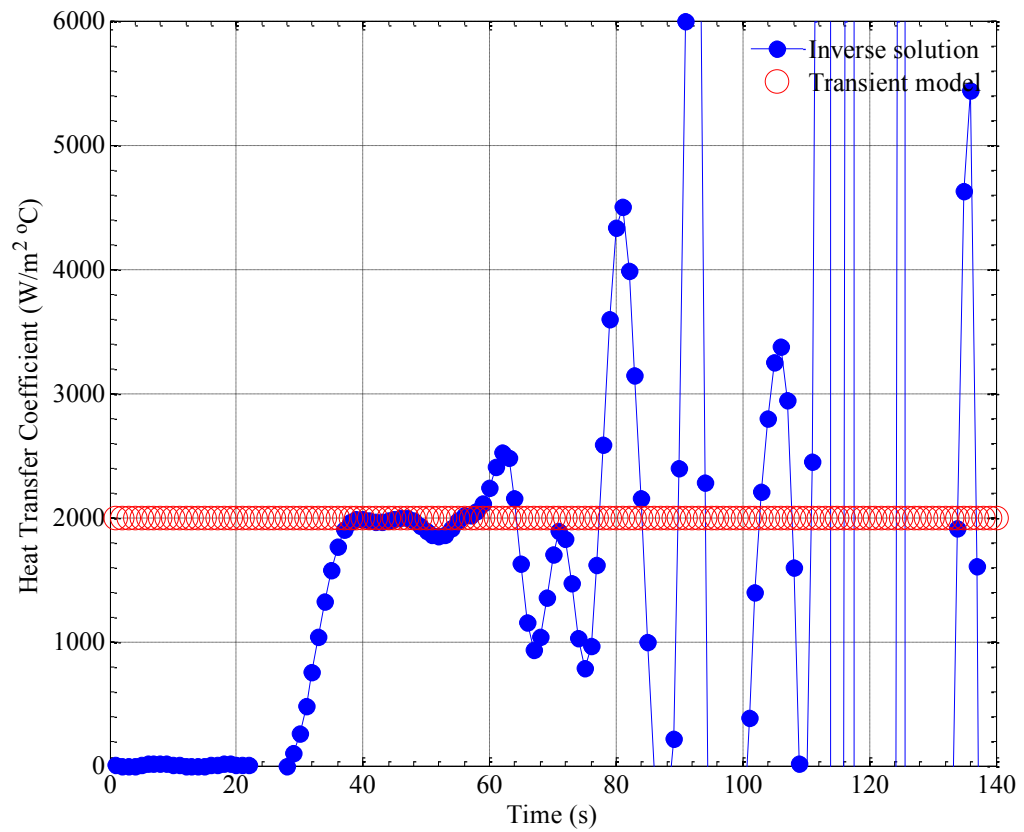
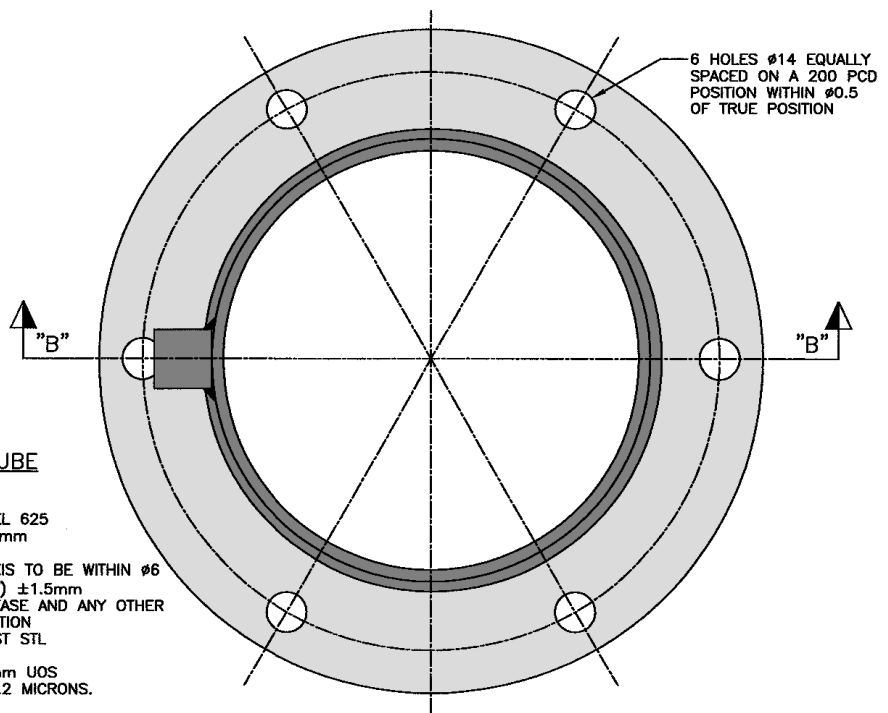
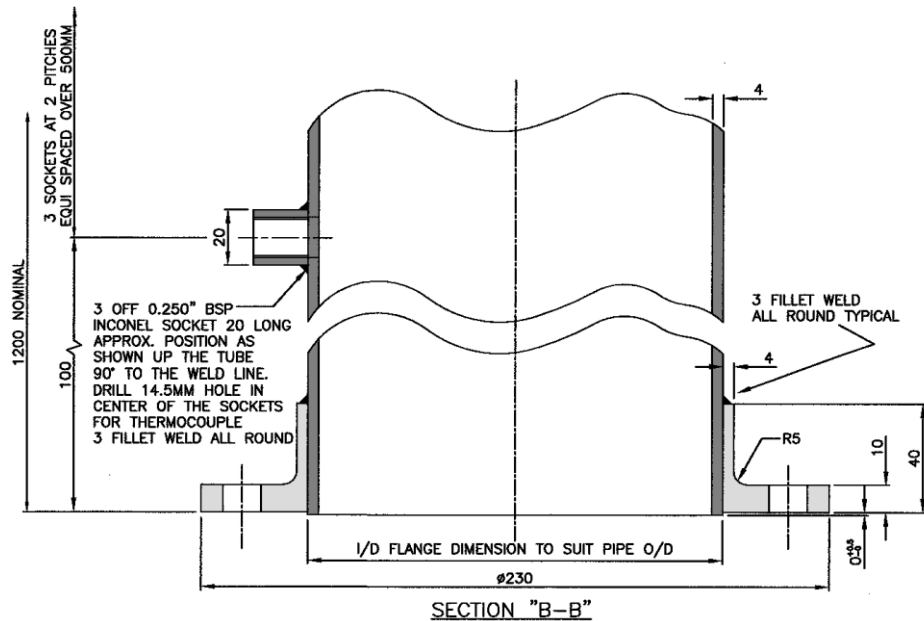


**Figure 5.8** Simulation of inverse solution of inside-wall heat transfer coefficient belonging to the inside surface of the wall at  $r = a = 72$  mm. Calculation of inside-wall heat transfer coefficient is achieved by dividing the calculated inverse heat flux of the inside surface of the wall at  $r = a = 72$  mm by the difference of the fluid temperature (equation (5.46)) and the calculated inverse temperature of the inside surface of the wall at  $r = a = 72$  mm.



#### ITEM 1 - FLANGED TUBE

MATERIAL - INCONEL 625  
FULLY WELDED CONSTRUCTION  
TUBE - MATERIAL - INCONEL 625  
TOLERANCES OD±1.5mm  
WALL ±0.25mm  
STRAIGHTNESS OF AXIS TO BE WITHIN Ø6  
ROUNDNESS (OVALITY) ±1.5mm  
FREE FROM OIL, GREASE AND ANY OTHER  
FORM OF CONTAMINATION  
FLANGE - MATERIAL - 304 ST STL  
MACHINE ALL OVER  
TOLERANCES ±0.25mm UOS  
SURFACE TEXTURE 3.2 MICRONS.  
SCALE - FULL SIZE

**Figure 5.9** A drawing of the inconel wall of the inconel cylinder used in the inverse analysis of the inside-wall heat transfer coefficient for air-water-swarf flow. Inconel bosses along the height of the column house mineral insulated thermocouples using PTFE compression fittings (Rolls-Royce drawings).

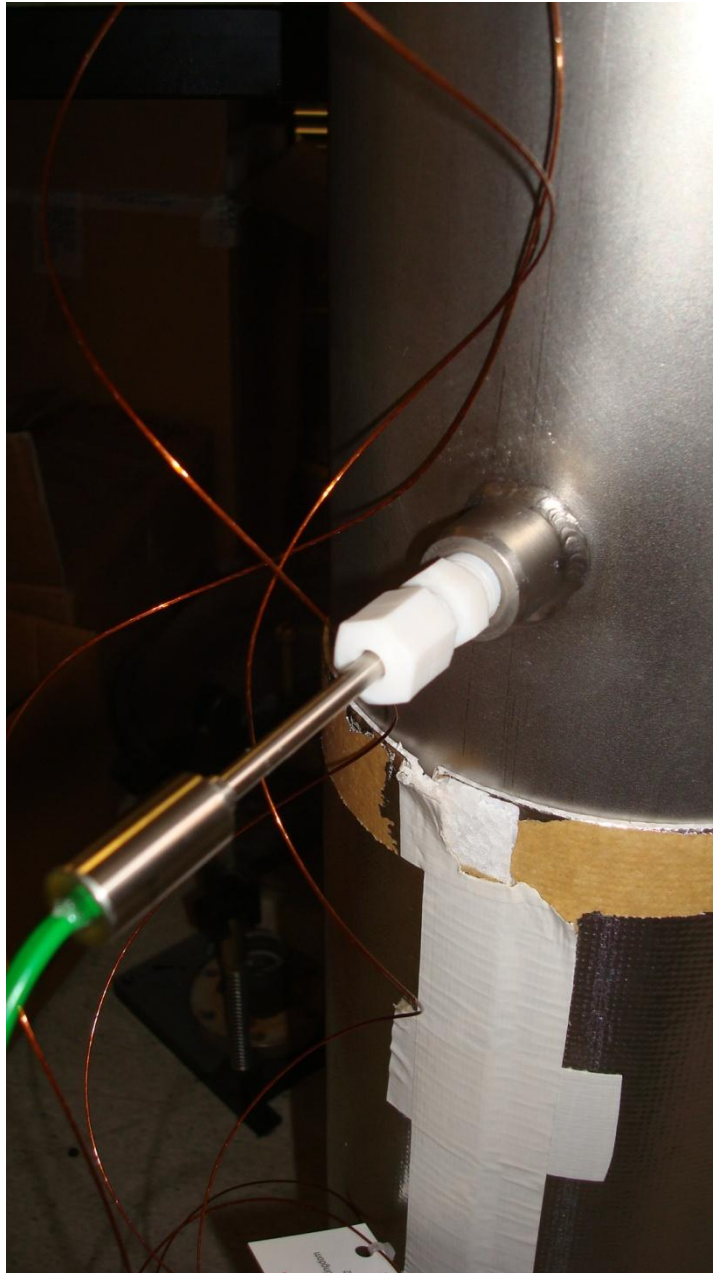


**Figure 5.10** A photograph of a PTFE compression fitting used to house mineral insulated thermocouples in inconel bosses.

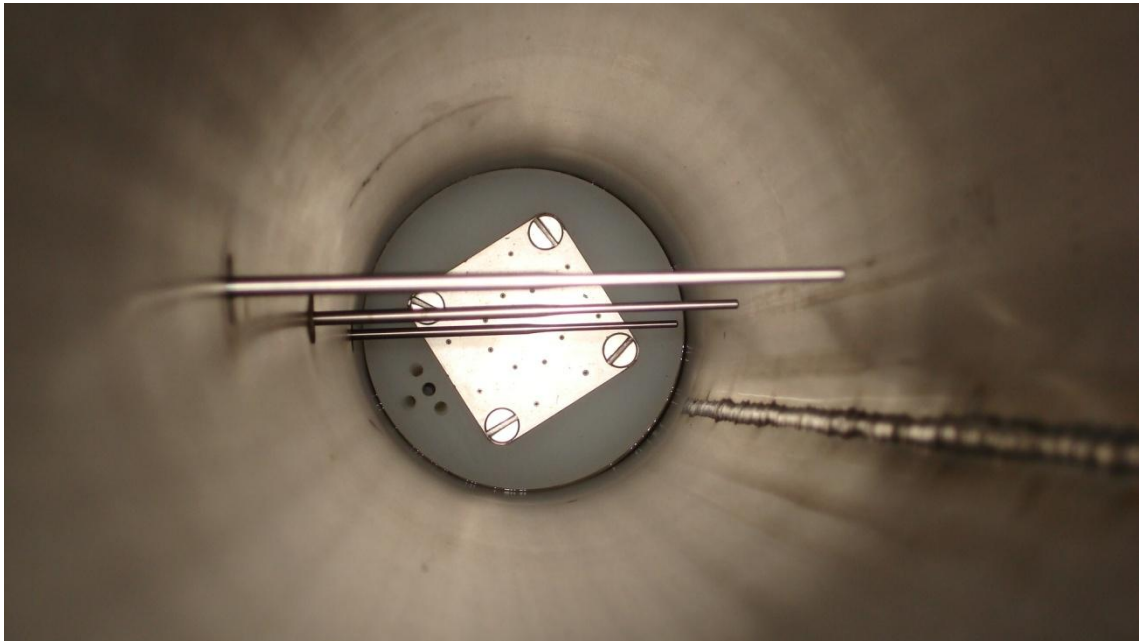


**Figure 5.11** A photograph of mineral insulated thermocouples inside inconel cylinder.

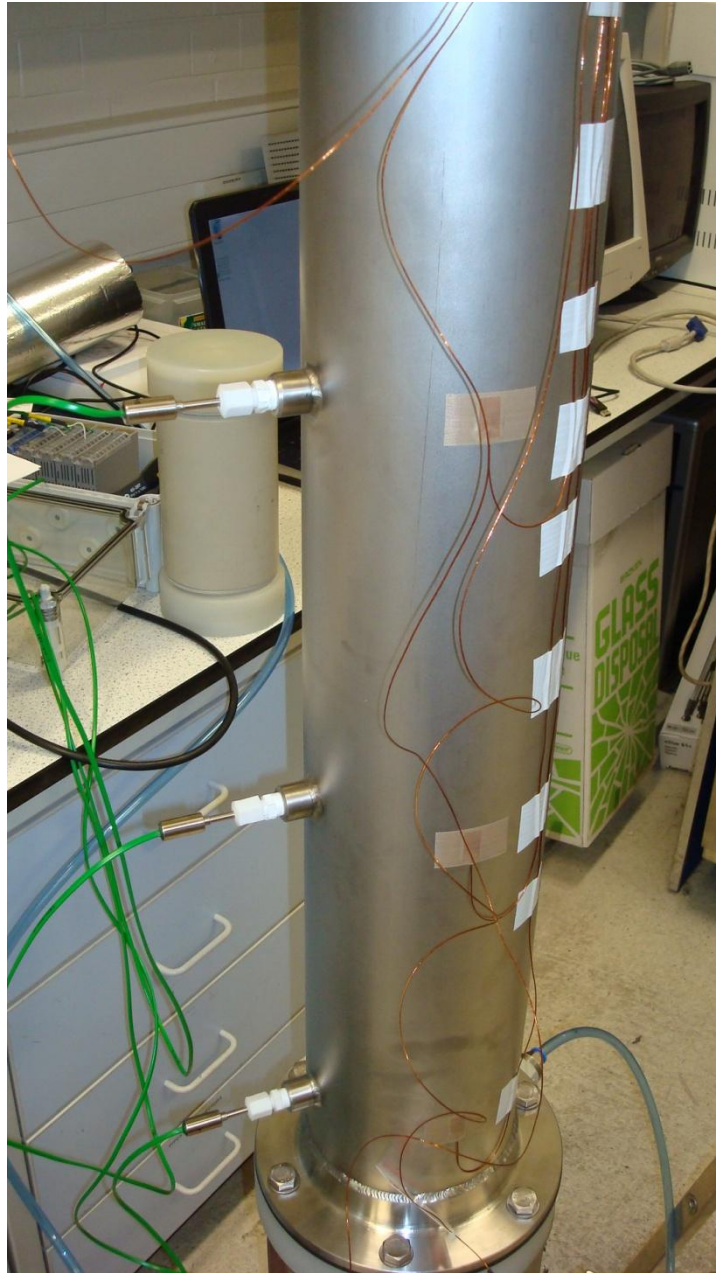


**Figure 5.12** A photograph of the location of polyimide thin film thermocouples on outside surface of inconel cylinder. Polyimide thermocouples are orthogonal to mineral insulated thermocouples.



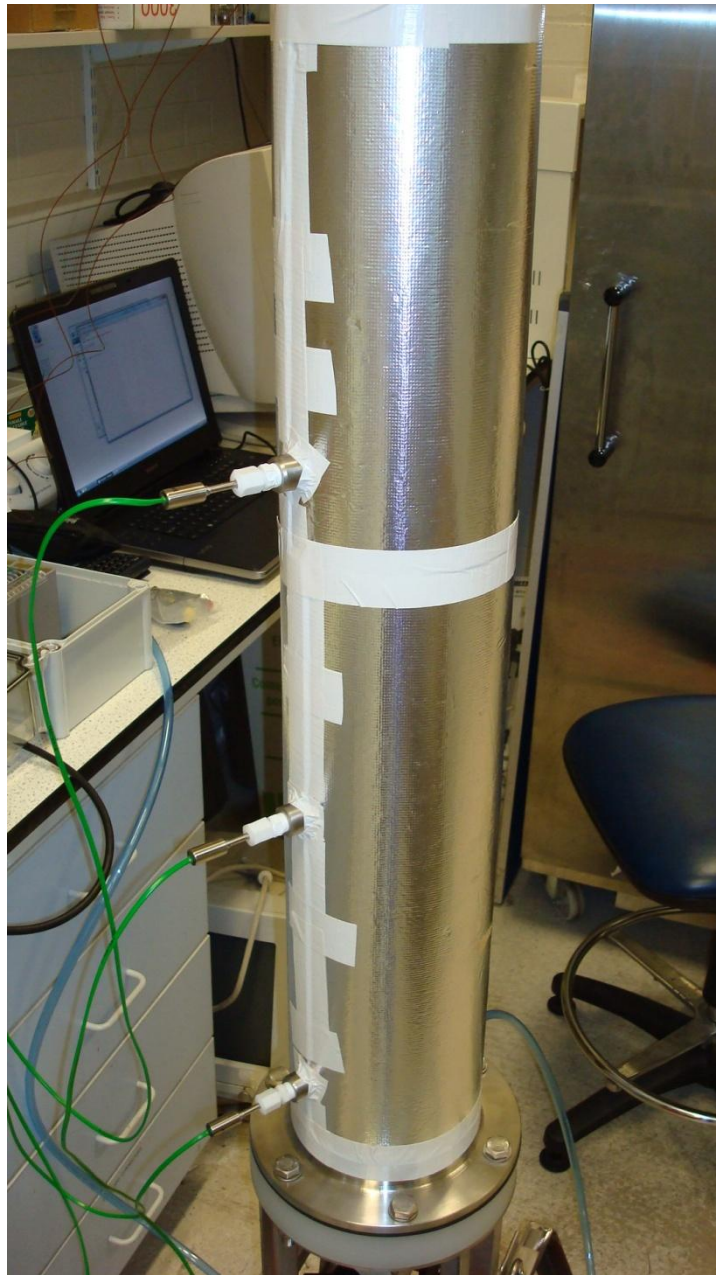


**Figure 5.13** A photograph of the insulated outside surface of inconel cylinder.

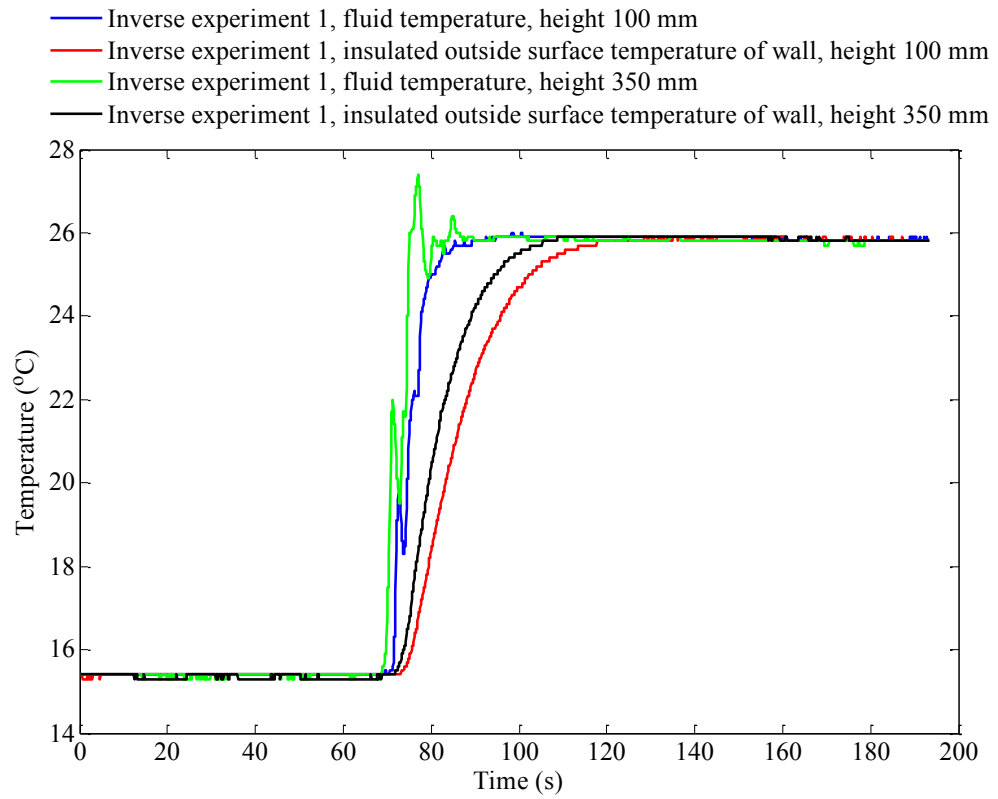


**Figure 5.14** Transient profile of temperature of fluid and insulated outside surface of the wall for inverse experiment 1 achieved from the addition of boiling water at the top of the inconel column. Temperature is measured at heights 100 mm and 350 mm.



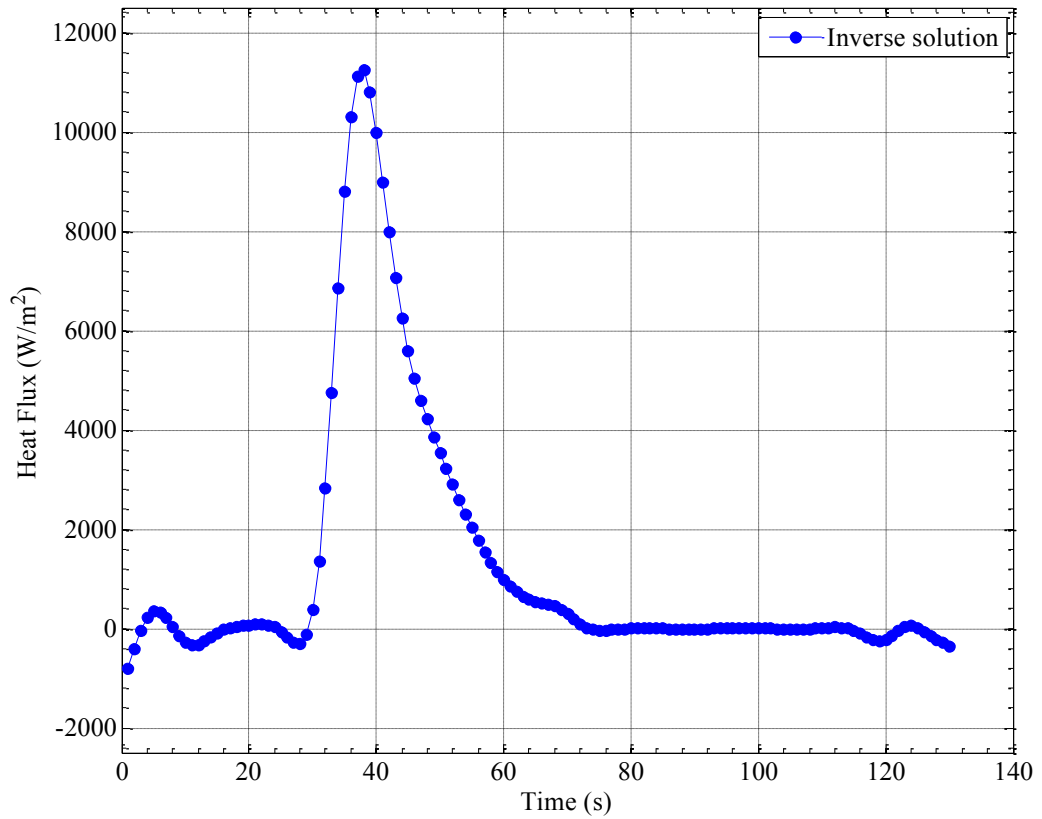


**Figure 5.15** Inverse solution of normal heat flux of inside surface of the wall at  $r = a = 72$  mm for experiment 1 at height 350 mm calculated using equation (5.15). The sensitivity matrix of equation (5.15) is constructed of sensitivity elements obtained from equation (5.37) for wall thickness  $(b - a) = 4.25$  mm. Superficial air velocity of 4.1 cm/s, 1 kg of dissolved sodium chloride, 500 g of loose swarf.

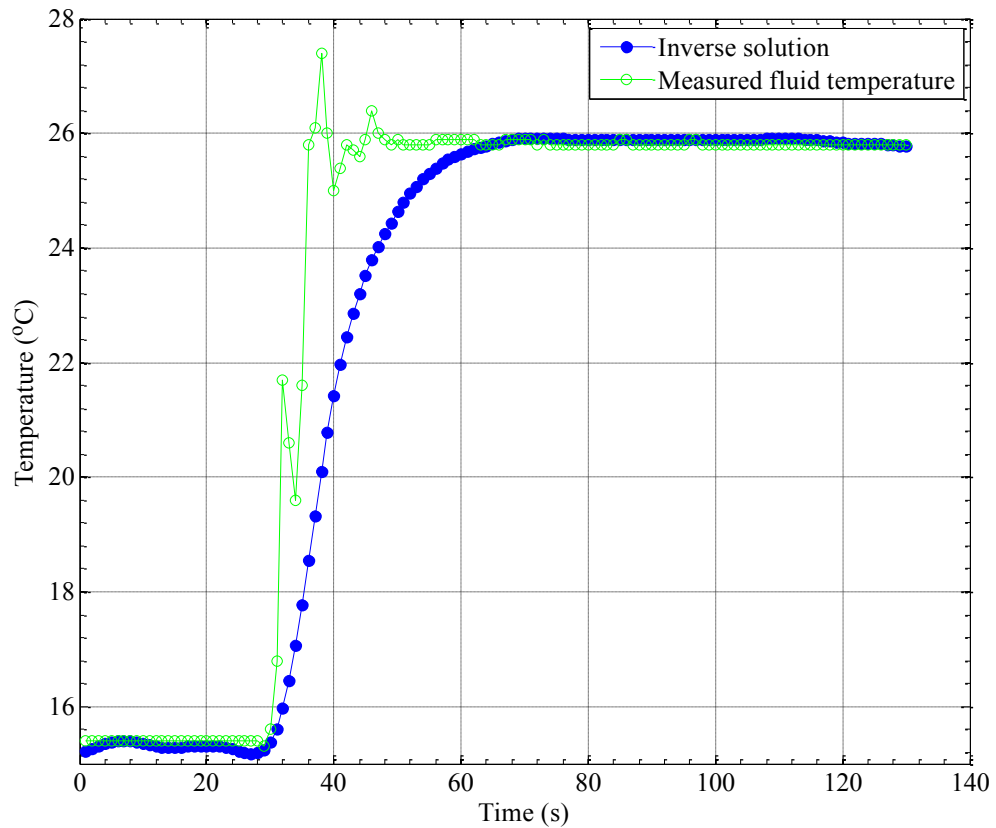


**Figure 5.16** Inverse solution of temperature of inside surface of the wall at  $r = a = 72$  mm for experiment 1 at height 350 mm calculated using equation (5.15). The sensitivity matrix of equation (5.15) is constructed of sensitivity elements obtained from equation (5.28) for wall thickness  $(b - a) = 4.25$  mm. Measured fluid temperature taken from mineral insulated thermocouple at height 350 mm. Superficial air velocity of 4.1 cm/s, 1 kg of dissolved sodium chloride, 500 g of loose swarf.

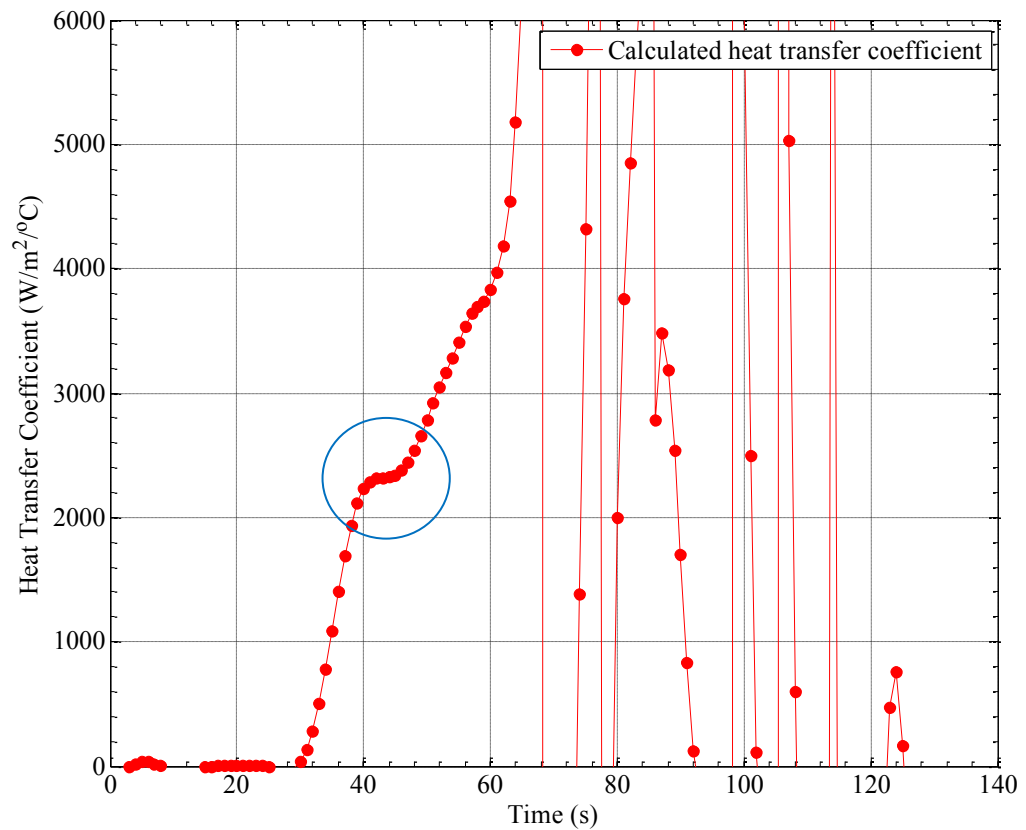


**Figure 5.17** Inverse solution of heat transfer coefficient belonging to inside surface of the wall at  $r = a = 72$  mm for experiment 1 at height 350 mm. The inverse normal heat flux is divided by the difference between the inverse temperature of the inside surface of the wall at  $r = a = 72$  mm and the measured fluid temperature at height 350 mm. The centre of the circle indicates where Tikhonov regularisation is localised and where the inside-wall heat transfer coefficient is resolved. Superficial air velocity 4.1 cm/s, 1 kg of dissolved sodium chloride, 500 g of loose swarf.

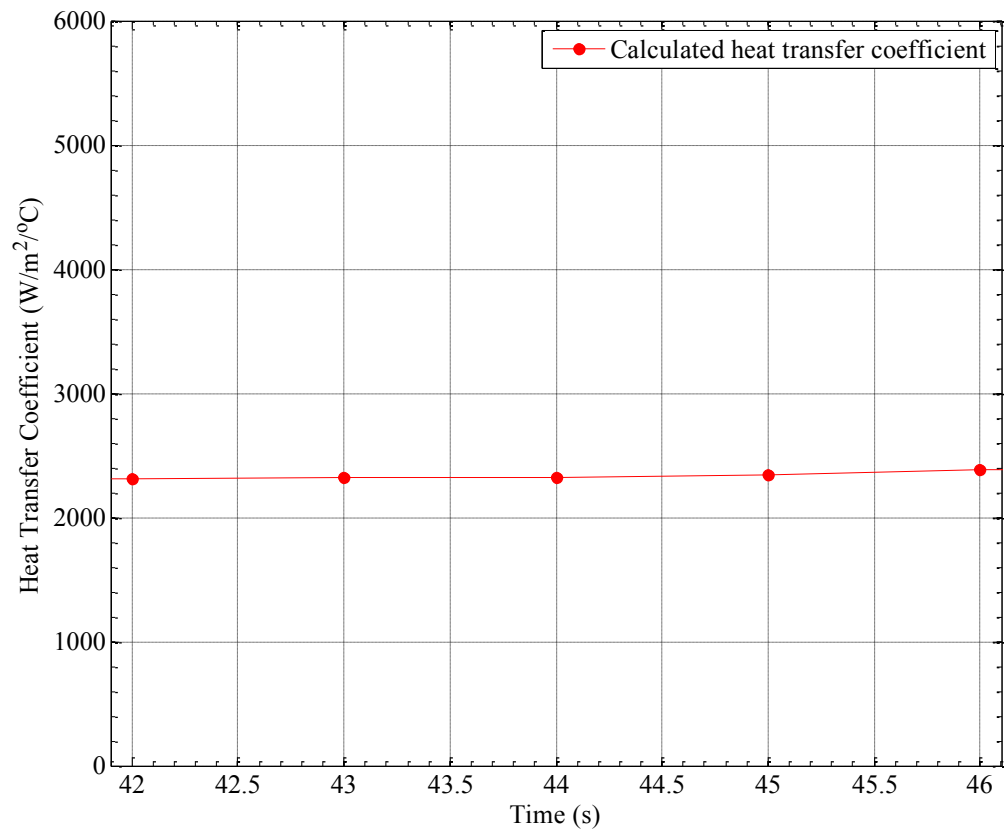


**Figure 5.18** Inverse solution of heat transfer coefficient belonging to inside surface of the wall at  $r = a = 72$  mm for experiment 1 at height 350 mm. The inverse normal heat flux is divided by the difference between the inverse solution of temperature of the inside surface of the wall at  $r = a = 72$  mm and the measured fluid temperature at height 350 mm. Superficial air velocity 4.1 cm/s, 1 kg of dissolved sodium chloride, 500 g of loose swarf.

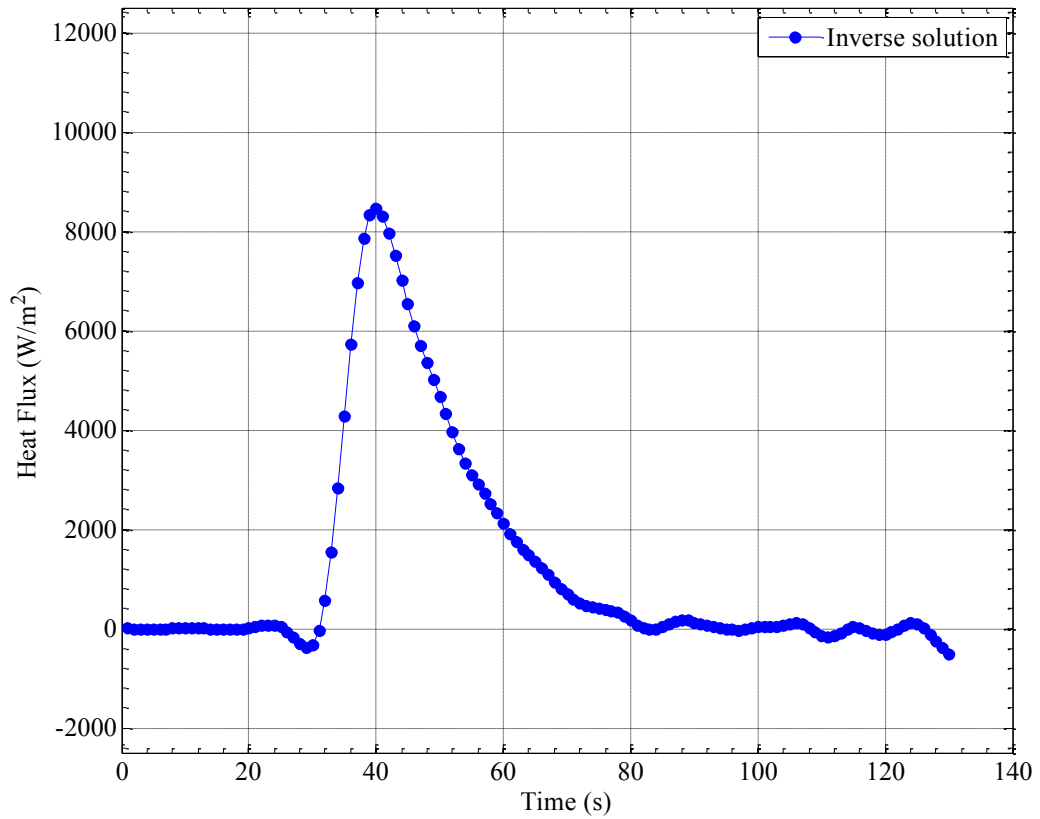


**Figure 5.19** Inverse solution of normal heat flux of inside surface of the wall at  $r = a = 72$  mm for experiment 1 at height 100 mm calculated using equation (5.15). The sensitivity matrix of equation (5.15) is constructed of sensitivity elements obtained from equation (5.37) for wall thickness  $(b - a) = 4.25$  mm. Superficial air velocity of 4.1 cm/s, 1 kg of dissolved sodium chloride, 500 g of loose swarf.

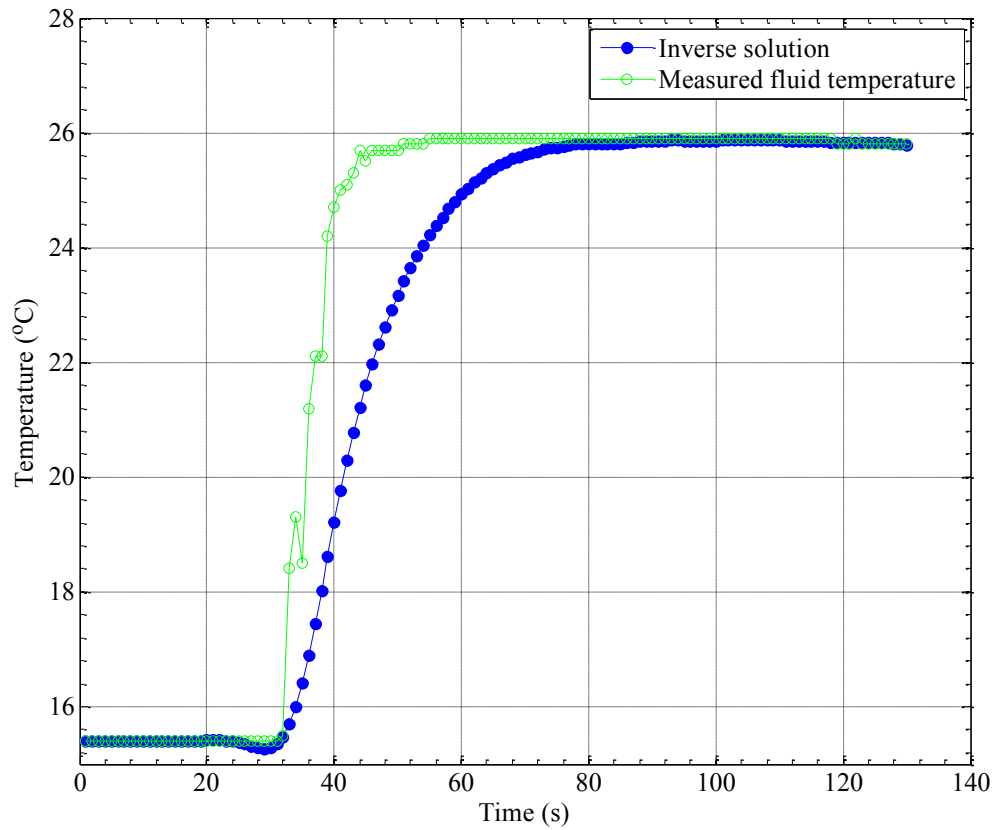


**Figure 5.20** Inverse solution of temperature of inside surface of the wall at  $r = a = 72$  mm for experiment 1 at height 100 mm calculated using equation (5.15). The sensitivity matrix of equation (5.15) is constructed of sensitivity elements obtained from equation (5.28) for wall thickness  $(b - a) = 4.25$  mm. Measured fluid temperature taken from mineral insulated thermocouple at height 100 mm. Superficial air velocity of 4.1 cm/s, 1 kg of dissolved sodium chloride, 500 g of loose swarf.

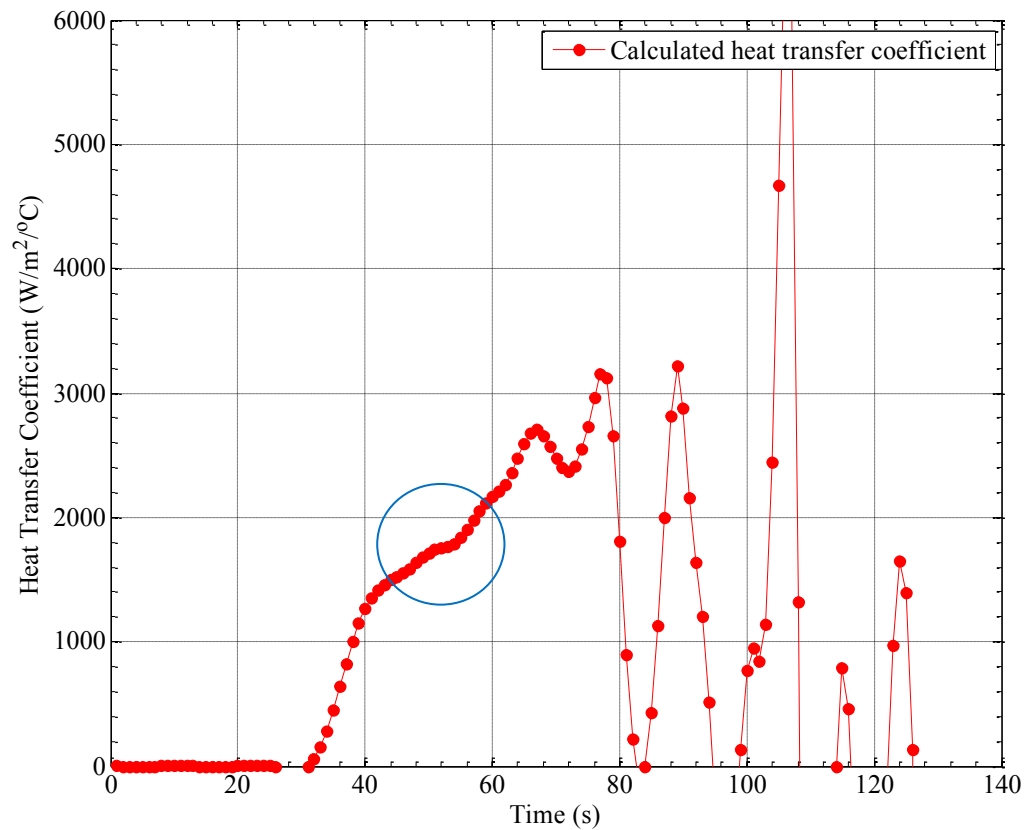


**Figure 5.21** Inverse solution of heat transfer coefficient belonging to inside surface of the wall at  $r = a = 72$  mm for experiment 1 at height 100 mm. The inverse normal heat flux is divided by the difference between the inverse temperature of the inside surface of the wall at  $r = a = 72$  mm and the measured fluid temperature at height 100 mm. The centre of the circle indicates where Tikhonov regularisation is localised and where the inside-wall heat transfer coefficient is resolved. Superficial air velocity 4.1 cm/s, 1 kg of dissolved sodium chloride, 500 g of loose swarf.

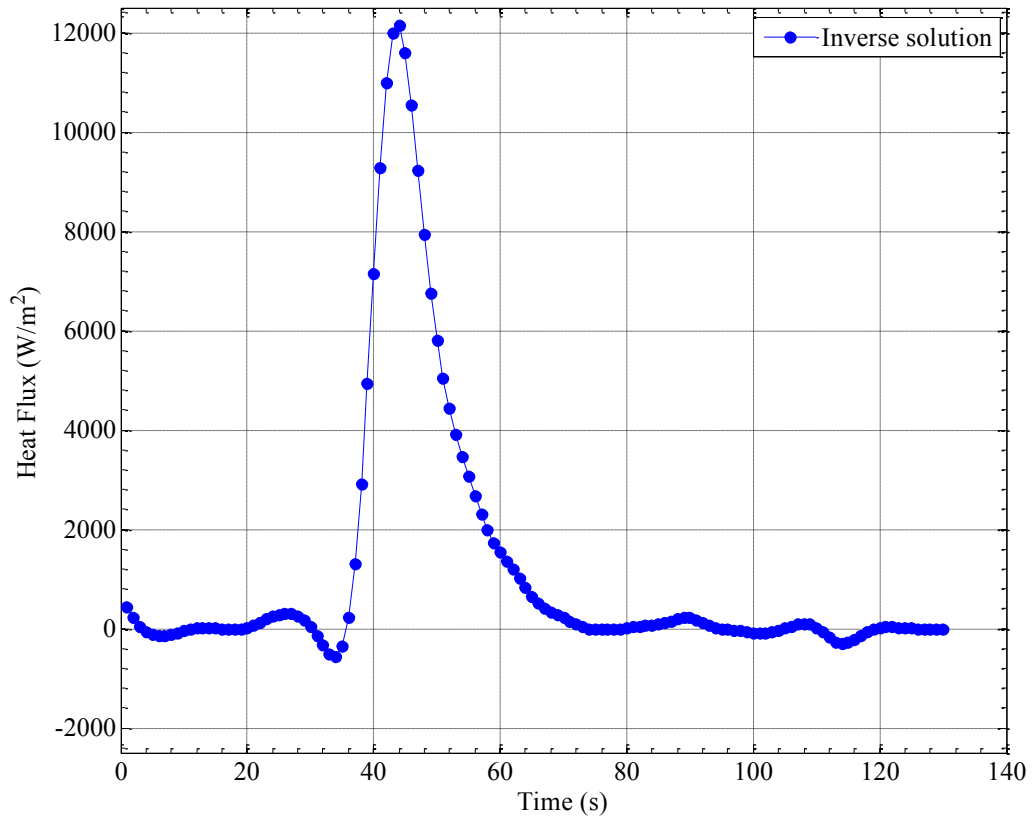


**Figure 5.22** Inverse solution of normal heat flux of inside surface of the wall at  $r = a = 72$  mm for experiment 2 at height 350 mm calculated using equation (5.15). The sensitivity matrix of equation (5.15) is constructed of sensitivity elements obtained from equation (5.37) for wall thickness  $(b - a) = 4.25$  mm. Superficial air velocity of 7.2 cm/s, 500 g of loose swarf.



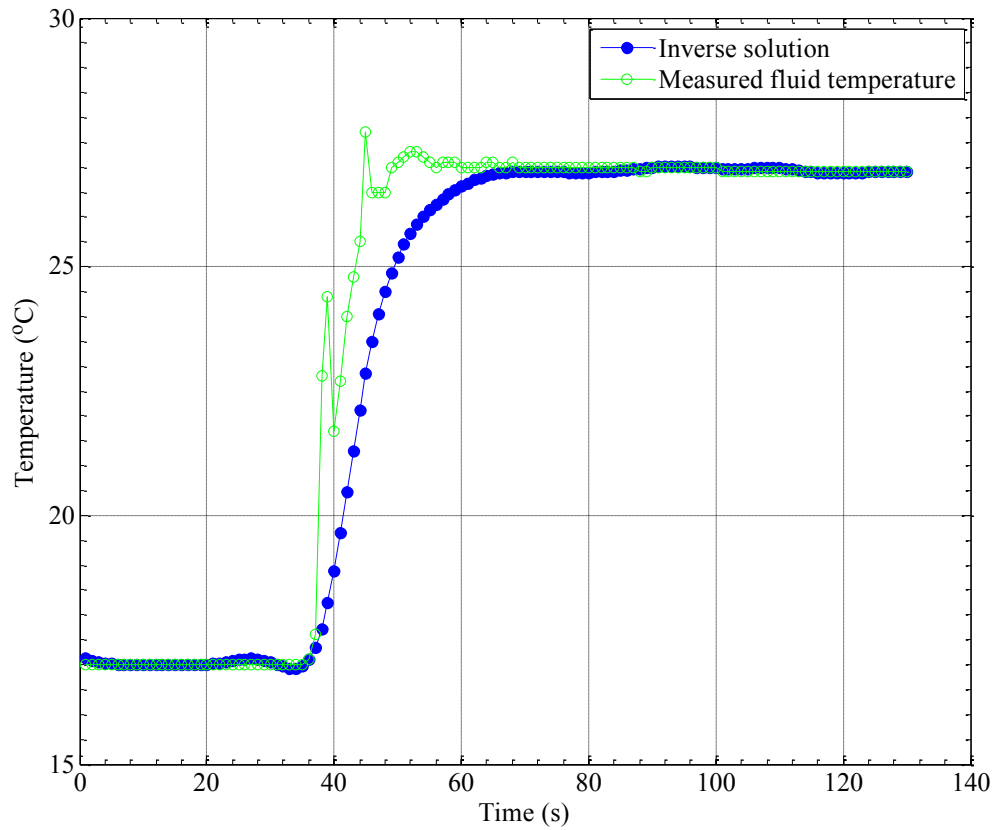


**Figure 5.23** Inverse solution of temperature of inside surface of the wall at  $r = a = 72$  mm for experiment 1 at height 350 mm calculated using equation (5.15). The sensitivity matrix of equation (5.15) is constructed of sensitivity elements obtained from equation (5.28) for wall thickness  $(b - a) = 4.25$  mm. Measured fluid temperature taken from mineral insulated thermocouple at height 350 mm. Superficial air velocity of 7.2 cm/s, 500 g of loose swarf.

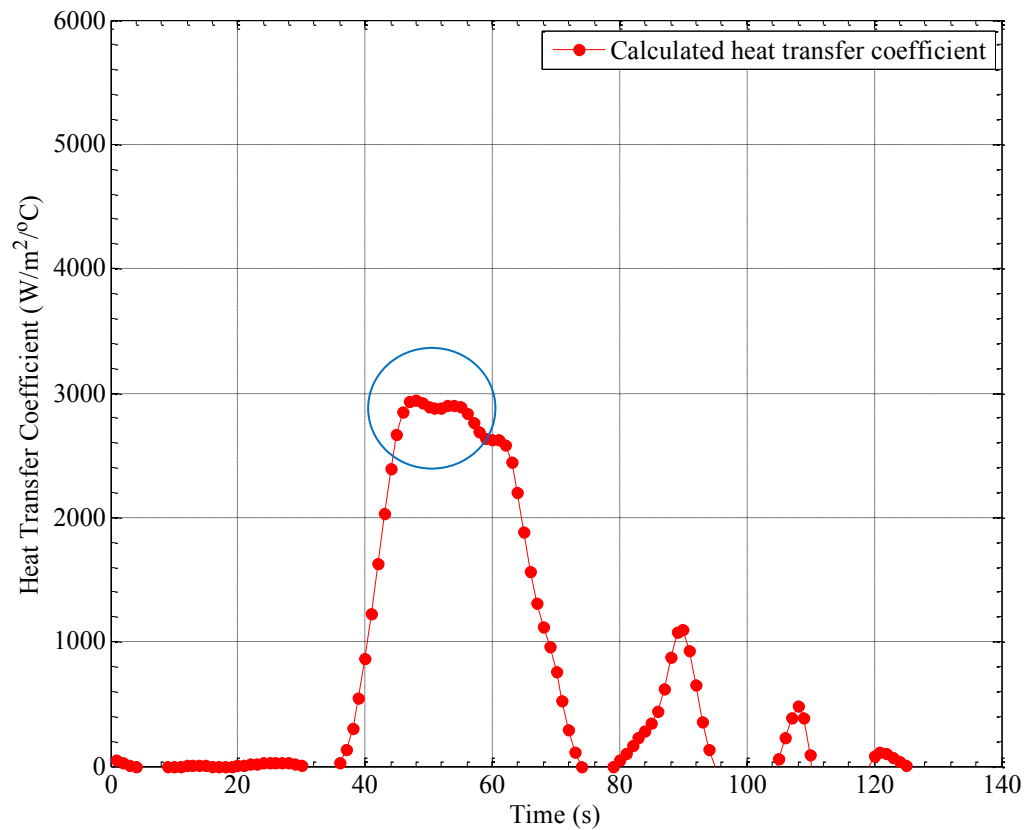


**Figure 5.24** Inverse solution of heat transfer coefficient belonging to inside surface of the wall at  $r = a = 72$  mm for experiment 2 at height 350 mm. The inverse normal heat flux is divided by the difference between the inverse temperature of the inside surface of the wall at  $r = a = 72$  mm and the measured fluid temperature at height 350 mm. The centre of the circle indicates where Tikhonov regularisation is localised and where the inside-wall heat transfer coefficient is resolved. Superficial air velocity 7.2 cm/s, 500 g of loose swarf.

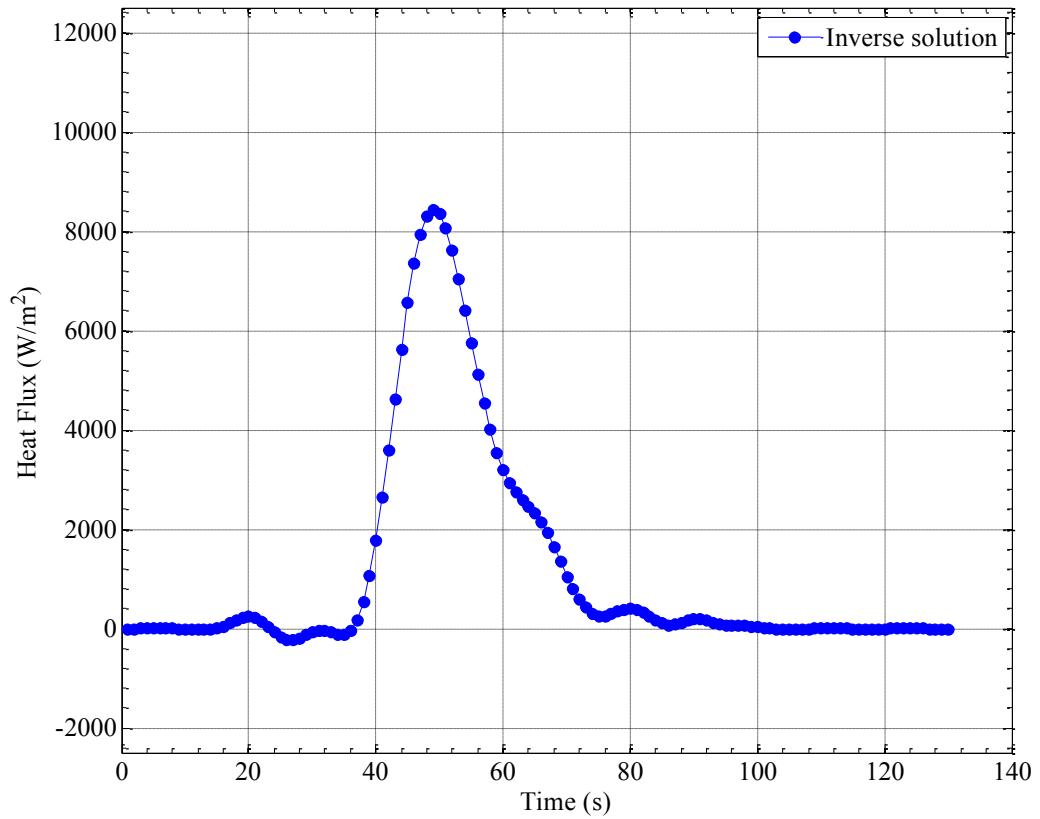


**Figure 5.25** Inverse solution of normal heat flux of inside surface of the wall at  $r = a = 72$  mm for experiment 2 at height 100 mm calculated using equation (5.15). The sensitivity matrix of equation (5.15) is constructed of sensitivity elements obtained from equation (5.37) for wall thickness  $(b - a) = 4.25$  mm. Superficial air velocity of 7.2 cm/s, 500 g of loose swarf.

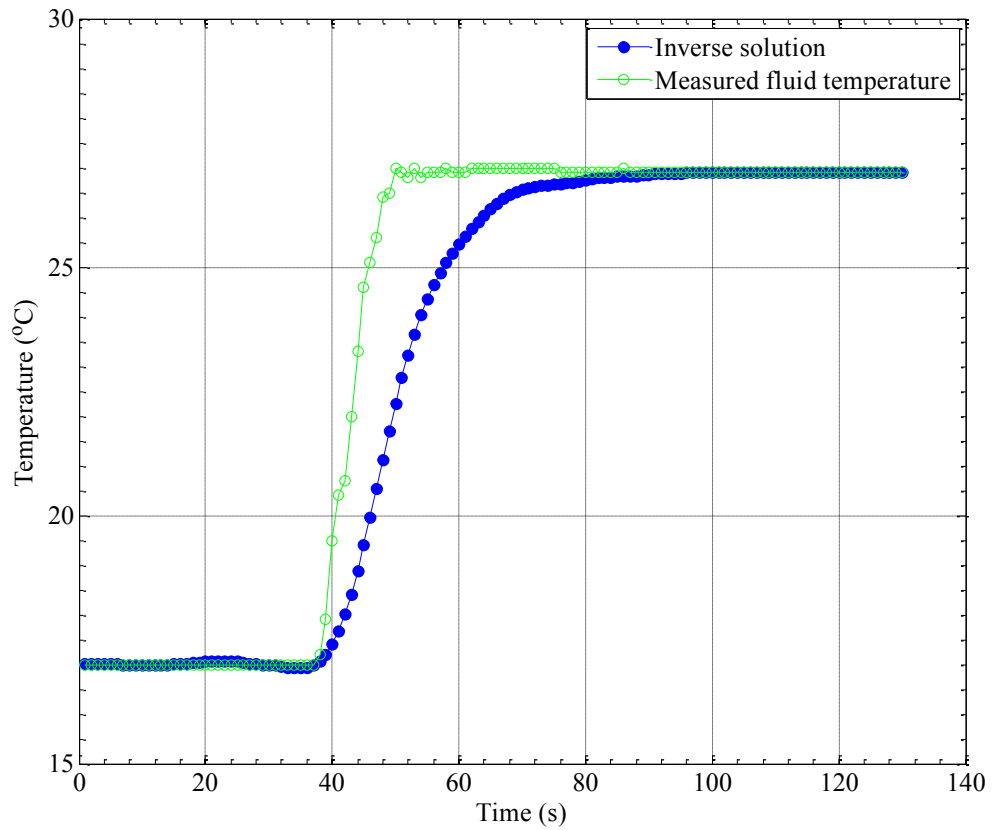


**Figure 5.26** Inverse solution of temperature of inside surface of the wall at  $r = a = 72$  mm for experiment 2 at height 100 mm calculated using equation (5.15). The sensitivity matrix of equation (5.15) is constructed of sensitivity elements obtained from equation (5.28) for wall thickness  $(b - a) = 4.25$  mm. Measured fluid temperature taken from mineral insulated thermocouple at height 100 mm. Superficial air velocity of 7.2 cm/s, 500 g of loose swarf.

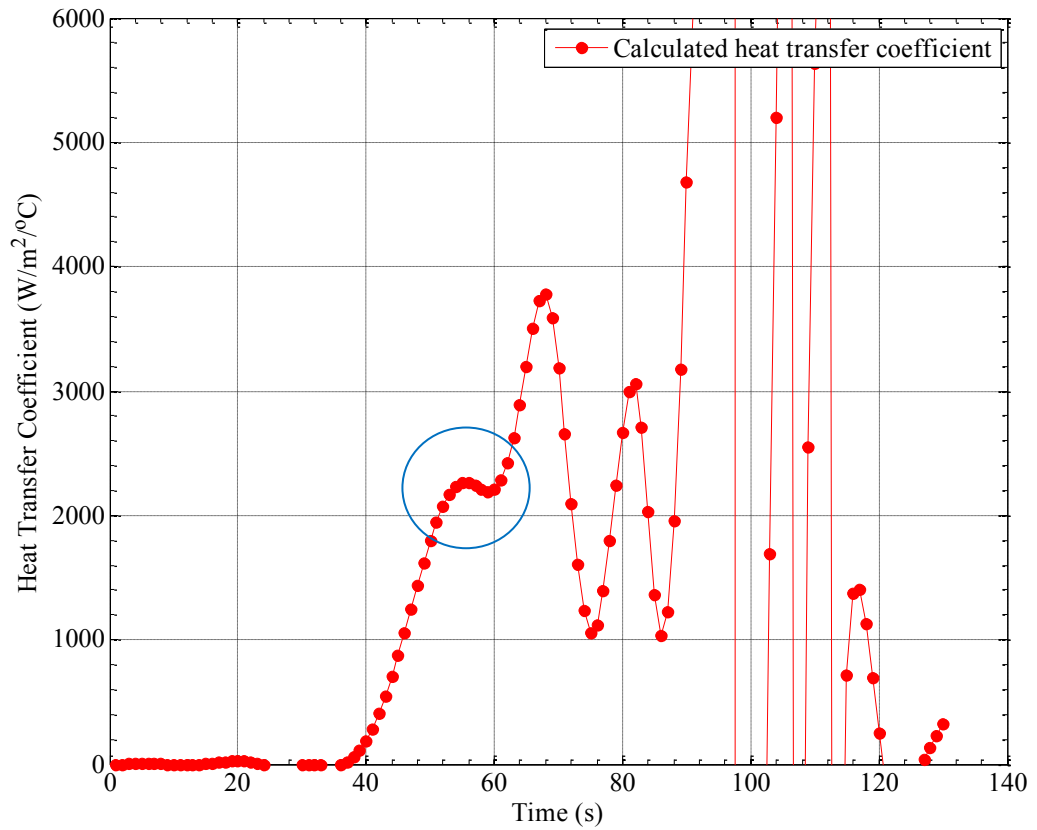


**Figure 5.27** Inverse solution of heat transfer coefficient belonging to inside surface of the wall at  $r = a = 72$  mm for experiment 2 at height 100 mm. The inverse normal heat flux is divided by the difference between the inverse temperature of the inside surface of the wall at  $r = a = 72$  mm and the measured fluid temperature at height 100 mm. The centre of the circle indicates where Tikhonov regularisation is localised and where the inside-wall heat transfer coefficient is resolved. Superficial air velocity 7.2 cm/s, 500 g of loose swarf.

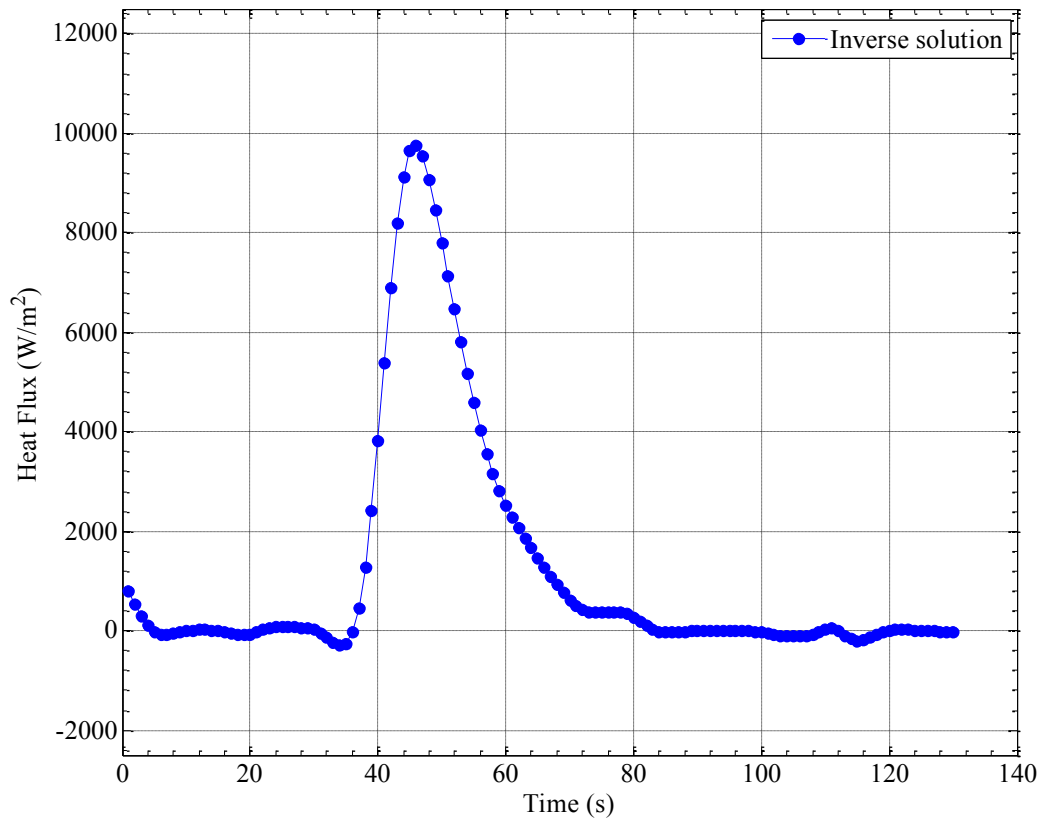


**Figure 5.28** Inverse solution of normal heat flux of inside surface of the wall at  $r = a = 72$  mm for experiment 3 at height 350 mm calculated using equation (5.15). The sensitivity matrix of equation (5.15) is constructed of sensitivity elements obtained from equation (5.37) for wall thickness  $(b - a) = 4.25$  mm. Superficial air velocity of 4.1 cm/s, 1 kg of dissolved sodium chloride, 500 g of loose swarf.

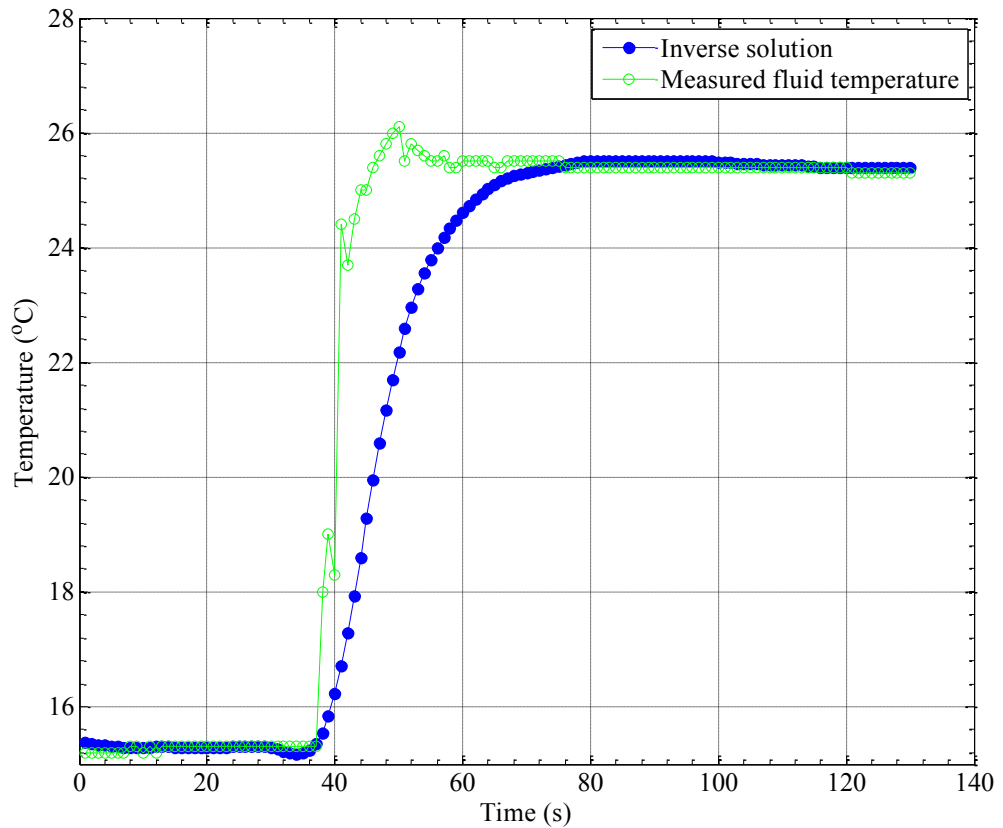


**Figure 5.29** Inverse solution of temperature of inside surface of the wall at  $r = a = 72$  mm for experiment 3 at height 350 mm calculated using equation (5.15). The sensitivity matrix of equation (5.15) is constructed of sensitivity elements obtained from equation (5.28) for wall thickness  $(b - a) = 4.25$  mm. Measured fluid temperature taken from mineral insulated thermocouple at height 350 mm. Superficial air velocity of 4.1 cm/s, 1 kg of dissolved sodium chloride, 500 g of loose swarf.

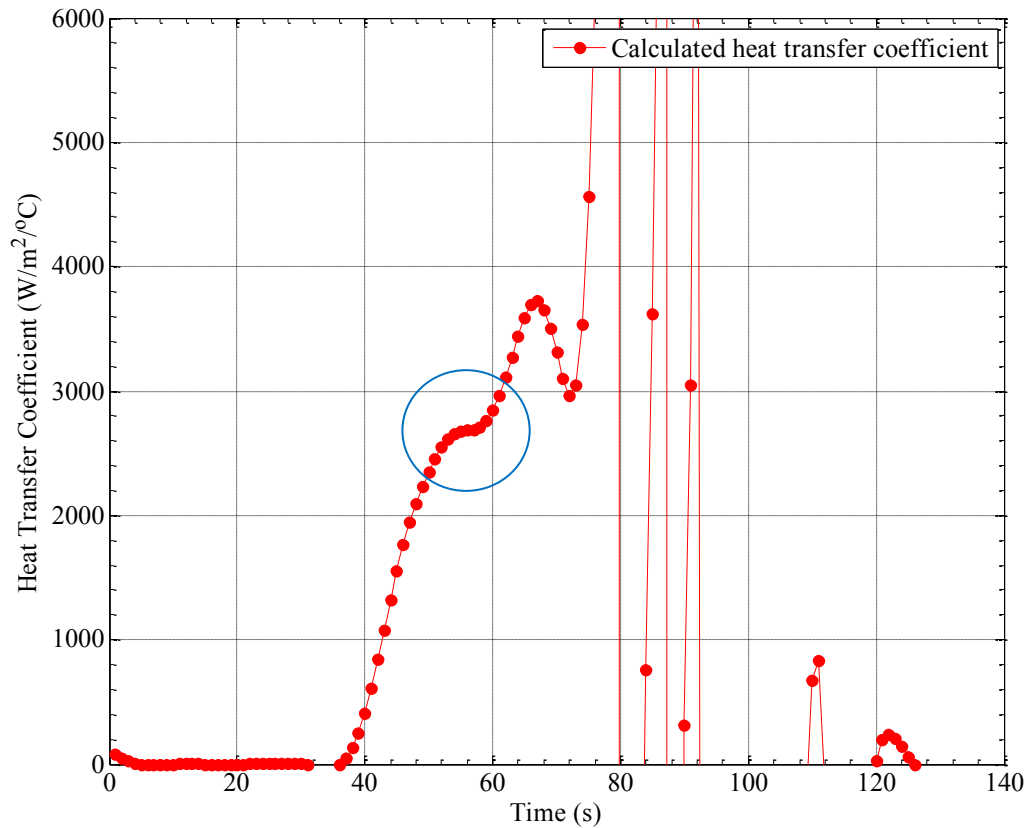


**Figure 5.30** Inverse solution of heat transfer coefficient belonging to inside surface of the wall at  $r = a = 72$  mm for experiment 3 at height 350 mm. The inverse normal heat flux is divided by the difference between the inverse temperature of the inside surface of the wall at  $r = a = 72$  mm and the measured fluid temperature at height 350 mm. The centre of the circle indicates where Tikhonov regularisation is localised and where the inside-wall heat transfer coefficient is resolved. Superficial air velocity 4.1 cm/s, 1 kg of dissolved sodium chloride, 500 g of loose swarf.



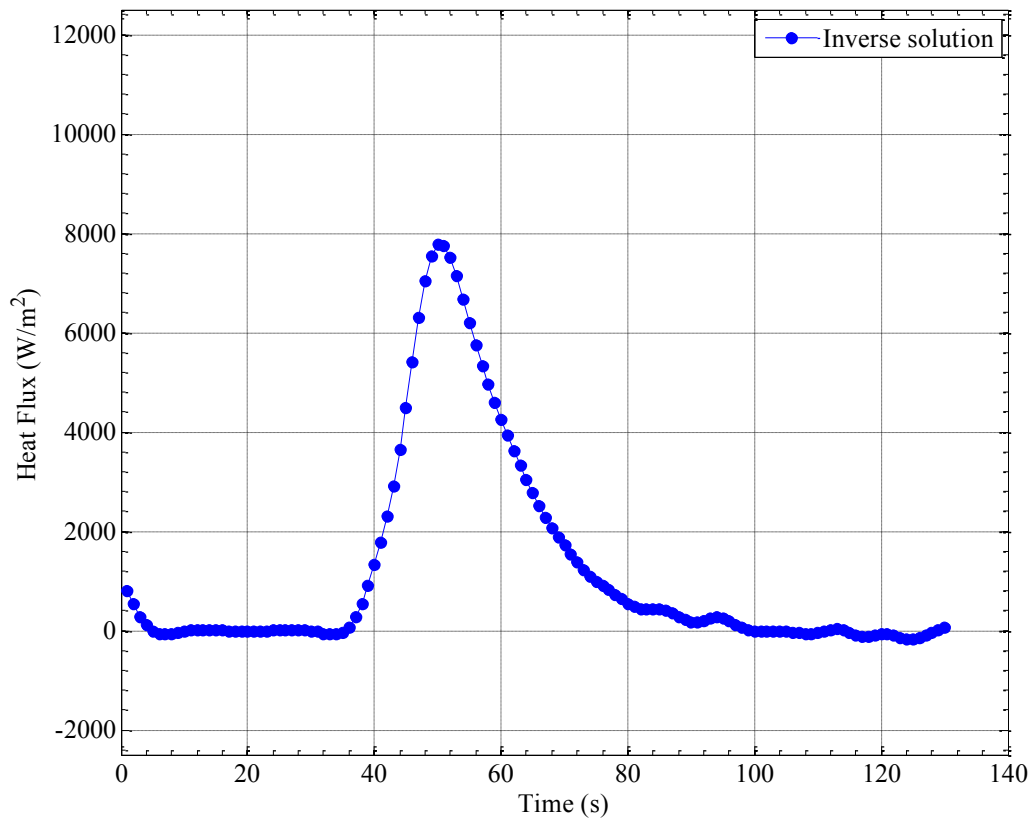


**Figure 5.31** Inverse solution of normal heat flux of inside surface of the wall at  $r = a = 72$  mm for experiment 3 at height 100 mm calculated using equation (5.15). The sensitivity matrix of equation (5.15) is constructed of sensitivity elements obtained from equation (5.37) for wall thickness  $(b - a) = 4.25$  mm. Superficial air velocity of 4.1 cm/s, 1 kg of dissolved sodium chloride, 500 g of loose swarf.

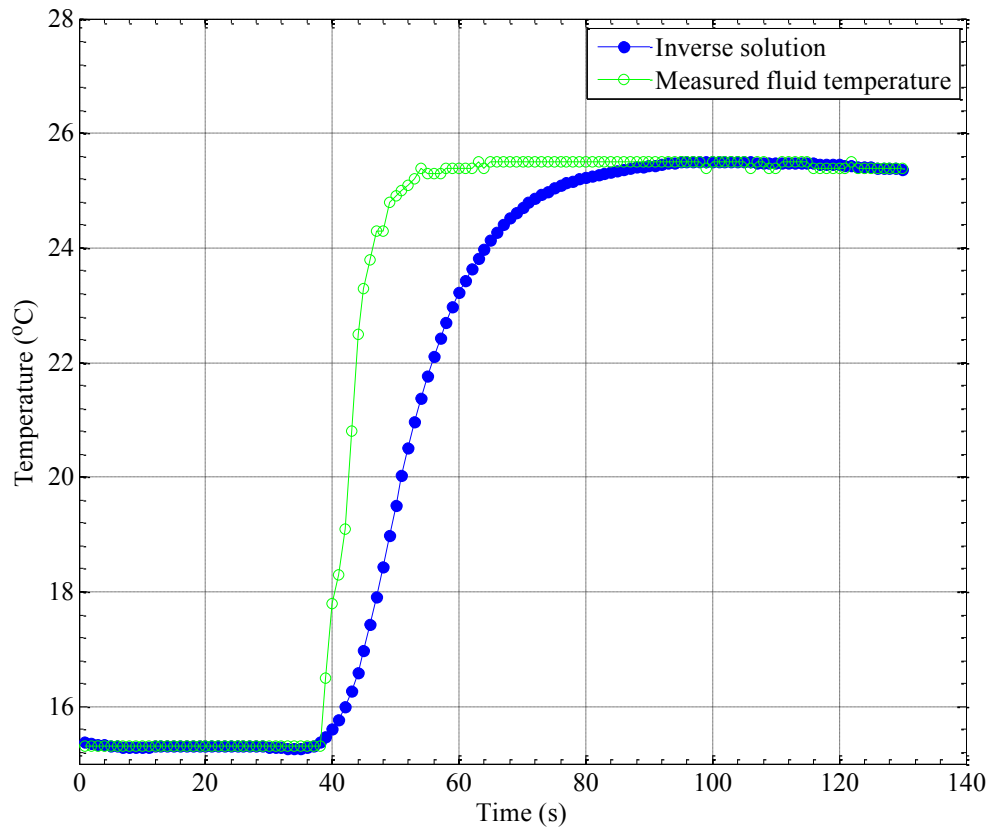


**Figure 5.32** Inverse solution of temperature of inside surface of the wall at  $r = a = 72$  mm for experiment 3 at height 100 mm calculated using equation (5.15). The sensitivity matrix of equation (5.15) is constructed of sensitivity elements obtained from equation (5.28) for wall thickness  $(b - a) = 4.25$  mm. Measured fluid temperature taken from mineral insulated thermocouple at height 100 mm. Superficial air velocity of 4.1 cm/s, 1 kg of dissolved sodium chloride, 500 g of loose swarf.

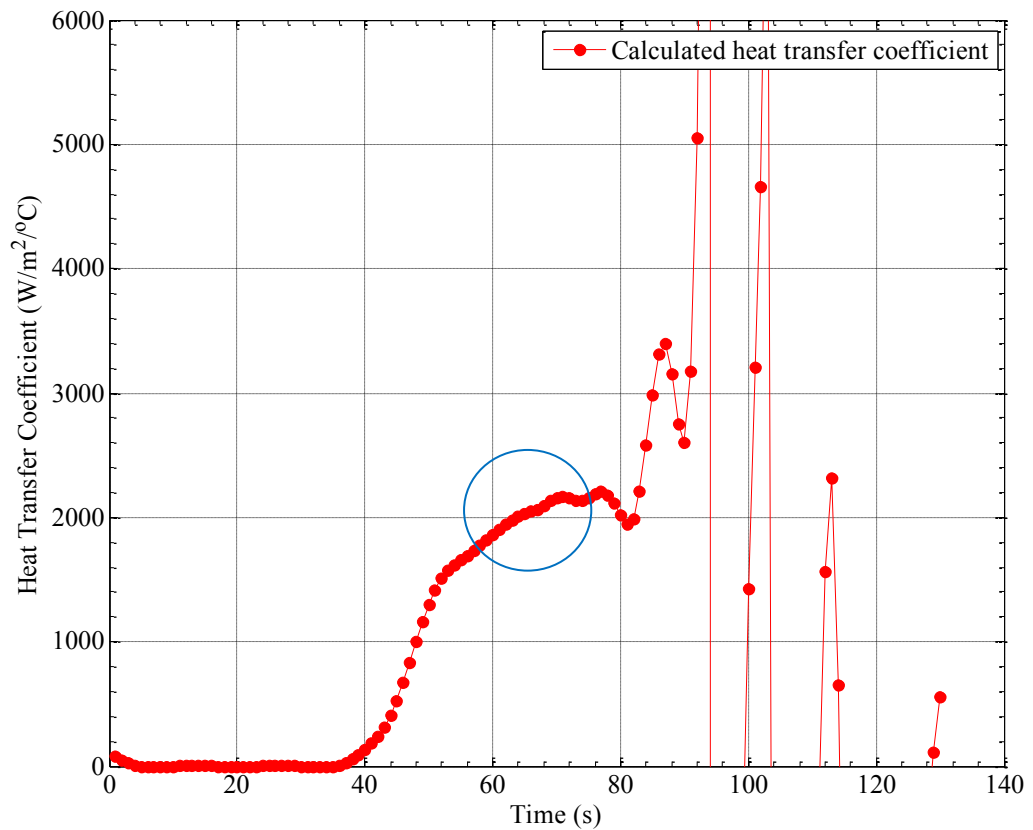


**Figure 5.33** Inverse solution of heat transfer coefficient belonging to inside surface of the wall at  $r = a = 72$  mm for experiment 3 at height 100 mm. The inverse normal heat flux is divided by the difference between the inverse temperature of the inside surface of the wall at  $r = a = 72$  mm and the measured fluid temperature at height 100 mm. The centre of the circle indicates where Tikhonov regularisation is localised and where the inside-wall heat transfer coefficient is resolved. Superficial air velocity 4.1 cm/s, 1 kg of dissolved sodium chloride, 500 g of loose swarf.

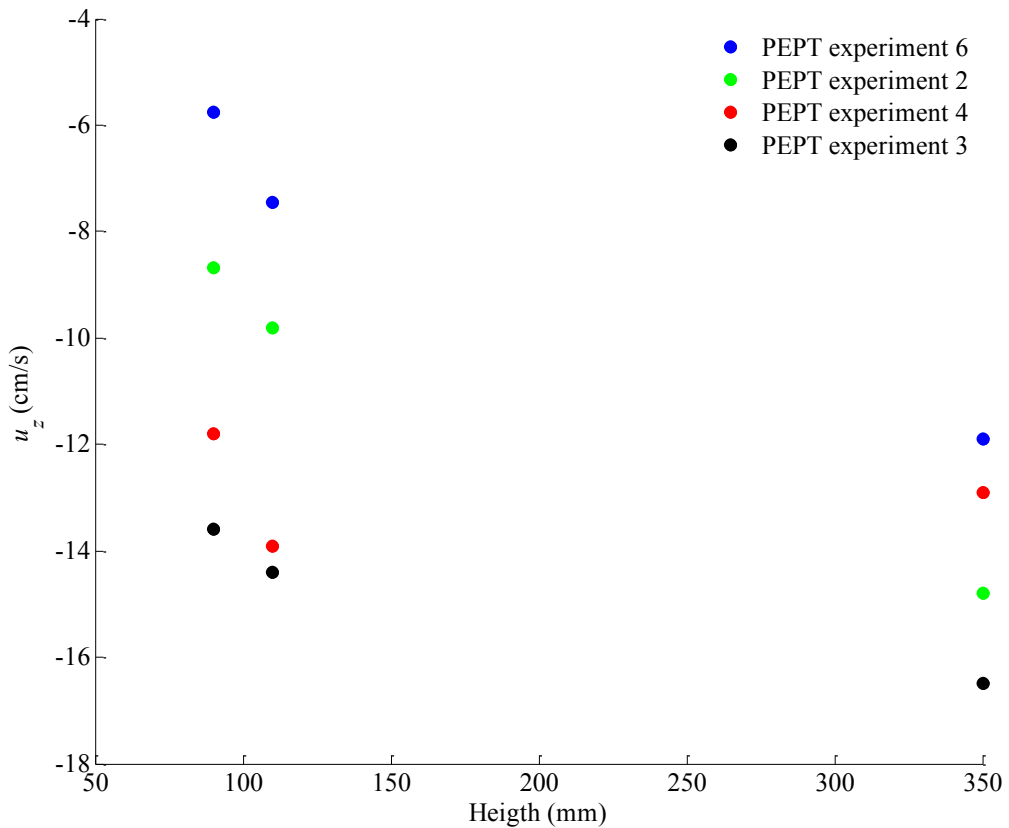


**Figure 5.34** Axial velocities of water close to the inside surface of the wall for flow investigated by inverse analysis. Axial velocity values are taken from tables 4.5, 4.6, 4.7 and 4.8 of reported PEPT measurements of corresponding flow. PEPT experiment 6: superficial air velocity 4.1 cm/s, 1 kg of dissolved sodium chloride, 500 g of loose swarf. PEPT experiment 2: superficial air velocity 4.1 cm/s, 1 kg of dissolved sodium chloride. PEPT experiment 4: superficial air velocity 7.2 cm/s, 500 g of loose swarf. PEPT experiment 3: superficial air velocity 7.2 cm/s. Values for height 90 mm taken from grid segments (5,4). Values for height 110 mm taken from grid segments (5,5). Values for height 350 mm taken from grid segments (5,17).

## CHAPTER 6

### CONCLUSION

In Chapter 1 the chemical constraint of the swarf dissolver process is the rate of heating, which is a function of both the dissolution rate of swarf and the enthalpy of the associated chemical equation(s) of dissolution (Chapter 2 Section 2.2). An operating envelope for arbitrary rates of dissolution can be drawn based upon known rates of cooling through the analysis of the overall heat transfer coefficient and fixed internal diameter of the cylinder concept (Chapter 2 Section 2.3). The calculated enthalpy displayed in Chapter 2 Section 2.2 couples both of these rates. The overall heat transfer coefficient is a series of resistances including the inside-wall heat transfer coefficient of the process, conduction across the wall and the outside-wall heat transfer coefficient within the annulus of the water jacket (Chapter 2 Section 2.3).

For the investigation contained within the previous chapters a air-water-swarf column of the same internal diameter of the cylinder concept is used in the analysis of the inside-wall heat transfer coefficient. This analysis includes a mixing study of both the water and swarf, and the measurement of the inside-wall heat transfer coefficient. The mass of loose swarf and the total volume of water within the column is the same as that proposed for the mass of loose swarf and total volume of prefill and acids for the cylinder concept (Chapter 1 Section 1.3). An electrolyte is used to mimic the effect of the ionic solution of acids and dissolved swarf (Chapter 4 Sections 4.7 and 4.9). A common global gas hold-up is used to segregate phenomena responsible for the transfer of momentum and heat (Chapter 5 Section 5.7).

## 6.1 Transfer of momentum within the air-water-swarf column

The inertial behaviour of the air-water-swarf turbulent flow is principally characterised by air voids that on average rise centrally across the height of the column, and the mixing of swarf is shown to be a direct effect of momentum transfer (Chapter 4 Sections 4.5 and 4.11). A source term of the volume force within the RANS equation balances its stress components, and allows the action of gravity through interfaces of multiphase flow to be investigated (Chapter 4 Section 4.5). For the volume force the buoyancy of the air-water interface provides the greatest inertia within the air-water-swarf flow and provides mixing of swarf (Chapter 4 Subheading 4.11.4). For the buoyancy term the difference in densities between the water/electrolyte and air dominates. Therefore, there is little difference between the volume force arising for different process gases and the air-water-swarf column is a good indicator of mixing for the swarf dissolution process within the cylinder concept (Chapter 4 Section 4.1).

The stresses of the turbulent flow acting between the different phases within the air-water-swarf column are resolved from the mean and instantaneous velocities of the water using PEPT (Chapter 4 Sections 4.5, 4.10 and 4.11). Asymmetric differencing is used along the trajectories of the PEPT particle tracers to calculate instantaneous quantities and allows for greater resolution of inertial flow behaviour (Chapter 4 Section 4.10). The calculated volume force coincides with the swarf occupancy and coalescence inhibition of dissolved sodium chloride (Chapter 4 Section 4.11.4).

The confidence in the capability of PEPT for the measurement of large scale turbulence is seen in the convergence of the components of the Reynolds stresses within the ensemble averaging of the stationary flow under the RANS framework (Chapter 4 Subheading 4.11.3). Because of the symmetry of the geometry and therefore flow, not all of the instantaneous quantities contribute towards the stationary dynamics (mass, force) (Chapter 4 Subheading

4.11.3). To improve the volume force and therefore the dispersion of swarf along the height of the column, fully 3-dimensional swirl flow is recommended. The azimuthal components of the stresses would then contribute towards the resolved axial volume force, and asymmetry in the azimuth of the perforated plate array should provide impetus (Chapter 4 Section 4.12).

## 6.2 Transfer of heat within the air-water-swarf column

A transient model of heat convection towards the inside-wall of the air-water-swarf column is used to optimise a regularised boundary inverse method by simulation (Chapter 5 Section 5.4). In this approach the measurement of the normal heat flux and inside-wall temperature from the outside-wall temperature history allows the calculation of the inside-wall heat transfer coefficient alongside the direct measurement of the fluid temperature (Chapter 5 Section 5.3). This inverse analysis across the wall of an inconel column is built from Green's function and allows for high precision and accuracy in the measurement of both the normal heat flux and inside-wall temperature, and therefore the inverse solution of the inside-wall heat transfer coefficient (Chapter 5 Sections 5.3, 5.4 and 5.7). For a superficial air velocity of 4.1 cm/s, 1 kg of dissolved sodium chloride and 500 g of loose swarf, magnitudes of 1700-1900 W/ m<sup>2</sup> °C are obtained for the inside-wall heat transfer coefficient at height 100 mm and 2300-2700 W/ m<sup>2</sup> °C at height 350 mm (Chapter 5 Section 5.7).

The sampling frequency as part of the sensitivity analysis of the inverse method and flow periodicity, resolves the inertial behaviour of the turbulent flow. The air-water-swarf flow of the inverse experiments corresponds with the flow investigated by PEPT and enables the effects of phenomena of momentum transfer to be related to the convection of heat towards the inside surface of the wall (Chapter 5 Section 5.6 and 5.7). In the region of high swarf occupancy the coalescence inhibition of the dissolved sodium chloride augments the reduced momentum transfer to the water reducing the periodicity of convection (Chapter 5 Section

5.7). For a given sampling rate of the inverse analysis a higher periodicity of convection results in the measurement of the inside-wall heat transfer coefficient for stationary flow.

### 6.3 Contributions and further work

PEPT has proved powerful in the measurement and characterisation of turbulence caused by the motion of the free-surface of the air-water interface and swarf-water interface through water (Chapter 4 Sections 4.5, 4.8, 4.10 and 4.11). The contributions of the characterisation of multiphase turbulent air-water-swarf flow arising from the motion of interfaces and measured using PEPT are:

1. Asymmetric differencing along the trajectory of the PEPT particle tracer following the motion of the water is consistent with the expression given by *Lu (1977, p. 335)* for the relative velocity of a viscous fluid (Chapter 4 Sections 4.4 and 4.10). The relative velocity can be related to the local deformation and rotation of the viscous fluid (Chapter 4 Section 4.4). In turn these contributions are considered a direct effect of the motion of the free-surface of interfaces acting through gravity. The relative velocity as calculated through asymmetric differencing is consistent with Euler's equation of Lagrangian motion and considers both deformations in space and time along the trajectory arising from the turbulent flow. Therefore, the inertial aspects of the flow are resolved to high precision (Chapter 4 Section 4.10). The truncation error of the asymmetric differencing is first-order in its time step and is reduced by second-order effects of the off-diagonal contributions that account for both the linear and rotational accelerative perturbations to the calculated instantaneous velocity or vorticity (Chapter 4 Section 4.10).
2. PEPT has provided the trajectories of a particle tracer within the water of a multiphase turbulent air-water-swarf column (Chapter 4 Section 4.11). Using asymmetric



differencing along the trajectories of the particle tracer the multiphase turbulence of an air-water-swarf column is characterised by both the mean and instantaneous velocities of the water consistent with the vectorised RANS equation (Chapter 4 Sections 4.5 and 4.11). The Eulerian stationary dynamics is reconstructed from the particle tracer trajectories and avoids the requirement of explicit volume fractions (Chapter 4 Sections 4.5 and 4.11). The convergence of Reynolds stresses through ensemble averaging towards the stationary dynamics of the air-water-swarf flow credits that PEPT can measure large scale turbulence (Chapter 4 Section 4.11). The accuracy in the calculation of the mean and instantaneous quantities from the trajectory measurements is high (Chapter 4 Section 4.11). The resolved volume force from the stress components of the vectorised RANS equation complements the observed swarf occupancy, and further credits the use of asymmetric differencing for the investigation of inertial flow (Chapter 4 Section 4.11).

3. In the calculation of instantaneous vorticity associated with the rise of air voids, asymmetric differencing of the trajectory of the PEPT particle tracer within the water of turbulent air-water flow, agrees well with values obtained using CFD (Chapter 4 Sections 4.8 and 4.11). The deformation and dynamics of the free-surface of the air-water interface is modeled during a simulation using the phase field method of COMSOL MULTIPHYSICS 4.3b (Chapter 4 Section 4.8). The decrease in magnitude of the measured instantaneous vorticity for air-water-swarf flow is consistent with swarf/air void collisions (Chapter 4 Section 4.11). The CFD simulation shows that the evolution of the air void shape is the most pertinent property of the flow and controls generation of vorticity; swarf/air void collisions will prevent the evolution of the void shape and therefore generation of vorticity.

A boundary inverse method with Tikhonov regularisation applied to a temperature transient has proved powerful in the measurement of the inside-wall heat transfer coefficient of the air-water-swarf column (Chapter 5 Sections 5.2, 5.3, 5.4 and 5.7). The contributions of the use of a temperature transient are:

1. The sampling frequency of the sensitivity analysis across the inconel wall selects the resolution of flow structures/phenomena responsible for the convection of heat to its inside surface (Chapter 5 Sections 5.2, 5.3, 5.4 and 5.7). This affords correct measurement of normal heat flux and inside-wall temperature by inverse analysis, and allows the inside-wall heat transfer coefficient to be calculated for stationary flow (Chapter 5 Sections 5.4 and 5.7).
2. Tikhonov regularisation can be applied locally to a section of a transient representing the desired flow and convection of heat (Chapter 5 Sections 5.4 and 5.7). This is achieved by selecting the Tikhonov regularisation operator that allows for stationary points along the form of the transient and therefore sought boundary condition (Chapter 5 Sections 5.3, 5.4 and 5.7). The stationary point prevents distortion of the inverse solutions caused by noise in the measured temperature history and proves accurate (Chapter 5 Sections 5.4 and 5.7).

### 6.3.1 Further work

Further investigation of the air-water-swarf column should include:

1. By the regularised boundary inverse method an investigation of a lower sampling rate and a transient of longer duration is necessary to obtain the inside-wall heat transfer coefficient at height 100 mm for stationary flow of superficial air velocity 4.1 cm/s, 1 kg of dissolved sodium chloride, and 500 g of loose swarf (Chapter 5 Section 5.7).

This will provide greater confidence in the reported value of the inside-wall heat transfer coefficient at height 100 mm necessary for the thermal operating envelope of the cylinder concept (Chapter 2 Section 2.3).

2. An investigation into the outside-wall heat transfer coefficient within the annulus of the water jacket for the cylinder concept. This is required for the thermal operating envelope of the cylinder concept (Chapter 2 Section 2.3).
3. An investigation of the effects of asymmetry in the azimuth of the perforated plate for air-water-swarf flow. This asymmetry should provide impetus for the contribution of azimuthal components of stress towards the resolved volume force and overall mixing of swarf (Chapter 4 Sections 4.5 and 4.12). From the present investigation of air-water-swarf flow it has been shown that PEPT can measure instantaneous angular velocities to high accuracy (Chapter 4 Sections 4.10 and 4.11) (Figure 4.21). Therefore, further investigation by PEPT can provide the azimuthal components of the stresses caused by asymmetry in the azimuth of the perforated plate (Chapter 4 Section 4.5).

## APPENDIX 1

### TAYLOR'S THEOREM AROUND INCIDENCE $i$

Velocity of particle tracer

$$ds = \mathbf{e}_r dr + r \mathbf{e}_\theta d\theta + \mathbf{e}_z dz \quad (\text{a.1})$$

$$\mathbf{s}_{i+1} = \mathbf{s}_i + \Delta t_2 \left. \frac{\partial \mathbf{s}}{\partial t} \right|_i + \frac{(\Delta t_2)^2}{2!} \left. \frac{\partial^2 \mathbf{s}}{\partial t^2} \right|_i + \dots \quad (\text{a.2})$$

$$\mathbf{s}_{i-1} = \mathbf{s}_i - \Delta t_1 \left. \frac{\partial \mathbf{s}}{\partial t} \right|_i - \frac{(\Delta t_1)^2}{2!} \left. \frac{\partial^2 \mathbf{s}}{\partial t^2} \right|_i + \dots \quad (\text{a.3})$$

$$\varepsilon_i \mathbf{s}_{i-1} = \varepsilon_i \mathbf{s}_i - \Delta t_2 \left. \frac{\partial \mathbf{s}}{\partial t} \right|_i - \frac{\Delta t_1 \Delta t_2}{2!} \left. \frac{\partial^2 \mathbf{s}}{\partial t^2} \right|_i + \dots, \quad \varepsilon_i = \frac{\Delta t_2}{\Delta t_1} \quad (\text{a.4})$$

$$\mathbf{s}_{i+1} - \varepsilon_i \mathbf{s}_{i-1} = (1 - \varepsilon_i) \mathbf{s}_i + 2\Delta t_2 \left. \frac{\partial \mathbf{s}}{\partial t} \right|_i + \frac{(\Delta t_2)^2}{2!} \left. \frac{\partial^2 \mathbf{s}}{\partial t^2} \right|_i - \frac{\Delta t_1 \Delta t_2}{2!} \left. \frac{\partial^2 \mathbf{s}}{\partial t^2} \right|_i + \dots \quad (\text{a.5})$$

$$\therefore \mathbf{u} = \left. \frac{\partial \mathbf{s}}{\partial t} \right|_i = \left[ \mathbf{s}_{i+1} - \varepsilon_i \mathbf{s}_{i-1} - (1 - \varepsilon_i) \mathbf{s}_i \right] / 2\Delta t_2 + O(\delta t) \quad (\text{a.6})$$

Vorticity of particle tracer

$$\Omega_\theta = \frac{\partial u_r}{\partial z} - \frac{\partial u_z}{\partial r} \quad (\text{a.7})$$

$$u_{r,i+1} = u_{r,i} + \Delta z_2 \left. \frac{\partial u_r}{\partial z} \right|_i + \frac{(\Delta z_2)^2}{2!} \left. \frac{\partial^2 u_r}{\partial z^2} \right|_i + \dots \quad (\text{a.8})$$

$$u_{r_{i-1}} = u_{r_i} - \Delta z_1 \left. \frac{\partial u_r}{\partial z} \right|_i - \frac{(\Delta z_1)^2}{2!} \left. \frac{\partial^2 u_r}{\partial z^2} \right|_i + \dots \quad (\text{a.9})$$

$$\varepsilon_z u_{r_{i-1}} = \varepsilon_z u_{r_i} - \Delta z_1 \left. \frac{\partial u_r}{\partial z} \right|_i - \frac{\Delta z_1 \Delta z_2}{2!} \left. \frac{\partial^2 u_r}{\partial z^2} \right|_i + \dots, \quad \varepsilon_z = \frac{\Delta z_2}{\Delta z_1} \quad (\text{a.10})$$

$$u_{r_{i+1}} - \varepsilon_z u_{r_{i-1}} = (1 - \varepsilon_z) u_{r_i} + 2\Delta z_2 \left. \frac{\partial u_r}{\partial z} \right|_i + \frac{(\Delta z_2)^2}{2!} \left. \frac{\partial^2 u_r}{\partial z^2} \right|_i - \frac{\Delta z_1 \Delta z_2}{2!} \left. \frac{\partial^2 u_r}{\partial z^2} \right|_i + \dots \quad (\text{a.11})$$

$$\therefore \left. \frac{\partial u_r}{\partial z} \right|_i \approx \left[ u_{r_{i+1}} - \varepsilon_z u_{r_{i-1}} - (1 - \varepsilon_z) u_{r_i} \right] / 2\Delta z_2 \quad (\text{a.12})$$

$$\text{by symmetry } \therefore \left. \frac{\partial u_z}{\partial r} \right|_i \approx \left[ u_{z_{i+1}} - \varepsilon_r u_{z_{i-1}} - (1 - \varepsilon_r) u_{z_i} \right] / 2\Delta r_2 \quad (\text{a.13})$$

$$\begin{aligned} \Omega_\theta &= \left[ u_{r_{i+1}} - \varepsilon_z u_{r_{i-1}} - (1 - \varepsilon_z) u_{r_i} \right] / 2\Delta z_2 - \dots \\ &\left[ u_{z_{i+1}} - \varepsilon_r u_{z_{i-1}} - (1 - \varepsilon_r) u_{z_i} \right] / 2\Delta r_2 + O(\delta z, \delta r) \end{aligned} \quad (\text{a.14})$$

## APPENDIX 2

### ERROR PROPAGATION IN CALCULATED VELOCITY AND REYNOLDS TENSOR COMPONENTS

#### Error propagation

Error propagation rules are used to calculate the errors on the measured velocity components that arise from the reported probable error in the coordinates of the PEPT particle tracer (*Pentz and Shott, 1988*). Where the general propagation rules are not clear the chain rule has been used to derive the components of error to which the scalar product is applied giving the magnitude of total error.

#### Coordinates

##### Probable error in coordinates

$$\delta x = \delta y = \delta z = \sigma / \sqrt{f_{opt} N} \quad (\text{a.1})$$

#### Velocity components

##### Error propagation in radial coordinate

$$r = \sqrt{x^2 + y^2} \quad (\text{a.2})$$

$$\delta r = \frac{\partial r}{\partial x} \delta x + \frac{\partial r}{\partial y} \delta y = (x \delta x / r) + (y \delta y / r) \quad (\text{a.3})$$

$$\delta r \cdot \delta r = (\delta r)^2 = (x \delta x / r)^2 + (y \delta y / r)^2 \quad (\text{a.4})$$

$$\therefore \delta r = \sqrt{(x\delta x/r)^2 + (y\delta y/r)^2} = \delta x = \delta y \quad (\text{a.5})$$

### Error propagation in azimuth

$$\theta = \tan^{-1}(y/x) \quad (\text{a.6})$$

$$\delta\theta = \frac{\partial\theta}{\partial x}\delta x + \frac{\partial\theta}{\partial y}\delta y = \frac{y\delta x}{x^2 + y^2} + \frac{\delta y}{x + (y^2/x)} \quad (\text{a.7})$$

$$\delta\theta \cdot \delta\theta = (\delta\theta)^2 = \left[ \frac{y\delta x}{x^2 + y^2} \right]^2 + \left[ \frac{\delta y}{x + (y^2/x)} \right]^2 \quad (\text{a.8})$$

$$\therefore \delta\theta = \sqrt{\left[ \frac{y\delta x}{x^2 + y^2} \right]^2 + \left[ \frac{\delta y}{x + (y^2/x)} \right]^2} \quad (\text{a.9})$$

### Error propagation in radial velocity

$$\delta u_r = \sqrt{(\delta r_{i+1})^2 + \varepsilon_t^2 (\delta r_{i-1})^2 + (1 - \varepsilon_t)^2 (\delta r_i)^2} / 2\Delta t_2 \quad (\text{a.10})$$

### Error propagation in axial velocity

$$\delta u_z = \sqrt{(\delta z_{i+1})^2 + \varepsilon^2 (\delta z_{i-1})^2 + (1 - \varepsilon)^2 (\delta z_i)^2} / 2\Delta t_2 \quad (\text{a.11})$$

### Error propagation in angular velocity

$$\delta\omega_\theta = \sqrt{(\delta\theta_{i+1})^2 + \varepsilon_t^2 (\delta\theta_{i-1})^2 + (1 - \varepsilon_t)^2 (\delta\theta_i)^2} / 2\Delta t_2 \quad (\text{a.12})$$

### Error propagation in azimuthal velocity

$$\delta u_\theta = r\delta\omega_\theta \quad (\text{a.13})$$

**Error propagation in mean radial velocity**

$$\delta\bar{u}_r = 1/n \sqrt{\sum (\delta u_r)^2} \quad (\text{a.14})$$

**Error propagation in mean azimuthal velocity**

$$\delta\bar{u}_\theta = 1/n \sqrt{\sum (\delta u_\theta)^2} \quad (\text{a.15})$$

**Error propagation in mean axial velocity**

$$\delta\bar{u}_z = 1/n \sqrt{\sum (\delta u_z)^2} \quad (\text{a.16})$$

**Error propagation in fluctuating radial velocity**

$$\delta u'_r = \sqrt{(\delta u_r)^2 + (\delta\bar{u}_r)^2} \quad (\text{a.17})$$

**Error propagation in fluctuating azimuthal velocity**

$$\delta u'_\theta = \sqrt{(\delta u_\theta)^2 + (\delta\bar{u}_\theta)^2} \quad (\text{a.18})$$

**Error propagation in fluctuating axial velocity**

$$\delta u'_z = \sqrt{(\delta u_z)^2 + (\delta\bar{u}_z)^2} \quad (\text{a.19})$$

Reynolds tensor components

**Error propagation in Reynolds tensor components**

$$\delta(u'_r u'_z) = u'_r u'_z \sqrt{\left(\frac{\delta u'_r}{u'_r}\right)^2 + \left(\frac{\delta u'_z}{u'_z}\right)^2} \quad \text{etc.} \quad (\text{a.20})$$



$$\delta(\overline{u'_r u'_z}) = 1/n \sqrt{\sum (\delta(u'_r u'_z))^2} \quad (\text{a.21})$$

## APPENDIX 3

### MATLAB<sup>®</sup> m-files

#### movie.m

```
%movie.m
%m-file for image processing of flow visulisation experiments
clear all
close all
files=fullfile('c:', 'users', 'axr665', 'my documents', 'mov', '60_ltr_min-1_2-
phase_NaCl_S001');
dirfiles=dir(fullfile(files, '60_ltr_*.tif'));
filenames={dirfiles.name}';
numframes=numel(filenames);
I=imread(filenames{1});
movsequence=zeros([size(I) numframes],class(I));
movsequence(:,:,2000)=I;
for p=2002:2726
    movsequence(:,:,p)=imread(filenames{p});
end
aviobj=avifile('60_NaCl_3.avi', 'fps', 50, 'compression', 'none');
scrsz=get(0, 'ScreenSize');
figure('Position', [1 scrsz(4)/2 scrsz(3)/4 scrsz(4)/4], 'color', 'k')
for q=2002:2726
    imshow(movsequence(:,:,q), 'Border', 'tight')
    M=getframe(gcf);
    aviobj=addframe(aviobj, M);
end
```

#### instantaneous\_velocity.m

```
%instantaneous_velocities.m
%m-file for the calculation of instantaneous velocities and errors from
%ASCII text file of TRACK algorithm
clear all; format longe; data=load('d.txt'); %d.txt is the ASCII text file
d=zeros(length(data(:,1)), 9);
for i=1:length(data(:,1)); d(i,1)=data(i,1); d(i,2)=data(i,2); d(i,3)=data(...
i,3); d(i,4)=data(i,4); d(i,5)=data(i,5); d(i,6)=data(i,6); d(i,7)=data(i,7) ...
; d(i,8)=data(i,8); d(i,9)=i;
end
data(any(data(:,5)>10,2),:)=[];
x=(d(:,2)-((max(data(:,2))+min(data(:,2)))/2)); y=(d(:,4)-...
((max(data(:,4))+min(data(:,4)))/2)); z=d(:,3); time=...
d(:,1); err=d(:,5); No_of_Events=d(:,8); m=zeros(length(d(:,1)), 38);
for i=1:length(d(:,1)); i
r=find(d(:,1)-d(i,1)>20,1, 'first');
s=find(d(:,1)-d(r,1)>20,1, 'first');
if isscalar(s)==0; break
```

```

end
%Cartesian trajectory
m(i,1)=x(i);
m(i,2)=y(i);
m(i,3)=z(i);
m(i,4)=time(i);
m(i,5)=err(i);
m(i,6)=No_of_Events(i);
m(i,7)=x(r);
m(i,8)=y(r);
m(i,9)=z(r);
m(i,10)=time(r);
m(i,11)=err(r);
m(i,12)=No_of_Events(r);
m(i,13)=x(s);
m(i,14)=y(s);
m(i,15)=z(s);
m(i,16)=time(s);
m(i,17)=err(s);
m(i,18)=No_of_Events(s);
%Radial coordinates
m(i,19)=(m(i,1)^2+m(i,2)^2)^0.5;
m(i,20)=(m(i,7)^2+m(i,8)^2)^0.5;
m(i,21)=(m(i,13)^2+m(i,14)^2)^0.5;
%Ratio of time steps
epsilon=(m(i,16)-m(i,10))/(m(i,10)-m(i,4));
%x,y,z and r velocity
m(i,22)=(m(i,13)-epsilon*m(i,1)-(1-epsilon)*m(i,7))/(2*...
(m(i,16)-m(i,10)));
m(i,23)=(m(i,14)-epsilon*m(i,2)-(1-epsilon)*m(i,8))/(2*...
(m(i,16)-m(i,10)));
m(i,24)=(m(i,15)-epsilon*m(i,3)-(1-epsilon)*m(i,9))/(2*...
(m(i,16)-m(i,10)));
m(i,25)=(m(i,21)-epsilon*m(i,19)-(1-epsilon)*m(i,20))/(2*...
(m(i,16)-m(i,10)));
%Azimuth
m(i,26)=atan2(m(i,2),m(i,1))+pi;
m(i,27)=atan2(m(i,8),m(i,7))+pi;
m(i,28)=atan2(m(i,14),m(i,13))+pi;
%Remove discontinuous angular trajectories
if (m(i,26)>m(i,27) && m(i,27)>m(i,28)) || (m(i,26)<m(i,27) && m(i,27)<...
m(i,28))
a=1;
else
a=0;
end
if m(i,28)>m(i,26) && m(i,26)>m(i,27) && a==1
m(i,28)=m(i,28)-2*pi;
elseif m(i,27)>m(i,28) && m(i,28)>m(i,26) && a==1
m(i,27)=m(i,27)-2*pi;
m(i,28)=m(i,28)-2*pi;
elseif m(i,27)>m(i,26) && m(i,26)>m(i,28) && a==1
m(i,28)=m(i,28)+2*pi;
elseif m(i,26)>m(i,28) && m(i,28)>m(i,27) && a==1
m(i,27)=m(i,27)+2*pi;
m(i,28)=m(i,28)+2*pi;
end
%Segregate angular and linear trajectories around axial axis
if abs(m(i,27)-m(i,26))>pi || abs(m(i,28)-m(i,27))>pi

```

```

        b=1;
    else
    b=0;
    end
    %Azimuthal velocity
    if b==1
    m(i,29)=0;
    else
    if (m(i,26)>m(i,27) && m(i,27)>m(i,28)) || (m(i,26)<m(i,27) && m(i,27)<...
        m(i,28))
    m(i,29)=1000*(m(i,28)-epsilon*m(i,26)-(1-epsilon)*m(i,27))/...
        (2*(m(i,16)-m(i,10)));
    else
    m(i,29)=0;
    end
    end
    %Probable errors for i-1, i, and i+1
    m(i,30)=m(i,5)/(m(i,6))^(1/2);
    m(i,31)=m(i,11)/(m(i,12))^(1/2);
    m(i,32)=m(i,17)/(m(i,18))^(1/2);
    %delta(theta) for i-1, i, and i+1
    m(i,33)=(((m(i,2)*m(i,30))/(m(i,19))^2)^2+(m(i,30))/(m(i,1)+...
        ((m(i,2))^2/(m(i,1))))^2)^(1/2);
    m(i,34)=(((m(i,8)*m(i,31))/(m(i,20))^2)^2+(m(i,31))/(m(i,7)+...
        ((m(i,8))^2/(m(i,7))))^2)^(1/2);
    m(i,35)=(((m(i,14)*m(i,32))/(m(i,21))^2)^2+(m(i,32))/(m(i,13)+...
        ((m(i,14))^2/(m(i,13))))^2)^(1/2);
    %delta(ur)
    m(i,36)=(((m(i,32))^2+((epsilon)^2)*m(i,30)^2+(1-epsilon)^2)*...
        (m(i,31))^2)^(1/2)/(2*(m(i,16)-m(i,10)));
    %delta(uz)
    m(i,37)=(((m(i,32))^2+((epsilon)^2)*m(i,30)^2+(1-epsilon)^2)*...
        (m(i,31))^2)^(1/2)/(2*(m(i,16)-m(i,10)));
    %delta(utheta)
    m(i,38)=(((m(i,35))^2+epsilon^2*(m(i,33))^2+(1-epsilon)^2*...
        (m(i,34))^2)^(1/2))/(2*(m(i,16)-m(i,10)));
    end
    %Probable error limit
    error_limit=5;m(any(m(:,5)>error_limit,2),:)=[];m(any(m(:,11)>...
        error_limit,2),:)=[];
    m(any(m(:,17)>error_limit,2),:)=[];m(any(m(:,4)==0,2),:)=[];
    %Write m to data file
    dlmwrite('d_20.txt',m,'delimiter','\t',...
        'precision',8)

```

## instantaneous\_vorticity.m

```
%instantaneous_vorticity.m
%m-file for the calculation of instantaneous vorticity
clear all
m=load('d_20.txt');%output file of instantaneous_velocity.m
%Global vorticity
for j=1:length(m(:,10));j
r=find(m(:,10)-m(j,10)>20,1,'first');
s=find(m(:,10)-m(r,10)>20,1,'first');
if isscalar(s)==0;break
end
epsilon_z=(m(s,9)-m(r,9))/(m(r,9)-m(j,9));
epsilon_r=(m(s,20)-m(r,20))/(m(r,20)-m(j,20));
o(j,1)=m(j,20);
o(j,2)=m(r,20);
o(j,3)=m(s,20);
o(j,4)=m(j,9);
o(j,5)=m(r,9);
o(j,6)=m(s,9);
if (m(s,9)-m(r,9))>1 && (m(r,9)-m(j,9))>1 && (m(r,20)-m(j,20))>1 &&
(m(s,20)-m(r,20))>1
o(j,7)=1000*((m(s,25)-epsilon_z*m(j,25)-(1-epsilon_z)*m(r,25))/(2*(m(s,9)-
m(r,9))))-...
((m(s,24)-epsilon_r*m(j,24)-(1-epsilon_r)*m(r,24))/(2*(m(s,20)-m(r,20))));
else
o(j,7)=0;
end
end
scrsz=get(0,'ScreenSize');
figure('Position',[1 scrsz(4)/6 scrsz(3)/1.8 scrsz(4)/2]);
q=o(:,7);
q(any(q(:,1)==0,2),:)=[];
plot(1:length(q),q,'--b','LineWidth',0.5)
set(gca,'FontSize',12,'FontName','Times')
xlabel('Incidence')
ylabel('\it{\Omega}_{\theta} (1/s)')
legend('\it{\Omega}_{\theta}')
legend('boxoff')
%Local vorticity
max_r=max([max(o(:,1)) max(o(:,2)) max(o(:,3))]);
min_z=min([min(o(:,4)) min(o(:,5)) min(o(:,6))]);
delta_z=20;
div_r=5;
omega=zeros(length(o(:,7)),5,19);
for j=1:19
for n=1:div_r
p=o;
p(any(p(:,2)>n*(max_r)/div_r,2),:)=[];
p(any(p(:,2)<(n-1)*(max_r)/div_r,2),:)=[];
p(any(p(:,5)>min_z+20+j*delta_z,2),:)=[];
p(any(p(:,5)<min_z+20+(j-1)*delta_z,2),:)=[];
omega(1:length(p(:,7)),n,j)=omega(1:length(p(:,7)),n,j)+p(:,7);
end
end
```



```

        ((u_z_r(1:length(m(:,25)),n,j))-U_z_r(n,j));
bar_uf_z_uf_z_r(n,j)=mean((uf_z_uf_z_r(1:length(m(:,25)),n,j)));
%theta terms
m(any(m(:,29)==0,2),:)=[];
length(m(:,29))
u_r_theta(1:length(m(:,29)),n,j)=u_r_theta(1:length(m(:,29)),n,j)+m(:,25);
U_r_theta(n,j)=mean(u_r_theta(1:length(m(:,25)),n,j));
u_z_theta(1:length(m(:,24)),n,j)=u_z_theta(1:length(m(:,24)),n,j)+m(:,24);
U_z_theta(n,j)=mean(u_z_theta(1:length(m(:,24)),n,j));
u_theta(1:length(m(:,29)),n,j)=u_theta(1:length(m(:,29)),n,j)+r_grid(n)*...
    m(:,29);
U_theta(n,j)=mean(u_theta(1:length(m(:,29)),n,j));
u_theta_u_r(1:length(m(:,29)),n,j)=u_theta_u_r(1:length(m(:,29)),n,j)+...
    (u_theta(1:length(m(:,29)),n,j)-U_theta(n,j)).*...
    (u_r_theta(1:length(m(:,29)),n,j)-U_r_theta(n,j));
u_theta_u_z(1:length(m(:,29)),n,j)=u_theta_u_z(1:length(m(:,29)),n,j)+...
    (u_theta(1:length(m(:,29)),n,j)-U_theta(n,j)).*...
    (u_z_theta(1:length(m(:,29)),n,j)-U_z_theta(n,j));
bar_u_theta_u_r(n,j)=mean(u_theta_u_r(1:length(m(:,29)),n,j));
bar_u_theta_u_z(n,j)=mean(u_theta_u_z(1:length(m(:,29)),n,j));
end
end
%Example of error analysis for tensor components within individual
%grid segments.
err_z=zeros(size,5,19);err_r=zeros(size,5,19);insterr_z=zeros(size,5,19);
merr_z=zeros(5,19);insterr_r=zeros(size,5,19);merr_r=zeros(5,19);
insterr_theta=zeros(size,5,19);error=zeros(size,1);merr_theta=zeros(5,19);
com_rz=zeros(size,5,19);mcom_rz=zeros(5,19);com_rr=zeros(size,5,19);
mcom_rr=zeros(5,19);com_zz=zeros(size,5,19);mcom_zz=zeros(5,19);
insterr_r_theta=zeros(size,5,19);insterr_z_theta=zeros(size,5,19);
err_theta=zeros(size,5,19);merr_r_theta=zeros(5,19);
err_r_theta=zeros(size,5,19);merr_z_theta=zeros(5,19);
err_z_theta=zeros(size,5,19);com_rtheta=zeros(size,5,19);
com_ztheta=zeros(size,5,19);mcom_rtheta=zeros(5,19);
mcom_ztheta=zeros(5,19);
for j=1:19
for n=1:div_r
m=data;
m(any(m(:,20)>n*(max_r)/div_r,2),:)=[];
m(any(m(:,20)<(n-1)*(max_r)/div_r,2),:)=[];
m(any(m(:,9)>min_z+20+j*delta_z,2),:)=[];
m(any(m(:,9)<min_z+20+(j-1)*delta_z,2),:)=[];
length(m(:,25));
%instantaneous axial velocity
insterr_z(1:length(m(:,37)),n,j)=insterr_z(1:length(m(:,37)),n,j)+m(:,37);
merr_z(n,j)=((length(m(:,37)))^-1)*(sum(insterr_z(:,n,j)).*...
    insterr_z(:,n,j))).^(1/2);
err_z(1:length(m(:,37)),n,j)=((insterr_z(1:length(m(:,37)),n,j)).*...
    (insterr_z(1:length(m(:,37)),n,j))+((merr_z(n,j))*(merr_z(n,j)))).^...
    (1/2);
%instantaneous radial velocity
insterr_r(1:length(m(:,36)),n,j)=insterr_r(1:length(m(:,36)),n,j)+m(:,36);
merr_r(n,j)=((length(m(:,36)))^-1)*(sum(insterr_r(:,n,j)).*...
    insterr_r(:,n,j))).^(1/2);
err_r(1:length(m(:,36)),n,j)=((insterr_r(1:length(m(:,36)),n,j)).*...
    (insterr_r(1:length(m(:,36)),n,j))+((merr_r(n,j))*(merr_r(n,j)))).^...
    (1/2);
%Reynold stress tensor (axial and radial terms)
com_rz(1:length(m(:,25)),n,j)=uf_r_uf_z(1:length(m(:,25)),n,j).*...

```

```

        ((err_r(1:length(m(:,36)),n,j))./...
        (u_r(1:length(m(:,25)),n,j)-U_r(n,j))).^2+...
        ((err_z(1:length(m(:,37)),n,j))./...
        (u_z_r(1:length(m(:,25)),n,j)-U_z_r(n,j))).^2).^^(1/2);
mcom_rz(n,j)=((length(m(:,25)))^-1)*(sum(com_rz(:,n,j).*...
        com_rz(:,n,j))).^(1/2);
com_rr(1:length(m(:,25)),n,j)=uf_r_uf_r(1:length(m(:,25)),n,j).*...
        (2*((err_r(1:length(m(:,25)),n,j))./...
        (u_r(1:length(m(:,25)),n,j)-U_r(n,j))).^2).^^(1/2);
mcom_rr(n,j)=((length(m(:,25)))^-1)*(sum(com_rr(:,n,j).*...
        com_rr(:,n,j))).^(1/2);
com_zz(1:length(m(:,25)),n,j)=uf_z_uf_z_r(1:length(m(:,24)),n,j).*...
        ((2*(err_z(1:length(m(:,24)),n,j))./(u_z_r(1:length(m(:,25)),n,j)-...
        U_z_r(n,j))).^2).^^(1/2);
mcom_zz(n,j)=((length(m(:,25)))^-1)*(sum(com_zz(:,n,j).*...
        com_zz(:,n,j))).^(1/2);
%instantaneous angular velocity
m(any(m(:,29)==0,2),:)=[];
insterr_theta(1:length(m(:,38)),n,j)=insterr_theta(1:length(m(:,38)) ...
,n,j)+r_grid(n)*m(:,38);
merr_theta(n,j)=((length(m(:,38)))^-1)*(sum(insterr_theta(:,n,j).*...
        insterr_theta(:,n,j))).^(1/2);
err_theta(1:length(m(:,38)),n,j)=(insterr_theta(1:length(m(:,38)),n,j).*...
        insterr_theta(1:length(m(:,38)),n,j)+merr_theta(n,j).*...
        merr_theta(n,j)).^(1/2);
insterr_r_theta(1:length(m(:,36)),n,j)=insterr_r_theta(1:length(m(:,36)) ...
),n,j)+m(:,36);
merr_r_theta(n,j)=((length(m(:,36)))^-1)*(sum(insterr_r_theta(:,n,j).*...
        insterr_r_theta(:,n,j))).^(1/2);
err_r_theta(1:length(m(:,36)),n,j)=(insterr_r_theta(1:length(m(:,36)) ...
,n,j).*insterr_r_theta(1:length(m(:,36)),n,j)+merr_r_theta(n,j).*...
        merr_r_theta(n,j)).^(1/2);
insterr_z_theta(1:length(m(:,37)),n,j)=insterr_z_theta(1:length(m(:,37)) ...
),n,j)+m(:,37);
merr_z_theta(n,j)=((length(m(:,37)))^-1)*(sum(insterr_z_theta(:,n,j).*...
        insterr_z_theta(:,n,j))).^(1/2);
err_z_theta(1:length(m(:,37)),n,j)=(insterr_z_theta(1:length(m(:,37)) ...
,n,j).*insterr_z_theta(1:length(m(:,37)),n,j)+merr_z_theta(n,j).*...
        merr_z_theta(n,j)).^(1/2);
%Reynolds stress tensor (azimuthal terms)
com_rtheta(1:length(m(:,25)),n,j)=u_theta_u_r(1:length(m(:,25)),n,j).*...
        ((err_theta(1:length(m(:,38)),n,j))./...
        insterr_theta(1:length(m(:,38)),n,j)).^2+...
        (err_r_theta(1:length(m(:,36)),n,j))./...
        insterr_r_theta(1:length(m(:,36)),n,j)).^2).^^(1/2);
com_ztheta(1:length(m(:,24)),n,j)=u_theta_u_z(1:length(m(:,24)),n,j).*...
        ((err_theta(1:length(m(:,38)),n,j))./...
        insterr_theta(1:length(m(:,38)),n,j)).^2+...
        (err_z_theta(1:length(m(:,37)),n,j))./...
        insterr_z_theta(1:length(m(:,37)),n,j)).^2).^^(1/2);
mcom_rtheta(n,j)=((length(m(:,25)))^-1)*(sum(com_rtheta(:,n,j).^2))^^(1/2);
mcom_ztheta(n,j)=((length(m(:,24)))^-1)*(sum(com_ztheta(:,n,j).^2))^^(1/2);
end
end
scrsz=get(0,'ScreenSize');
figure('Position',[1 scrsz(4)/6 scrsz(3)/1.8 scrsz(4)/2]);
q=com_rz(:,2,5);
q(any(q(:,1)==0,2),:)=[];
a=uf_r_uf_z(:,2,5);

```



```

a(any(a(:,1)==0,2),:)=[];
plot(1:length(a),a,'--b','LineWidth',0.5)
hold on
plot(1:length(q),abs(q),'-g','LineWidth',2)
set(gca,'FontSize',12,'FontName','Times')
ylim([-0.3 0.6])
xlabel('Incidence')
ylabel('\it{u}_{r}u_{z}} (m^2/s^2)')
legend('\it{u}_{r}u_{z}}','\delta{\it{u}_{r}u_{z}}')
legend('boxoff')
hold off
scrsz=get(0,'ScreenSize');
figure('Position',[1 scrsz(4)/6 scrsz(3)/1.8 scrsz(4)/2]);
w=insterr_z(:,2,5);
w(any(w(:,1)==0,2),:)=[];
b=u_z_r(:,2,5);
b(any(b(:,1)==0,2),:)=[];
plot(1:length(b),b,'--b','LineWidth',0.5)
hold on
plot(1:length(w),w,'-g','LineWidth',2)
set(gca,'FontSize',12,'FontName','Times')
ylim([-0.8 1.9])
xlabel('Incidence')
ylabel('\it{u}_{z}} (m/s)')
legend('\it{u}_{z}}','\delta{\it{u}_{z}}')
legend('boxoff')
hold off
%Data table
data_matrix=zeros(95,11);
for n=1:11
for i=1:19
for j=1:5
q=uf_r_uf_z(:,j,i);
q(any(q(:,1)==0,2),:)=[];
length(q);
if n==1
data_matrix((i*5)-(5-j),n)=length(q);
elseif n==2
data_matrix((i*5)-(5-j),n)=U_z_r(j,i)*100;
elseif n==3
data_matrix((i*5)-(5-j),n)=merr_z(j,i)*10000;
elseif n==4
data_matrix((i*5)-(5-j),n)=U_r(j,i)*100;
elseif n==5
data_matrix((i*5)-(5-j),n)=merr_r(j,i)*10000;
elseif n==6
data_matrix((i*5)-(5-j),n)=bar_uf_r_uf_z(j,i)*1000;
elseif n==7
data_matrix((i*5)-(5-j),n)=mcom_rz(j,i)*10000;
elseif n==8
data_matrix((i*5)-(5-j),n)=bar_uf_r_uf_r(j,i)*1000;
elseif n==9
data_matrix((i*5)-(5-j),n)=mcom_rr(j,i)*10000;
elseif n==10
data_matrix((i*5)-(5-j),n)=bar_uf_z_uf_z_r(j,i)*1000;
elseif n==11
data_matrix((i*5)-(5-j),n)=mcom_zz(j,i)*10000;
else
end
end

```

```

end
end
end
%Example of convergence in rz plane within individual grid segments.
time=zeros(100);
ut_r=zeros(40000,5,19,100);
Ut_r=zeros(5,19,100);
ut_z_r=zeros(40000,5,19,100);
Ut_z_r=zeros(5,19,100);
uft_r_uf_z=zeros(40000,5,19,100);
bar_uft_r_uf_z=zeros(100,5,19);
Utt_z_r=zeros(100,5,19);
for k=1:100
for j=1:19
for n=1:div_r
m=data(1:k*2513,:);
time(k)=data(k*2513,10);
m(any(m(:,20)>n*(max_r)/div_r,2),:)=[];
m(any(m(:,20)<(n-1)*(max_r)/div_r,2),:)=[];
m(any(m(:,9)>min_z+20+j*delta_z,2),:)=[];
m(any(m(:,9)<min_z+20+(j-1)*delta_z,2),:)=[];
ut_r(1:length(m(:,25)),n,j,k)=ut_r(1:length(m(:,25)),n,j,k)+m(:,25);
Ut_r(n,j,k)=mean((ut_r(1:length(m(:,25)),n,j,k)));
ut_z_r(1:length(m(:,22)),n,j,k)=ut_z_r(1:length(m(:,22)),n,j,k)+m(:,24);
Ut_z_r(n,j,k)=mean((ut_z_r(1:length(m(:,22)),n,j,k)));
uft_r_uf_z(1:length(m(:,25)),n,j,k)=uft_r_uf_z(1:length(m(:,25)),n,j,k ...
)+( ((ut_r(1:length(m(:,25)),n,j,k))-Ut_r(n,j,k)).* ...
((ut_z_r(1:length(m(:,25)),n,j,k))-Ut_z_r(n,j,k)));
bar_uft_r_uf_z(k,n,j)=mean((uft_r_uf_z(1:length(m(:,25)),n,j,k)));
Utt_z_r(k,n,j)=mean((ut_z_r(1:length(m(:,22)),n,j,k)));
end
end
end
scrsz=get(0,'ScreenSize');
figure('Position',[1 scrsz(4)/6 scrsz(3)/1.8 scrsz(4)/4.8]);
plot(time./60000,bar_uft_r_uf_z(1:100,3,7),'--b','LineWidth',2)
set(gca,'FontSize',12,'FontName','Times')
xlabel('Time (minutes)')
ylabel('\it{u_{r}}u_{z}} (m^2/s^2)')
figure('Position',[1 scrsz(4)/6 scrsz(3)/1.8 scrsz(4)/4.8]);
plot(time./60000,Utt_z_r(1:100,3,7),'--b','LineWidth',2)
set(gca,'FontSize',12,'FontName','Times')
xlabel('Time (minutes)')
ylabel('\it{u_{z}} (m/s)')
%Spatial grid.
[Xg,Yg]=meshgrid(0.72e-2:1.44e-2:6.48e-2,3e-2:2e-2:39e-2);
[X,Y]=meshgrid(0.72:1.44:6.48,3:2:39);
Z1=transpose(U_r);
Z2=transpose(U_z_r);
Z3=transpose(bar_uf_r_uf_z);
Z4=transpose(bar_uf_z_uf_z_r);
Z5=transpose(bar_uf_r_uf_r);
[frs,fzs]=gradient(Z3,0.0144,0.02);
[frn,fzn]=gradient(Z4,0.0144,0.02);
[frv,fzv]=gradient(Z2,0.0144,0.02);
[frr,fzr]=gradient(Z1,0.0144,0.02);
[f1,f2]=gradient(Z5,0.0144,0.02);
%Viscous mean field stresses
mu=0.8541e-3;%dynamic viscosity of water (Pa.s)

```

```

%ez components
[fzrv,fzv2]=gradient(fzv,0.0144,0.02);
[frv2,frzv]=gradient(frv,0.0144,0.02);
az_vis=mu*fzv2+mu*frv2+(mu./Xg).*frv;
%er components
[frr2,fzrr]=gradient(frr,0.0144,0.02);
[frzr,fzz2]=gradient(fzr,0.0144,0.02);
ar_vis=mu*frr2+(mu./Xg).*frr-(mu./Xg.^2).*Z1+...
mu*fzz2;
%Divergence of Reynolds stress tensor components
az_tensor=((1./Xg).*Z3+frs)+fzn;
ar_tensor=((1./Xg).*Z5+f1);
%Convective acceleration
az_con=Z1.*frv+Z2.*fzv;
ar_con=Z1.*frr+Z2.*fzr;
%Combined inertial volume force
rho=996.56+1/11.25e-3;%density of sodium chloride solution (kg/m^3)
az=(rho/1000)*az_tensor-(1/1e3)*az_vis+(rho/1000)*az_con;
ar=(rho/1000)*ar_tensor-(1/1e3)*ar_vis+(rho/1000)*ar_con;
%Example of spatial grid.
scrsz=get(0,'ScreenSize');
figure('Position',[1 scrsz(4)/6 scrsz(3)/3 scrsz(4)/1]);
grid on
hold on
axis equal
axis([0 7.2 2 40])
[Xd,Yd]=meshgrid(0.72:1.44:6.48,3:2:39,0:1);
[Xs,Ys]=meshgrid(0.72:1.44:6.48,3:2:39);
set(gca,'FontSize',12,'FontName','Times',...
'XTick',0:1.44:7.2,'YTick',2:2:40,...
'TickDir','out','YAxisLocation','right')
hold off
xlabel('\it{r} (cm)')
ylabel('\it{z} (cm)')
%Plot of volume force and swarf occupancy.
s=1;
scrsz=get(0,'ScreenSize');
figure('Position',[1 scrsz(4)/6 scrsz(3)/2.2 scrsz(4)/1],'Nextplot','add');
axis equal
[XG,YG,ZG]=meshgrid(-7.2:1.44:7.2,-7.2:1.44:7.2,2:2:40);
grid on
axis([-7.3 7.3 -7.3 7.3 2 40])
subplot(1,1,1)
hold on
occu=load('occu.txt');
[x,y]=meshgrid(0.72:1.44:6.48,3:2:39);
[xi,yi]=meshgrid(0.72:0.1:6.48,3:0.1:39);
zi=interp2(x,y,occu,xi,yi,'cubic');
I=mat2gray(zi,[0 2]);
J=imadjust(I);
[XM,map]=gray2ind(J,1000);
RGB=ind2rgb(XM,map);
for i=1:361
for k=1:58
x=zeros(1,4);
y=[(k-1)*0.1+0.72 (k-1)*0.1+0.72 k*0.1+0.72 k*0.1+0.72];
z=[(i-1)*0.1+3 i*0.1+3 i*0.1+3 (i-1)*0.1+3];
C=[RGB(i,k,1) RGB(i,k,2) RGB(i,k,3)];
fill3(x,y,z,C,'EdgeColor','none','FaceLighting','none')

```

```

end
end
%%%%%%%%%%%%%%%%%%%%%%%%%%%%%%%%%%%%%%%%%%%%%%%%%%%%%%%%%%%%%%%%%%%%%%%%
[X,Y,Z]=meshgrid(0:1,0.72:1.44:6.48,3:2:39);
Ar=transpose(ar);
Az=transpose(az);
dy=zeros(5,2,19);
dz=zeros(5,2,19);
for j=1:19
dy(:,:,j)=horzcat(Ar(:,j),Ar(:,j));
dz(:,:,j)=horzcat(Az(:,j),Az(:,j));
end
set(gcf,'Nextplot','add')
set(gcf,'Colormap',jet)
set(gca,'Nextplot','add')
c=coneplot(X,Y,Z,0*dy,dy,dz,X(:,1,:),Y(:,1,:),Z(:,1:), (dy.^2+dz.^2).^...
0.5,s);
set(c,'EdgeColor','none')
%%%%%%%%%%%%%%%%%%%%%%%%%%%%%%%%%%%%%%%%%%%%%%%%%%%%%%%%%%%%%%%%%%%%%%%%
[X,Y,Z]=meshgrid(0:1,-0.72:-1.44:-6.48,3:2:39);
Ar=transpose(ar);
Az=transpose(az);
dy=zeros(5,2,19);
dz=zeros(5,2,19);
for j=1:19
dy(:,:,j)=horzcat(Ar(:,j),Ar(:,j));
dz(:,:,j)=horzcat(Az(:,j),Az(:,j));
end
c=coneplot(X,Y,Z,0*dy,-1.*dy,dz,X(:,1,:),Y(:,1,:),Z(:,1:), (dy.^2+dz.^2)...
.^0.5,s);
set(c,'EdgeColor','none')
%%%%%%%%%%%%%%%%%%%%%%%%%%%%%%%%%%%%%%%%%%%%%%%%%%%%%%%%%%%%%%%%%%%%%%%%
[X,Y,Z]=meshgrid(((0.72:1.44:6.48).^2).*0.5).^0.5,((0.72:1.44:6.48)...
.^2).*0.5).^0.5,3:2:39);
Ar=transpose(ar);
Az=transpose(az);
dy=zeros(5,5,19);
dz=zeros(5,5,19);
for j=1:19
dy(:,:,j)=horzcat(Ar(:,j),Ar(:,j),Ar(:,j),Ar(:,j),Ar(:,j));
dz(:,:,j)=horzcat(Az(:,j),Az(:,j),Az(:,j),Az(:,j),Az(:,j));
end
c=coneplot(X,Y,Z,dy,1.*dy,dz,X(1,1,:),Y(1,1,:),Z(1,1:), (dy.^2+dz.^2)...
.^0.5,s);
set(c,'EdgeColor','none')
c=coneplot(X,Y,Z,dy,1.*dy,dz,X(2,2,:),Y(2,2,:),Z(2,2:), (dy.^2+dz.^2)...
.^0.5,s);
set(c,'EdgeColor','none')
c=coneplot(X,Y,Z,dy,1.*dy,dz,X(3,3,:),Y(3,3,:),Z(3,3:), (dy.^2+dz.^2)...
.^0.5,s);
set(c,'EdgeColor','none')
c=coneplot(X,Y,Z,dy,1.*dy,dz,X(4,4,:),Y(4,4,:),Z(4,4:), (dy.^2+dz.^2)...
.^0.5,s);
set(c,'EdgeColor','none')
c=coneplot(X,Y,Z,dy,1.*dy,dz,X(5,5,:),Y(5,5,:),Z(5,5:), (dy.^2+dz.^2)...
.^0.5,s);
set(c,'EdgeColor','none')
%%%%%%%%%%%%%%%%%%%%%%%%%%%%%%%%%%%%%%%%%%%%%%%%%%%%%%%%%%%%%%%%%%%%%%%%
[X,Y,Z]=meshgrid(-1.*((0.72:1.44:6.48).^2).*0.5).^0.5,-1.*...

```

```

        ((0.72:1.44:6.48).^2).*0.5).^0.5,3:2:39);
Ar=transpose(-1.*ar);
Az=transpose(az);
dy=zeros(5,5,19);
dz=zeros(5,5,19);
for j=1:19
dy(:,:,j)=horzcat(Ar(:,j),Ar(:,j),Ar(:,j),Ar(:,j),Ar(:,j));
dz(:,:,j)=horzcat(Az(:,j),Az(:,j),Az(:,j),Az(:,j),Az(:,j));
end
c=coneplot(X,Y,Z,dy,1.*dy,dz,X(1,1,:),Y(1,1,:),Z(1,1:), (dy.^2+dz.^2)...
.^0.5,s);
set(c,'EdgeColor','none')
c=coneplot(X,Y,Z,dy,1.*dy,dz,X(2,2,:),Y(2,2,:),Z(2,2:), (dy.^2+dz.^2)...
.^0.5,s);
set(c,'EdgeColor','none')
c=coneplot(X,Y,Z,dy,1.*dy,dz,X(3,3,:),Y(3,3,:),Z(3,3:), (dy.^2+dz.^2)...
.^0.5,s);
set(c,'EdgeColor','none')
c=coneplot(X,Y,Z,dy,1.*dy,dz,X(4,4,:),Y(4,4,:),Z(4,4:), (dy.^2+dz.^2)...
.^0.5,s);
set(c,'EdgeColor','none')
c=coneplot(X,Y,Z,dy,1.*dy,dz,X(5,5,:),Y(5,5,:),Z(5,5:), (dy.^2+dz.^2)...
.^0.5,s);
set(c,'EdgeColor','none')
%%%%%%%%%%%%%%%%%%%%%%%%%%%%%%%%%%%%%%%%%%%%%%%%%%%%%%%%%%%%%%%%%%%%%%%%
[X,Y,Z]=meshgrid(((0.72:1.44:6.48).^2).*0.5).^0.5,-1.*...
((0.72:1.44:6.48).^2).*0.5).^0.5,3:2:39);
Ar=transpose(-1.*ar);
Az=transpose(az);
dy=zeros(5,5,19);
dz=zeros(5,5,19);
for j=1:19
dy(:,:,j)=horzcat(Ar(:,j),Ar(:,j),Ar(:,j),Ar(:,j),Ar(:,j));
dz(:,:,j)=horzcat(Az(:,j),Az(:,j),Az(:,j),Az(:,j),Az(:,j));
end
c=coneplot(X,Y,Z,-1.*dy,1.*dy,dz,X(1,1,:),Y(1,1,:),Z(1,1:), (dy.^2+dz...
.^2).^0.5,s);
set(c,'EdgeColor','none')
c=coneplot(X,Y,Z,-1.*dy,1.*dy,dz,X(2,2,:),Y(2,2,:),Z(2,2:), (dy.^2+dz...
.^2).^0.5,s);
set(c,'EdgeColor','none')
c=coneplot(X,Y,Z,-1.*dy,1.*dy,dz,X(3,3,:),Y(3,3,:),Z(3,3:), (dy.^2+dz...
.^2).^0.5,s);
set(c,'EdgeColor','none')
c=coneplot(X,Y,Z,-1.*dy,1.*dy,dz,X(4,4,:),Y(4,4,:),Z(4,4:), (dy.^2+dz...
.^2).^0.5,s);
set(c,'EdgeColor','none')
c=coneplot(X,Y,Z,-1.*dy,1.*dy,dz,X(5,5,:),Y(5,5,:),Z(5,5:), (dy.^2+dz...
.^2).^0.5,s);
set(c,'EdgeColor','none')
%%%%%%%%%%%%%%%%%%%%%%%%%%%%%%%%%%%%%%%%%%%%%%%%%%%%%%%%%%%%%%%%%%%%%%%%
[X,Y,Z]=meshgrid(-1.*((0.72:1.44:6.48).^2).*0.5).^0.5,1.*...
((0.72:1.44:6.48).^2).*0.5).^0.5,3:2:39);
Ar=transpose(1.*ar);
Az=transpose(az);
dy=zeros(5,5,19);
dz=zeros(5,5,19);
for j=1:19
dy(:,:,j)=horzcat(Ar(:,j),Ar(:,j),Ar(:,j),Ar(:,j),Ar(:,j));

```

```

dz(:,:,j)=horzcat(Az(:,j),Az(:,j),Az(:,j),Az(:,j),Az(:,j));
end
c=coneplot(X,Y,Z,-1.*dy,1.*dy,dz,X(1,1,:),Y(1,1,:),Z(1,1:,:),(dy.^2+dz...
.^2).^0.5,s);
set(c,'EdgeColor','none')
c=coneplot(X,Y,Z,-1.*dy,1.*dy,dz,X(2,2,:),Y(2,2,:),Z(2,2:,:),(dy.^2+dz...
.^2).^0.5,s);
set(c,'EdgeColor','none')
c=coneplot(X,Y,Z,-1.*dy,1.*dy,dz,X(3,3,:),Y(3,3,:),Z(3,3:,:),(dy.^2+dz...
.^2).^0.5,s);
set(c,'EdgeColor','none')
c=coneplot(X,Y,Z,-1.*dy,1.*dy,dz,X(4,4,:),Y(4,4,:),Z(4,4:,:),(dy.^2+dz...
.^2).^0.5,s);
set(c,'EdgeColor','none')
c=coneplot(X,Y,Z,-1.*dy,1.*dy,dz,X(5,5,:),Y(5,5,:),Z(5,5:,:),(dy.^2+dz...
.^2).^0.5,s);
set(c,'EdgeColor','none')
%%%%%%%%%%%%%%%%%%%%%%%%%%%%%%%%%%%%%%%%%%%%%%%%%%%%%%%%%%%%%%%%%%%%%%%%
[X,Y,Z]=meshgrid(0.72:1.44:6.48,0:1,3:2:39);
Ar=(ar);
Az=(az);
dy=zeros(2,5,19);
dz=zeros(2,5,19);
for j=1:19
dy(:,:,j)=vertcat(Ar(j,:),Ar(j,:));
dz(:,:,j)=vertcat(Az(j,:),Az(j,:));
end
c=coneplot(X,Y,Z,1*dy,0*dy,dz,X(1,::),Y(1,::),Z(1,::), (dy.^2+dz.^2)...
.^0.5,s);
set(c,'EdgeColor','none')
%%%%%%%%%%%%%%%%%%%%%%%%%%%%%%%%%%%%%%%%%%%%%%%%%%%%%%%%%%%%%%%%%%%%%%%%
[X,Y,Z]=meshgrid(-0.72:-1.44:-6.48,0:1,3:2:39);
Ar=(ar);
Az=(az);
dy=zeros(2,5,19);
dz=zeros(2,5,19);
for j=1:19
dy(:,:,j)=vertcat(Ar(j,:),Ar(j,:));
dz(:,:,j)=vertcat(Az(j,:),Az(j,:));
end
c=coneplot(X,Y,Z,-1*dy,0*dy,dz,X(1,::),Y(1,::),Z(1,::), (dy.^2+dz.^2)...
.^0.5,s);
set(c,'EdgeColor','none')
%%%%%%%%%%%%%%%%%%%%%%%%%%%%%%%%%%%%%%%%%%%%%%%%%%%%%%%%%%%%%%%%%%%%%%%%
%Cylinder outline.
[th,r]=meshgrid((0:5:360)*pi/180,7.2);
[X,Y]=pol2cart(th,r);
p1=plot3(X,Y,2*ones(1,73));
set(p1,'Color','k')
p2=plot3(X,Y,40*ones(1,73));
set(p2,'Color','k')
l1=line([0 0],[7.2 7.2],[2 40]);
set(l1,'Color','k')
l2=line([-7.2 -7.2],[0 0],[2 40]);
set(l2,'Color','k')
l3=line([0 0],[-7.2 -7.2],[2 40]);
set(l3,'Color','k')
l4=line([7.2 7.2],[0 0],[2 40]);
set(l4,'Color','k')

```

```

set(gca, 'FontSize', 12, 'FontName', 'Times')
xlabel('{\it{r}} (cm)')
ylabel('{\it{r}} (cm)')
zlabel('{\it{z}} (cm)')
colorbar
hold off

```

## occupancy.m

```

%occupancy.m
%m-file for the calculation of swarf occupancy from ASCII text file of
%the TRACK algorithm
clear all; data=load('40.txt'); %40.txt is the ASCII text file
data1=data;
data(:,9)=1:length(data(:,1));
data1(any(data1(:,5)>0.4,2),:)=[];
x=(data1(:,2)-((max(data1(:,2))+min(data1(:,2)))/2));
y=(data1(:,4)-((max(data1(:,4))+min(data1(:,4)))/2));
z=data1(:,3);
r=(x.^2+y.^2).^0.5;
max_x=max(data1(:,2));
max_y=max(data1(:,4));
min_x=min(data1(:,2));
min_y=min(data1(:,4));
max_r=max(r)
min_z=min(z);
data(any(data(:,5)>10,2),:)=[];
x1=(data(:,2)-(max_x+min_x)/2);
y1=(data(:,4)-(max_y+min_y)/2);
z1=data(:,3);
time=data(:,1);
r1=(x1.^2+y1.^2).^0.5;
m1(:,1)=r1;m1(:,2)=z1;m1(:,3)=data(:,9);m1(:,4)=time;
total_events=length(data(:,1));
delta_z=20;
div_r=5;
for j=1:19
for n=1:div_r
m=m1;
m(any(m(:,1)>n*(max_r)/div_r,2),:)=[];
m(any(m(:,1)<(n-1)*(max_r)/div_r,2),:)=[];
m(any(m(:,2)>min_z+20+j*delta_z,2),:)=[];
m(any(m(:,2)<min_z+20+(j-1)*delta_z,2),:)=[];
o(n,j)=length(m(:,1));
end
end
occu=100.*(transpose(o))./length(m1(:,1));
dlmwrite('occu.txt',occu,'delimiter','\t')
scrsz=get(0,'ScreenSize');
figure('Position',[1 scrsz(4)/6 scrsz(3)/3.6 scrsz(4)/1]);
set(gca, 'FontSize', 12, 'FontName', 'Times', ...
'XTick', 0:1.44:7.2, 'YTick', 2:2:40, ...
'YAxisLocation', 'right')
[X,Y]=meshgrid(0:1.44:7.2, 2:2:40);
hold on
colormap gray
[Xq,Yq]=meshgrid(0.72:1.44:6.48, 3:2:39);

```

```

[xi,yi]=meshgrid(0.72:0.01:6.48,3:0.01:39);
zi=interp2(Xq,Yq,occu,xi,yi,'cubic');
contourf(xi,yi,zi,100,'LineStyle','none')
colorbar('FontSize',12,'FontName','Times','Location','WestOutside',...
'YTickLabel',{'0%','0.2%','0.4%','0.6%','0.8%','1%','1.2%','1.4%',...
'1.6%','1.8%','2.0%'})
hold off
axis equal
axis([0 7.2 2 40])
xlabel('\it{r} (cm)')
ylabel('\it{z} (cm)')

```

## dirichlet.m

```

function BC_first_kind(b)
format shorte
%parameters
a=144e-3/2;noBm=30000;it=40;root=zeros(it,noBm);k=9.8;rho=8440;cp=410;
alpha=k/(rho*cp);t=0:(alpha/b^2)*1:(alpha/b^2)*100;
%bisection method applied to transcendental equation
for m=1:noBm;
m
if rem(m,2)==0
x=root(it,m-1)+1:10:root(it,m-1)+100;
for n=1:length(x)
if (besselj(0,x(n).*(a/b)))*(bessely(1,x(n).*1)-(besselj(1,x(n).*1))*...
(bessely(0,x(n).*(a/b)))<0;break;end
l=n+1;
end
delta=(x(l)-x(l-1))/2;
ihalf=x(l-1)+delta;
for i=1:it
if (besselj(0,ihalf.*(a/b)))*(bessely(1,ihalf.*1)-(besselj(1,ihalf.*...
1))*(bessely(0,ihalf.*(a/b)))>0
ihalf=ihalf+(1/2^i)*delta;
root(i,m)=ihalf;
else
ihalf=ihalf-(1/2^i)*delta;
root(i,m)=ihalf;
end
end
else
if m==1
u=root(it,m)+1:10:root(it,m)+100;
else
u=root(it,m-1)+10:1:root(it,m-1)+100;
end
for p=1:length(u)
if (besselj(0,u(p).*(a/b)))*(bessely(1,u(p).*1)-(besselj(1,u(p).*1))*...
(bessely(0,u(p).*(a/b)))>0;break;end
e=p+1;
end
delta=(u(e)-u(e-1))/2;
ihalf=u(e-1)+delta;
for i=1:it
if (besselj(0,ihalf.*(a/b)))*(bessely(1,ihalf.*1)-(besselj(1,ihalf.*...
1))*(bessely(0,ihalf.*(a/b)))<0

```



```

ihalf=ihalf+(1/2^i)*delta;
root(i,m)=ihalf;
else
ihalf=ihalf-(1/2^i)*delta;
root(i,m)=ihalf;
end
end
end
end
%eigenvalue vector
Bm=zeros(1,noBm);
for i=1:noBm
Bm(i)=root(it,i);
end
%normalisation coefficient vector
N=zeros(1,noBm);
i=1:noBm;
N(i)=0.5.*(bessely(1,Bm(i).*1).^2).* (1.^2).* (besselj(0,Bm(i).*1).^2)-...
0.5.*(bessely(1,Bm(i).*1).^2).* ((a./b).^2).* (besselj(1,Bm(i).* (a./b)).^2)-
...
0.5.*(bessely(1,Bm(i).*1).^2).* ((a./b).^2).* (besselj(0,Bm(i).* (a./b)).^2)-
...
bessely(1,Bm(i).*1).*besselj(1,Bm(i).*1).* (1.^2).*besselj(0,Bm(i).*1).*...
bessely(0,Bm(i).*1)+...
bessely(1,Bm(i).*1).*besselj(1,Bm(i).*1).* ((a./b).^2).*besselj(1,Bm(i).*...
(a./b)).*bessely(1,Bm(i).* (a./b))+...
bessely(1,Bm(i).*1).*besselj(1,Bm(i).*1).* ((a./b).^2).*besselj(0,Bm(i).*...
(a./b)).*bessely(0,Bm(i).* (a./b))+...
0.5.*(besselj(1,Bm(i).*1).^2).* (1.^2).* (bessely(0,Bm(i).*1).^2)-...
...
0.5.*(besselj(1,Bm(i).*1).^2).* ((a./b).^2).* (bessely(1,Bm(i).* (a./b)).^2)-
...
0.5.*(besselj(1,Bm(i).*1).^2).* ((a./b).^2).* (bessely(0,Bm(i).* (a./b)).^2);
%auxiliary solution for unit temperature rise
sol=zeros(noBm,length(t));
for m=1:noBm
n=1:length(t);
sol(m,n)=((a/b).* (N(m)).^-1).* (besselj(0,Bm(m).*1).*bessely(1,Bm(m).*...
1)-besselj(1,Bm(m).*1).*bessely(0,Bm(m).*1)).*(Bm(m).^-1).*...
(1-exp(-1.*Bm(m).^2.*t(n))).*(besselj(1,Bm(m).*1).*...
bessely(1,Bm(m).* (a./b))-besselj(1,Bm(m).* (a./b)).*bessely(1,Bm(m).*1)).*1);
end
transpose(sum(sol))%auxiliary temperature vector
dlmwrite('T_9.8n130.txt',transpose(sum(sol)), 'delimiter','\t',...
'precision',8)

```

## neumann.m

```

function BC_second_kind(b)
format shorte
%parameters
a=144e-3/2;noBm=30000;it=40;root=zeros(it,noBm);k=9.8;rho=8440;cp=410;
alpha=k/(rho*cp);mT=b/k;t=0:(alpha/b^2)*1:(alpha/b^2)*140;
%bisection method applied to transcendental equation
for m=1:noBm;
m

```

```

if rem(m,2)==0
x=root(it,m-1)+1:1:root(it,m-1)+100;
for n=1:length(x)
if (besselj(1,x(n).*(a/b)))*(bessely(1,x(n).*1)-(besselj(1,x(n).*1))*...
    (bessely(1,x(n).*(a/b)))>0;break;end
end
k=n+1;
delta=(x(k)-x(k-1))/2;
ihalf=x(k-1)+delta;
for i=1:it
if (besselj(1,ihalf.*(a/b)))*(bessely(1,ihalf.*1)-(besselj(1,ihalf.*...
    1))*(bessely(1,ihalf.*(a/b)))<0
ihalf=ihalf+(1/2^i)*delta;
root(i,m)=ihalf;
else
ihalf=ihalf-(1/2^i)*delta;
root(i,m)=ihalf;
end
end
else
if m==1
u=root(it,m)+1:1:root(it,m)+100;
else
u=root(it,m-1)+1:1:root(it,m-1)+100;
end
for p=1:length(u)
if (besselj(1,u(p).*(a/b)))*(bessely(1,u(p).*1)-(besselj(1,u(p).*1))*...
    (bessely(1,u(p).*(a/b)))<0;break;end
d=p+1;
end
delta=(u(d)-u(d-1))/2;
ihalf=u(d-1)+delta;
for i=1:it
if (besselj(1,ihalf.*(a/b)))*(bessely(1,ihalf.*1)-(besselj(1,ihalf.*...
    1))*(bessely(1,ihalf.*(a/b)))>0
ihalf=ihalf+(1/2^i)*delta;
root(i,m)=ihalf;
else
ihalf=ihalf-(1/2^i)*delta;
root(i,m)=ihalf;
end
end
end
end
%eigenvalue vector
Bm=zeros(1,noBm);
for i=1:noBm
Bm(i)=root(it,i);
end
%normalisation coefficient vector
N=zeros(1,noBm);
i=1:noBm;
N(i)=0.5.*(bessely(1,Bm(i).*1).^2).*(1.^2).*(besselj(0,Bm(i).*1).^2)-...
0.5.*(bessely(1,Bm(i).*1).^2).*((a./b).^2).*(besselj(1,Bm(i).*(a./b)).^2)-...
...
0.5.*(bessely(1,Bm(i).*1).^2).*((a./b).^2).*(besselj(0,Bm(i).*(a./b)).^2)-...
...
bessely(1,Bm(i).*1).*besselj(1,Bm(i).*1).*(1.^2).*besselj(0,Bm(i).*1).*...
bessely(0,Bm(i).*1)+...

```

```

bessely(1,Bm(i).*1).*besselj(1,Bm(i).*1).*((a./b).^2).*besselj(1,Bm(i).*...
(a./b)).*bessely(1,Bm(i).*(a./b))+...
bessely(1,Bm(i).*1).*besselj(1,Bm(i).*1).*((a./b).^2).*besselj(0,Bm(i).*...
(a./b)).*bessely(0,Bm(i).*(a./b))+...
0.5.*(besselj(1,Bm(i).*1).^2).*(1.^2).*(bessely(0,Bm(i).*1).^2)-...
0.5.*(besselj(1,Bm(i).*1).^2).*((a./b).^2).*(bessely(1,Bm(i).*(a./b)).^2)-
...
0.5.*(besselj(1,Bm(i).*1).^2).*((a./b).^2).*(bessely(0,Bm(i).*(a./b)).^2);
%auxiliary solution for unit heat flux
sol=zeros(noBm,length(t));
for m=1:noBm
n=1:length(t);
if m==1
sol(m,n)=1.*(a/b).*(N(m)).^-1.*(besselj(0,Bm(m).*1).*bessely(1,Bm(m).*...
1)-besselj(1,Bm(m).*1).*bessely(0,Bm(m).*1)).*(1.*Bm(m).^2).^-1.*...
(1-exp(-1.*Bm(m).^2.*t(n))).*(besselj(0,Bm(m).*(a/b)).*...
bessely(1,Bm(m).*1)-besselj(1,Bm(m).*1).*bessely(0,Bm(m).*(a/b))).*...
1+1*(a/b)*(2/(1^2-(a/b)^2))*t(n)*1;
else
sol(m,n)=1.*(a/b).*(N(m)).^-1.*(besselj(0,Bm(m).*1).*bessely(1,Bm(m).*...
1)-besselj(1,Bm(m).*1).*bessely(0,Bm(m).*1)).*(1.*Bm(m).^2).^-1.*...
(1-exp(-1.*Bm(m).^2.*t(n))).*(besselj(0,Bm(m).*(a/b)).*...
bessely(1,Bm(m).*1)-besselj(1,Bm(m).*1).*bessely(0,Bm(m).*(a/b))).*1;
end
end
transpose(sum(sol))*mT%auxiliary temperature vector
dlmwrite('q_9.8n130.txt',transpose(sum(sol))*mT,'delimiter','\t',...
'precision',8)

```

## transient\_model.m

```

function transient_model(b,h)
format shorte
%parameters
a=144e-3/2;no_eigenvalues=30000;no_bisections=40;
root=zeros(no_bisections,no_eigenvalues);k=9.8;rho=8440;cp=410;
alpha=k/(rho*cp);t=0:1:120;
%eigenvalues
for m=1:no_eigenvalues;
m
if rem(m,2)==0
x=root(no_bisections,m-1)+1:100:root(no_bisections,m-1)+4000;
for n=1:length(x)
if -x(n)*besselj(1,x(n)*a)*bessely(1,x(n)*b)+x(n)*besselj(1,x(n)*b)*...
bessely(1,x(n)*a)-(h/k)*besselj(0,x(n)*a)*bessely(1,x(n)*b)+...
(h/k)*besselj(1,x(n)*b)*bessely(0,x(n)*a)>0;break
end
l=n+1;
end
delta=(x(l)-x(l-1))/2;
ihalf=x(l-1)+delta;
for i=1:no_bisections
if -ihalf*besselj(1,ihalf*a)*bessely(1,ihalf*b)+ihalf*besselj(1,ihalf*...
b)*bessely(1,ihalf*a)-(h/k)*besselj(0,ihalf*a)*bessely(1,ihalf*b)+...
(h/k)*besselj(1,ihalf*b)*bessely(0,ihalf*a)<0
ihalf=ihalf+(1./2.^i)*delta;
root(i,m)=ihalf;
end
end

```

```

else
ihalf=ihalf-(1/2^i)*delta;
root(i,m)=ihalf;
end
end
else
if m==1
u=root(no_bisections,m)+1:10:root(no_bisections,m)+1000;
else
u=root(no_bisections,m-1)+1:100:root(no_bisections,m-1)+4000;
end
for p=1:length(u)
if -u(p)*besselj(1,u(p)*a)*bessely(1,u(p)*b)+u(p)*besselj(1,u(p)*b)*...
bessely(1,u(p)*a)-(h/k)*besselj(0,u(p)*a)*bessely(1,u(p)*b)+...
(h/k)*besselj(1,u(p)*b)*bessely(0,u(p)*a)<0;break
end
d=p+1;
end
delta=(u(d)-u(d-1))/2;
ihalf=u(d-1)+delta;
for i=1:no_bisections
if -ihalf*besselj(1,ihalf*a)*bessely(1,ihalf*b)+ihalf*besselj(1,ihalf*...
b)*bessely(1,ihalf*a)-(h/k)*besselj(0,ihalf*a)*bessely(1,ihalf*b)+...
(h/k)*besselj(1,ihalf*b)*bessely(0,ihalf*a)>0
ihalf=ihalf+(1/2^i)*delta;
root(i,m)=ihalf;
else
ihalf=ihalf-(1/2^i)*delta;
root(i,m)=ihalf;
end
end
end
end
Bm=zeros(1,no_eigenvalues);
i=1:no_eigenvalues;
Bm(i)=root(no_bisections,i);
%normalisation coefficients
N=zeros(1,no_eigenvalues);
i=1:no_eigenvalues;
N(i)=0.5.*bessely(1,Bm(i).*b).^2.*b.^2.*besselj(0,Bm(i).*b).^2-...
0.5.*bessely(1,Bm(i).*b).^2.*a.^2.*besselj(1,Bm(i).*a).^2-...
0.5.*bessely(1,Bm(i).*b).^2.*a.^2.*besselj(0,Bm(i).*a).^2-...
bessely(1,Bm(i).*b).*besselj(1,Bm(i).*b).*b.^2.*besselj(0,Bm(i).*b).*...
bessely(0,Bm(i).*b)+bessely(1,Bm(i).*b).*besselj(1,Bm(i).*b).*a.^2.*...
besselj(1,Bm(i).*a).*bessely(1,Bm(i).*a)+bessely(1,Bm(i).*b).*...
besselj(1,Bm(i).*b).*a.^2.*besselj(0,Bm(i).*a).*bessely(0,Bm(i).*a)+...
0.5.*besselj(1,Bm(i).*b).^2.*b.^2.*bessely(0,Bm(i).*b).^2-...
0.5.*besselj(1,Bm(i).*b).^2.*a.^2.*bessely(1,Bm(i).*a).^2-...
0.5.*besselj(1,Bm(i).*b).^2.*a.^2.*bessely(0,Bm(i).*a).^2;
%solution with IC=0
sol=zeros(no_eigenvalues,length(t));
for m=1:no_eigenvalues
n=1:length(t);
sol(m,n)=(alpha*a*h*3.675*exp(1)/k).*(1./N(m)).*(besselj(0,Bm(m).*a).*...
bessely(1,Bm(m).*b)-besselj(1,Bm(m).*b).*bessely(0,Bm(m).*a)).*...
(1./(alpha.*Bm(m).^2)-1./(alpha.*Bm(m).^2-0.5).*exp(-0.5.*t(n))-1./...
(alpha.*Bm(m).^2).*exp(-alpha.*Bm(m).^2.*t(n))+1./(alpha.*Bm(m).^2-...
0.5).*exp(-alpha.*Bm(m).^2.*t(n))).*(besselj(0,Bm(m).*b).*...
bessely(1,Bm(m).*b)-besselj(1,Bm(m).*b).*bessely(0,Bm(m).*b));

```

```

end
X=transpose(sum(sol))%temperature vector

```

## IBPn.m

```

function IBP(ridge_param1,ridge_param2,Ch_no,h_f,sr)
format shorte
close all
%sensitivity matrix T
uauxT=load('T_9.8n130.txt');
length(uauxT)
max=length(uauxT)-1;
matT=zeros(length(uauxT)-1);
for i=1:max
for j=1:max
if i>=j
matT(i,j)=uauxT(2+i-j)-uauxT(1+i-j);
else
matT(i,j)=0;
end
end
end
%sensitivity matrix q
uauxq=load('q_9.8n130.txt');
max=length(uauxq)-1;
matq=zeros(length(uauxq)-1);
for i=1:max
for j=1:max
if i>=j
matq(i,j)=uauxq(2+i-j)-uauxq(1+i-j);
else
matq(i,j)=0;
end
end
end
uout=load('3_40_NaCl.txt');
%inverse solution
fmat2=zeros(length(uauxT)-1);
for n=1:length(uauxT)-3
for m=1:length(uauxT)-1
if n==m
fmat2(n,m)=1;
elseif n==m-1
fmat2(n,m)=-2;
elseif n==m-2
fmat2(n,m)=1;
end
end
end
T0=ones(1,130).*15.3;
T=transpose(T0)+(((transpose(matT)*matT+ridge_param1*transpose(fmat2)*fmat2)
)^-1)...
*(transpose(matT)*(downsample(uout(uout(1,2):uout(1,3),2*Ch_no+1),sr)-
T0(1,1))));
q=(((transpose(matq)*matq+ridge_param2*transpose(fmat2)*fmat2)
)^-1)...
*(transpose(matq)*(downsample(uout(uout(1,2):uout(1,3),2*Ch_no+1),sr)-
T0(1,1))));

```


```

%graphics
w=1:length(uauxT)-1;
scrsz=get(0,'ScreenSize');
figure('Position',[1 scrsz(4)/6 scrsz(4)/1.2 scrsz(3)/2.4]);
plot(w,T,'bo-','LineWidth',1,'MarkerFaceColor','b')
hold on
plot(w,downsample(uout(uout(1,2):uout(1,3),4),sr)-0.5,'go-','LineWidth',1)
hold off
set(gca,'FontSize',14.5,'FontName','Times','XMinorTick','on','YMinorTick','on','XGrid','on','YGrid','on')
%title('temperarure of internal surface')
legend('Inverse solution','Measured fluid temperature')
ylabel('Temperature (^oC)')
xlabel('Time (s)')
ylim([15 28])
scrsz=get(0,'ScreenSize');
figure('Position',[1 scrsz(4)/6 scrsz(4)/1.2 scrsz(3)/2.4]);
plot(w,q,'bo-','LineWidth',1,'MarkerFaceColor','b')
set(gca,'FontSize',14.5,'FontName','Times','XMinorTick','on','YMinorTick','on','XGrid','on','YGrid','on')
%title('heat flux normal to internal surface')
legend('Inverse solution')
ylabel('Heat Flux (W/m^2)')
ylim([-0.25e4 1.25e4])
xlabel('Time (s)')
scrsz=get(0,'ScreenSize');
figure('Position',[1 scrsz(4)/6 scrsz(4)/1.2 scrsz(3)/2.4]);
q./(uout(1,1+Ch_no+2*h_f)-T)
plot(w,q./(uout(1,1+Ch_no+2*h_f)-T),'ro-','MarkerFaceColor','r')
set(gca,'FontSize',14.5,'FontName','Times','XMinorTick','on','YMinorTick','on','XGrid','on','YGrid','on')
%title('heat transfer coefficient normal to internal surface')
legend('Calculated heat transfer coefficient')
ylabel('Heat Transfer Coefficient (W/m^2/^oC)')
xlabel('Time (s)')
ylim([0 6000])
%xlim([51.9 56.1])
uout(1,1+Ch_no+2*h_f)

```

# APPENDIX 4

## Schedule of Accreditation issued by United Kingdom Accreditation Service 21 - 47 High Street, Feltham, Middlesex, TW13 4UN, UK

 <b>0564</b> Accredited to <b>ISO/IEC 17025:1999</b>	<b>TC Ltd</b> <b>Issue No: 014    Issue date: 09 February 2007</b>	
	<b>Brimington Road North</b> <b>Whittington Moor</b> <b>Chesterfield</b> <b>Derbyshire</b> <b>S41 9BD</b>	<b>Contact: Mr L R Walker</b> <b>Tel: +44 (0)1246 454672</b> <b>Fax: +44 (0)1895 273540</b> <b>E-Mail: laboratory@tc.co.uk</b> <b>Website: www.tc.co.uk</b>

**Calibration performed at the above address only**

### DETAIL OF ACCREDITATION

Measured Quantity Instrument or Gauge	Range	Best Measurement Capability Expressed as an Expanded Uncertainty (k=2)	Remarks
<b>TEMPERATURE</b>			
Resistance thermometers	Triple point of water (0.01 °C) -30 °C to 200 °C 200 °C to 620 °C	0.05 °C 0.20 °C 0.6 °C	3 wire and 4 wire resistance thermometers
Thermocouples - noble metal	20 °C to 620 °C 620 °C to 1100 °C 1100 °C to 1590 °C	1.1 °C 1.3 °C 1.9 °C	
Thermocouples - base-metal	-30 °C to 200 °C 200 °C to 620 °C  620 °C to 1100 °C 1100 °C to 1370 °C	0.3 °C 0.6 °C  1.3 °C 1.9 °C	
Temperature indicators with probes	Ranges as for probe type	As for probe type	
END			



TC Ltd, Units 1-6, Brimington Road North, Chesterfield, S41 9BD, England  
 E Mail: calibration@tc.co.uk Website: www.tc.co.uk  
 Telephone: 01895 252222 Fax: 01895 273540

## CERTIFICATE OF CALIBRATION

**Date of Issue:** 30th November 2009  
**Customer:** Rolls Royce Marine Power  
**Address:** Raynesway Derby  
**Order Number:** 5200014196  
**Our Reference:** 14867C  
**Date Received:** 14th October 2009  
**Type:** K  
**Serial Number:** 09K18066 c/w 14867C/2A (Ch1) & 14867C/2C (Ch2)  
**Product Code:** HTIB-T13 High Accuracy Control Module Ranged 0.0/400°C  
 c/w 402-716 & 12-K-200-176-4.5-2G-3P4CL-2Mtrs A30KX  
**Ambient Temp:** 20°C +/- 2°C

Page 1 of 1  
**Approved Signatory**  
 L R Walker  
 I S Sheppard  
 K Donaldson

*L R Walker*

**Certificate**  
**Number : 17788 - 2A**

**Calibration Procedure:** The thermocouple and indicator were calibrated by comparison with two reference resistance thermometers. The calibration took place in a stirred liquid bath and a stirred water bath. All measurements are traceable to recognised national standards. The thermocouple wires were referenced to 0 Degrees Celsius with the cold junction of the unit under test at ambient. The resistance and voltage outputs were measured on a precision digital multimeter. All tests were carried out in a controlled environment using devices having known and traceable values. The temperature measurements are traceable to ITS-90. The thermocouple voltages were converted using IEC584-1:1995.

REFERENCE TEMPERATURE (°C)	MEASURED VOLTAGE (µV)	INDICATED TEMPERATURE (°C)	ERROR (°C)	CHANNEL NUMBER	UNCERTAINTY (+/- °C)
10.02	n/a	9.90	-0.12	1	0.3*
10.02	n/a	10.03	0.01	2	0.3*
40.03	n/a	40.08	0.05	1	0.3*
40.03	n/a	40.40	0.37	2	0.3*
70.01	n/a	69.93	-0.08	1	0.3*
70.02	n/a	70.50	0.48	2	0.3*

\* An additional value of +/- 1 least significant digit of the indicator applies to the uncertainty.  
 The depth of immersion of the test thermocouple was a minimum of 125mm  
 The resolution of the indicator was 0.1°C.

**Calibrated by:** T Heath

**Calibration date:** 25th November 2009

The reported expanded uncertainty is based on a standard uncertainty multiplied by a coverage factor of  $k = 2$ , providing a level of confidence of approximately 95%. The uncertainty evaluation has been carried out in accordance with UKAS requirements.

Note: It is the user's responsibility to determine the long-term drift and the uncertainty under the conditions of use

This certificate is issued in accordance with the laboratory accreditation requirements of the United Kingdom Accreditation Service. It provides traceability of measurement to recognised national standards, and to units of measurement realised at the National Physical Laboratory or other recognised national standards laboratories. This certificate may not be reproduced other than in full, except with the prior written approval of the issuing laboratory.

Issue 01/09





TC Ltd, Units 1-6, Brimington Road North, Chesterfield, S41 9BD, England  
 E Mail: calibration@tc.co.uk Website: www.tc.co.uk  
 Telephone: 01895 252222 Fax: 01895 273540



## CERTIFICATE OF CALIBRATION

**Date of Issue:** 30th November 2009  
**Customer:** Rolls Royce Marine Power  
**Address:** Raynesway Derby  
**Order Number:** 5200014196  
**Our Reference:** 14867C  
**Date Received:** 14th October 2009  
**Type:** K  
**Serial Number:** 09K18068 c/w 14867C/4A (Ch1) & 14867C/4C (Ch2)  
**Product Code:** HTIB-T13 High Accuracy Control Module Ranged 0.0/400°C  
 c/w 402-716 & 12-K-200-176-4.5-2G-3P4CL-2Mtrs A30KX  
**Ambient Temp:** 20°C +/- 2°C

**Page 1 of 1**  
**Approved Signatory**  
 L R Walker  
 I S Sheppard  
 K Donaldson

*L R Walker*

**Certificate**  
**Number : 17788 - 4A**

**Calibration Procedure:** The thermocouple and indicator were calibrated by comparison with two reference resistance thermometers. The calibration took place in a stirred liquid bath and a stirred water bath. All measurements are traceable to recognised national standards. The thermocouple wires were referenced to 0 Degrees Celsius with the cold junction of the unit under test at ambient. The resistance and voltage outputs were measured on a precision digital multimeter. All tests were carried out in a controlled environment using devices having known and traceable values. The temperature measurements are traceable to ITS-90. The thermocouple voltages were converted using IEC584-1:1995.

REFERENCE TEMPERATURE (°C)	MEASURED VOLTAGE (µV)	INDICATED TEMPERATURE (°C)	ERROR (°C)	CHANNEL NUMBER	UNCERTAINTY (+/- °C)
10.03	n/a	9.75	-0.28	1	0.3*
10.03	n/a	9.75	-0.28	2	0.3*
40.03	n/a	40.20	0.17	1	0.3*
40.03	n/a	40.40	0.37	2	0.3*
70.05	n/a	69.65	-0.40	1	0.3*
70.04	n/a	69.95	-0.09	2	0.3*

\* An additional value of +/- 1 least significant digit of the indicator applies to the uncertainty.  
 The depth of immersion of the test thermocouple was a minimum of 125mm  
 The resolution of the indicator was 0.1°C.

**Calibrated by:** T Heath

**Calibration date:** 25th November 2009

The reported expanded uncertainty is based on a standard uncertainty multiplied by a coverage factor of  $k = 2$ , providing a level of confidence of approximately 95%. The uncertainty evaluation has been carried out in accordance with UKAS requirements.

Note: It is the user's responsibility to determine the long-term drift and the uncertainty under the conditions of use

This certificate is issued in accordance with the laboratory accreditation requirements of the United Kingdom Accreditation Service. It provides traceability of measurement to recognised national standards, and to units of measurement realised at the National Physical Laboratory or other recognised national standards laboratories. This certificate may not be reproduced other than in full, except with the prior written approval of the issuing laboratory.

Issue 01/09



TC Ltd, Units 1-6, Brimington Road North, Chesterfield, S41 9BD, England  
 E Mail: calibration@tc.co.uk Website: www.tc.co.uk  
 Telephone: 01895 252222 Fax: 01895 273540

## CERTIFICATE OF CALIBRATION

**Date of Issue:** 30th November 2009  
**Customer:** Rolls Royce Marine Power  
**Address:** Raynesway Derby  
**Order Number:** 5200014196  
**Our Reference:** 14867C  
**Date Received:** 14th October 2009  
**Type:** K  
**Serial Number:** 09K18065 c/w 14867C/1A (Ch1) & 14867C/1C (Ch2)  
**Product Code:** HTIB-T13 High Accuracy Control Module Ranged 0.0/400°C  
 c/w 402-716 & 12-K-200-176-4.5-2G-3P4CL-2Mtrs A30KX  
**Ambient Temp:** 20°C +/- 2°C

Page 1 of 1  
**Approved Signatory**  
 L R Walker  
 I S Sheppard  
 K Donaldson

*L R Walker*

**Certificate**  
**Number : 17788 - 1A**

**Calibration Procedure:** The thermocouple and indicator were calibrated by comparison with two reference resistance thermometers. The calibration took place in a stirred liquid bath and a stirred water bath. All measurements are traceable to recognised national standards. The thermocouple wires were referenced to 0 Degrees Celsius with the cold junction of the unit under test at ambient. The resistance and voltage outputs were measured on a precision digital multimeter. All tests were carried out in a controlled environment using devices having known and traceable values. The temperature measurements are traceable to ITS-90. The thermocouple voltages were converted using IEC584-1:1995.

REFERENCE TEMPERATURE (°C)	MEASURED VOLTAGE (µV)	INDICATED TEMPERATURE (°C)	ERROR (°C)	CHANNEL NUMBER	UNCERTAINTY (+/- °C)
10.02	n/a	10.03	0.01	1	0.3*
10.02	n/a	10.05	0.03	2	0.3*
40.03	n/a	40.00	-0.03	1	0.3*
40.03	n/a	40.30	0.27	2	0.3*
70.02	n/a	69.78	-0.24	1	0.3*
70.01	n/a	70.48	0.47	2	0.3*

\* An additional value of +/- 1 least significant digit of the indicator applies to the uncertainty.  
 The depth of immersion of the test thermocouple was a minimum of 125mm  
 The resolution of the indicator was 0.1°C.

**Calibrated by:** T Heath

**Calibration date:** 25th November 2009

The reported expanded uncertainty is based on a standard uncertainty multiplied by a coverage factor of  $k = 2$ , providing a level of confidence of approximately 95%. The uncertainty evaluation has been carried out in accordance with UKAS requirements.

Note: It is the user's responsibility to determine the long-term drift and the uncertainty under the conditions of use

This certificate is issued in accordance with the laboratory accreditation requirements of the United Kingdom Accreditation Service. It provides traceability of measurement to recognised national standards, and to units of measurement realised at the National Physical Laboratory or other recognised national standards laboratories. This certificate may not be reproduced other than in full, except with the prior written approval of the issuing laboratory.

Issue 01/09



TC Ltd, Units 1-6, Brimington Road North, Chesterfield, S41 9BD, England  
 E Mail: calibration@tc.co.uk Website: www.tc.co.uk  
 Telephone: 01895 252222 Fax: 01895 273540

## CERTIFICATE OF CALIBRATION

**Date of Issue:** 30th November 2009  
**Customer:** Rolls Royce Marine Power  
**Address:** Raynesway Derby  
**Order Number:** 5200014196  
**Our Reference:** 14867C  
**Date Received:** 14th October 2009  
**Type:** K  
**Serial Number:** 09K18067 c/w 14867C/3A (Ch1) & 14867C/3C (Ch2)  
**Product Code:** HTIB-T13 High Accuracy Control Module Ranged 0.0/400°C  
 c/w 402-716 & 12-K-200-176-4.5-2G-3P4CL-2Mtrs A30KX  
**Ambient Temp:** 20°C +/- 2°C

**Page 1 of 1**  
**Approved Signatory**  
 L R Walker  
 I S Sheppard  
 K Donaldson

*L R Walker*

**Certificate**  
**Number : 17788 - 3A**

**Calibration Procedure:** The thermocouple and indicator were calibrated by comparison with two reference resistance thermometers. The calibration took place in a stirred liquid bath and a stirred water bath. All measurements are traceable to recognised national standards. The thermocouple wires were referenced to 0 Degrees Celsius with the cold junction of the unit under test at ambient. The resistance and voltage outputs were measured on a precision digital multimeter. All tests were carried out in a controlled environment using devices having known and traceable values. The temperature measurements are traceable to ITS-90. The thermocouple voltages were converted using IEC584-1:1995.

REFERENCE TEMPERATURE (°C)	MEASURED VOLTAGE (µV)	INDICATED TEMPERATURE (°C)	ERROR (°C)	CHANNEL NUMBER	UNCERTAINTY (+/- °C)
10.02	n/a	9.95	-0.07	1	0.3*
10.02	n/a	9.78	-0.24	2	0.3*
40.03	n/a	39.98	-0.05	1	0.3*
40.03	n/a	40.10	0.07	2	0.3*
70.02	n/a	69.83	-0.19	1	0.3*
70.01	n/a	70.48	0.47	2	0.3*

\* An additional value of +/- 1 least significant digit of the indicator applies to the uncertainty.  
 The depth of immersion of the test thermocouple was a minimum of 125mm  
 The resolution of the indicator was 0.1°C.

**Calibrated by:** T Heath

**Calibration date:** 25th November 2009

The reported expanded uncertainty is based on a standard uncertainty multiplied by a coverage factor of  $k = 2$ , providing a level of confidence of approximately 95%. The uncertainty evaluation has been carried out in accordance with UKAS requirements.

Note: It is the user's responsibility to determine the long-term drift and the uncertainty under the conditions of use

This certificate is issued in accordance with the laboratory accreditation requirements of the United Kingdom Accreditation Service. It provides traceability of measurement to recognised national standards, and to units of measurement realised at the National Physical Laboratory or other recognised national standards laboratories. This certificate may not be reproduced other than in full, except with the prior written approval of the issuing laboratory.

Issue 01/09

## REFERENCES

- Alifanov, O. M., (1994) Inverse heat transfer problems. Berlin: Springer-Verlag.
- Antanovskii, L. K. (1995) A phase field model of capillarity. **Physics of fluids**, 7: 747-753
- Atkins, P. W. (1998) Physical chemistry. 6<sup>th</sup> ed. Oxford: Oxford University Press
- Bakalis, S., Fryer, P. J. (2004) Measuring velocity distributions of viscous fluids using positron emission particle tracking (PEPT). **American Institute of Chemical Engineers**, 50 (7): 1606-1613
- Batchelor, G. K. (1994) An introduction to fluid dynamics. Cambridge: Cambridge University Press.
- Beck, J. V. (1967) Surface heat flux determination using an integral method. **Nuclear Engineering and Design**, 7: 170-178
- Beck, J. V. (1977) Criteria for comparison of methods of solution of the inverse heat conduction problem. **Nuclear Engineering and Design**, 53: 11-22
- Beck, J. V., Blackwell, B., Charles R. St. Clair. (1985) Inverse heat conduction. New York: John Wiley & Sons, Inc.
- Boas, M. L. (1983) Mathematical methods in the physical sciences. Canada: John Wiley & Sons.
- Bradshaw, P. (1970) Experimental fluid mechanics. 2<sup>nd</sup> ed. Oxford: Pergamon Press Ltd.
- Bradshaw, P. (eds.) (1978) Turbulence. 2<sup>nd</sup> ed. Berlin: Springer-Verlag.
- Bureau International des Poids et Mesures. (2006) The International System of Units (SI). 8<sup>th</sup> ed. Sèvres: Bureau International des Poids et Mesures.
- Cahn, J. W., Hilliard, J. E. (1958) Free energy of a nonuniform system. I. Interfacial Free Energy, **Journal of Chemical Physics**, 28: 258-267
- Carslaw, H. S., Jaeger, J. C. (1947) Conduction of heat in solids. Oxford: Clarendon Press.
- Chitti, F., Bakalis, S., Bujalski, W. et al. (2011) Using positron emission particle tracking (PEPT) to study the turbulent flow in a baffled vessel agitated by a Rushton turbine: Improving data treatment and validation. **Chemical Engineering Science**, 89: 1947-1960
- COMSOL AB. (2008) Modeling Guide. Version 3.5 a.
- COMSOL AB. (2013) CFD Module User's Guide. Version 4.3 b.

- Cordfunke, E. H. P., Ouweltjes, W., Vlanderen, P. van (1989) The standard molar enthalpies of formation of the lithium zirconates. **Journal of Chemical Thermodynamics**, 21: 1095-1100
- Coulson, J. M., Richardson, J. F., Backhurst, J. R., Harker, J. H. (2003) Fluid flow, heat transfer and mass transfer. Oxford: Butterworth-Heinemann.
- Deckwer, W-D. (1992) Bubble column reactors. Chichester: John Wiley & Sons Ltd.
- Degaleesan, S, Dudukovic, M, Pan, Y, (2001) Experimental study of gas-induced liquid-flow structures in bubble columns. **American Institute of Chemical Engineers**, 47 (9): 1913-1931
- Drew, A. D., Passman, S. L. (1999) Theory of multicomponent fluids. New York: Springer-Verlag.
- Duhamel, J. M. C. (1830) Mémoire sur la méthode générale relative au mouvement de la chaleur dans les corps solides plongés dans un milieu dont la température varie avec le temps. **Journal de l'Ecole Polytechnique**, 14: 20-77
- Fan, L-S. and Tsuchiya, K. (1990) Bubble wake dynamics in liquids and liquid-solid suspensions. Boston: Butterworth-Heinemann.
- Fan, X., Parker, D. J., Smith, M. D. (2006) Labelling a single particle for positron emission particle tracking using direct activation and ion-exchange techniques. **Nuclear Instruments and Methods in Physics Research Section A**, 562: 345-350
- Fornberg, B. (1988) Generation of finite difference formulas on arbitrarily spaced grids. **American Mathematical Society**, 51: 699-706
- Freedman, W, PhD Thesis, University of Cambridge, 1968.
- Gebhart, B., Jaluria, Y., Mahajan, R. L., Sammakia, B. (1988) Buoyancy induced flows and transport. New York: Hemisphere Publishing Corporation.
- Goldstein, R. J. (1983) Fluid mechanics measurements. Washington: Hemisphere Publishing Corporation.
- Guida, A., Nienow, A. W., Barigou, M. (2010) PEPT measurements of solid-liquid flow field and spatial phase distribution in concentrated monodisperse stirred suspensions. **Chemical Engineering Science**, 65: 1905-1914
- Haimes, Y. Y. (2009) "Risk Management." In Sage, A. P., Rouse, W. B. (ed.) **Handbook of systems engineering and management**. Hoboken, New Jersey: John Wiley & Sons, Inc. pp. 155-201

Hawkesworth, M. R., O'Dwyer, M. A. Walker, J. et al. (1986) A positron camera for industrial application. **Nuclear Instruments and Methods in Physics Research Section A: Accelerators, Spectrometers, Detectors and Associated Equipment**, 253 (1): 145-157

Hazelrigg, G. A. (1996) Systems engineering: An approach to information-based design. Prentice Hall.

Heinz, S. (2003) Statistical mechanics of turbulent flows. Berlin: Springer.

Henein, H., Brimacombe, J. K., Watkinson, A. P. (1983) Experimental study of transverse bed motion in rotary kilns. **Metallurgical and Material Transactions B**, 14: 191-205

Hills, J. H. (1974) Radial non-uniformity of velocity and voidage in a bubble column. **Institution of Chemical Engineers**, 52: 1-9

Hinze, J. O. (1975) Turbulence. 2<sup>nd</sup> ed. New York: McGraw-Hill Book Company.

Hood, C., Jones, D. K. C. (1996) Accident and design: contemporary debates in risk management. London: UCL Press.

Imber, M., Khan, J. (1972) Prediction of transient temperature distributions with embedded thermocouples. **AIAA Journal**, 10: 784-789

Jacqmin, D. (1999) Calculation of two-phase Navier-Stokes flows using phase field modelling. **Journal of Computational Physics**, 155: 96-127

Kantarci, N., Borak, F., Ulgen, K. O. (2005) Bubble column reactors. **Process Biochemistry**, 40: 2263-2283

Kim, S. D., Kang, Y., Kwon, H. K. (1986) Heat transfer characteristics in two- and three-phase slurry-fluidized beds. **American Institute of Chemical Engineers Journal**, 32: 1397-1400

Klein, R., Jacob, I., O'Hare, P. A. G., Goldberg, R. N. (1994) Solution-calorimetric determination of the standard molar enthalpies of formation of the pseudobinary compounds  $Zr(Al_xFe_{1-x})_2$  at the temperature 298.15 K. **Journal of Chemical Thermodynamics**, 26: 599-608

Kletz (1998) Process plant: A handbook for inherently safer design. Philadelphia: Taylor & Francis.

Kumar, S., Kusakabe, K., Raghunathan, K., Fan, L.-S (1992) Mechanism of heat transfer in bubbly liquid and liquid-solid systems: single bubble injection. **American Institute of Chemical Engineers Journal**, 38: 733-741

Laufer, J. (1975) New trends in experimental turbulence research. **Annual Review of Fluid Mechanics**, 7: 307-326



- Leadbeater, T. W., Parker, D. J., Gargiuli, J. (2012) Positron imaging systems for studying particulate, granular and multiphase flows. **Particuology**, 10: 146-153
- Li, H., Prakash, A. (2002) Analysis of flow patterns in bubble and slurry bubble columns based on local heat transfer measurements. **Chemical Engineering Journal**, 86: 269-276
- Liu, W., Takase, K. (2012) Development of measurement technology for surface heat fluxes and temperatures. **Nuclear engineering and design**, 249: 166-171
- Lu, P-C. (1977) Introduction to the mechanics of viscous fluids. London: Hemisphere Publishing Corporation.
- McComb, W. D. (1990) The physics of fluid turbulence. Oxford: Oxford University Press.
- McQuarrie, D. A., Simon, J. D. (1997) Physical chemistry – A molecular approach. Sausalito: University Science Books.
- Menzel, T., in der Weide, T. and Staudacher, O. et al. (1990) Reynolds shear stress for modelling of bubble column reactors. **Industrial & Engineering Chemistry Research**, 29: 988-993
- Morse, M. P., Feshbach, H. (1953) Methods of theoretical physics. New York: McGraw-Hill Book Company
- Ottino, J.M. (1990) The kinematics of mixing: stretching, chaos, and transport. Cambridge: Cambridge University Press.
- Özisik, M. N. (1968) Boundary value problems of heat conduction. Scranton: International Textbook Company.
- Özisik, M. N. (1993) Heat conduction. 2<sup>nd</sup> ed. New York: John Wiley & Sons, INC.
- Parker, D. J., Broadbent, C. J., Fowles, P. et al (1993) Positron emission particle tracking – a technique for studying flow within engineering equipment. **Nuclear Instruments and Methods in Physics Research Section A: Accelerators, Spectrometers, Detectors and Associated Equipment**, 326 (3): 592-607
- Parker, D. J., Allen, D. A., Benton, D. M. et al. (1997a) Developments in particle tracking using the Birmingham positron camera. **Nuclear Instruments and Methods in Physics Research Section A: Accelerators, Spectrometers, Detectors and Associated Equipment**, 392: 421-426
- Parker, D. J., Dijkstra, A. E., Martin, T. W., Seville, J. P. K. (1997b) Positron emission particle tracking studies on spherical particle motion in rotating drums. **Chemical Engineering Science**, 52 (13): 2011-2022

- Parker, D. J., Forster, R. N., Fowles, P., Takhar, P. S. (2002) Positron emission particle tracking using the new Birmingham positron camera. **Nuclear Instruments and Methods in Physics Research Section A: Accelerators, Spectrometers, Detectors and Associated Equipment**, 477: 540-545
- Pentz, M. and Shott, M. (1988) Handling experimental data. Milton Keynes: Open University Press.
- Prakash, A. (1999) Analysis of bubble dynamics and local hydrodynamics based on instantaneous heat transfer measurements in a slurry bubble column. *Chemical Engineering Science*, 54: 5265-5271
- Prakash, A., Margaritis, A., Bergougnou, M. A. (2001) Hydrodynamics and local heat transfer measurements in a bubble column with suspension of yeast. **Biochemical Engineering Journal**, 9: 155-163
- Reynolds, O. (1883) An experimental investigation of the circumstances which determine whether the motion of water shall be direct or sinuous, and of the law of resistance in parallel channels. **Philosophical Transactions**, 174: 935-982
- Riley, K. F., Hobson, M. P., Bence S. J. (2001) Mathematical methods for physics and engineering. Cambridge: Cambridge University Press.
- Rogers, G. F. C., Mayhew, Y. R. (1980) Thermodynamic and transport properties of fluids. 3<sup>rd</sup> ed. Oxford: Basil Blackwell
- Rowlinson, J. S. (1978) Translation of J. D. Van der waals' "The thermodynamic theory of capillarity under the hypothesis of a continuous variation of density". **Journal of Statistical Physics**, 20: 197-244
- Schön, D. A. (1983) The reflective practitioner: how professionals think in action. New York: Basic Books.
- Scott, E. P., Beck, J. V. (1985) "Analysis of order of sequential regularisation solution of inverse heat conduction problem." In **Winter Annual Meeting of The American Society of Mechanical Engineers. Miami Beach, Florida, 17-21 November 1985**. pp.1-8.
- Stewart, P. A. E., Rogers, J. D., Skelton, R. T. et al. (1988) "Positron emission tomography – a new technique for observing fluid behaviour in engineering systems." In **4<sup>th</sup> European Conference on Non-Destructive Testing. London**. pp.2718-2726 (Pergamon, Oxford).
- Stewart, R. L., Bridgwater, J., Parker, D. J. (2001) Granular flow over a flat-bladed stirrer. **Chemical Engineering Science**, 56: 4257-4271
- Stoll, H. W. (1990) Design for manufacturing. In Allen, C. W. (ed.) Simultaneous Engineering. Dearborn, MI: SME Press.



Stolz, G., (1960) Numerical solutions to an inverse problem of heat conduction for simple shapes. **Journal of Heat Transfer**, 82: 20-26

Tennekes, H. and Lumley, J. L. (1972) A first course in turbulence. 3<sup>rd</sup> edn. Massachusetts: The MIT Press.

Tikhonov, A. N. (1963) **Soviet Mathematics**, 4: 1035-1038

Tikhonov, A. N., Glasko, V. V. (1967) **USSR Computational Mathematics and Mathematical Physics**, 7: 267-273

Tikhonov, A. N., Arsenin, V. Y. (1977) Solutions of ill-posed problems. Washington, DC: V. H. Winston & Sons.

Weber, C. F. (1981) Analysis and solution of the ill-posed inverse heat conduction problem. **International Journal of Heat and Mass Transfer**, 24: 1783-1792

White, K. P. (2009) "Systems Design." In Sage, A. P., Rouse, W. B. (ed.) **Handbook of systems engineering and management**. Hoboken, New Jersey: John Wiley & Sons, Inc. pp. 507-531

Yasuhara, M., Suh, N. P. (1980) "A quantitative analysis of design based on the axiomatic approach." In Computer Applications in Manufacturing Systems. New York: ASME Press. pp. 1-20

Yue, P., Feng, J. J., Liu, C. et al. (2004) A diffuse-interface method for simulating two-phase flows of complex fluids. **Journal of Fluid Mechanics**, 515: 293-317

Yue, P., Zhou, C., Feng, J. J. et al. (2006) Phase-field simulations of interfacial dynamics in viscoelastic fluids using finite elements with adaptive meshing. **Journal of Computational Physics**, 219: 47-67